Novel photocatalytic TiO2-based porous membranes prepared by plasma-enhanced chemical vapor deposition (PECVD) for organic pollutant degradation in water

Ming Zhou

To cite this version:

Ming Zhou. Novel photocatalytic TiO2-based porous membranes prepared by plasma-enhanced chemical vapor deposition (PECVD) for organic pollutant degradation in water. Material chemistry. Université Montpellier; Technical University of chemistry and technology (Prague); Università degli studi della Calabria. Dipartimento di Chimica e Tecnologie Chimiche, 2015. English. NNT : 2015MONTS090 . tel-01693147

HAL Id: tel-01693147

https://theses.hal.science/tel-01693147v1

Submitted on 25 Jan 2018

THESIS
To obtain the grade of Doctor

Issued by
University of Montpellier
University of Chemistry and Technology, Prague
University of Calabria

Prepared in the graduate school
Sciences Chimiques Balard (ED 459)
And research Unit
Institut Européen des Membranes IEM (UMR 5635)

Speciality:
Chemistry and Physico-chemistry of Materials

Presented by MING ZHOU

NOVEL PHOTOCATALYTIC TiO_2-BASED POROUS MEMBRANES PREPARED BY PLASMA-ENHANCED CHEMICAL VAPOR DEPOSITION (PECVD) FOR ORGANIC POLLUTANT DEGRADATION IN WATER

Defended on 23 July 2015 in front of the esteemed jury comprising

Mr. Zoltán HÓRVÖLGYI, Professor, BME Budapest	Reviewer
Mr. Petr ŠPATENKA, Professor, Czech Technical Univ. Prague	Reviewer
Mr. Jean-Christophe REMIGY, Assistant Professor, UPS Toulouse	Reviewer
Mr. Efrem CURCIO, Professor, University of Calabria	Examiner
Mr. Vasile HULEA, Professor, ENSCM Montpellier	Examiner, President of the jury
Mrs. Enrica FONTANANOVA, Research Scientist ITM-CNR Rende	Thesis co-director
Mr. Vlastimil FILA, Assistant Professor, UCTP Prague	Thesis co-director
Mr. André AYRAL, Professor, Univ. Montpellier	Thesis co-director
Mrs. Stéphanie ROUALDES, Assitant Professor, Univ. Montpellier	Thesis director

Outline

Acknowledgements

The Doctorate of Ming ZHOU has been completed at the European Institute of Membranes (IEM) and carried out in three Universities: University of Montpellier (France), University of Chemistry and Technology, Prague (Czech Republic) and University of Calabria, Rende (Italy). It was financed by the scholarship of European Commission - Education, Audiovisual and Culture Executive Agency (EACEA) under the program "Erasmus Mundus Doctorate in Membrane Engineering" (EUDIME, FPA No. 2011-0014, Edition I, http://eudime.unical.it).

Ming ZHOU would like to thank the main contributors to this work:

The three reviewers:

Mr. Zoltán HÓRVÖLGYI, *Professor, BME Budapest*

Mr. Petr ŠPATENKA, *Professor, Czech Technical Univ. Prague*

Mr. Jean-Christophe REMIGY, *Assistant Professor, UPS Toulouse*

The examiners:

Mr. Efrem CURCIO, *Professor, University of Calabria*

Mr. Vasile HULEA, *Professor, ENSCM Montpellier*

The supervisors:

Stéphanie Roualdès[1], André Ayral[1], Vlastimil Fila[2], Josef Krysa[2], Enrica Fontananova[3], Teresa Poerio[3], Enrico Drioli[3]

[1] *Institut European of Membranes (IEM), University of Montpellier, France*

[2] *University of Chemistry and Technology, Prague (UCTP), Czech Republic*

[3] *Institute on Membrane Technology (ITM), University of Calabria, Rende, Italy*

Introduction

Wastewater source is consisting of industrial, municipal and agricultural water discharges. Globally there is about 171 km^3 of wastewater produced annually including liquid releases from homes, businesses, industries and storm water run-off. [1] Each year from 40% to 60% of energy consumption has been utilized for operations and maintenances in treating wastewater and the total expense of power used for wastewater treatment is $10 billion a year on the earth. [1] Industry processes including paper manufacture, dyeing, painting, coaling and mining have employed a great amount of water due to washing, mixing and cooling. Removal of toxic organic contaminants (e.g. alkanes, alcohols, haloalkanes and aromatics) from high-level contaminant wastewater before discharging is supervised by environmental legalization. On the other hand, reusing the low-level wastewater (from municipal and rural discharges) for agricultural and industrial purposes is one appealing strategy to offset the clean water distributions. However, the presence of organic pollutants keeps arising in the releases from households, hospitals and rural areas due to increasing consumption of chemicals. Efficient and less costly treating process for sorts of discharged water is required today.

In typical wastewater treatment (WWT) routine, physical, chemical and biological approaches are accordingly performed. Adsorption and coagulation procedures are first operated to remove solids and large particles from water. Filtration, sedimentation and membrane separation could concentrate soluble pollutants into another phase but with no degradation consequence. Oxidation and decomposition of tedious contaminants can be carried out through chemical and/or biological pathways, however, sometimes the chemical process can possibly bring additives and/or by-products as a secondary pollution to the water. A conception of advanced oxidation processes (AOPs) was stated by Glaze and et al. in 1987 [2], which lead to a rapid development in the field as innovative water treatment technology. Oxidation processes are carried out through in-situ hydroxyl radical $^{\bullet}OH$ having high oxidation potential as E^0 ($^{\bullet}OH_{aq}/H_2O$) = 2.59 V at pH=0. [3] Some other strong reactive oxygen species (ROSs) such as $^{\bullet}O_2^{-}$, O_3 and H_2O_2 might be also involved in the processes. AOPs are particularly effective in eliminating stubborn pollutants as dyes, surfactants, pharmaceuticals, pesticides, herbicides and petroleum constituents in water. Nowadays, most of AOP facilities are built in Europe and USA due to a high expense of conventional AOP procedures working with costly oxidant reagents for instance H_2O_2 and O_3 in order to produce

$^\bullet$OH. For a large volume of wastewater to be treated, a large amount of the oxidant reagents is demanded in an AOP plant.

Photocatalyzed AOP system consisting of TiO_2/UV/O_2 has been developed since illuminated TiO_2 was found as a photocatalytic electrode in water splitting experiment made by Fujishima and Honda in 1972. [4] A common mechanism is described as $^\bullet$OH radical is generated by charge separation of e^- and h^+ on TiO_2 by absorbing photo energy larger than the band gap energy (E_g). [5] With the catalytic reactions, ambient O_2 could replace the pricy oxidants such as H_2O_2 and O_3 in AOP operations. TiO_2 photocatalyzed oxidation has been applied to deal with numerous pollutants including degradation of organic contaminant in water [6, 7], deactivation of bacteria [8] and virus [9], and removal of inorganic substances as nitrides, sulfides and heavy metals [10]. Slurry reactor using dispersed TiO_2 catalyst (e.g. Degussa P25 powder from Evonik: specific surface area 50 m^2 g^{-1} and particle size 25 nm) in feed flow has very often been practiced in aqueous purification. However, filtrating the catalyst particles is the bottleneck to scale up to industrial application. [10] Moreover, TiO_2 nanoparticles have a tendency to aggregate due to large surface area.

Overall heterogeneous catalytic reaction includes steps as 1) in-diffusion, 2) intraparticle in-diffusion, 3) adsorption, 4) surface reactions, 5) desorption, 6) out-diffusion and 7) intraparticle out-diffusion. Catalytic rate limiting steps could be film diffusion control (steps 1 and 7), pore diffusion control (steps 2 and 6) and intrinsic reaction kinetics control (steps 3 and 5). For highly exo/endo-thermic reactions the heat transfer could also affect heterogeneous catalysis process (e.g. steam reforming) in addition to the mass transfer effects as mentioned previously. An active catalyst has typically good selectivity for products over by products, good stability at reaction conditions, good accessibility of reactants and products and presents adequate rates of reactions. A photocatalyst would also be photo-responsible, that is a photon excites a free electron and forms positive-charged holes both leading to redox reactions in catalytic route.

Photocatalytic membrane reactors (PMRs) integrate membrane separation and photodegradation for purifying water. Slurry reactors coupled with pressure-driven membrane separation was presented in Ollis' review in 2003 [11] and then a design of functionalized photocatalytic membrane was contemplated in Mozia's review in 2010. [12] Fabricated membranes as TiO_2-ceramic composite [13, 14], TiO_2-polymer composite [15] and pure TiO_2 membranes [16] have been reported in a few studies. A general conclusion can be drawn that membrane coated with TiO_2 showed higher catalytic efficiency than that of membrane entrapped with TiO_2 since photoactive surface could supply more active sites to reactants and light. A membrane reactor is preferred to a slurry reactor in terms of higher compactness, better integrity and separation feasibility, yet manufacturing TiO_2-composite or pure TiO_2 membranes in large scale at low cost is the key step to realize PMR industrial application in wastewater remediation. Common methods to immobilize TiO_2 on substrate include thermal spray [17], sol-gel process [18], physical vapor deposition (PVD) [19], and chemical vapor deposition (CVD) [20]. Either depositing temperature (e.g. ≥ 450 °C in thermal spray, PVD and CVD) or annealing temperature (e.g. ≥ 500 °C after sol dip-coating) is required as high as to prepare TiO_2 anatase (the crystal phase considered as the most photoactive) according to the literature.

Plasma-enhanced chemical vapor deposition (PECVD) can facilitate deposition of thin films at low temperature with the aid of thermal/plasma decomposition of precursor [21], making it potentially compatible to many types of membrane support (thermal-sensitive polymeric ones in particular). PECVD is capable of growing and tuning microstructure of TiO_2 coating in terms of particle size, porosity and thickness that could have noticeable impacts on the photocatalytic performance regarding to quantum size effect [22], surface area [23] and mass/light transfer [24]. Huang and et al. reported a minimal substrate temperature T_s = 450 °C in PECVD process is needed for in-situ formation of anatase TiO_2 on silicon from precursor TTIP with power equal to 100 W in 2002 [25, 26]. Wu and et al. deposited amorphous TiO_2 layer on silicon performing PECVD at T_s = 200 °C and power 100 W from TTIP and obtained crystalline anatase by post-annealing at 400 °C [26]. Lastly some groups have applied bias voltage (from -50 V to -150 V) in PECVD chamber and prepared anatase on silicon at T_s less than 150 °C using the same precursor [27, 28]. Yet the bias voltage may damage substrate surface with strong ion bombardment and/or consecutive local increase of temperature and it is impossible to maintain the bias voltage on insulating polymeric materials [29, 30]. The “hard” conditions as high substrate temperature (450 °C) and/or high bias voltage (-150 V) are not suitable for membrane supports that are thermal-sensitive, less inert and insulate. Regarding to PECVD TiO_2 thin films, no lower post-heating temperature less than 400 °C has ever been reported before our group’s work published on anatase formation in PECVD process at T_s = 150 °C and post-heating at 300 °C for 5 h in 2015 [31].

The ojective of the thesis is to fabricate porous nano-structured photocatalytic membrane (for instance TiO_2-ceramic composite membrane) for degrading organic impurities in water. Photocatalysis (a heterogenous catalytic process) coupled with membrane process as an integration operation is interested for its feasibility of separation and compactness. A thin film of TiO_2 will be deposited on mechanical support with plasma-enhanced chemical vapor deposition (PECVD) method. So that TiO_2-coated membranes can be prepared and photocatalytic function will be examined accordingly. The fabricated photocatalytic TiO_2-composite membrane is in fact a functionalized porous ceramic membrane with a TiO_2 thin film deposited on top of it. TiO_2 coating layers would be deposited in PECVD process from working gases of TTIP + Ar + O_2 possibly followed with a post-annealing step for crystallization. Effect of PECVD operating parameters (including substrate temperature, partial pressure, plasma distance and RF power) on physico-chemical properties of silicon-supported TiO_2 thin films have been first studied. Deposition rate, thickness homogeneity, Ti-O abundance in the film, crystal structure and band gap energy can be reflected from SEM, FTIR, XRD, XRR and UV/Vis measurement. Minimal crystallization temperature in the post-thermal treatment would be found and reduced with substrate with seeding-effect. In the continuous work, alumina porous disks with top-layer pore size 100 nm and 800 nm are supplied as the substrates for TiO_2-layer coating (membrane type M100: TiO_2 thickness > 10 times of support pore size) and TiO_2-skin coating (membrane type M800: TiO_2 thickness < 0.5 times of pore size) respectively. Photodegradation efficiency of organic solutes in water by the illuminated M100 and M800 membranes are examined in lab-scale and pilot-scale membrane reactors built at two institutes IEM-UM (France) and ITM-UNICAL (Italy) in the partnership of the doctoral program. The established preparing procedure of TiO_2-composite membrane with PECVD approach combined with post-annealing is wished to be a solution to large-scale manufacturing TiO_2-based water purifier for photocatalytic AOP treatment on wastewater.

Structure of the thesis contains four chapters in total on bibliography fundamentals, experimental details, physico-chemical properties and functional performance of the synthesized materials. The literature review (chapter I) is focused on mechanisms of photocatalysis process and up-to-date application and preparation of TiO_2 materials. The experimental part (chapter II) describes the applied low-temperature PECVD technique to produce supported TiO_2 thin films, followed with information of characterization instrument and construction of homemade photocatalytic membrane reactors. Afterward, chapter III is dedicated for physico-chemical properties of optimal PECVD TiO_2 thin films. Properties of TiO_2 thin film including morphology, nanocrystal structure, density (or porosity), surface hydrophilicity and band gap energy (E_g) are analyzed and presented in this third chapter. Lastly, chapter IV is for functional performance of PECVD TiO_2-coated ceramic membrane. Photodegrading efficiency of aqueous organic pollutant by the illuminated TiO_2/Al_2O_3 composite membrane (Photodegradation tests have been made in both concentration-driven and pressure-driven membrane processes) and the mathematical modeling of photoreactions are discussed in this fourth chapter. Lastly, a general conclusion of the Ph.D. work and perspectives for future research interest are given in the end of the thesis.

Chapter I Bibliography fundamentals

The literature review in this chapter focuses on two fields: photocatalytic TiO_2 membrane for environment remediation and the common preparing methods for TiO_2-based membranes. The first part is extended into photocatalysis mechanism, properties of TiO_2 and photocatalytic membrane reactors (PMRs). The second part is started with general principles of chemical vapor deposition (CVD) and plasma-enhanced chemical vapor deposition (PECVD) and followed with recent studies on TiO_2 synthesis with PECVD approach.

1 Photocatalytic titanium dioxide (TiO_2) membrane for wastewater treatment

Titanium dioxide (TiO_2) is photocatalytic active by absorbing ultraviolet (UV) spectrum (specifically the light energy of wavelength from 310 – 390 nm). Crystalline TiO_2 (anatase phase) is widely used as a photocatalyst due to its high catalytic efficiency, stability, bio-compatibility and inexpensive cost. Immobilized form of TiO_2 (e.g. as composite membrane) has attracted researchers' attention on photocatalytic oxidation treating for organic pollution in wastewater. Photocatalysis mechanism, coupling photocatalytic oxidation and membrane process, properties and applications of TiO_2 materials and explored photocatalytic membrane reactors (PMRs) will be explained and discussed in this chapter.

1.1 Photocatalysis process

Photocatalysis is an acceleration of photoreactions in the presence of light and a catalyst. Photocatalytic oxidation is triggered by photo-generated hydroxyl radical ($^\bullet OH$) resulted from charge separation on photocatalyst (most often as semiconductors) when it is exposed to irradiation. Separated charge carriers include electron and positive hole, which diffuse in semiconductor and produce $^\bullet OH$ radical by interacting with species such as water and oxygen. Produced $^\bullet OH$ is a strong and non-selective oxidant that can dynamically oxidize many tedious organic molecules.

1.1.1 Band gap energy of semiconductor

Some inorganic materials such as semiconductor are found to be photocatalytic active. They can accelerate photoreactions for instance splitting the water molecules, oxidizing organic compounds and deactivating organisms. Photon energy is transferred to chemical activation energy leading to molecular decomposition. In order to understand photo-electronic processes on semiconductor particles, it is necessary to clarify band gap theory first.

Band gap is energy range in solids where electrons cannot exist, which is relevant of the electric conductivity of materials. It is the referred property to define metal, semiconductor and insulator. There is generally no band gap in metal conductors, but a large almost insurmountable gap (greater than 3 eV) in insulators. In semiconductors the gap is typically of intermediate value (at temperature below the melting point) in comparison with metallic and insulating solids. A schematic illustration of band gap in different materials is displayed in Figure 1-1[32].

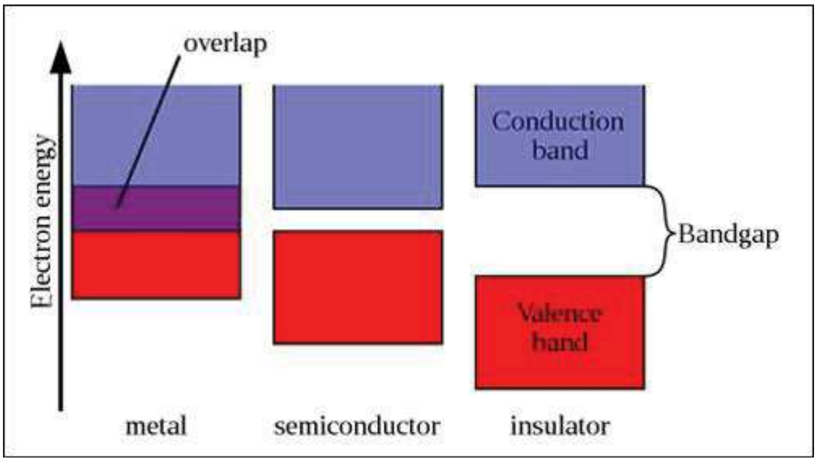

Fig. 1-1 Band gap in different materials: metal, semiconductor and insulator. [32]

Band gap indicates an energy difference between valence band and conduction band as in the electronic energy levels. The valence band (a "bonding" band) is filled with electrons that are strongly attracted by atomic nuclear and tied on molecular orbitals. In the conduction band (an "anti-bonding" band), electrons are not tightly confined since the nuclei's attraction is getting weaker and they are free to flow with higher energy. In Figure 1-1 the highest occupied state in valence band (E_{VB}) being filled with electrons is colored in red, and the lowest unoccupied state in conduction band (E_{CB}) devoid of electrons is colored in blue.

Accordingly, the band gap energy (E_g) is defined as in Equation 1-1:

$$E_g = E_{CB,min} - E_{VB,max} \tag{1-1}$$

where E_g is band gap energy, $E_{CB,min}$ is the minimal energy level in conduction band and $E_{VB,max}$ is the maximum energy level in valence band.

Common semiconductors such as gallium arsenide (GaAs) and cadmium selenide (CdSe) have E_g less than 3 eV; others such as silicon carbide (SiC), titanium oxide (TiO_2) and zinc oxide (ZnO) have E_g value around 3 eV as shown in Figure 1-2. [33] SiC, TiO_2 and ZnO are considered as semiconductors with large band gap by the modern ceramists. [34] The gap defines the required photon energy to excite an electron from lower energy level to higher one. An electron in the semiconductor can undergo inter-band transition with irradiation power of at least its band gap energy. Consequently, a positive hole is created locally when the electron leaves its position. Then charge-carriers are separated and responsible for following redox reaction on illuminated semiconductor particles. [35]

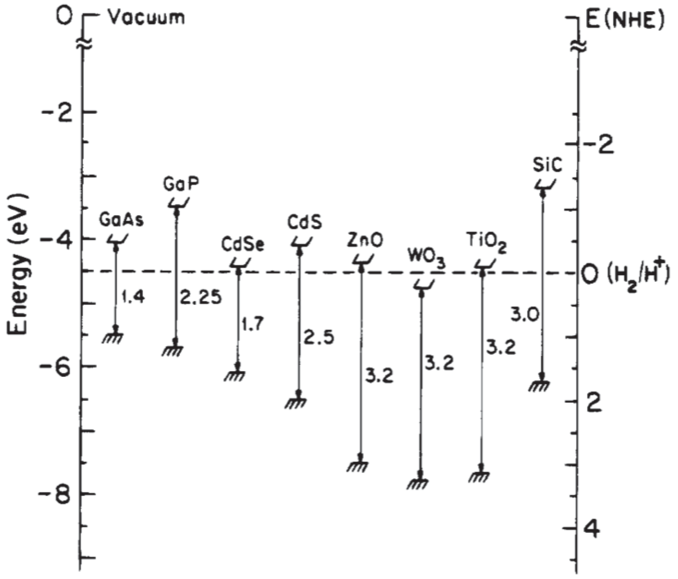

Fig. 1-2 Energies for various semiconductors in aqueous electrolytes at pH=1. [33]

Light of photon energy less than E_g will penetrate the semiconductor without separating the charges. In contrast, photon energy larger than E_g will cause electronic transition and form electron-hole pairs. The excessive energy can be dissipated through radiative and/or thermal (non-radiative) ways. Energy of the light (an electromagnetic wave) is described with its frequency as Planck-Einstein relation as given in Equation 1-2. Frequency (v) is a ratio of speed (c) over wavelength (λ) as $v=c/\lambda$, so that Planck-Einstein relation can be also expressed in Equation 1-3.

$$E = hv \qquad (1\text{-}2)$$

Or

$$E = h\frac{c}{\lambda} \qquad (1\text{-}3)$$

where E is light energy, h is Planck constant (6.63×10^{-34} J s), v is frequency, c is velocity of light (in vacuum) and λ is wavelength.

As mentioned previously, the energy threshold (E) of liberating an electron and forming a positive hole locally is at least equal to the band bap (E_g) as shown in Equation 1-4. Combining it with Plank-Einstein relation (Equation 1-3), one can generally deduce which range of spectrum is capable to separate the charges depending on semiconductor's band gap. An overall calculation on the compatible wavelength is obtained in Equation 1-5. Taking a semiconductor of band gap 3 eV as an example, light energy of wavelength shorter than 414 nm (in the UV band) is needed to form electron-hole pairs on the mentioned semiconductor.

$$E \geq E_g \qquad (1\text{-}4)$$

Hence,

$$\lambda \leq h\frac{c}{E_g} \qquad (1\text{-}5)$$

where E is light energy, E_g is band gap energy, h is Planck constant (6.63×10^{-34} J s), c is velocity of light in vacuum (3×10^{8} m s^{-1}) and λ is wavelength.

There are always two types of existing band gaps: either direct or indirect. [36] The difference is depending on the momentum of the inter-band electronic transition. In fact, the top level of valence band and the bottom level of conduction band are not always in the same momentum vector. When the transition momentum is the same it is named as direct band gap; otherwise it is indirect one. The lattice momentum P for an electron in a crystal lattice is $P_{crystal} = \hbar k$, where $\hbar$ is the reduced Planck constant ($\hbar = h/2\pi$) and k is wave vector of the lattice. [37]

Energy diagrams (*E-k* diagrams) describe the band edges by plotting band energies (*E*) as a function of momentum vector (*k*) as in Figure 1-3. [37] In a direct band gap as shown in Figure 1-3(a), the highest state of valence band (VB) and the lowest state of conduction band (CB) occur at the same momentum value. In indirect situation as shown in Figure 1-3(b), the maximum energy level in VB exists at a different momentum to the minimum energy level in CB. In the second situation, thermal particle "phonon" (due to lattice vibration), in addition to the radiative "photon", is involved in energy transferring between the system and the photocatalyst itself.

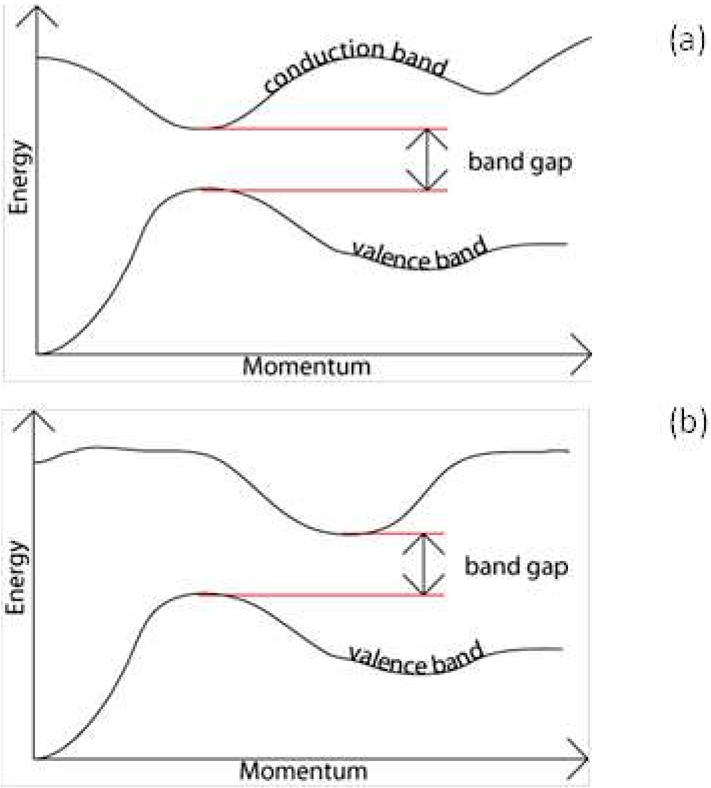

Fig. 1-3 *E-k* diagrams of direct (a) and indirect (b) band gap in semiconductor. [37]

A photon has a momentum $P_{photon} = E/c$, where E is energy of light and c is velocity of light. According to Planck-Einstein relation as in Equation 1-3, momentum of the photon can be also written as $P = h/\lambda = h\sigma$, where h the Planck constant, λ the wavelength and σ the wavenumber. Taking account that $h = 6.63\times10^{-34}$ J s and λ is in the magnitude of 10^{-7} m, an optical photon has a small value of momentum in the order of 10^{-8} J s m^{-1}. As a result, a photon of energy equal to band gap (E_g) can separate the charges more easily in semiconductor of direct band gap than that of indirect one. [36] The straightforward electron transition demands smaller momentum change cross the direct band gap. In the contrast, an electron has to undergo a more significant momentum change in order to transit in the indirect gap. [37] Energy evolution in indirect gap is more complex including both radiation and vibration process. Consequently, the indirect process has a slower kinetics rate. With the same reason, charge recombination is also less efficient in the indirect band gap. [38] Longer lifetime of separated charges with slower recombination rate (e.g. with the indirect gap) is an advantage for photocatalysis process, which is going to be further discussed in the next session 1.1.2.

1.1.2 Mechanisms in semiconductor photocatalysis

A graphic illustration of photocatalysis process is presented in Figure 1-4, where the photoelectron (e^-) and photohole (h^+) are separated on the illuminated photocatalyst (i.e. semiconductor). By absorbing a photon of energy hv vaE_g, an electron is excited from the “bonding” orbital in VB to the “anti-bonding” orbital in CB. At the meantime, a positive hole is left over in-situ at VB. Separated charge-carriers would be diffusing, trapped, and/or recombining on the photocatalyst particle. [39] The liberated electron (e_{CB}^-) could react with electron acceptor (A) in reduction reaction; while the positive hole (h_{VB}^+) could react with electron donor (D) in oxidation reaction. On the other hand, recombination of the charges is limiting the photoreaction efficiency. [38]

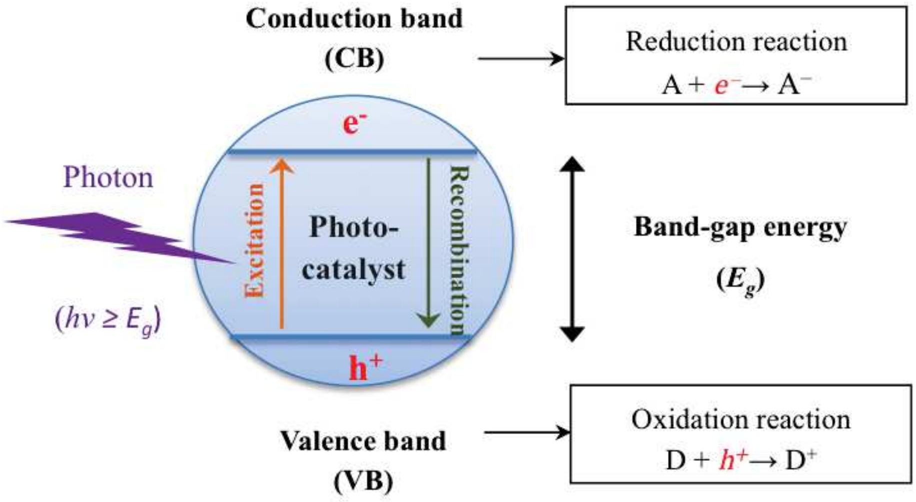

Fig. 1.4 Mechanism of photocatalysis process.

In aqueous circumstance, the photo-generated electron (e_{CB}^-) could reduce dissolved O_2 molecule in water and form oxidant species such as superoxide ion radical ($^{\bullet}O_2^-$). Meanwhile, the simultaneously generated positive hole (h_{VB}^{+}) could oxidize H_2O molecule and form hydroxyl radical ($^{\bullet}OH$). [40] Radical $^{\bullet}OH$ as one of the strongest oxidizing species has an oxidizing potential E^0 ($^{\bullet}OH_{aq}/H_2O$) = 2.59 V at pH=0. [3] It could oxidize almost all sorts of organic molecules (sometimes also for inorganic species). Molecular oxidation caused by $^{\bullet}OH$ radical attack is known as advanced oxidation process (AOP) [2], which will be further discussed in the session 1.3. Global photochemical reactions catalyzed by illuminated semiconductor in water (dissolved with ambient oxygen) are written as following:

$$h\nu \rightarrow e_{CB}^{-} + h_{VB}^{+} \qquad (1\text{-}6)$$

$$O_2 + e_{CB}^{-} \rightarrow {}^{\bullet}O_2^{-} \qquad (1\text{-}7)$$

$$H_2O + h_{VB}^{+} \rightarrow {}^{\bullet}OH + H^{+} \qquad (1\text{-}8)$$

Lifetime of the separated e_{CB}^{-} and h_{VB}^{+} on semiconductor particle is crucial for the photocatalytic activity. Most of the charge carries recombine themselves sooner or later either in a radiative or non-radiative (by heat) way. Charge recombination will weaken formation of hydroxyl radicals ($^{\bullet}OH$) due to less detached charges. Tracing e_{CB}^{-} and h_{VB}^{+} formation, transfer, capture and recombination has been studied with various time-resolved spectroscopy techniques and the results on their lifetimes are summarized in a review by Fujishima et al in 2008. [38] Trapped electrons and holes absorb light in the visible and near-infrared spectra [41, 42], whereas free electrons absorb in the infrared or microwave regions [43, 44]. Optical absorbance by the charge carriers has been recorded by means of transient absorption (TA) [41], transient diffuse reflectance (TDR) spectroscopies [45], as well as time-resolved microwave conductivity (TRMC) [43]. After all, e^{-} and h^{+} involved in photocatalysis process have been accurately measured in their different states. Conclusive timescale indication is illustrated in Figure 1-5 with collective results of studying TiO_2 samples in different forms of film and powder. [38] In general, photo-generated e^{-} and h^{+} have experienced from femtosecond (10^{-15} s) as formation until microsecond (10^{-6} s) as recombination according to those studied samples.

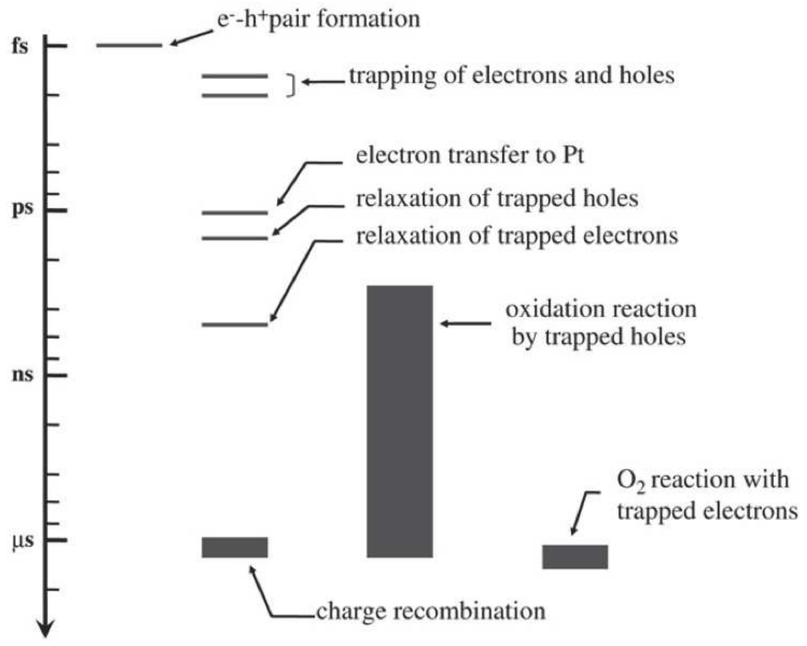

Fig. 1-5 Time scales in photocatalysis. [38]

Charge formation of electron-hole pair starts from femtosecond (10^{-15} s) as photon being absorbed on photocatalyst. [38] Charge capture takes place just afterward. Photoelectron is trapped in less than 200 fs and photohole less than 150 fs [42]. Charge diffusion/transfer occurs in the order of picosecond (10^{-12} s). [46] Relaxation of positive hole could happen faster (~ 100 ps) than that of electrons (~ 500 ps) [52]. For a nanocrystalline TiO_2 film, half-life of electron-hole recombination is found ca. 1 μs for a film dipped in N_2-saturated deuterated water excited by low-intensity laser pulse. [44] Charge recombination undergoes when charge-carriers “randomly” walk and meet the opposite one no matter in the trapped or free status described as in the following:

$$e^- + h_{tr}^+ \rightarrow hv \text{ or heat} \quad (1\text{-}9)$$

$$e_{tr}^- + h^+ \rightarrow hv \text{ or heat} \quad (1\text{-}10)$$

$$e^- + h^+ \rightarrow hv \text{ or heat} \quad (1\text{-}11)$$

Oxidation reaction induced by h_{tr}^+ has begun in less than 2 μs when water is involved in the system, whereas oxidation would only begin within 80 μs when no H_2O has been interacted with. [43] Oxidation reaction of organic molecules caused by trapped hole (starting from less than ns) and reduction reaction of O_2 caused by trapped electrons (in a few μs) are also indicated in the time line of Figure 1-5.

Charge capture on semiconductor particle is an essential step for photocatalytic performance. It suppresses recombination and assists interfacial charge transfer leading to larger amount of "hot" e^- and h^+ could sustain in the solid material. In some electron paramagnetic resonance (EPR) study on illuminated TiO_2 particles, trapped electrons have been found in the form of Ti^{3+}, at the meantime, O_2 adsorption on surface has caused Ti^{3+} signal decayed. [47, 48] Trapped holes have been observed in more complex and deeply scavenged states. For instance, surface hydroxyl (Ti–$^{\bullet}$O–Ti–OH), surface oxygen radicals (Ti–O–Ti–$^{\bullet}$O) and lattice oxygen radical ion ($^{\bullet}O^{-}$) are proposed as the sites where positive holes could be confined. [47, 48] In other studies, two types of surface hydroxyl groups as Ti^{4+}–$^{\bullet}$OH radicals (hole trapping) and Ti^{3+}–OH groups (electron trapping) have been investigated both by experiments and theoretical calculations. [49] A density functional theory (DFT) study on hydroxylated TiO_2 surface demonstrated an electron-trapping nature of Ti–OH bridges on crystal faces. [50] Such theoretical result is consistent with an experimental work of Henderson et al [51].

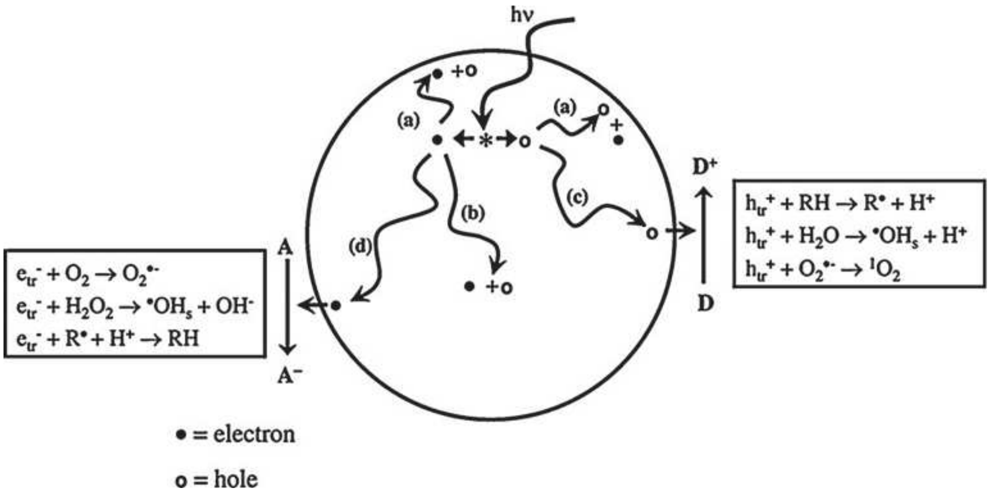

Fig. 1-6 Process occurring on bare TiO_2 particle after UV excitation. [38]

Process occurring on bare TiO_2 particle after UV excitation is shown in Figure 1-6: radical $^{\bullet}$OH being formed from h_{tr}^{+} reacting with H_2O or e_{tr}^{-} reacting with H_2O_2. Generation of $^{\bullet}$OH radical from H_2O has been understood in various possible pathways. Some have found that $^{\bullet}$OH is formed from h^+ interacting with H_2O or with absorbed OH^- ion. [52, 53] Some others have proposed an alternative way: $^{\bullet}OH$ is produced on surface lattice oxygen (hole trapping site) where H_2O experiences nucleophilic attack [54, 55].

The most commonly accepted mechanism of photocatalytic oxidation is hydroxyl radical ($^{\bullet}OH$) attack [56]; however, some studies suggest that the role of radical is probably overestimated (in another word, primary oxidation is proposed be initiated by free or trapped holes) [57, 58]. In a study on methanol, both oxidation routes through $^{\bullet}OH$ and h^+ were proven to result in the same product formaldehyde [59]:

By $^{\bullet}OH$ radical:

$$CH_3OH + {}^{\bullet}OH \rightarrow {}^{\bullet}CH_2OH + H_2O \tag{1-12}$$

$$^{\bullet}CH_2OH \rightarrow HCHO + H^+ + e^- \tag{1-13}$$

By trapped hole:

$$CH_3OH + h^+ + OH^- \rightarrow {}^{\bullet}CH_2OH + H_2O \tag{1-14}$$

$$^{\bullet}CH_2OH \rightarrow HCHO + H^+ + e^- \tag{1-15}$$

In addition to the $^{\bullet}OH$ radical, positive hole (h^+), superoxide radical ion ($^{\bullet}O_2^-$) and singlet state oxygen ($^1O_2$) are also involved as oxidant species in photocatalysis process. Superoxide radical ion ($^{\bullet}O_2^-$) is less often found to trigger oxidation of organic compound in comparison with $^{\bullet}OH$ and h^+. Yet $^{\bullet}O_2^-$ is easily transferred to $^{\bullet}OH$ by interacting with e^- and H^+ leading to contribution to photocatalytic efficiency. [60] Moreover, singlet oxygen $^1O_2$, a strong oxidant, is proposed being formed by reaction between $^{\bullet}O_2^-$ and trapped hole, which has been only recently detected with near-IR phosphorescence in a TiO_2 suspension system. [61] Lifetime of $^1O_2$ is determined close to 2 μs rather shorter than that of $^{\bullet}OH$ ca. 10 μs and trapped holes, possibly due to faster deactivation of O_2 at TiO_2 surface.

General factors impacting a heterogeneous photocatalysis process include 1) photocatalyst, 2) light, 3) dissolved oxygen in water, 4) organic containments in water and 5) temperature. Catalyst having large surface area can provide more active sites in adsorption and reaction process. Recombination rate could be reduced due to increase of specific surface area and removal of structural defects in a study of photocatalytic oxidation of phenol compound. [23] Excessive catalyst loading (can create a light screening effect) should be avoided to ensure efficient photon absorption. [62] UV irradiation includes UVA (315 – 400 nm i.e. 3,10 – 3.94

eV), UVB (280 – 315 nm i.e. 3.94 – 4.43 eV) and UVC (100 – 280 nm i.e. 4.43 – 12.4 eV) spectra. In most studies, UVA irradiation provides sufficient photonic activation energy to semiconductor catalyst. [63] In addition, oxygen plays an indispensable role as electron acceptor in photocatalysis process especially for environmental application. Oxygen promotes charge splitting as an electron entrapment and develops into active oxygen species including $^{\bullet}O_2^{-}$, H_2O_2, $^{1}O_2$ and etc. [52] It also maintains the oxidant states of photocatalyst ($Ti^{3+} \rightarrow +Ti^{4+}$) throughout the process. Therefore, maintaining adequate dissolved oxygen in water should not be neglected in reactor operation. Moreover, diffusion and reaction kinetics of organic molecules depend on their molecular weight, initial concentration and chemical potential. Additionally, pH is one important parameter affecting charge on the catalyst particle and position of valence and conduction bands. [64] On the other hand, reaction temperature is found to be suitable between 20 °C and 80 °C since lower temperatures would be thermodynamically disfavored and higher temperatures would accelerate charge recombination rate. [65]

In a summary of this session, direct and indirect band gap of semiconductor has been explained regarding to electronic transition process. Lifetime of photo-generated electron and hole on semiconductor photocatalyst is known by means of time-resolved spectroscopy techniques. Photocatalysis mechanism is mainly understood through hydroxyl radical $^{\bullet}OH$ attack and/or trapped hole (h^{+}), whereas superoxide radical ($^{\bullet}O_2^{-}$) and singlet oxygen ($^{1}O_2$) have been detected in the recent studies. Photocatalytic efficiency can be affected from photocatalyst, light, oxygen, pH and temperature. Higher photoreaction rate could be achieved by using catalyst of large specific surface area and mass below saturation level, using UVA irradiation and using adequate dissolved oxygen in water.

1.2 TiO_2 as photocatalytic material

TiO_2 is commonly found as white pigment used in paints, constructions, plastic packages and cosmetics. Once it was observed that paints consisting of “titanium white” went fading under exposure to sunlight. After years, it has been recognized that the discoloration phenomenon was caused by oxidation and removal of organic painting component when TiO_2 is illuminated. Lately, it has been further discovered that the atmospheric O_2 was reduced on TiO_2 simultaneously when the organic pigment was bleached. A historical view and modern applications of photoactive TiO_2 is discussed in this session.

Structure of TiO_2 material is important for its photocatalytic activity in terms of crystal structure (photo-chemical step), nanoparticle size (quatum effect for light efficiency) and specific surface area (adsorption/desorption step). For instance, amorphous materials are usually not highly photoactive since the non-regular arrangement of the atoms does not allow longer lifetime of seprated charges. Very small size of nanocrystals could have quatum effect when the particle dimension is comparable with Bohr radius and accordingly the band-gap energy could be shifted. Moreover, high porosity in a thin film has large surface area that could improve catalytic reaction rate.

1.2.1 Historical overview and up-to-date applications of TiO_2

In 1921, Renz at University of Lugano (Switzerland) discovered that TiO_2 could be partially reduced in organic solvent glycerol under illumination [66]. The color of titania turned from white to dark. They suggested a reaction at that time as:

$$TiO_2 + \text{light} \rightarrow Ti_2O_3 \text{ or } TiO \qquad (1\text{-}16)$$

In 1938, Goodeve and Kitchener at University College London performed an inspiring experiment on TiO_2 powder that photo-decomposed a dye "chlorazol sky blue" in the air. [67] They correlated the photoreaction to ultraviolet (UV) light and even pointed out the quantum efficiency (i.e. the number of dye molecules photo-decomposed against the number of quanta absorbed) of the catalyst. [68] In the 1950s, production of hydrogen peroxide (H_2O_2) on illuminated zinc oxides has been studied, on which Markham (Catholic University of America, USA) [69] and Stephens et al. (Wayne State University, USA) [70] have individually carried out the experiments. Yet both of them were focusing on ZnO samples since no detectable amount of H_2O_2 has been observed on TiO_2 particles in their experiments. The general reaction was proposed as:

$$2e^- + 2H^+ + O_2 \rightarrow H_2O_2 \qquad (1\text{-}17)$$

Until then an overall mechanism could be abstracted as an organic compound was oxidized meanwhile ambient oxygen molecule was reduced on illuminated semiconductors. Reasonably, studies about O_2 adsorption on photocatalyst have been followed up to know more about photocatalysis process. In 1958, Kennedy et al. at University of Edinburgh (UK) experimented photo-adsorption of O_2 on TiO_2 and they demonstrated that it was the electron that transferred from TiO_2 to surface; adsorbed O_2 have reduced the molecular O_2. [71] In the experiment, they used the same dye "chlorazol sky blue" as in the work of Goodeve.

Filimonov at University of Petersburg (Russia) compared photo-activity of ZnO and TiO_2 for oxidizing isopropanol to acetone. [72] It is claimed that the adsorbed O_2 was thoroughly reduced to H_2O on TiO_2 sample, whereas O_2 could merely be reduced to H_2O_2 on ZnO sample. This result could explain why the researchers in America could not detect H_2O_2 release on TiO_2 at that time and thus focused analysis on ZnO in the 1950s. Further on in 1964, Kato and Mashio at Kyoto Institute of Technology (Japan) have proved that H_2O_2 could also be produced on different TiO_2 powders when oxidizing hydrocarbons and alcohol. [73] It is remarkable that they concluded that the anatase form of TiO_2 powder showed higher activity than the rutile form.

In McLintock and Ritchie's study at University of Edinburgh (UK), superoxide radical ion ($^{\bullet}O_2^-$) has been found on TiO_2 particle when oxidizing ethylene and propylene. [74] In their experiment, they observed a complete oxidation of ethylene and propylene into products CO_2 and H_2O. The radical ion $^{\bullet}O_2^-$ was produced from oxygen as proposed in equation below:

$$e^- + O_2 \rightarrow {}^{\bullet}O_2^- \qquad (1\text{-}18)$$

Honda and Fujishima (Honda's Ph.D. student at that time) at University of Tokyo (Japan) have made a breaking-through experiment on TiO_2 photo-electrode in 1972. [4] Photo-electrochemical cell was constructed and single TiO_2 crystal was used as an electrode for water splitting. They found that oxygen was generated on TiO_2 electrode (illuminated with visible light) and hydrogen was produced on Pt electrode without applying external voltage. Afterwards, a great amount of research work has been devoted to study on producing H_2 from water through illuminated TiO_2.

The first time that TiO_2 being used to photodegrade pollutants in water treatment was reported by Frank and Bard at University of Texas (USA) in 1977. [75, 76] They applied TiO_2 under irradiation and oxidized cyanide (CN^-) and sulfite (SO^{3-}) into cyanate (OCN^-) and sulfate (SO^{4-}) respectively. Other semiconductors including ZnO, CdS, Fe_2O_3 and WO_3 have been also experimented. In addition, they anticipated that it is also possible to use TiO_2 to decompose organic substance in addition to the tested inorganic species.

Up-to-date applications of photoactive TiO_2 have developed in domains including air purification [77-79], liquid purification [11, 38, 80, 81] and sterilization [9, 82]. Published documents on “TiO_2 photocatalysis for environmental purification” experienced different growing booms in terms of papers and patents since 1995 as shown in Appendix 1. In scientific papers, the field on water purification went through a faster growth in comparison with air purification from 1995 to 2007. However, it is the contrast for the accepted patents in the same period, that is, air purification had a more robust growth. Technical bottleneck on filtrating and recycling catalyst particles in liquid phase is the main reason for the difference. Manufacturing large-scale TiO_2 water purifier is the crucial point to link science research to market exploration.

An example of TiO_2 photocatalysis application in field of water purification is displayed in Figure 1-7. [40] The consecutive system is devoted to treat relatively large volume of water kept at low energy consumption. The electrolysis- and photocatalysis-treatment system is composed of boron-doped diamond (BDD) electrode and TiO_2 photocatalyst in the individual unit. High-level wastewater passed through a pre-filter and circulated in an electrolysis unit containing the BDD electrode. Then the water source was converted into low-level wastewater, which was continually circulated in a photocatalysis unit. The photoreactor was packed with TiO_2 coated quartz tubes under the sunlight. In the last step, the wastewater was flowing into a final-filter and ion exchange filter unit. All the electricity power was supplied from solar energy through the photovoltaic cells in this work, which is another attractive characteristic of this system.

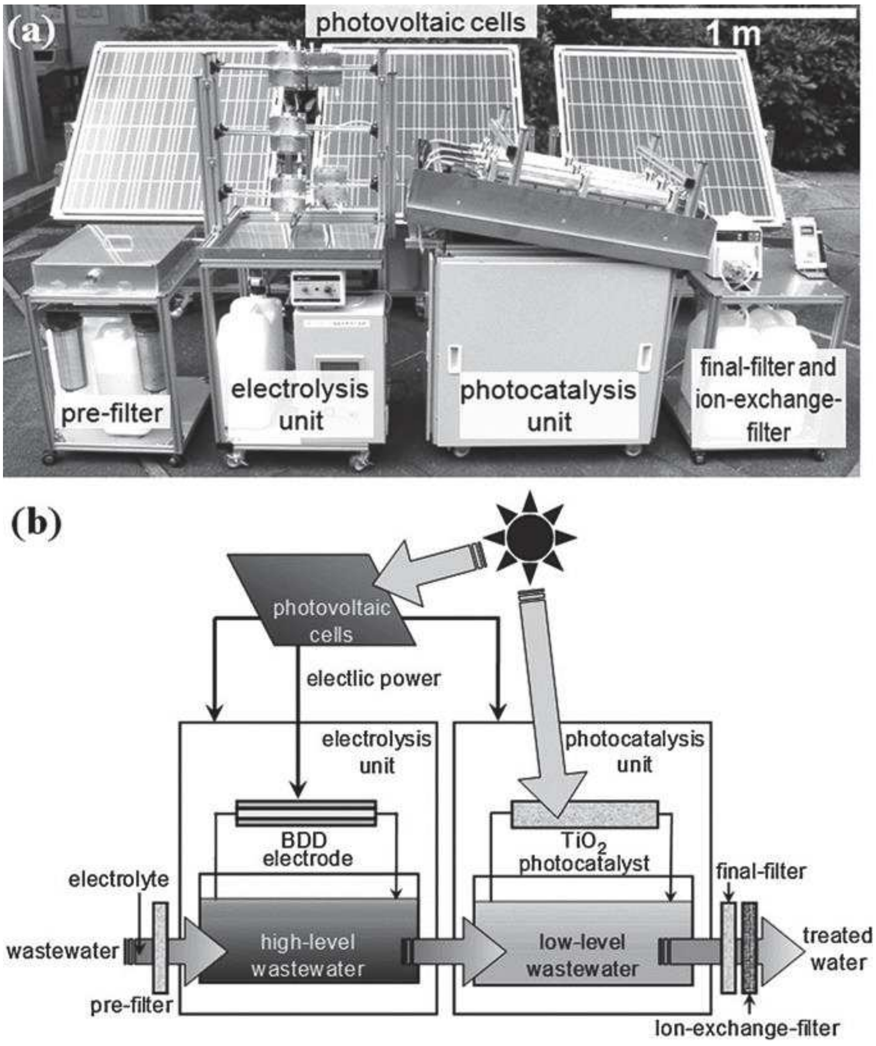

Fig. 1-7 Solar-driven electrochemical and photocatalytic water treatment system (a) photograph and (b) graphic illustration. [40]

1.2.2 Crystal phase, band gap and surface reactions of TiO_2

In the nature crystalline TiO_2 materials exists in three phases as: rutile, anatase and brookite. Rutile is the most thermal stable form of TiO_2 crystal, while anatase and brookite phases could transform into rutile at high temperature. Anatase has been pointed out having the highest photocatalytic efficiency according to the most studies. [36, 83, 84] Yet some have claimed that a mixture of anatase and rutile with certain composition ratio could work better. [47, 85] Nevertheless, brookite is the phase that has been the less rarely studied for photocatalytic activity. [86, 87]

Band gap (E_g) of anatase, rutile and brookite differs depending on the crystal structures and electronic band edges. It is one of the reasons that the specific TiO_2 crystal phase has different photocatalytic efficiency. Anatase is a common phase obtained from sol-gel and chemical deposition synthesis. Rutile structure would be usually developed when TiO_2 is annealed more than 700 °C. Pure brookite without the other two phases is difficult to prepare and it could be sometimes observed as a by-product in acidic-medium and low-temperature preparation. [86] Schematic unit cells of anatase, rutile and brookite are presented in Figure 1-8 and their symmetry and physical properties are listed in Table 1-1.

The prevalent crystal face (110) in anatase phase and the prevalent face (110) in rutile are highlighted in a grey color in Figure 1-9(a) and Figure 1-9(b) respectively, where the lattice constants in unit angstrom (Å) and *x*, *y* and *z*-axes corresponding to (100), (010) and (001) directions. The major crystal faces contained in anatase, rutile and brookite are listed in Table 1-2.

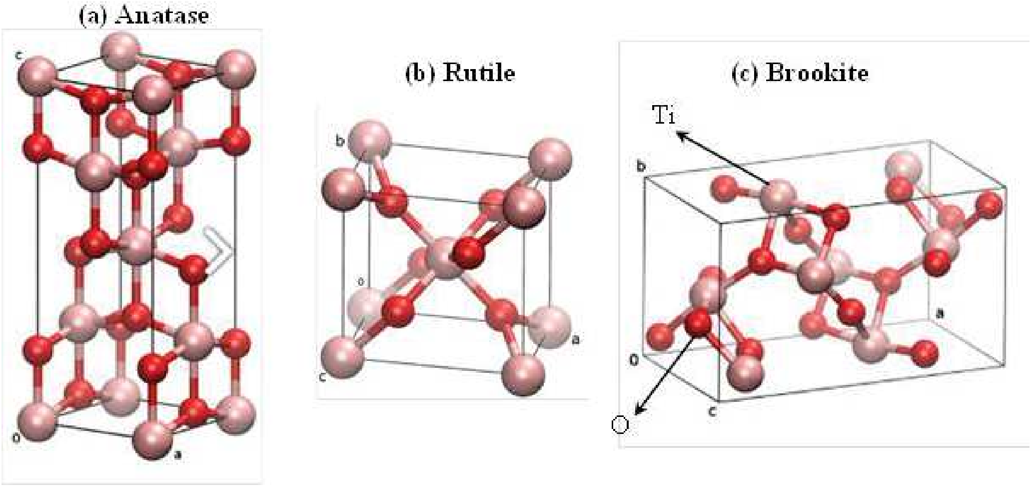

Fig. 1-8 Schematic unit cell of TiO_2 (a) anatase, (b) rutile and (c) brookite presenting Ti atom with bigger ball and O atom with smaller ball. [88]

Table 1-1 Unit cell indices and physical properties of TiO_2 anatase, rutile and brookite. [36, 83]

Crystal phase	**Anatase**	**Rutile**	**Brookite**
Molecular formula	TiO_2	TiO_2	TiO_2
Formula weight (g mol^{-1})	79.89	79.89	79.89
Z (formula units per unit cell)	4	2	8
Crystal system	Tetragonal	Tetragonal	Orthorhombic
Point group	4/mmm	4/mmm	mmm
Space group	$I4_1$/amd	$P4_2$/mnm	Pbca
Unit cell			
a (Å)	3.784	4.585	9.184
b (Å)	3.784	4.585	5.447
c (Å)	9.514	2.953	5.145
Volume (Å^3)	136.25	62.07	257.38
Molar volume (cm^3 mol^{-1})	20.156	18.693	19.377
Density (g cm^{-3})	3.895	4.274	4.123
Refractive index (n_0)	2.609	2.488	2.583

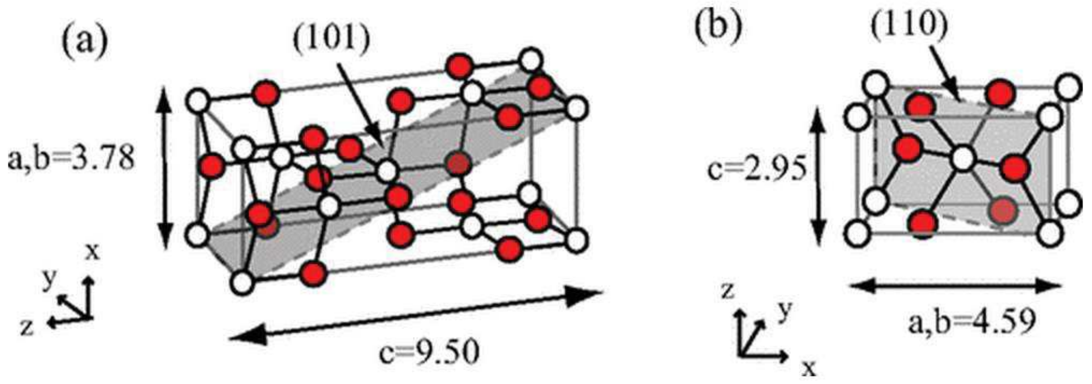

Fig. 1-9 Schematic crystal faces of TiO_2 with Ti (white color) and O (red color) atoms and lattice length in Å: (a) the anatase (101) surface and (b) the rutile (110) surface. [89]

Table 1-2 Main crystal faces of TiO_2 anatase, rutile and brookite. [36, 89, 90]

Crystal phase	Anatase	Rutile	Brookite
Main crystal faces	(101) (001) (100)	(110) (100) (001)	(100) (110) (010)

Anatase has three main faces (101), (001) and (100), among which the first two faces are low in energy and thermally stable. [91, 92] Surface (101) is the most commonly observed one in anatase material. Surface (001) can undergo a 4-folded reconstruction so that (004) can be usually observed in XRD analysis on anatase phase. [91, 93] Similarly surface (100) can undergo a 2-folded reconstruction into (200), which is more often detected in rod-like anatase. [93] In the bulk structure, anatase has Ti atom as 6-coordinating, while O atom bonding with three Ti atoms. On the surface (101) there are rows of bridging oxygen (just connecting two Ti atoms) and rows of 5-coordinated Ti atoms. [94] The exposed Ti atoms are low in electron density acting as Lewis acid sites. Schematic graphs and SEM images of anatase single crystal are exhibited in Figure 1-10 with surfaces (001) and (101) being pointed out. [95]

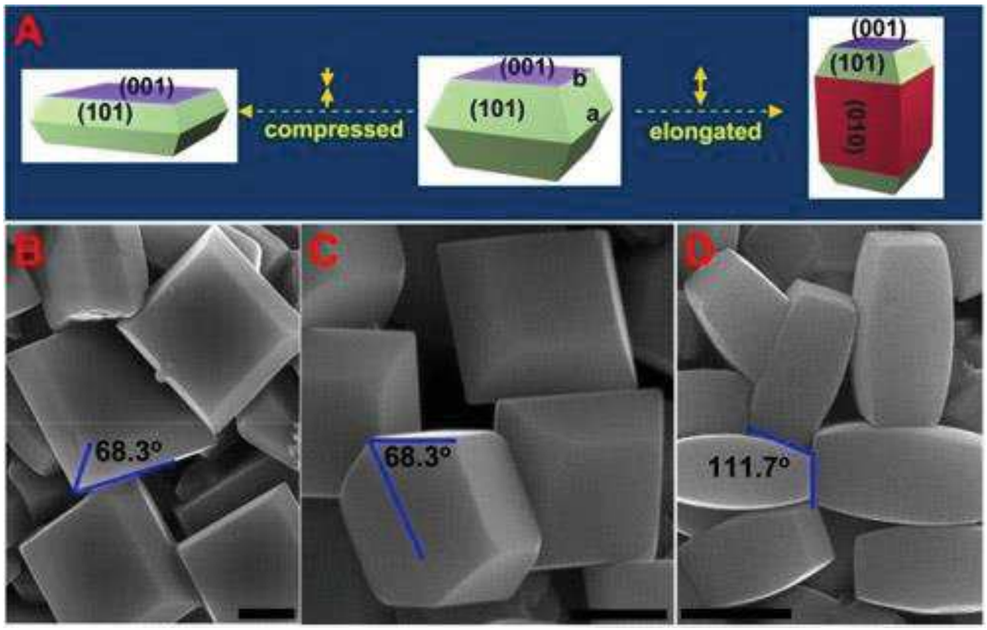

Fig. 1-10 Anatase TiO_2 crystals with a predominance of low index facets: Schematic (A) and SEM images (B-D) of anatase TiO_2 single crystals with different percentages of (001), (101), and (010) facets. [95]

Rutile has three major crystal faces as (110), (100) and (001) with the first two surfaces low in energy. [96] Surface (110) is most thermally stable and has rows of bridging oxygen with alternating 5-coordinate Ti atoms running parallel on oxygen row as schematically presented in Figure 1-11. [38] The red rectangle framed (O-Ti^{4+}-O) is active site for water adsorption, electron transfer and proton transfer. The blue rectangle included bridging oxygen is responsible for electron and proton transfer. The green rectangle of (Ti^{4+}-O-Ti^{4+}) is available for oxygen-oxygen coupling and desorption. Surface (100) has similar rows of bridging oxygen and alternating Ti atoms in a different geometric relationship.

Brookite includes major crystal faces (100), (110) and (010) whose thermal stability reduces along in the order. [97] As mentioned previously, brookite is more difficult to synthesize in its pure form and is less studied as a catalyst.

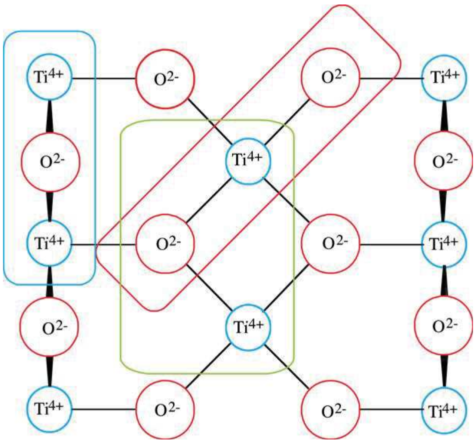

Fig. 1-11 Schematic top view of the rutile (110) surface with bridging oxygen and 5-coordinated Ti atoms: colored rectangle (blue, red and green) responsible for various possible interactions. [38]

General photocatalytic reactions over TiO_2 particle include: 1) electron scavenger (e.g. Ti^{3+}) interacting with surface adsorbed oxygen and forming superoxide radical ion ($^{\bullet}O_2^-$) and 2) hole scavenger (e.g. lattice oxygen) interacting with adsorbed water and forming hydroxyl radical ($^{\bullet}OH$). Hydroxyl radical $^{\bullet}OH$, superoxide ion $^{\bullet}O_2^-$ and trapped hole h^+ could all possibly degrade aqueous organic compounds (R) through intermediate reactions to the mineralized products as CO_2 and H_2O. [33]

TiO_2 surface reaction:

$$\text{Ti (IV)} + e^- \rightarrow \text{Ti (III)} \qquad (1\text{-}19)$$

$\mathrm{Ti\ (III)} + O_2 \rightarrow \mathrm{Ti\ (IV)} + {}^{\bullet}O_2^{-}$ (1-20)

$H_2O + h^+ \rightarrow {}^{\bullet}OH + H^+$ (1-21)

Degradation of organic molecules (R):

$R + {}^{\bullet}OH \rightarrow \ldots \rightarrow \mathrm{Intermediates} \rightarrow \ldots \rightarrow CO_2 + H_2O$ (1-22)

$R + {}^{\bullet}O_2^{-} \rightarrow \ldots \rightarrow \mathrm{Intermediates} \rightarrow \ldots \rightarrow CO_2 + H_2O$ (1-23)

$R + h^+ + {}^{\bullet}O_2^{-} \rightarrow \ldots \rightarrow \mathrm{Intermediates} \rightarrow \ldots \rightarrow CO_2 + H_2O$ (1-24)

Band gap energy (E_g) of TiO_2 is the energy difference between its valance band maximal level (VBM) and conduction band minimal level (CBM). The concept of direct and indirect E_g has been explained in details in the previous session 1.1. TiO_2 anatase of indirect band gap and rutile of direct band gap are presented in Figure 1-12(a) and 1-12(b), respectively. [36]

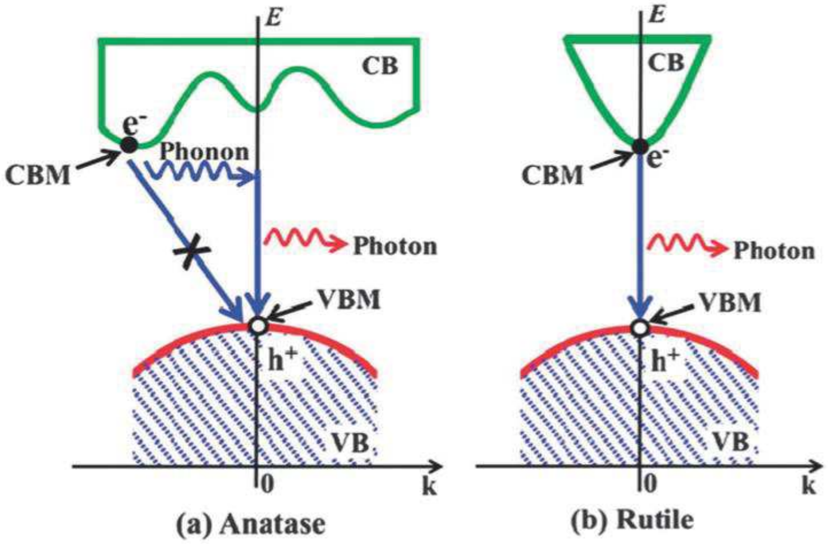

(a) Anatase

(b) Rutile

Fig. 1-12 Indirect band gap of (a) anatase and direct band gap of (b) rutile. [36]

The outer electron orbitals of Ti and O atoms are given as below:

Ti: $3s^2\,3p^6\,3d^2\,4s^2$

O: $2s^2\,2p^4$

The “bonding” valence band in TiO_2 consists of hybridization of Ti 3d and O 2p states. The “anti-bonding” conduction band contains electrons mainly from Ti 3d state (with a few O 2p state and Ti 3p state). [36] Energy is dissipating through thermal vibration via “phonon” particles and/or irradiation via particle “photon” particles during charges relaxation and recombination processes. Indirect transition requires more change of momentum and thus charge recombination rate is slower in anatase (indirect transition) than that of rutile (direct transition). It is considered as one reason that anatase could usually perform better photocatalytic efficiency than rutile does.

Band gap energy (E_g) of TiO_2 depends on crystal phase, composite purity and structural properties and the relevant values have been experimentally and theoretically studied in many works. Optical techniques are common used to determine E_g experimentally [34, 98, 99], whereas molecular orbitals calculation and density function theory (DFT) are often applied to calculate E_g theoretically [88, 100]. Generally, anatase is commonly reported having E_g as 3.23 eV, rutile 3.02 eV and brookite 3.14 eV. [10] In more recent studies, observed E_g value of anatase has been reported varying from 3.0 to 3.6 eV (310 – 390 nm) according to synthetic TiO_2 materials from different works. [36, 98, 101, 102]

Utilizing solar energy could greatly reduce the cost of photocatalyzed AOP treatment in wastewater, however, only 5% of UV energy (required in pure TiO_2 photocatalysis process) is composed in the sunlight. On the other hand, sunlight is especially abundant in some area where clean water severely lacks (e.g. in the deserts). An example of solar-driven electrochemical and photocatalytic water treatment system has been presented in Figure 1-7 of session 1.2.1.

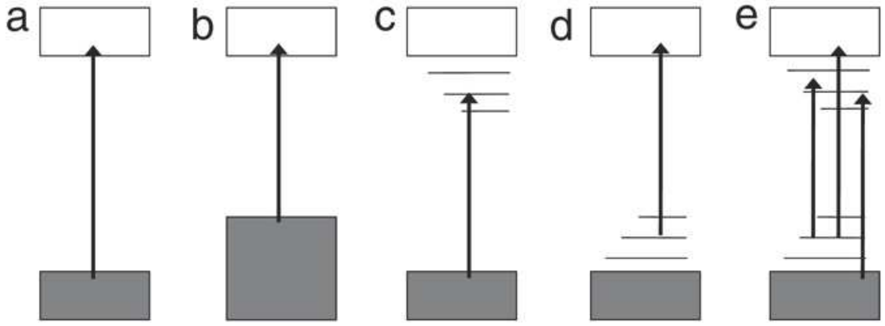

Fig. 1-13 Various schematic graphs of possible band gap of pure or modified TiO_2 materials for visible-light photocatalysis process: (a) pure TiO_2, (b) non-metal doped TiO_2, (c)

oxygen-deficient TiO_2, (d) midgap energy levels for non-metal doped TiO_2 and (e) both oxygen vacancy and non-metal doped midgap levels are considered. [38]

Narrowing the band gap by doping heteroatoms in TiO_2 materials could lead to absorbance shift from UV to visible light. A graphic mechanism on E_g reduction due to dopant atoms and/or oxygen deficient is given in Figure 1-13. [38] Either electron acceptor or oxygen deficient could degrade the minimal energy levels of conduction band as shown in Figure 1-13(c). Meanwhile, electron-donor atoms could upgrade the maximum energy levels of valence band as shown in Figure 1-13(d). The least band gap would be obtained in a case of both oxygen vacancy and non-metal dopants are present in the photocatalyst as seen in Figure 1-13(e). As a result, midgap levels reduce the band gap so that solar energy of its visible band is sufficient to initiate photocatalyzed oxidation reactions.

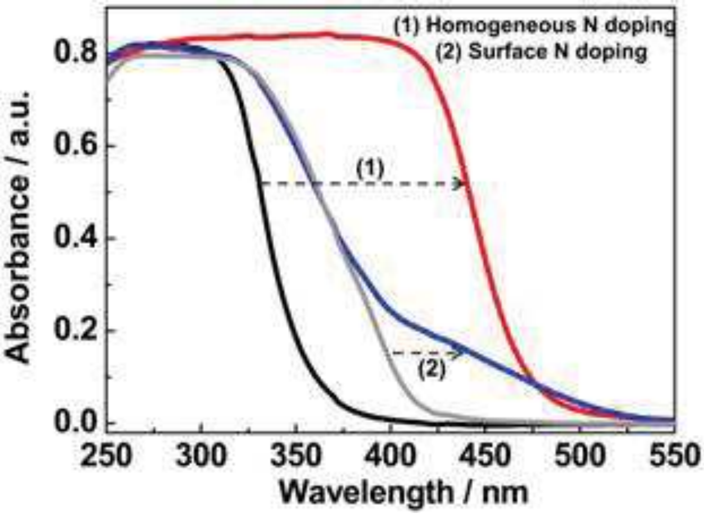

Fig. 1-14 Homogeneous N doping in $Cs_{0.68}Ti_{1.83}O_4$. The left panel: UV-visible absorption spectra of (1) homogeneous N doped $Cs_{0.68}Ti_{1.83}O_4$ and (2) surface N doped TiO_2. [103]

Doping TiO_2 materials with heteroatoms such as non-metal atoms (e.g. N and F) [6, 103-107] and metal atoms (e.g. W and Ag) [108, 109] has been carried out in several works aimed at solar harvesting. Dopant TiO_2 could sustain a smaller band gap (i.e. larger absorbance wavelength) when electron acceptor (non-metal atoms as dopant) and electron acceptor (metal atoms) are incorporated. A comparison between pure TiO_2 and nitrogen-dopant TiO_2 (either N is homogeneous in the material or on surface) is presented in Figure 1-14 as an example.

[103] Apparent absorbance shift to the visible spectrum has been witnessed on the N-dopant TiO_2 sample.

1.3 TiO_2 photocatalytic membrane reactors (PMRs)

Photocatalyzed oxidation initiated by photo-generated $^{\bullet}OH$ radical and/or trapped holes is clarified as an innovative technology of advanced oxidation processes (AOPs). Since concept of AOPs was first stated in 1987 by Glaze and et al. [2], there are about 500 industrial-scale AOP plants all over the world today. Photocatalyzed AOP operation using $TiO_2/UV/O_2$ reduces the process cost by replacing the expensive oxidant reagents H_2O_2 and O_3 with ambient oxygen. Integration of photocatalytic oxidation with membrane process is essential for industry-scale application of PMRs in wastewater treatment filed.

1.3.1 Advanced oxidation processes (AOPs) for degrading pollutants

Advanced oxidation processes (AOPs) indicate a specific treating technique by decomposing contaminants in water through $^{\bullet}OH$ oxidation reaction. [2] Some other strong oxygen species such as $^{\bullet}O_2^-$, O_3 and H_2O_2 are also possibly involved in the process. It has been proven that membrane process coupled with AOP operation can be particularly effective in eliminating non-degradable pollutants such as aromatics, pesticides, herbicides, volatile organic compounds (VOCs) and petroleum constituents in wastewater. [12, 110, 111] Proposed routes on phenol oxidation on illuminated TiO_2 (as in $^{\bullet}OH$ radical attack mechanism) are presented in Figure 1-16 as an example. [112]

A major advantage of AOP treatment is to remove contaminants without bringing any secondary hazardous substances. And the treatment efficiency relies heavily on in-situ production of $^{\bullet}OH$ radicals. Hydroxyl radical $^{\bullet}OH$, one of the strongest oxidant species next to fluorine, has oxidizing potential E^0 ($^{\bullet}OH_{aq}/H_2O$) = 2.59 V at pH=0 [3] making it possible to oxidize almost all types of organic compound. However, pre-treating the water source is sometimes needed to ensure reliability of AOP performance considering the chemistry of $^{\bullet}OH$ radical. For instance bicarbonate ion (HCO_3^-), which can act as $^{\bullet}OH$ scavenger, should be wiped away before the AOP procedure. [113]

In conventional homogeneous AOP treatment, $^{\bullet}OH$ radical could be formed by adding ozone (O_3) and/or hydrogen peroxide (H_2O_2). Common homogenous AOP systems include photochemical process containing O_3/UV or H_2O_2/UV and catalytical process containing

H_2O_2/Fe^{2+}. More recently, solid semiconductor (Sc) for instance TiO_2 photocatalyst is added in the liquid phase and thus a heterogeneous AOP system is consisting as $Sc/O_2/UV$. Homogeneous/heterogeneous APO operations with or without irradiation are compared in Table 1-3. High cost of O_3 and H_2O_2 used in conventional homogeneous AOP treatment is limiting its industrial application to large-scale water plant.

Table 1-3 AOP operated systems to produce hydroxyl radical ($^{\bullet}$OH). [2, 113]

	With irradiation	**Without irradiation**
Homogeneous systems	O_3/UV	O_3/H_2O_2
	H_2O_2/UV	O_3/OH^-
	$H_2O_2/Fe^{2+}/UV$	H_2O_2/Fe^{2+}
Heterogeneous systems	$*Sc/O_3/UV$	-
	$*Sc/H_2O_2/UV$	-
	$*Sc/O_2/UV$	-

*Sc: semiconductor

Meanwhile, using semiconductor catalyst (TiO_2) could lead to $^{\bullet}$OH radical formation by replacing the costly oxidant reagents with only ambient oxygen. Furthermore, the membrane based AOP is in particular interested in water treatment method since immobilized phase of TiO_2 (instead of suspetion) could be used in treated water. Therefore, no loss or separation of the photocatalyst particles is necessary in the photocatalytical membrane process.

A schematic illustration on photocatalytic AOP pathway degrading organic pollutions into CO_2 and H_2O is presented in Figure 1-15. Photon energy is transferred to chemical energy resulting in the formation of $^{\bullet}$OH radical as the catalyst is in contact with H_2O and O_2. In the presence of semiconductor (Sc) catalyst, O_3 or H_2O_2 is no more mandatory for $^{\bullet}$OH generation, yet the presence of them could still enhance the catalytic activity reported in some studies. [110, 111, 114]

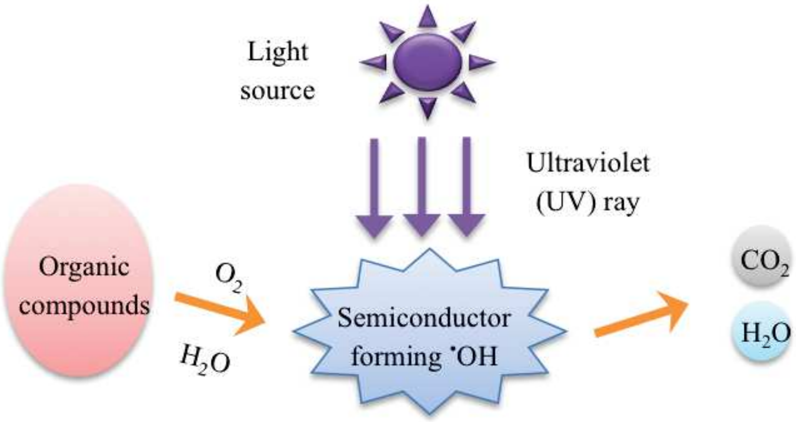

Fig. 1-15 Concept of photocatalytic AOP system (containing Sc/UV/O_2) that mineralizes organic compounds into the end products H_2O and CO_2.

TiO_2 is the most-often applied photocatalyst in current research works. Photocatalytic AOP system of TiO_2/UV/O_2 works as effective and economical technique degrading aqueous organic pollutants for environmental remediation. Proposed photodegradation mechanism of phenol over illuminated TiO_2 (through radical attack) is given as an example in figure 1-16. Continuous oxidation including aromatic ring opening and carbon bond breaking (through many intermediate reactions) could lead to mineralization of the organic compound ending in the final products as water and carbon dioxide.

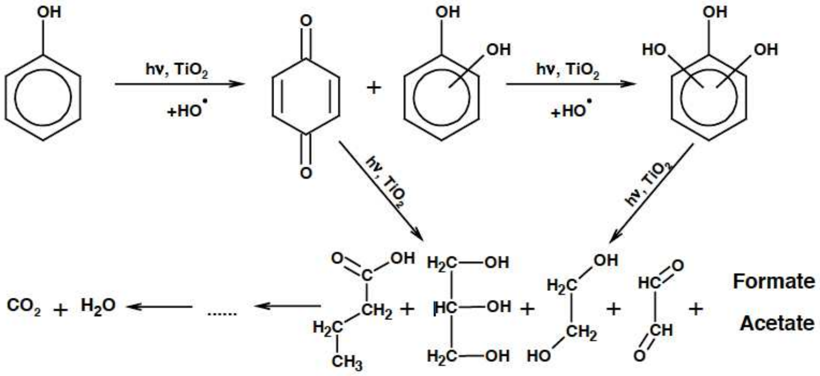

Fig. 1-16 A possible mechanism of phenol destruction on illuminated TiO_2. [112]

Dispersed TiO_2 as suspension in solution has been first frequently experimented in many works. [76, 94, 115] Degussa P25 TiO_2 powder (from Evonik) as a “gold standard” commercial photocatalyst is most commonly used in many laboratory researches. It is a mixture of anatase and rutile in a ratio 80% : 20% in weight. The particles have surface area ca. 50 m^2/g and size less than 25 nm. Both the nature of photocatalyst and conditions in the solution and irradiation source are found as important parameters for photodegradation efficiency. However, it is quite often reported that removing TiO_2 powders from the treated liquid flow is very difficult. [38, 40] Filtration is obliged after treatment with catalyst powder and loss of the catalyst is found to be 30% when recycling reported in one study [59]. It is indeed the technical "bottleneck" of the suspended system when scaling up it to industrial application.

Subsequently, a lot of efforts are made on integrating membrane separation and immobilizing TiO_2 particles (e.g. the P25 powders) on mechanical support. In the beginning, TiO_2 layers have been immobilized on glass and silicon supports with methods including sol dip-coating, physical vapor deposition and chemical vapor deposition. [90, 116, 117] More recently, TiO_2 has been coated on membrane substrate and consequently surface reaction and separation process could be integrated in one photoreactor. [15, 114, 118] Producing porous TiO_2 coating layer with large specific surface area is aimed at improving catalytic efficiency in the immobilized phase.

1.3.2 Membrane separation integrated with photocatalytic AOP treatment

Membrane is a thin and selective barrier through which both matter and energy could pass under some certain force. Since the 19th century artificial membranes have been attempted and manufactured for different functions as contactor, distributor and reactor. Artificial membranes are found in polymers, inorganic composites, ceramics and metals nowadays. General membrane modules include flat-sheet, spiral wound, tubular and hollow fibers. Membrane processes are spatially economical, consuming less energy and depleting fewer less chemicals in continuous and stable performance. They can be found in daily life as producing clean water, recovering valuable resources, concentrating solutes (e.g. in beverages and pharmaceutics) and separating gases/vapors.

Driving force indicates the thermodynamic potential on membrane and it contains the difference in concentration, pressure, temperature and electric potential. Definition of driving force (F) is given as the ratio between differential potentials against membrane thickness as written in Equation 1-25.

$$F = \frac{\Delta X}{\delta} \tag{1-25}$$

where F is driving force, ΔX is differential potential and δ is membrane thickness.

Concentration-driven membrane have been employed in gas separation (e.g. CO_2 capture and natural gas syntheses), pervaporation (e.g. organic solvent purification), dialysis and osmosis processes. Pressure-driven membrane processes are categorized according to the applied pressure (ΔP) as: microfiltration (MF) with $\Delta P \leq 2$ bar, ultrafiltration (UF) with $\Delta P = 1 - 10$ bar and reverse osmosis (RO) with $\Delta P = 10 - 25$ bar. The components are separated when they are passing through porous membrane under certain pressure according to components' molecular sizes. Membrane's pore sizes are decreasing along with an increased pressure enforced from MF, UF to RO process so that molecules with smaller size can be separated. Nanofiltration (NF) is driven with even higher ΔP *(*15 – 80 bar) and separation mechanism is based on molecular weight. Moreover, membrane processes driven electrically are often practiced in electro-dialysis and fuel cells for separating salts and ions.

Mass transfer in the membrane is important to be clarified before scaling up membrane module. A flux (J) in a membrane is defined as the quantity of a component that is passing through per unit membrane surface per unit time. The flux is proportional to the driving force (F) with a proportional factor (A). And by inserting the Equation 1-25 about the driving force, the flux can be also expressed as in Equation 1-26.

$$J = A \times F = A \times \frac{\Delta X}{\delta} \tag{1-26}$$

where J is flux through membrane, A is proportional factor, F is driving force, ΔX is differential potential and δ is membrane thickness.

In earlier researches, TiO_2 photocatalysis process has been combined in pressure-driven membrane processes including MF, UF and RO reported in Ollis' review in 2003. [11] Membrane processes were integrated in photoreactor, in the most cases, to filtrate the dispersed catalyst particles after water treatment. Four types of reactor operation have been discussed in the review including: 1) photocatalysis (suspension) + MF for catalyst recycle, 2) photocatalysis (suspension) + UF for catalyst and reactant recycle, 3) photocatalysis (catalyst immobilized) + UF/RO for reactant recycle and 4) immobilized photocatalyst on UF/RO for membrane self-cleaning. The author has pointed out that further effort is indeed necessary to improve the reactor configuration and thus figure out the optimized coupling manner.

Coupling photocatalytic oxidation and membrane separation is considered as a very encouraging prospect in industrial-scale water purification. More recent progress on photocatalytic membrane reactors (PMRs) has been reviewed in Mozia's review in 2010. [12] In addition, pressure-driven NF processes has been studied in photoreactor. Some other membrane technologies including dialysis, pervaporation (PV) and direct contact membrane distillation (DCMD) have been also integrated in PMRs for self-cleaning surface function.

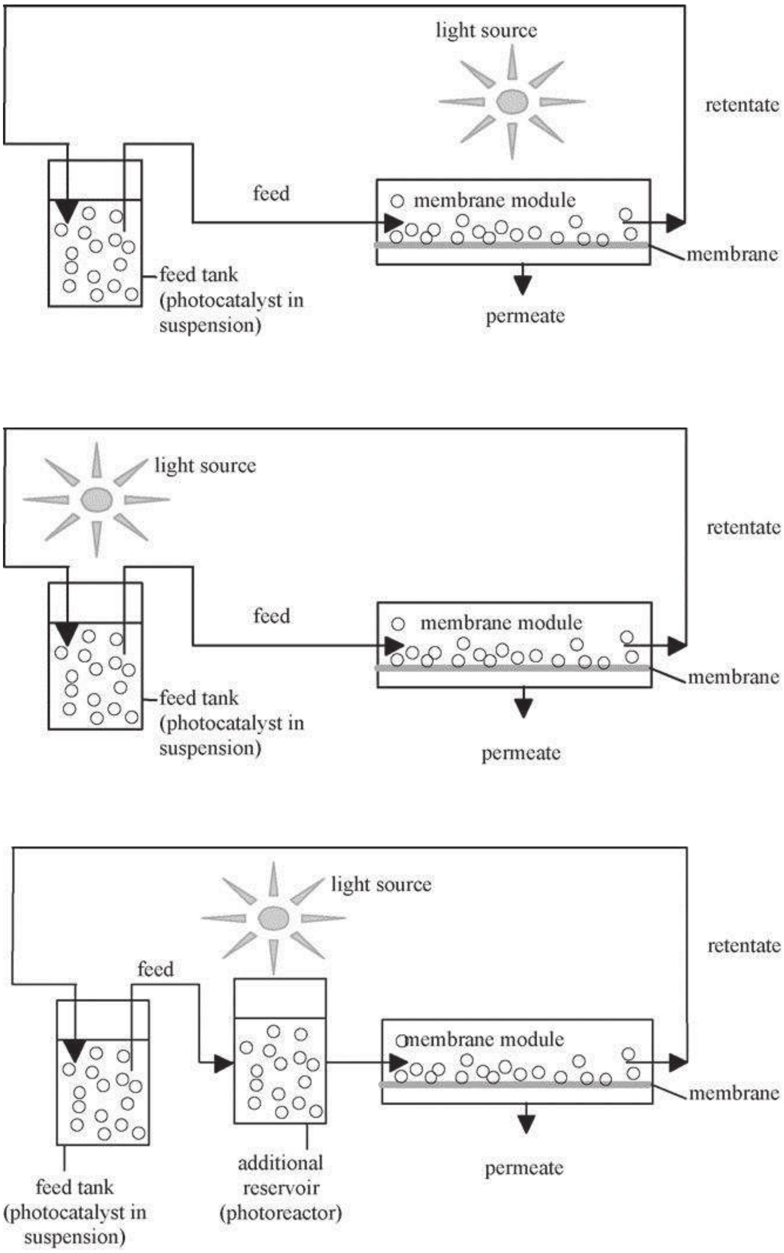

Fig. 1-17 Photocatalytic membrane reactors (PMRs) with dispersed catalyst (shown as the spherical particles) in aqueous solution: (a) photoreactor as the feed tank, (b) photoreactor as the membrane cell and (c) photoreactor tank between feed and membrane compartments. [12]

First of all, the slurry reactor with dispersing catalyst integrated with filtrating membrane is illustrated in Figure 1-17, in which the photoreactor can be located differently in the loop. Either the membrane cell can be the photoreactor as shown in Figure 1-17 (a) or the feed tank can be the photoreactor as shown in Figure 1-17 (b). In a third situation, an additional reservoir between the feed tank and membrane cell works as the photoreactor as shown in Figure 1-17 (c). As reported in Mozia's review, the third configuration has been most often applied in practice. It could be explained with the feasibility by adding a reservoir without too much change of the other compartments.

Further on, modified membrane with photocatalytic function provides a new solution for separation-and-photoreaction coupling. Functionalized membrane works as both contactor and reactor in the process. Photocatalytic membrane instead of using dispersed catalyst in liquid phase is presented in Figure 1-18. [12] Such type of PMRs solves the problem of powder filtration and catalyst loss in the slurry reactor. Yet the reduced surface area and limited mass transfer could possibly exist as the immobilized phase.

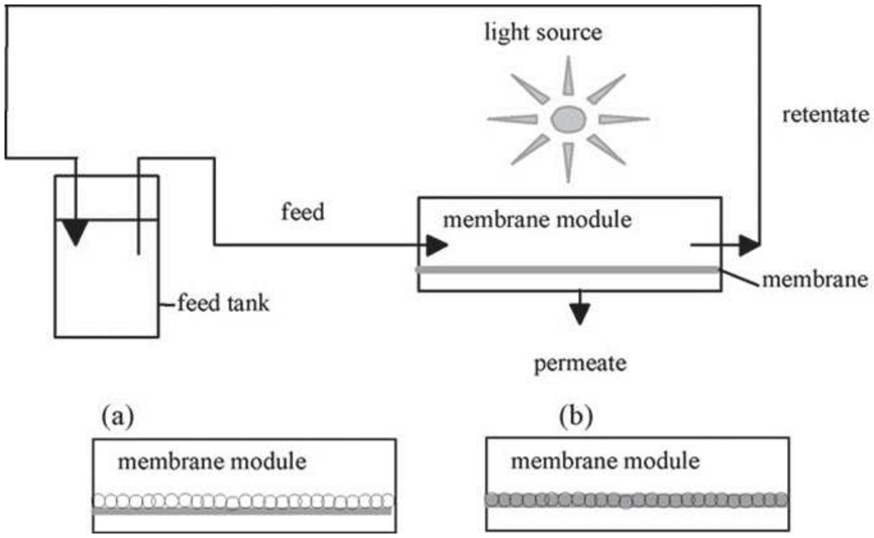

Fig. 1-18 Photocatalytic membrane reactors (PMRs) with immobilized catalyst: (a) on and (b) in the membrane. [12]

The configuration as shown in Figure 1-18 (a), the photocatalyst coating layer (on the membrane) is in contact with the feed flow, which has been frequently applied in laboratory researches. [110, 119-121] The flow direction is from the photoactive side to the non-active side in this situation. As the light energy is supplied from the feed solution then onto the catalyst surface, photodegrading reactions take place with the raw organic molecules existing in the feed. As a result, the permeated solution could be composed of water molecules, products and/or by-products of decomposing reactions, and possibly non-degradable containments. One advantage of using this membrane asset is that surface fouling can be reduced since the adsorbed species should be degraded with illuminated photocatalyst layer. On the other hand, the permeate flux through the membrane could maintain stable due to less blocking in the pores. For instance, it is found that TiO_2-coated and TiO_2-entrapped membranes with enhanced hydrophilicity property have strengthened fouling mitigation. [15, 122] It should be noted that light-transmitting efficiency might be restricted when passing through a feed solution of high concentration of organic contaminants.

Another possible membrane asset is that the non-photoactive membrane support is in contact with feed solution and the photocatalyst coating layer is toward the permeate solution as illustrated in Figure 1-19. Light source is supplied from permeate solution then onto the active surface. In this situation only the species that passed through the membrane (for instance according to the molecular sizes) would react on the illuminated photoactive surface. When there is no differential pressure applied on the two sides of membrane, a concentration-driven process is in the diffusion cell as show in Figure 1-19 (a). When pressure is applied, organic solute is driven more severely by the transmembrane pressure as shown in Figure 1-19 (b).

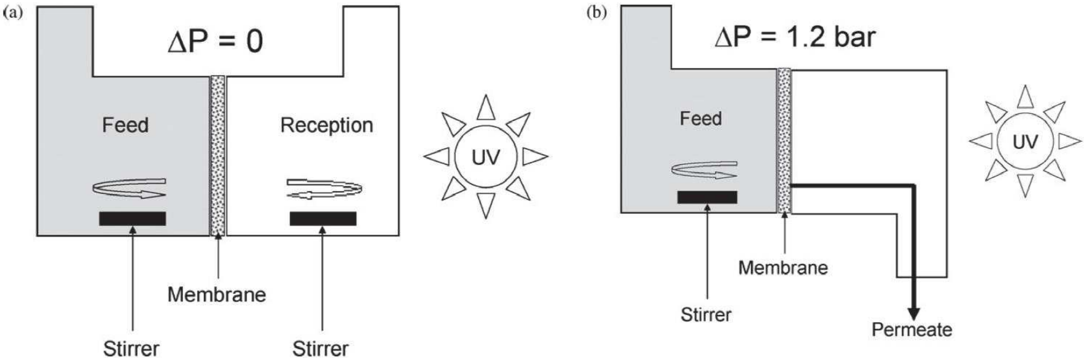

Fig. 1-19 Cell configuration for testing the photocatalytic efficiency of the titania membrane: (a) diffusion cell and (b) permeation cell. [14]

It enables to produce high quality permeation since mineralization of the permeated compounds occurs in permeate solution. Nevertheless, only the permeate solution is purified while leaving the feed flow untreated.

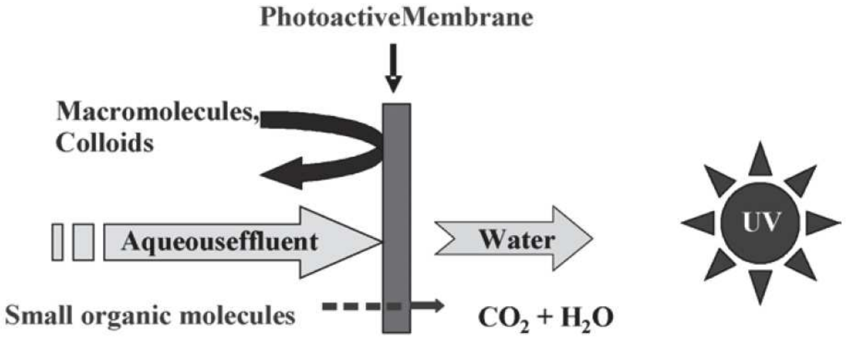

Fig. 1-20 Schematic presentation of a potential use of PMR configuration in the case of ultrafiltration of wastewater: the permeation layer in contact with the feed enables the retention of macromolecules and colloids; the small organic molecules which are not retained by the membrane are degraded by UV irradiation of the opposite side of the membrane consisting in a photocatalytic porous support. [123]

Number of the publications with topic on “photocatalytic membrane” shows a steady increase from the year 2000 till 2014 (September) as presented in Appendix 2. Photocatalytic membranes have been synthesized as modules including fat-sheet, tubular and fiber modules. [84, 124, 125] In the year of 2000 there were only 10 relevant papers published yet the number of papers rises to more than 160 publications in 2013. At the mean time, publications on “photocatalytic membrane” specified for “wastewater treatment” underwent a growth from none paper in 2000 to more than 20 papers in 2013. Photocatalytic membrane process normally works one for the steps in wastewater-treating course. Up to now TiO_2 and dopant-TiO_2 are the most wide-spreading photocatalyst used to modify membranes. Fabricating TiO_2-based membranes in large scale is the key point to bloom industrial application of PMRs for environmental remediation.

1.3.3 TiO_2 membranes

TiO_2 photocatalytic membranes have been prepared as pure and composite ones as reported with their progresses as reported in individual reviews of Leong [126], Zhang [127] and Pelaez [128]. Membrane preparing methods, properties of the synthesized membranes (either pure or hybrid) and photocatalytic performance of them are discussed and compared in this session.

1.3.3.1 Pure TiO_2 membranes

Pure TiO_2 membranes can be prepared in the modules as nanofibers [84], nanowires [16, 129, 130] and nanotubes [125, 131-133]. TiO_2 nanofibers have be obtained in some works by spinning-sintering [134] and electrospinning [135]. In the latter work, Ag particles were added in TiO_2 nanofibers leading to the solar-driven degradation of organic pollutant (MB dye). SEM and TEM images of Ag-TiO_2 fibers are presented in Figure 1-21. In addition, TiO_2 nanowires can be fabricated by hydrothermal growth method using sodium hydroxide and TiO_2 precursor (e.g. Degussa P25 and titanium foil) in some other works. [16, 130]

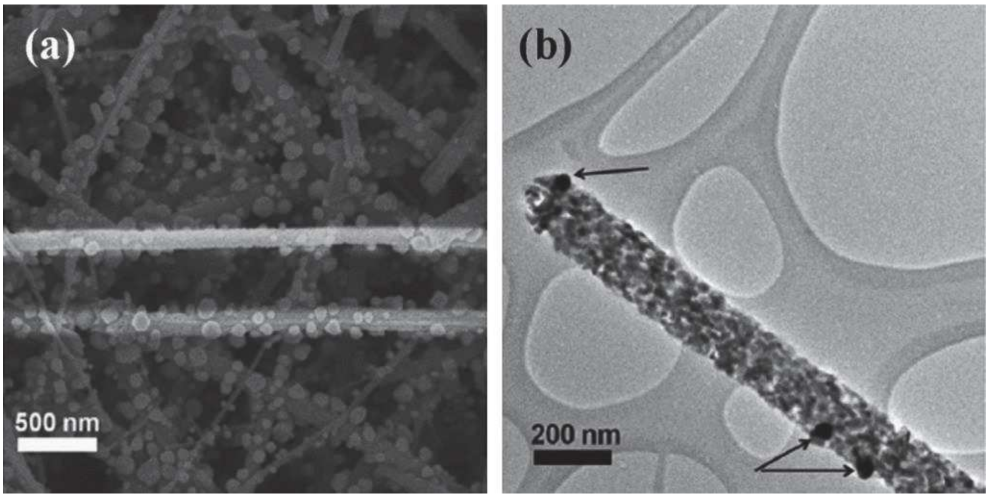

Fig. 1-21 (a) SEM image and (b) TEM image TiO_2 nanofibers with Ag. [135]

TiO_2 nanotube membrane can be synthesized by anodization using titanium foil as a working electrode. This is a simple and effective bottom-up preparation method without using etching solution. TiO_2 nanotubes were transferred from amorphous to anatase phase with calcination at 600 °C. The rutile phase was developed at annealing temperature above 650 °C. Example of SEM images of TiO_2 nanotubes are presented in Figure 2-22. In another work, vertically oriented, double-sided and opened TiO_2 nanotubes were produced in electrochemical process. [131] The titanium foil was removed by dissolution in water-free CH_2OH/Br_2 solution. Opening the bottom of the tube was accomplished by exposure to HF vapor.

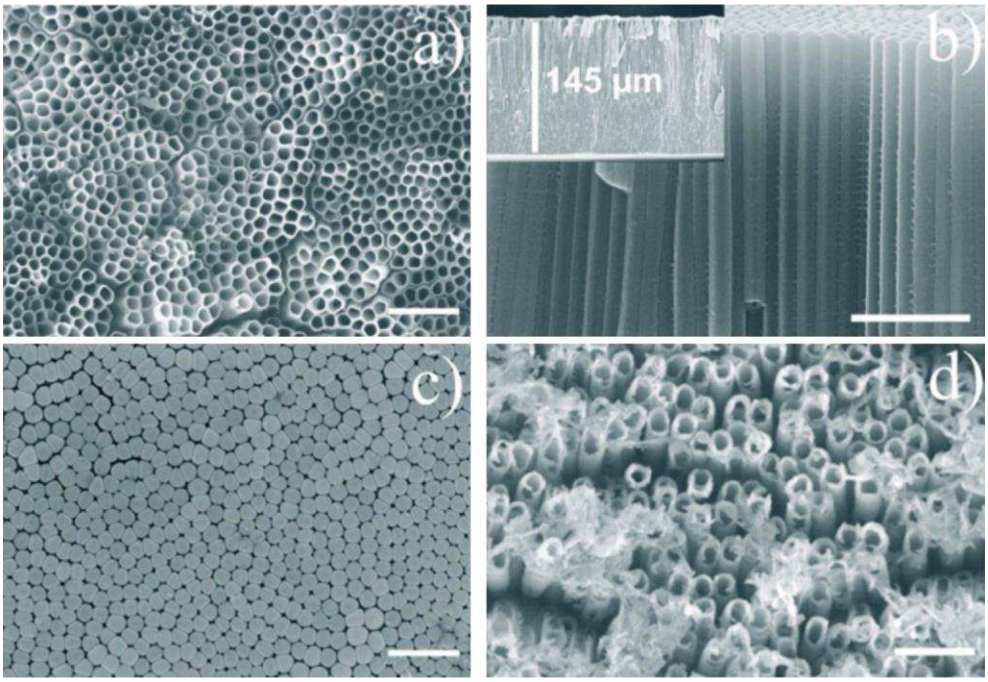

Fig. 1-22 SEM images of pure TiO_2 nanotubes: (a) top view and (b) side view. [131]

1.3.3.2 TiO_2-polymer hybrid membranes

Polymeric membranes are the most-popular membrane type and they are often employed in wastewater treatment. Manufacture of polymeric membranes is a matured technology in industry in comparison with ceramic, inorganic and metallic ones. Polymer materials including polyvinylidenefluoride (PVDF), polyethersulfone (PES), polyethylene terephthalate (PET), polytetrafluoroethylene (PTFE), polyacrylonitrile (PAN), polyester and polyamide have been used as mechanical support for photocatalyst. TiO_2-polymer composite membranes can be designed in two ways: 1) TiO_2 particles immobilized on surface or 2) TiO_2 particles entrapped in polymer pore structure. The first type can be obtained by coating and depositing approaches and the second one can be prepared by dispersing TiO_2 in polymer solution during membrane casting and then the catalyst is blended in polymer membrane.

In one work on TiO_2-coated polymer membrane, PVDF-PEG membrane prepared using concentration of 12 wt% PVDF and 2 wt% PEG has a high water flux and rejection. [136] Three-dimensional AFM surface images of the neat PVDF-PEG membrane and the TiO_2-PVDF-PEG composite membrane are displayed in Fig. 1-23. The membrane flux decreased when the concentration of added TiO_2 particles in the range of 0.5 – 0.5 w% and then the flux increased gradually again with adding TiO_2 in the range of 0.5 – 2.0 wt%. It was explained as larger pores in the membrane could be formed as TiO_2 nanoparticles aggregating due to higher concentration. A smoother surface of TiO_2 composite membrane is found in AFM scanning as given in Figure 1-23 (right), which improves the membrane's antifouling property. Moreover, UV illuminated TiO_2-composite surface photodegraded the foulants in the applied cross-flow ultrafiltration process and maintained the flux as found in the presented work.

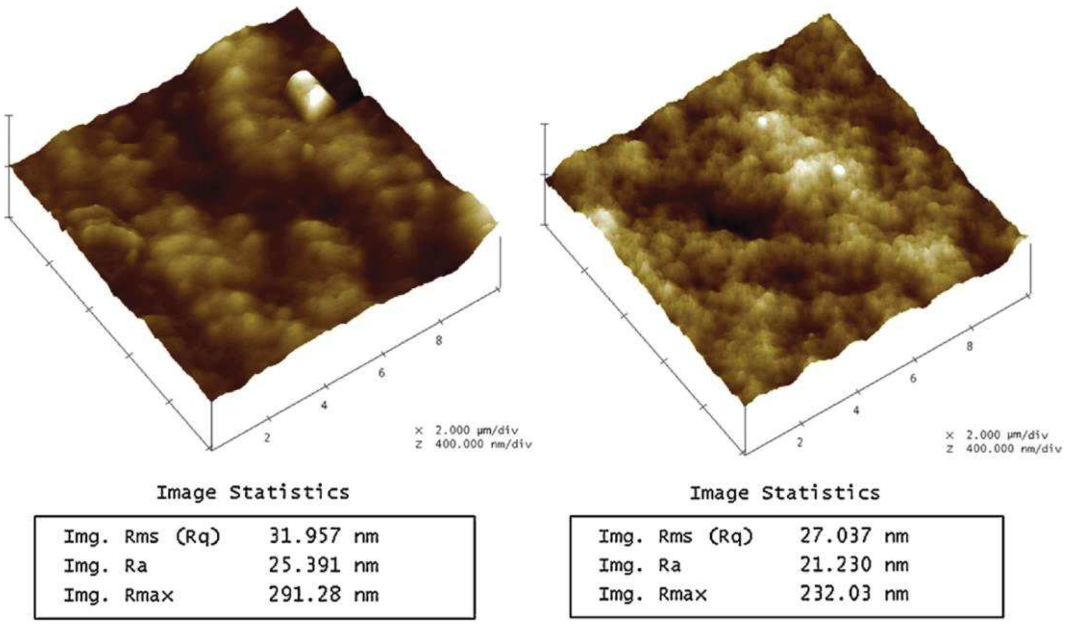

Image Statistics

Img. Rms (Rq)	31.957 nm
Img. Ra	25.391 nm
Img. Rmax	291.28 nm

Image Statistics

Img. Rms (Rq)	27.037 nm
Img. Ra	21.230 nm
Img. Rmax	232.03 nm

Fig. 1-23 Three-dimension AFM surface images of PVDF-PEG membrane: the neat membrane (left) and TiO_2 composite membrane (right). [136]

In another work, water flux of PVDF-g-PAA-TiO_2 composite membranes decreased with an increasing concentration of TiO_2 in the range of 0.5 – 3.0 wt% in the coating process due to pore blockage. [15] SEM images of the PVDF-g-PAA-TiO_2 composite membranes containing 0.5 wt% and 3.0 wt% TiO_2 are presented in Figure 1-24. It clearly shows that more blockage in the membrane pores at higher coated ratio.

As for TiO_2-blended polymer membranes, the addition of TiO_2 in casting solution sometimes could lead to a more porous membrane. [15, 137-139] For instance, cross-sectional SEM images of TiO_2-blended polymer membrane with various TiO_2 loaded ratios are presented in Figure 1-25. [138] Catalyst TiO_2 was embedded in PVDF/PES membranes with a weight ratio equal to 1 wt% and 4 wt% respectively as presented in the figure. It is revealed that when the TiO_2 concentration was increased the hybrid membranes had less porous sub-layer but had more interconnectivity of sub-layer microvoids. [138] The membrane water flux was reduced after adding TiO_2 nanoparticles in the range of 1 – 4 wt% but slightly increased when TiO_2 was increased up to 6% according to the presented study. In another work, water flux of 1 wt% TiO_2 blended PVDF membranes is higher than that of the neat membrane, while the flux was decreasing when the blending TiO_2 was increased to 4 wt%. [139]

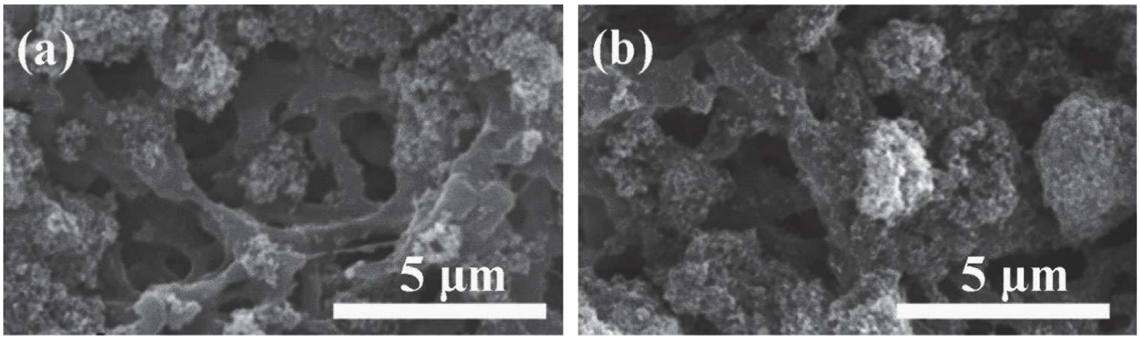

Fig. 1-24 SEM images of PVDF-g-PAA-TiO_2 composite membrane of (a) 0.5 wt% TiO_2 and (b) 3.0 wt% TiO_2. [15]

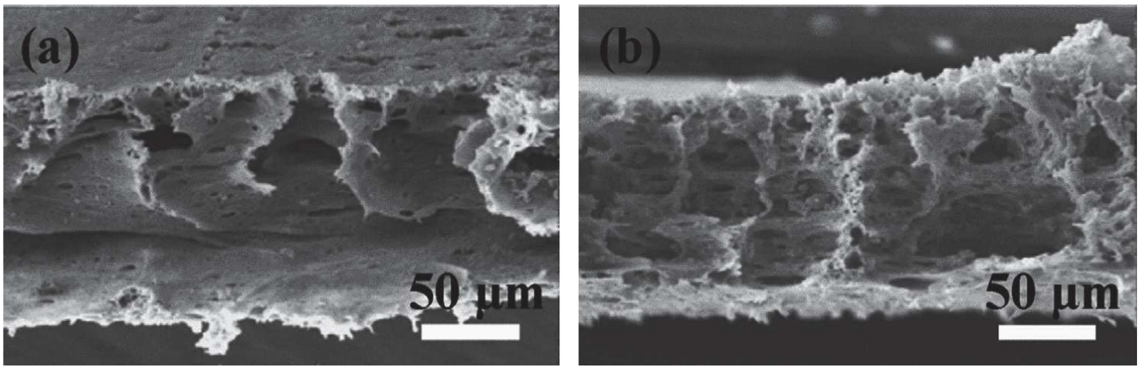

Fig. 1-25 Cross-sectional SEM images of PVDF/PES membrane for (a) 1 wt% TiO_2 and (b) 4 wt% TiO_2. [138]

When employing polymeric membrane as mechanical support, TiO_2 adhesion to polymer and the polymer's durability to UV irradiation should be carefully considered. As for coating TiO_2 on polymer surface, Ti^{4+} is connected to carboxylate group (-COOH) through the two oxygen atoms. [140] In addition, hydrogen bonds (for instance H to O atoms 21 kJ mol^{-1}) are formed between the carbonyl group on polymers and surface hydroxyl group on TiO_2. [141] Since such adhesion is generally weak, introducing more COOH functional groups to polymer could enhance surface hydrophilicity and thus strengthen the attachment with TiO_2. Nevertheless, some study demonstrated that chemical bonds between TiO_2 and polymer were not strong enough and it was inevitable that TiO_2 would be lost as being used. For instance, it is discovered that TiO_2 particles detached from the membrane after 30 min osmosis operation but no further loss occurred in the following 7 day in a study. [142] On the other hand, with constantly exposure to UV irradiation the long-term stability of applied polymer membrane should also be examined. Some work indicated that PES membranes have not been degraded/damaged within 4 h UV illumination coupled with filtration experiment base on SEM observation. [137] Some other work found that the structure of TiO_2-PVDF-PEG membrane was damaged after 12 h UV irradiation. [136]

In general, TiO_2-coated membranes performed higher photocatalytic efficiency [137] and better hydrophilicity [15] in contrast to TiO_2-blended polymer membranes. The blended ones are limited in light penetration since the catalyst is embedded inside the membrane. Diffusion and adsorption of reactant species to active sites is less effective in the bulk structure. Moreover, TiO_2-coated membranes exhibited better anti-fouling property and long-term water flux stability. [15, 138]

1.3.3.3 TiO_2-ceramic hybrid membranes

Ceramic membranes, in particular alumina (Al_2O_3), have been explored to serve as mechanic support for immobilizing TiO_2 in more recent studies. Ceramics are chemically inert and thermally stable in the membrane processes. However, the rigidity of ceramic materials can be a limitation under high-pressure application. Fixing TiO_2 nanoparticles onto porous ceramic supports has been realized with sol dip-coating approach [14, 18, 143, 144], hydrothermal [145], chemical vapor deposition (CVD) [13, 146], atmospheric plasma spraying (APS) [147] and plasma-enhanced CVD (PECVD) [148].

Sol-gel dip-coating is an approach carried out by immersing a substrate into sol solution and then withdrawing it with controlled velocity. Drying and calcination treatment is usually continued after sol coating in order to remove organic solvent in the sol solution. Quality of TiO_2 coating layer greatly depends on the sol mixture and the dip-coating procedure. In the works of Bosc et al. [123] and Djafer et al. [14], uniform TiO_2 layers have been successfully deposited on mesoporous ceramic supports (Figure 1-26(a)) and on macroporous ceramic support (Figure 1-26(b)) respectively. Dip-coating step has been repeated a few times in order to obtain 3-µm thick TiO_2 deposited layer on porous Al_2O_3 substrate in the later work as presented in Figure 1-26 (b). [14] Choi et al. [18] dip-coated TiO_2 nanoparticles (particle size 3 – 7 nm) on Al_2O_3 membrane and Hong et al. [149] dip-coated TiO_2 nanofibers on Al_2O_3-ZrO_2 porous support.

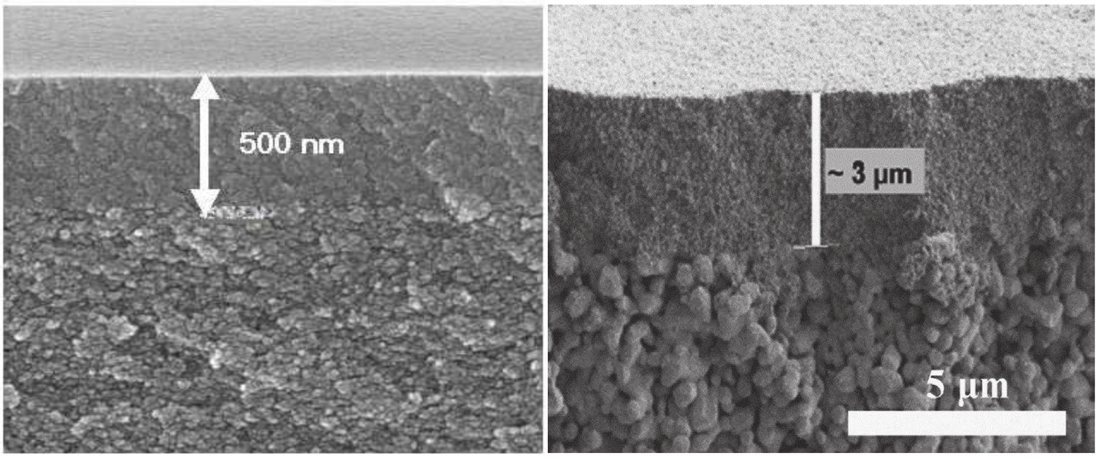

Fig. 1-26 SEM images of TiO_2/Al_2O_3 composite membrane : dip-coated TiO_2 layers on (a) 5 nm pore-sized top layer Al_2O_3 [123] and (b) tubular macroporous Al_2O_3. [14]

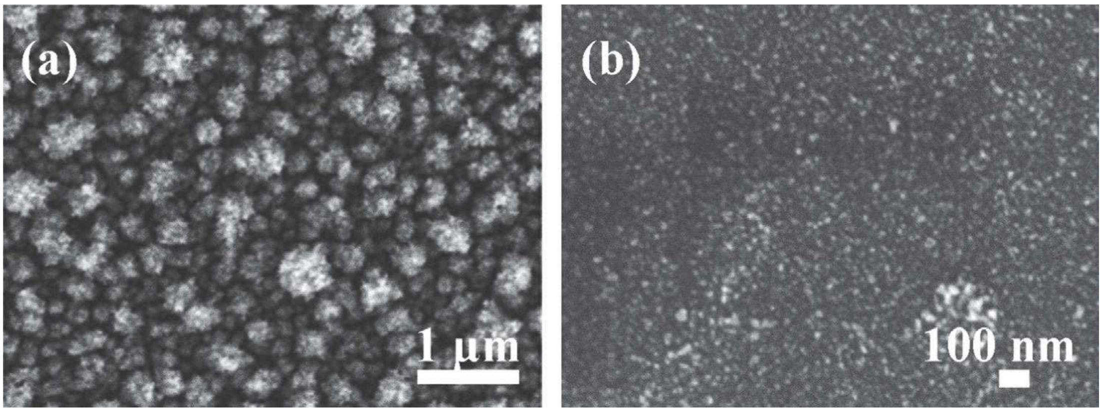

Fig. 1-27 SEM images of the TiO_2 nanoparticles deposited on tubular Al_2O_3 membrane with CVD method: (a) internal surface and (b) external surface. [146]

Chemical vapor deposition (CVD) is another common technique to immobilized TiO_2 (from vapors of Ti-based precursor via a bring gas) on Al_2O_3 substrate with substrate heating above 500 °C in the reactor. [13, 146] Romanos et al. applied CVD method to deposit TiO_2 nanoparticles on both sides of a γ- Al_2O_3 nanofiltration membrane, whose SEM images are displayed in Figure 1-27. [146] Inner surface has been uniformly deposited with anatase TiO_2 nanoparticles (but with significantly declined deposition toward the outlet of the CVD reactor), whereas outer surface of the tubular membrane is more slightly deposited in comparison to the inside one. It this work, it is found that CVD TiO_2-coated membrane resulted in water flux reduction, similarly to the other coating methods. Plasma-enhanced CVD (PECVD) enables to deposit TiO_2 nanoparticles at lower substrate temperature (e.g.

room temp) [148], which makes this method compatible with thermal sensitive substrates. Principles and application of PECVD process for depositing TiO_2 thin films will be further described in the session 2.2. Atmospheric plasma spraying (APS) is another possible technique to spray TiO_2 solids and deposit them on membrane with an aid of plasma discharge. [147]

Physical vapor deposition (PVD) has been also used to deposit TiO_2 thin film on different mechanical supports in many studies. [150-156] In general, no chemical surface reaction takes place upon the depositing step in PVD process. Sputtering [150, 154, 157, 158] and evaporation [157, 159, 160] methods are often applied in PVD procedure aimed at obtaining crystalline layer at reduced temperature and increasing deposition rate. Sputter deposition of TiO_2 film can be obtained from pure Ti target in O_2 or O_2/Ar atmosphere. Pulse mode used in magnetron sputtering technique would impact particle bombardment on growing film, and possibly enable to synthesize crystallite film at low temperature. On the other hand, plasma-activated evaporation method could increase deposition rate due to reactive electron beam, supplying higher energy to the condensing particles during deposition.

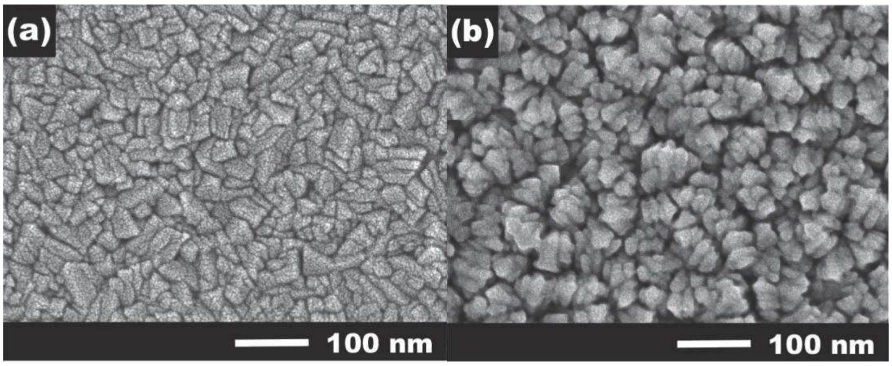

Fig.1-28 Surface morphology of glass-supported TiO_2 thin film (250 nm thick) obtained from PVD method at two working pressures: (a) 0. 92 Pa and (b) 2.77 Pa with electric power 300 W. [154]

In one study, TiO_2 thin films of thickness 250 nm were deposited on glass substrate by magnetron sputtering PVD. [154] Operating conditions as total working pressure from 0.7 to 3 Pa and substrate temperature equal to 60, 160 and 280°C have been experimented; SEM images of two samples are displayed in Figure 1-28. Photocatalytic property of the catalyst films made from different conditions has been compared when degrading methylene blue in water solution. Anatase crystal face (101) was found in the TiO_2 film deposited at substrate temperature 280°C and its catalytic efficiency (decomposing 80% methylene blue in water within 100 minutes) is higher with comparison to the samples made at 60 and 160°C.

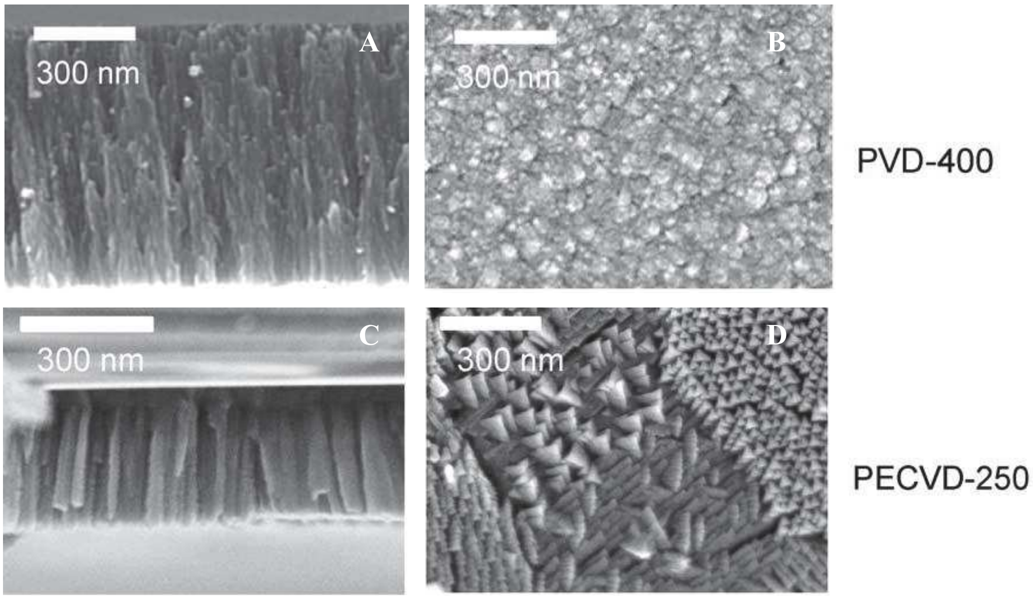

Fig. 1-29 SEM cross-section (A) and surface (B) images of TiO_2 thin film made from PVD method at 400°C and cross-section (C) and surface (D) images of TiO_2 thin film made from PECVD method at 250°C. [161]

In addition, PVD method using plasma discharge/glancing angle deposition (GLAD) technique to produce TiO_2 with oriented columnar-like structure has been studied. [151, 155, 161] Rotating the substrate at certain angle could vary the particle's incident angle from the target to the substrate. Such incident angle variation leads to shadow effect and influences on nanostructure, crystalline and surface properties of deposited TiO_2 thin films. Reversible transfer between super-hydrophobicity and super-hydrophilicity has been witnessed and it has been proved that UV illumination greatly improved the surface wetting property [151, 155]. Furthermore, PVD and PECVD prepared TiO_2 thin films have been compared in one study (SEM images presented in Figure 1-29): preferential growth of (004) and (112) crystal plances were found in PVD-400 sample (TiO_2 deposited at 400°C), while preferential growth of (101) plane was found in PECVD-250 sample (TiO_2 deposited at 250°C) [161]. In this work, the thickness of film prepared at glancing angle (85°) was smaller than that of normal evaporation due to the geometric condition in PVD process, while porosity of the glance-deposited sample was larger as witnessed by SEM observation.

In another work, TiO_2-polymer composite layer was prepared by magnetron sputtering PVD method at room temperature (about 25°C), supplied with substrate bias voltage equal to -60 V. [153] Poly(vinilidene fluoride) (PVDF) was applied as the polymer substrate. The mechanical performance (stress-strain) of the composite film/polymer substrate has been analyzed in the study. Raman spectroscopy experiments revealed that the as-deposited coatings (100 – 300 nm thick) on polymer substrates are mostly amorphous; however evidence of anatase and rutile nano-crystalline phase can be found.

In a summary, photocatalytic TiO_2-based membranes including pure TiO_2 membrane (as nanotubes, nanofibers and nanowires) and composite TiO_2 membrane (as TiO_2-polymer and TiO_2-ceramic hybrid ones) have been reviewed in this session. Membrane types, preparing techniques, photocatalytic performance and membrane permeability have been summarized on the discussed membranes as listed in Table 1-4 (adapted version according to the review of Zhang et al. [127]).

Table 1-4 Summary of TiO_2-based membranes with their photocatalytic performance and permeability. (adapted from [127])

Membrane types	Fabrication method	Light source	Pollutants	Photocatalytic performance	Membrane permeability	Ref
Free-standing TiO_2 nanotube membrane	Anodization	UV 325, 500 W m^{-2}	MB (6.4 mg L^{-1})	90% (within 20 h)	n.a.	[131]
TiO_2 nanowire MF membrane	Filtration calcination	UV 254, 11 W	HA (15 mg L^{-1})	100% (within 1 h)	3600 (L m^{-1} h^{-1} bar^{-1})	[130]
TiO_2 nanowire UF membrane	Filtration press-calcination	UV 254, 11 W	E. coli. (106 CFU ml^{-1})	99.9% (within 1 h)	300 – 600 (L m^{-1} h^{-1} bar^{-1})	[129]
TiO_2 hollow fiber membrane	Spinning sintering	UVA, 32 W	AO7 (20 mg L^{-1})	30–70% (within 1 h)	13.5 (L m^{-1} h^{-1} bar^{-1})	[134]
TiO_2-PVDF membrane	Entrapping	UVC, 15 W	RB5	> 99% (within 1 h)	50 – 130 (L m^{-1} h^{-1}, 0.2 bar)	[139]
TiO_2-CA membrane	Filtration	UV 254, 400 W m^{-2}	HA	60–70% (within 1 h)	5.3 (L m^{-1} h^{-1} bar^{-1})	[162]
TiO_2/Al_2O_3 membrane	Sol-gel dip-coating	UV 365, 30 W	MB (9.6 mg L^{-1})	100% (within 5 h)	3.5 – 10.4 (L m^{-2} h^{-1} bar^{-1})	[18]
TiO_2/Al_2O_3 tube membrane	Chemical vapor deposition (CVD)	UVA, 36 W	MO (6.5 mg L^{-1})	40–80% (within 6 h)	0.6 (L m^{-2} h^{-1} bar^{-1})	[146]
TiO_2/Al_2O_3 nanotube membrane	Atmospheric plasma spraying (APS)	UVC, 15 W	RB5 (100 mg L^{-1})	100% (within 1.2 h)	120 – 150 (L m^{-1} h^{-1} bar^{-1})	[147]
TiO_2/silica nanotube membrane	Sol-gel	UV 365, 300 W	DB168 (50 mg L^{-1})	80% (within 3 h)	55 – 65 (L m^{-2} h^{-1}, 0.5 bar)	[143]
Ag-TiO_2/HAP /Al_2O_3 membrane	Sol-gel	UV 365, 400W	HA (TOC 15 mg L^{-1})	90% (within 1h)	400 – 1000 (L m^{-2} h^{-1}, 1 bar)	[144]
C, N and Ce co-doped TiO_2 membrane	Sol-gel	Visible light, 500 W	MO (5 mg L^{-1})	100% (within 2h)	4 – 5 (L m^{-1} h^{-1} bar^{-1})	[163]
TiO_2/glass	Physical vapor deposition (PVD)	UV, 13 W m^{-2}	MB (16 mg L^{-1})	80% (within 1.5 h)	n.a.	[154]

Note: MB: methylene blue, HA: humic acid, AO7: acid orange 7, RB5: Reactive black 5, MO: methylene orange and DB168: direct black 168.

1.3.4 Reaction kinetics

Kinetics of photodegradation reaction has been studied with some simple models with respect to the experimented conditions including membrane asses, solution, dynamic parameters and so on. The kinetics describes how fast the pollutants are being degraded in the PMR unit. At the mean time, it can reveal whether the degradation process is reactant dependent or independent.

Degradation rate is in relevant with mass transfer (in the bulk solution and internal membrane) and reaction rate (specifically for tested pollutant compound). Some experimental results showed that photodegradation rate is usually pseudo-first-order [13, 15, 16, 130, 132, 135, 139, 143, 146, 147, 164], which means the rate depends on initial concentration of organic contaminant but regardless of pollutant type. A few other researches found that photodegradation rates of phenol [165-167] and dye molecules [168] using TiO_2-PE membranes were zero-order. In such cases, the reaction rate was independent of pollutant concentration. In the study of Molinari et al. [164], it is revealed that degradation rate of "patent blue" dye is zero-order when the concentration ≥ 100 mg L^{-1} and pseudo-first-order when the concentration ≤ 100 mg L^{-1}. When the initial concentration of organic compound in feed solution is generally low, a zero-order or first-order kinetics could be applicable concerning different photodegradation reactors.

Photodegradation rate has been found going up to a plateau as a function of continuous irradiation time. This phenomenon agrees with Langmuir-Hinshelwood (L-H) reaction mechanism as described in Equation 1-27. Reaction rate (r) is proportional to surface coverage (θ_i) with a reaction constant (k_r). Assumptions are presumed when applying L-H model as 1) the system is in equilibrium, 2) reactions are taking place on surface and 3) substances competing for active sites are not limiting.

$$r = -\frac{dC}{dt} = k_r\theta_i \tag{1-27}$$

where r is the degradation rate, C is the concentration of organic compound, k_r is the reaction rate constant and θ_i is surface coverage

The surface coverage (θ) is dependent on adsorption of reactants onto the surface and desorption from the surface, with the sorption rates given in Equation 1-28 and Equation 1-29.

$$r_{ads} = k_{ads}(1-\theta)C \tag{1-28}$$

$$r_{des} = k_{des}\,\theta \tag{1-29}$$

In equilibrium, when the adsorption rate (r_{ads}) equals to desorption rate (r_{des}) as in Equation 1-30, then the coverage ratio (θ) can be obtained as in Equation 1-31.

$$r_{ads} = r_{des} \tag{1-30}$$

where r_{ads} *and* r_{des} *are* adsorption and desorption rates, k_{ads} and k_{des} are adsorption and desorption constants, θ is surface coverage *and* C is the concentration.

$$\theta_i = \frac{KC}{1+KC} \tag{1-31}$$

where K is Langmuir adsorption constant as $K=k_{ads}/k_{des}$.

Therefore

$$r = k_r \frac{KC}{1+KC} \tag{1-32}$$

where r is the degradation rate, C is the concentration and K is Langmuir adsorption constant.

When the concentration (C) is very low: $1+KC \approx 1$, then the degradation rate is derived to be in first-order as given in Equation 1-33.

$$r = -\frac{dC}{dt} \approx k_r KC = k'C \tag{1-33}$$

where k' is the first-order constant as $k'=k_rK$.

With a rearrangement, the pseudo-first-order model can be expressed in Equation 1-34:

$$\ln\left(\frac{C}{C_0}\right) = -k't \tag{1-34}$$

Dynamic Langmuir adsorption constant K could be determined with measuring reaction rate and concentration according to Equation 1-32. By plotting $1/r$ against $1/C$, K parameter could be known with the linear relationship as in the following Equation 1-35.

$$\frac{1}{r_0} = \frac{1}{k_r} + \frac{1}{k_r K C_0} \tag{1-35}$$

Experimental degradation rate constant k' (min^{-1}) has been reported in many studies by using sorts of TiO_2 membrane type and model pollutant compounds. The summarized results on the obtained rate constants by pure TiO_2 membrane and TiO_2-composite membranes (hybrid with ceramic and polymer ones) are listed in Table 1-5 and Table 1-6 respectively. Test pollutant model compounds tested in aqueous solution include pharmaceuticals and dye molecules such as methyl orange (MO), methylene blue (MB), rhodamine B (RB) and reactive black 5 (RB 5), direct black 168 (DB 168) Indigo Carmin (IC) and brilliant green (BG).

Table 1-5 Photocatalytic reaction kinetics of pharmaceuticals and dyes by pure TiO_2 membranes.

Membrane type	**Rate constant, *k'* (min^{-1})**	***R^2***	**Fabrication method**	**Pollutant removal**	**Ref**
UV-TiO_2 nanowires	0.1239	0.999	Hydro-thermal	Norfluoxetine	[169]
	0.0688	0.999		Atorvastatin	
	0.0430	0.999		Lincomycin	
	0.0408	0.995		Fluoxetine	
	0.0319	0.997		Venlafaxin	
	0.0422	0.989		Sulfamethoxazole	
	0.0398	0.999		Diclofenac	
	0.0269	0.997		Trimethoprim	
	0.0277	0.988		Bisphenol A	
	0.0159	0.993		Gemfibrozil	
	0.0155	0.999		Atrazine	
	0.0008	0.971		Carbamazepine	
	0.0005	0.945		Ibuprofen	
UV-TiO_2 nanowire membrane	0.022	0.97	-	Humic Acid	[130]
UV-TiO_2 nanotube membrane	0.0001	n.a.	-	RB	[132]

As for pure TiO_2 material, the photodegradation rate constant (min^{-1}) was found very differently depending on the types of pharmaceutical compound in a study using UV irradiated TiO_2 nanowires. [169] The fastest photodegrading rate in the magnitude of order 10^{-1} min^{-1} was found for model compounds such as Norfluoxetine, medium rate in the order of 10^{-2} min^{-1} was found for compounds such as Fluoxetine and Bisphenol A, and the slowest rate in the order of 10^{-4} min^{-1} was for compound such as Ibuprofen by the same type of UV-irradiated TiO_2 nanowires (as seen in Table 1-5).

Table 1-6 Photocatalytic reaction kinetics of dyes by TiO_2-composite membranes.

UV-irradiated membrane type	**Rate constant, *k'* (min^{-1})**	**R^2**	**Fabrication method**	**Pollutant removal**	**Ref**
UV-H_2O_2-TiO_2-Al_2O_3	0.0118	n.a.	Sol-gel dip-coating	DB 168	[143]
UV-TiO_2-Al_2O_3	0.0071				
UV-H_2O_2	0.0043				
UV-TiO_2-Al_2O_3	0.004	n.a.	CVD	MO	[13]
UV-TiO_2-α-Al_2O_3	0.0049	0.999	CVD	MO	[146]
UV-TiO_2-Al_2O_3	0.076	n.a.	APS	MB	[147]
UV-0.5%TiO_2-PVDF-g-PAA	0.0031	0.989	Self-assembling	RB 5	[15]
UV-1.5%TiO_2-PVDF-g-PAA	0.0033	0.943			
UV-3.0%TiO_2-PVDF-g-PAA	0.0042	0.988			
UV-TiO_2-PVDF	0.0605	0.99	Blending	IC	[170]
	0.0986	0.98		BG	
UV-0%TiO_2-PVDF	0.0433	0.956	Blending	RB 5	[139]
UV-1%TiO_2-PVDF	0.0621	0.906			
UV-2%TiO_2-PVDF	0.0634	0.923			
UV-4%TiO_2-PVDF	0.0632	0.952			
UV-TiO_2-PTFE	0.033[a]	n.a.	Blending	TOC[c]	[171]
	0.024[b]				
UV-TiO_2 nanotubes-PU	0.0088	n.a.	Activation reaction	RB	[172]

Note: [a] wavelength 254 nm illumination, [b] wavelength 185 nm illumination and [c] TOC: total organic carbon.

As for TiO_2-Al_2O_3 hybrid membranes, some researcher has proved that adding H_2O_2 in the reactor resulted in photodegrading rate enhancement of DB 168 dye from 0.0071 min^{-1} to 0.0118 min^{-1}. [143] Photolysis effect of MB compound by using H_2O_2 alone with the membrane was measured as *k'* = 0.0043 min^{-1} in the mentioned work, which implies that adding oxidant reagent H_2O_2 contributes the photoreaction irrelevant to affect TiO_2 surface reaction. Very close degradation rate of MO dye has been known experimentally as *k'* = 0.004 min^{-1} [13] and *k'* = 0.049 min^{-1} [146] from two individual works using illuminated TiO_2-Al_2O_3 membranes that have been both prepared with CVD method. Besides, photodegradation rate of MB dye was found very efficient to be *k'* = 0.076 min^{-1} using TiO_2-Al_2O_3 membrane synthesized in APS process. [147]

Table 1-7 Photocatalytic reaction kinetics in solar-driven TiO_2 disinfection process.

Membrane type	**Rate constant, *k'* (min^{-1})**	**Fabrication method**	**Pollutant removal**	**Ref**
Solar only	0.0011	Filtration	E. coli	48
TiO_2 nanofiber membrane	0.0014			
Solar-TiO_2 nanofiber membrane	0.0100			
P25 deposited membrane	0.0021			
Solar-P25 deposited membrane	0.0078			
Ag/TiO_2 fiber membrane	0.0171			
Solar-Ag/TiO_2 fiber membrane	0.0342			

As for TiO_2-polymer hybrid membranes, some researcher found that faster degradation rate could be obtained with more TiO_2 loaded polymer membranes. In one work, degrading rate constant (*k'* = 0.0042 min^{-1}) of RB 5 dye was obtained with more TiO_2 loaded (3.0 wt%) PVDF-g-PAA membrane than those of less loaded membranes (0.5 and 1.5 wt%). [15] Similar improvement of reaction kinetics of the same dye (yet *k' is* averagely 10 times higher than that of the previous study) was found in another work using TiO_2-blended PVDF membranes with increased TiO_2 concentration from 0 wt% – 2 wt%, but no more reaction acceleration with continuous loading up to 4 wt%. [139] Moreover, in one study it is discovered that UV source of larger wavelength 254 nm leads to a faster mineralization rate indicated by TOC value (*k'* = 0.033 min^{-1}) than using smaller wavelength 185 nm (*k'* = 0.024 min^{-1}) by the same TiO_2-PTEF membrane. [171] By using other dye molecules as IC and BG, degrading rate by TiO_2-PVDF membrane was found higher to be *k'* = 0.0605 min^{-1} and *k'* = 0.0986 min^{-1} respectively in comparison to the work using RB 5 dye. [170]

Research work of deactivation E. coli using solar-illuminated TiO_2 nanofiber membrane, P25 deposited membrane and Ag/TiO_2 fiber membrane is presented in Table 1-7.

1.4 Conclusion

Band gap energy (E_g) is the energy difference between valence band and conduction band in solid materials. When semiconductor particles absorb photo energy larger than its band gap energy, radical $^{\bullet}OH$ can be formed due to charge separation of e^- and h^+. Photo-generated $^{\bullet}OH$ (a radical of very high oxidizing potential) can oxide/degrade almost all sorts of organic pollutants in aqueous solution. The photocatalytic advanced oxidation processes (AOPs) leads to an innovative water treatment technology. TiO_2 is found as an effective photocatalyst since 1972 and then attracts a lot of interest in research work on photocatalysis mechanisms. Degussa P25 TiO2 powder from Evonik (a mixture of anatase and rutile) serves as the gold standard photocatalyst in many laboratory studies. Crystalline anatase TiO_2 (in the pure form) is found of the highest photocatalytic efficiency in comparison to the other two phases as rutile and brookite. E_g of synthesized anatase TiO_2 is reported in the range of 3.0 – 3.3 eV depending on the material preparation methods and characterization methods.

Membrane separation has been recently integrated in TiO_2-AOP procedure regarding to membrane reactor of higher compactness, better integrity and separable feasibility is preferred to the slurry reactor for industrial-scale use. Great efforts have been made on synthesizing TiO_2-polymer membranes, TiO_2-ceramic membranes and TiO_2 pure membranes for water purifying purpose in recent studies. Membrane coated with TiO_2 is proven as more effective and efficient than membrane entrapped with TiO_2 since more active sites for reactants and photons are provided as the catalyst on the surface. Photocatalytic membrane reactors (PMRs) have been contemplated in variant possible configurations of the photoactive TiO_2 layer either in contact with feed or with permeate solutions. When the catalyst is toward the feed flow, liquid-solid contact/reaction times can be repeated by circulating the feed but the passed species through the membrane remains in the permeate solution (if without further treatment). When the catalyst is toward the permeate flow, mineralization of organic pollutant could be carried out for the organic species passing through the membrane.

2 Plasma-Enhanced Chemical Vapor Deposition (PECVD) for TiO_2 membrane manufacture

Since the 50s, PECVD method has been applied in materials processing to deposit inorganic films especially for solar cell and integrated circuits fabrication. More recently, it has been implemented for the manufacture of TiO_2 films for photocatalytic applications. Principles of plasma-assisted CVD procedures, focusing on as a low temperature deposition process, will be first explained in this part. To follow up, some specific examples on preparation of inorganic and more particularly TiO_2 films with PECVD approach will be discussed.

2.1 Generalities on PECVD process

2.1.1 Chemical Vapor Deposition (CVD) methods

Chemical vapor deposition (CVD) is a process where a solid material is deposited from a precursor vapor with chemical reactions occurring on or in the vicinity of a substrate surface.[173] Deposited materials can be obtained as coatings, powders or single crystals. In particular, CVD processes have been widely employed to prepare films of uniform-thickness, high-purity and high-performance. Produced films may be amorphous, monocrystalline, polycrystalline, and epitaxial according to the precursor(s) and reactor conditions. In comparison with physical vapor deposition (PVD) process, CVD has many advantages as 1) allowing three-dimensional and complete-coverage coating, while PVD is typically line of sight deposition, 2) CVD using high precursor flow rates leading to higher deposition rates than that of PVD, 3) ultra-high vacuum is not obliged for CVD and the reactor is relatively simple to scale up, 4) controlling the stoichiometry more easily by monitoring flow rates of precursors in CVD than by monitoring evaporation rate in PVD and 5) CVD enables to fabricate abrupt junctions, which is not the case for PVD.

The CVD process generally comes in different categories as atmospheric pressure CVD (APCVD), low pressure CVD (LPCVD), plasma-enhanced CVD (PECVD), photon (laser) induced CVD (PHCVD) and so forth. In thermal CVD processes (e.g. APCVD and LPCVD), heating is the energy source for the chemical reactions in gas phase and at the gas-solid interface. In the plasma process (e.g. PECVD), electric power is the energy source to assist precursor decomposition and high surface temperature is no longer necessary to active the reactions. Nevertheless, optional heating of substrate can enable to tune the structure of the prepared solid material; so the substrate temperature is a critical factor in thin film manufacturing.

A comparison between thermal CVD and PECVD methods for depositing inorganic films such as silicon nitride (Si_xN_y), silicon dioxide (SiO_2) and amorphous silicon (α-Si) is presented in Table 1-8, where the different substrate temperatures required in the processes are listed.

Table 1-8 Substrate temperature in thermal CVD and PECVD. [173, 174]

Film	Precursors	Thermal CVD	PECVD
Silicon nitride (Si_xN_y)	SiH_4 and NH_3	750 °C	200 – 500 °C
Silicon dioxide (SiO_2)	SiH_4 and O_2	350 – 550 °C	200 – 400 °C
Amorphous silicon (α-Si)	SiH_4	550 – 650 °C	200 – 400 °C

Since high deposition temperature (higher than 350°C) is required in thermal CVD processes, it is unsuitable for thermally sensitive substrate especially for the polymer ones normally not bearing up to 250°C. This limitation doesn't systematically occur for PECVD process since electric field acts as the main energy source for the decomposition of precursor(s).

In PECVD process, vapor molecules are more easily broken up with the bonds due to ionization and hot electrons. Plasma reactivity enables films to grow at low substrate temperature (room temp. – 500 °C) with reasonable deposition rate. In addition, low-pressure plasma (a few mbar) leading surface-kinetics controlled deposition produces films of good uniformity. Some drawbacks of PECVD process include difficulties in controlling stoichiometry due to variations in bond strengths of precursors. Moreover, some substrate surface may potentially be damaged due to ion bombardment occurring in plasma. In terms of equipment, PECVD (as low-pressure CVD, LPCVD) requires the use of a pumping system to maintain a low pressure that leads to higher complexity and cost of reactor than in atmospheric-pressure CVD (APCVD) process. In a summary, advantages and limitation of thermal CVD process and PECVD approaches are presented in Table 1-9. Their applications in preparing inorganic films and the relevant process conditions are also given in the table.

Table 1-9 Characteristics of APCVD, LPCVD and PECVD processes. [173, 174]

Type	Advantage	Limit	Application	Conditions
APCVD	Simple reactor, Fast deposition	Poor step-coverage, Autodoping	Oxides	0.1 – 1 bar 350 – 1200 °C
LPCVD	High purity, Uniformity	High temperature, Low deposition rate	Polysilicon, nitrides, oxides	0.001 bar 550 – 600 °C
PECVD	Low temperature, Uniformity	Risk of particle and chemical contamination	Oxides, passivation nitrides	0.002 – 0.006 bar 50 – 400 °C

2.1.2 PECVD: a low temperature deposition approach

The ionized gas, as formed in PECVD reactor, is called a plasma. It is a fourth state of matter in addition to gas, liquid and solid. The plasma state is a mixture of free charged species (electrons, positive and negative ions), radicals, photons, atoms and molecules moving in random directions. The system is electrically neutral on average since the density of electrons equals to that of positive ions after the neutral particles are ionized in plasma as written in Equation 1-36. In plasma at thermodynamic equilibrium (as these found in the universe), the temperature of ions is as high as the hot electrons (seen in Equation 1-37).

Density of charged particles in plasma:

$$n_e \approx n_i \approx n \tag{1-36}$$

where n_e is the density of electrons, n_i is the density of positive ions and n is the common density of both kinds of species.

In a thermal-equilibrium plasma:

$$T_e = T_i = T \tag{1-37}$$

where T_e is the temperature of electrons, T_i is the temperature of ions and T is the common temperature of both kinds of species.

Non-equilibrium and weakly ionized plasma is involved in PECVD technique, which include the following features 1) discharges are electrically driven, 2) collisions between charged particles with neutral gas molecules are important, 3) ionization of neutrals sustains the plasma in the steady state, 4) the electrons are not in thermal equilibrium with the ions, i.e. only the electrons are “hot” not the ions and 5) there are boundaries of plasma where surface losses. Occurring events during PECVD process are schematically illustrated in Figure 1-30.

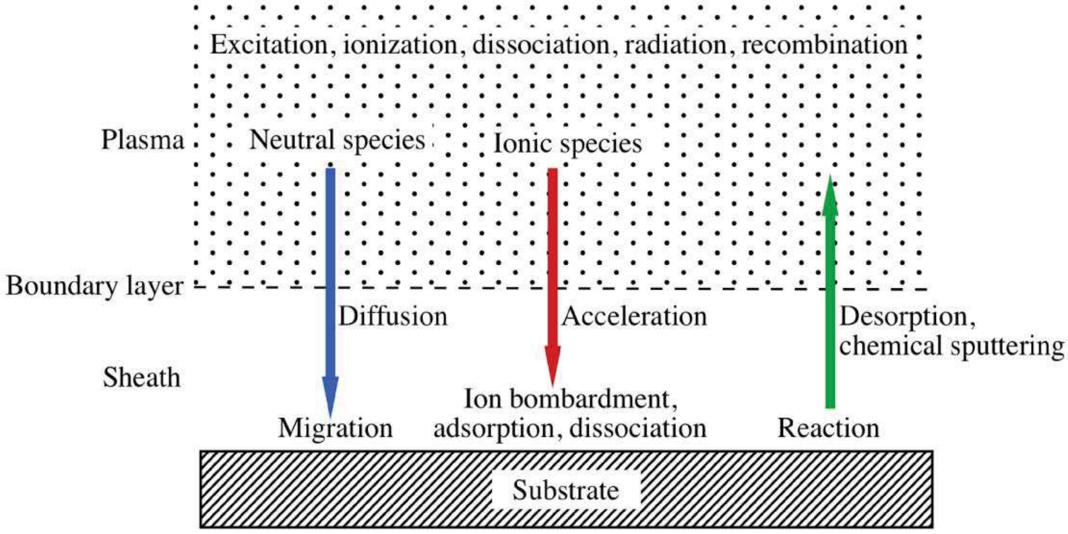

Fig. 1-30 Occurring events in a PECVD reactor. [174]

In plasma deposition process, collisions between fast-moving electrons and particles can be either elastic (kinetic energy exchange) or inelastic (internal energy changed). Inelastic collisions change potential of the particles and lead to excitation, ionization, dissociation and radiation. In such condition, plasma is quasi-neutral ($n_e\ n\ n_i$) and would join to wall surface across which positively charged thin layer exists; this layer is called “sheath”. Neutral species are diffusing through the layer to the substrate. Meanwhile, ionic species are accelerated through the sheath layer and can cause ion bombardment at substrate surface. Adsorption, dissociation and reaction are taking place on substrate surface. Eventually, the by-products are desorbed from the surface and diffuse out of the deposition region.

In some PECVD reactors, reactant gases are either introduced radially at the edges of the reactor then pumped out from the center, or gases can be entering from the center and pumped at the edges. In some other PECVD reactors, the gases are introduced through hole(s) drilled in the upper electrode as shown in Figure 1-31. Such type of gas injection improves gaseous molecules distribution. An extended inlet source can be made with more drilled holes as showerhead-alike as shown in Figure 1-31(b). The modified extension can not only distribute emitted angles widely but also enlarge the distribution of arrival angle. Substrate wafer is mounted at the lower electrode that is normally grounded. Sometimes, the substrate is rotated to randomize its position during processing.

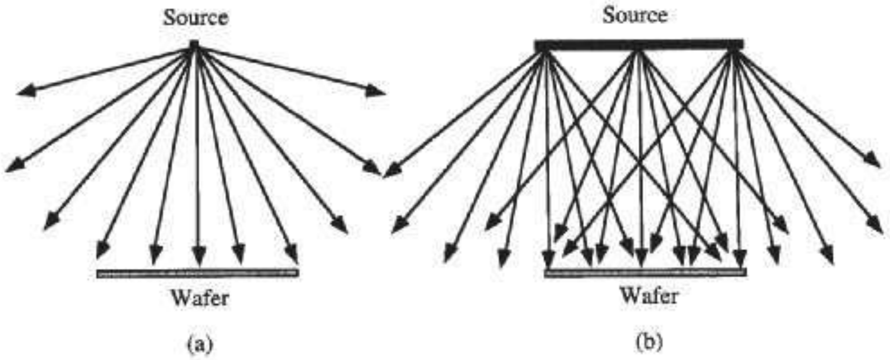

Fig. 1-31 Flux lines of atoms from small area and extended sources: (a) flux lines from a point or small area with a wide emitted angle distribution but arrow arrival angle distribution and (b) flux lines from an extended source with a wider arrival angle distribution. [174]

Radio frequency (RF) discharge of 13.65 MHz is commonly employed in the current PECVD techniques. Power with frequencies faster than 100 kHz will only induce the electrons to respond to the switching electric field but not the ions. Alternative current (AC) potential at top and bottom electrodes in RF plasma is presented in Figure 1-32. Plasma exists in the space between the two electrodes and there is no differential potential in the plasma on average.

RF plasma process is capable of depositing materials even of insulating nature, whereas it is not the case for direct current (DC) glow discharge in which insulators cannot sustain plasma. Furthermore, RF plasma avoids accumulating charges on insulators; however, the ion current in DC plasma would charge the insulator positively and extinguish the plasma eventually.

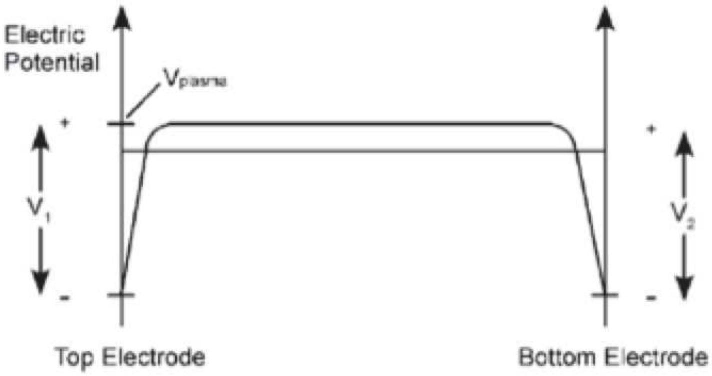

Fig. 1-32 Electrical potential at electrodes in RF plasma. [173]

A sheath layer is concentrated with more positive ions (n_i) than electrons (n_e), which is caused by a loss of electrons at plasma's surface. Electron thermal velocity is at least hundred times higher than that of ion because electron has much lower weight and higher temperature. Average thermal energy of an electron is around 2 eV corresponding to a temperature about 23,000 K; in contrast, the temperature of neutral particles of energy 0.025 eV is about 293 K (room temp). As a result, the hot electrons of high mobility are not confined because the net charge density is zero in plasma. Then electrons will be rapidly be lost on the walls leading to a positively charged zone in the vicinity of substrate.

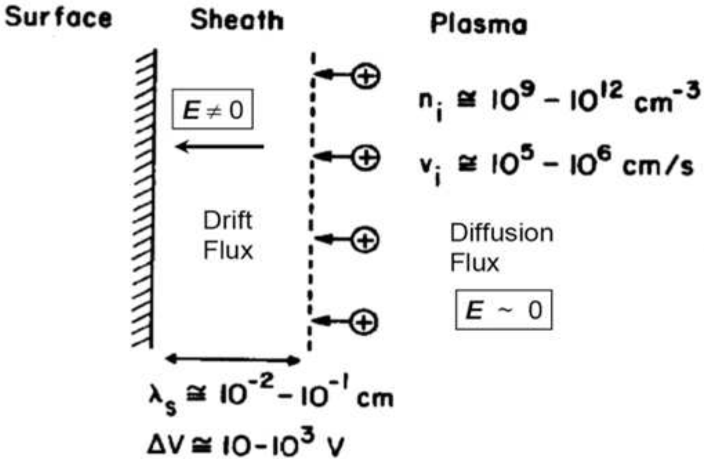

Fig. 1-33 Plasma and sheath in PECVD process. [173]

Sheath thickness (λ_s) is typically about 0.01 – 0.1 cm in a plasma. Density of positive ions (n_i) is around $10^9 - 10^{12}$ particles/cm^3 and velocity of ions (v_i) is around $10^5 - 10^6$ cm/s in the bulk plasma. Electric filed (E) is close to zero on average because the number of electrons equals to the number of ions in the plasma. But in the sheath layer there is a larger density of positive ions ($n_i > n_e$) so that the layer is positively charged. The sheath interface balances the opposite negative charge on the substrate surface. The electric field (E) in sheath layer is no longer zero and increases to about $10 - 10^3$ V. Consequently, the electrons would reflect from the wall (sheath) back to the plasma and the ions would enter and be accelerated through sheath layer as presented in Figure 1-33.

A number of simulating tools have been developed for simulation of deposition mechanisms in CVD process. [175] An illustrated graph about fluxes involved in low pressure process is displayed in Figure 1-34. Mathematical description of the various possible fluxes is clarified as seen in Equation 1-38. The net flux of particles takes account about the effects from direct flux of neutrals $F^i_{direct(neutrals)}$, direct flux of ions $F^i_{direct(ions)}$, redeposited fluxes F^i_{redep} (both from emitted and resputtered particles), flux of diffusion-in $F^i_{diff.in}$, flux of diffusion-out $F^i_{diff.out}$, emitted flux $F^i_{emmitted}$ and sputtered flux $F^i_{sputtered}$.

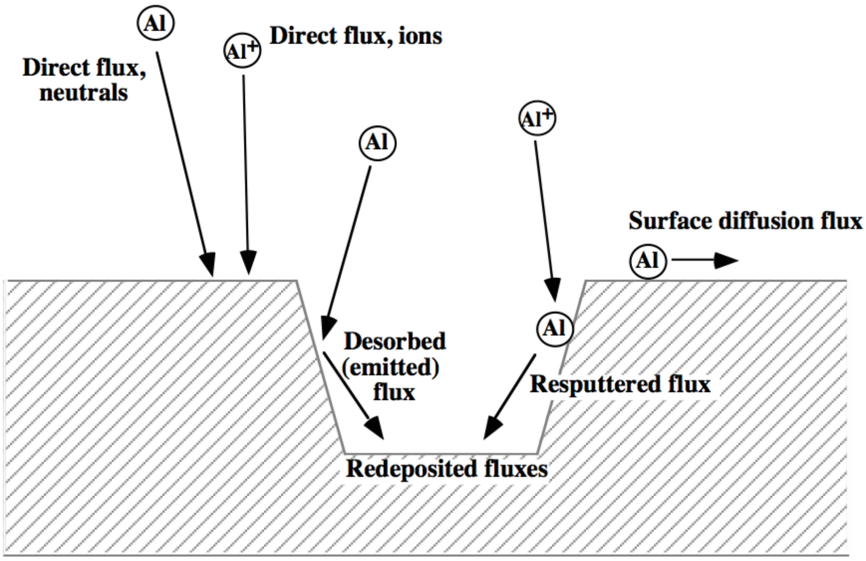

Fig. 1-34 Possible fluxes of particles in CVD process. [174]

The net flux of particles in CVD:

$$F^i_{net} = F^i_{direct(neutrals)} + F^i_{direct(ions)} + F^i_{redep} + F^i_{diff.in} - F^i_{emitted} - F^i_{sputtered} - F^i_{diff.out} \qquad (1\text{-}38)$$

Modeling PECVD system is first based on figuring out the types of fluxes involved in the electronical-assisted process. A graph of RF PECVD reactor depositing SiO_2 films from SiH_4 and O_2 is illustrated in Figure 1-35 (on the left). The relevant fluxes of ions and neutrals during deposition are presented in Figure 1-35 (on the right).

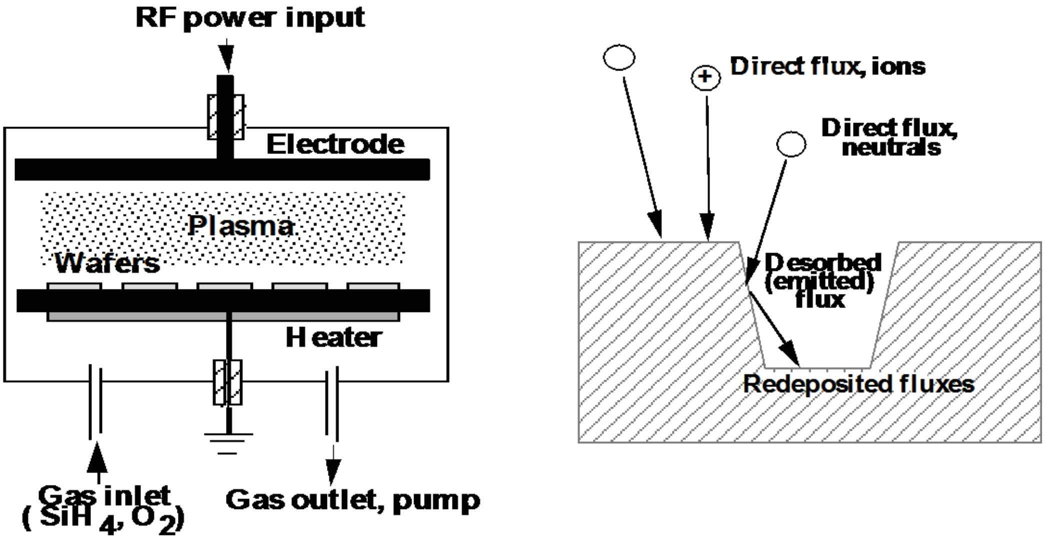

$F^i_{direct(neutrals)}$	Yes
$F^i_{direct(ions)}$	No
$F^i_{diff(net)} = F^i_{diff(in)} - F^i_{diff(out)}$	No
$F^i_{emitted}$	Yes
$F^i_{redep(emitted)}$	Yes
$F^i_{sputtered}$	No
$F^i_{redep(sputtered)}$	No
$F^i_{ion-induced}$	Yes

Fig. 1-35 PECVD reactor and relevant fluxes in the deposition process. [173]

Direct fluxes of neutrals (F_d) are the main portion in depositing fluxes as the weakly ionized plasma being involved in PECVD process. Ion-induced fluxes (F_i) are characteristic in plasma deposition since the ions could enhance particles transporting by collisions. Moreover, desorbed particles can be emitted and then contribute to redepositing fluxes.

Accordingly, deposition rate can be calculated as in Equation 1-39 taking account the mentioned depositing fluxes in PECVD process.

$$rate = \frac{(s_c k_d F_d) + (k_i F_i)}{N} \tag{1-39}$$

where s_c is the striking coefficient, k_d and k_i are the relative rate constants for neutrals and ion-induced components respectively, F_d and F_i are the fluxes of neutrals and ion-induced components respectively and N is the density of the atoms in the film.

The deposition rate (or film growth rate) in PECVD depends on both substrate temperature and reactant concentration as shown in Figure 1-36. At high temperatures, plasma deposition is diffusion controlled, and at low temperatures it is reaction limited. For intermediate temperatures, competition of gas transport and feed rate determines film-growing kinetics in which a fast and stable deposition rate can be attained. On the other hand, there is a growing rate plateau when the reactant concentration is neither too much nor too little; in such conditions, adequate precursor vapor induced nucleation in gas phase is affecting deposition process leading to a reasonable film-growing velocity. Usually maximum deposition rates in the range 0.1 – 100 nm/min can be achieved.

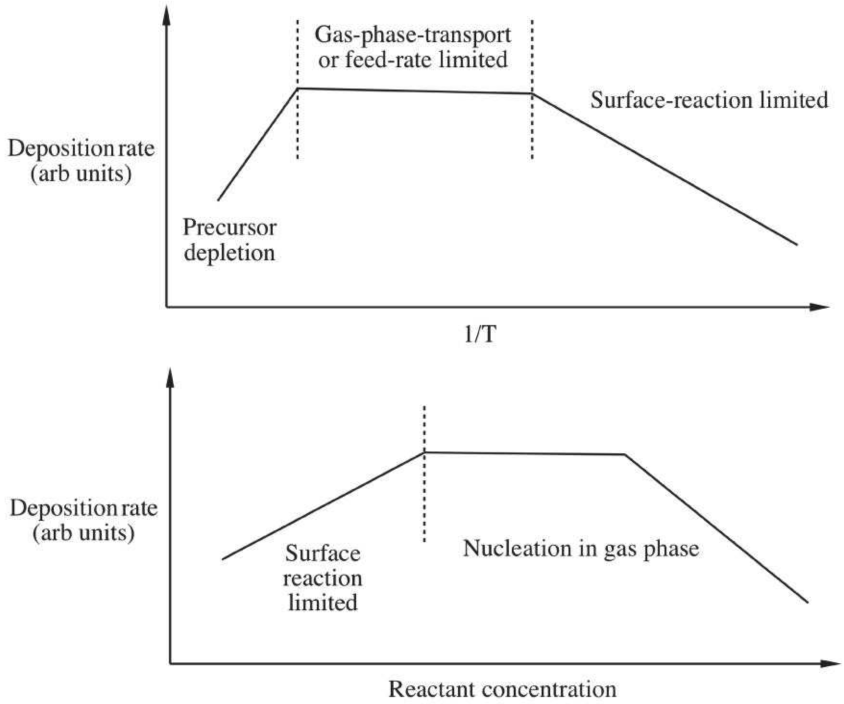

Fig. 1-36 Deposition rate depending on substrate temperature and reactant concentration. [[173, 174]

2.2 PECVD process for the preparation of TiO_2 films

Thin film typically indicates a material of thickness less than 1000 nm. Properties of thin films are different from bulk materials in terms of the non-fully dense and defect structures. Such quasi-2D materials (very thin thickness) are under stress and strongly influenced by surface/interface effects and ion bombardment. Increasing ion bombardment tends to make films denser and cause the film stress to become more compressive. [176] However, excessive compressive stress can lead to impaired films. In general, quality of a film refers to physico-chemical (e.g. density and composition), electrical (e.g. breakdown voltage), mechanical (e.g. stress and adhesion) and optical (e.g. transparency and refractive index) properties. Defect structure, grain size and orientation in film and impurity level (or doping) are critical for the film's performance. Fortunately, films properties and performance can be adjusted by the optimization of the PECVD parameters, the chamber geometry and the energy excitation source.

2.2.1 Deposition of inorganic film

PECVD synthesized inorganic films include elements, oxides, nitrides, carbides and borides. Common inorganic films obtained in PECVD process with corresponding gas sources and required deposition temperatures are listed in Table 1-10. Typically, amorphous silicon (α-Si) and crystalline silicon (c-Si) have been deposited from $SiH_4 + H_2$ respectively at 300 and 400 °C. Silicon oxide (SiO_2) and titanium oxide (TiO_2) films have been obtained respectively from gases $SiCl_4 + O_2$ and $TiCl_4 + O_2$ respectively at temperatures as low as 100 °C. Silicon nitride (Si_3N_4) film has been possibly formed from $SiH_4 + NH_3 + N_2$ at room temperature 25 °C.

Silicon nitride (Si_xN_y) films are particularly representative of PECVD inorganic materials. SEM picture of silicon nitride film prepared from $SiH_4 + NH_3$ reactant gases by PECVD method is presented in Figure 1-37. The film is of good conformity, step-coverage, and homogeneous thickness. A stoichiometry synthesis of Si_3N_4 from $SiH_4 + NH_3$ is written in equation (1-40). Yet it is often that composition of inexact stoichiometry is obtained in PECVD films due to different bond strength in precursor molecules, which are experiencing thermal/plasma decomposition.

Formation of Si_3N_4 from SiH_4 +NH_3:

$$3\ SiH_4\ (g) + NH_3\ (g) \rightarrow Si_3N_4\ (s) + 12\ H_2\ (g) \qquad (1\text{-}40)$$

Table 1-10 Main PECVD inorganic films with corresponding reactant gases and required relevant deposition temperatures. [173]

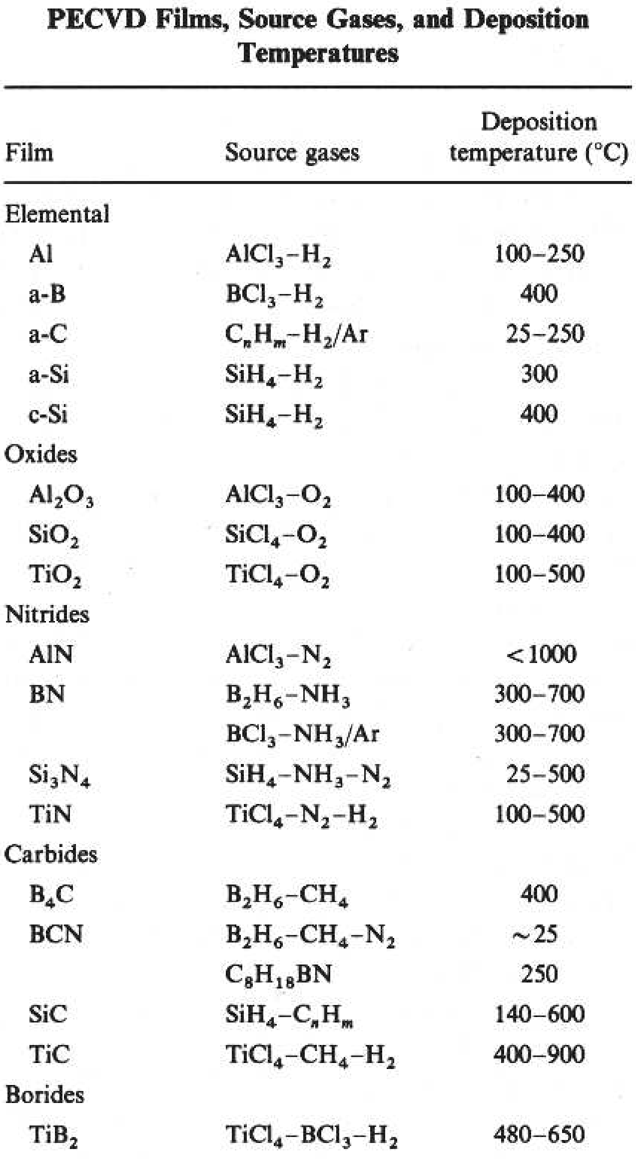

PECVD Films, Source Gases, and Deposition Temperatures

Film	Source gases	Deposition temperature (°C)
Elemental		
Al	$AlCl_3$–H_2	100–250
a-B	BCl_3–H_2	400
a-C	C_nH_m–H_2/Ar	25–250
a-Si	SiH_4–H_2	300
c-Si	SiH_4–H_2	400
Oxides		
Al_2O_3	$AlCl_3$–O_2	100–400
SiO_2	$SiCl_4$–O_2	100–400
TiO_2	$TiCl_4$–O_2	100–500
Nitrides		
AlN	$AlCl_3$–N_2	<1000
BN	B_2H_6–NH_3	300–700
	BCl_3–NH_3/Ar	300–700
Si_3N_4	SiH_4–NH_3–N_2	25–500
TiN	$TiCl_4$–N_2–H_2	100–500
Carbides		
B_4C	B_2H_6–CH_4	400
BCN	B_2H_6–CH_4–N_2	~25
	$C_8H_{18}BN$	250
SiC	SiH_4–C_nH_m	140–600
TiC	$TiCl_4$–CH_4–H_2	400–900
Borides		
TiB_2	$TiCl_4$–BCl_3–H_2	480–650

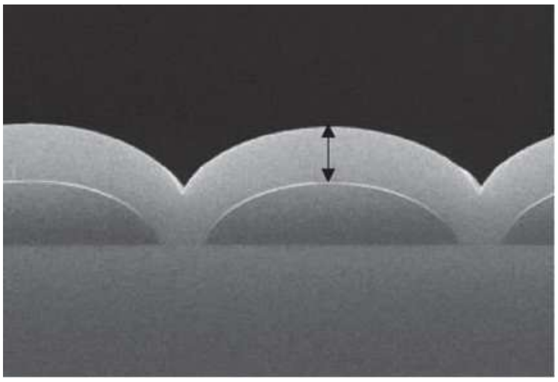

Fig. 1-37 Conformal step coverage of PECVD Si_xN_y film. [177]

Silicon nitride (Si_xN_y) films produced IN APCVD, LPCVD and PECVD processes from gas mixture $SiH_4 + NH_3$ are compared in terms of the films' physical and chemical properties as given in Table 1-11. Film of Si_3N_4 has been deposited at 900 °C by APCVD, hydrogenated $Si_3N_4(H)$ has been deposited by 750 °C in LPCVD and Si_xN_y has been deposited at 300 °C by PECVD. Process temperature has been reduced by 600 °C and 450°C in PECVD compared to APCVD and LPCVD, respectively. It can be seen that PECVD film has a lower density, better conformity and higher water permeability.

In the presented examples as shown in Table 1-11, a more compressive PECVD silicon nitride film is obtained due to ion bombardment effect as the energetic ions being accelerated through a sheath layer from plasma toward substrate. Definition of film stress (σ) is given in Equation 1-41. The film stress is depending on film thickness, substrate thickness, position in the film and Young's modulus of materials. Different film stress could be formed in different interfaces.

Thin film stress σ:

$$\sigma_f = \frac{t_f E_S}{6\rho}[\left(\frac{t_s}{t_f}\right)^2 + 6\frac{E_f}{E_s}\frac{Y_f}{t_f}] \qquad (1\text{-}41)$$

where $-1/2 < Y_f/t_f < 1/2$, t_f is the film thickness, t_s is the substrate thickness, t_f is the film thickness, ρ is the radius of curvature, Y_f is distance from neutral plane to a point in the film, E_s is the substrate Young's modulus and E_f is the film Young's modulus.

Table 1-11 Physical and chemical properties of Si_xN_y films deposited from mixing

Properties	Si_3N_4 APCVD (900 °C)	Si_3N_4(H) LPCVD (750 °C)	SiNH PECVD (300 °C)
Density (g cm^{-3})	2.8 – 3.1	2.9 – 3.1	2.5 – 2.8
Refractive index	2.0 – 2.1	2.01	2.0 – 2.1
Dielectric constant	6 – 7	6 – 7	6 – 9
Bulk resistivity (Ω-cm)	$10^{15} – 10^{17}$	10^{16}	10^{15}
Stress at 23 °C (GPa)	0.7 – 1.2 (T)	0.6 (T)	0.3 – 1.1 (C)
H_2O permeability	Zero	-	Low - none
Thermal stability	Excellent	-	Variable > 400 °C
Si/N ratio	0.75	0.75	0.8 – 1.0
Step coverage	Fair	-	Conformal

Note: T = tensile, C = compressive.

Film stress in multiple layers could exist as schematically presented in Figure 1-38 (a). Hypothesized chemical reactions responsible for stress development in Si_xN_y film with Si-H and N-H bonds are presented in Figure 1-38 (b). The proposed reaction is also an explanation for silicon rich composition in PECVD produced film. Factors including deposition rate, process temperature and gas composition can influence the stress progress as the film is growing on the substrate.

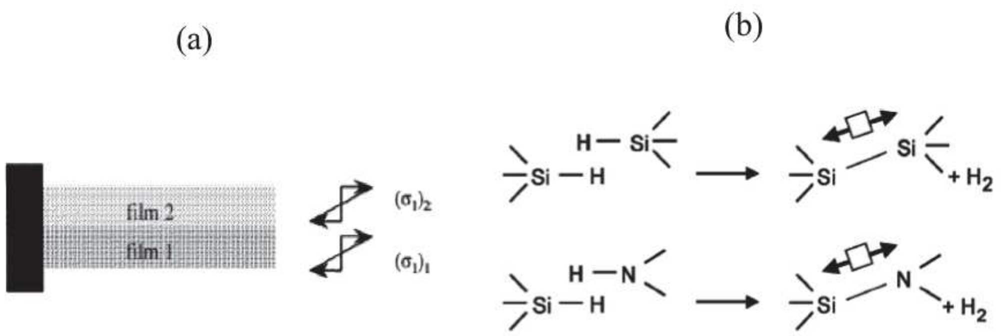

Fig. 1-38 (a) schematic different stress in films: $(\sigma_1)_1$ in the film 1 and $(\sigma_1)_2$ in the film 2 and (b) proposed chemical reactions responsible for stress development in PECVD Si_xN_y film with Si-H and N-H bonds. [176]

In terms of application, dielectric materials of insulating nature, commonly used in electronic devices for isolating multiple conductive layers and capacitors and for surface passivation, may be prepared in RF PECVD process. [176] Furthermore, PECVD inorganic films are also employed in encapsulation of devices to protect the devices from corrosion by atmospheric elements including moisture and oxygen. PECVD prepared amorphous silicon (α-Si) has been coated in solar cells and silicon dioxide (SiO_2) has been used as inter-level dielectric materials. In addition, PECVD SiN_x has been used as chip passivation layer, and doped poly-Si has been integrated in MOS gates. Diamond like carbons (DLC), which are very stable capping materials against radiation-hardening for wear, optical and military, have been also produced with PECVD method. A list of PECVD deposited materials and their applications are given in Table 1-10, where the preparing conditions and current status of synthesis technique are also indicated. Manufacture of α-Si, SiO_2 and Si_3N_4 by PECVD technique has already been practiced in large-scale production. Fabrication of diamond like carbons (DLC), $TiSi_2$, WSi_2 and boro-phospho-silicate by PECVD process is in the semi-production development. A few materials including epitaxial-Si, W, TiC, TiN and TiO_2 synthesized with PECVD approach are currently in R & D stage.

2.2.2 State-of-the-art on TiO_2 deposits

As mentioned in the first part of this chapter, functionalizing membranes with photocatalytic activity is the crucial step for coupling of membrane separation with AOP wastewater treatment. Immobilizing photoactive TiO_2 materials (usually as coatings) on membrane has been recently investigated using PECVD approach. Such one-step plasma deposition procedure is able to harvest TiO_2 thin film on a wide range of substrates including polymers, metals and ceramics at low temperatures. Nanoparticle size, porosity and loaded mass/thickness of TiO_2 could be tuned by adjusting plasma conditions. Microstructure and thickness have noticeable effects on performance of photocatalytic membrane regarding to quantum size effect [22], mass transfer and light efficiency [24]. In addition, PECVD makes doping of TiO_2 deposits possible (e.g. adding N_2 or NH_3 as nitrogen-dopant) in order to shift the band gap energy to lower value and consequently improve the solar light efficiency. [103, 105, 106]

In general, supported TiO_2 thin films have been commonly prepared from the precursor tetra-isopropoxide ($Ti(OC_3H_7)_4$, TTIP) in PECVD equipped with RF 13.56 MHz in many undergoing studies. Dense substrates including silicon and glass are often used to support TiO_2 deposition for material characterization purpose. Carrier gas (e.g. Ar and N_2) is supplied to bring the precursor vapor to PECVD reactor. Oxygen is sometimes added in the reactor as an oxidant gas for reducing decomposition temperature. Deposited TiO_2 layer is expected to be of large specific surface areas, homogeneous and stable for photocatalytic membranes application. Crystalline anatase TiO_2 is desired being synthesized either with in-situ PECVD process or with post-annealing afterward. Reducing preparation temperatures either in plasma deposition process or in followed annealing step is a key issue to widely apply PECVD approach for all sorts of membrane substrate (polymeric ones in particular).

As-grown TiO_2 films deposited at 450 °C in PECVD process from mixture gas TTIP + N_2 + O_2 have been prepared by Huang et al. in 2002. [25] PECVD conditions were adjusted at total pressure at 0.37 mbar and RF power from 50 – 150 W with 60 min duration. SEM surface images of TiO_2 prepared at different RF powers have been compared in Figure 1-39. Smaller sizes of TiO_2 nanoparticles were observed when the electric power increased. The film deposited at 450 °C with 100 W plasma discharge presented a partially crystallized anatase structure with a very small diffraction anatase peak (101) being detected by XRD.

Post-annealing the PECVD as-deposit TiO_2 thin films was studied by Maeda et al. in 2005. [178] TiO_2 films were prepared at 350 °C in PECVD method from reactant gases TTIP + Ar + O_2 with working pressure 1.33 mbar and RF power 100 W. The in-situ deposited TiO_2 film presented a weak crystallite structure with small anatase peaks (101), (004) and (112) being observed in XRD. As-deposited films were post-annealed to 600 °C and 900 °C resulting in anatase and rutile crystalline structure respectively. AFM images of the as-grown, 600

°C-annealed and 900 °C-annealed films have been displayed in Figure 1-40. It can be seen that heating to 900 °C results in particle aggregation, whereas surface roughness did not change much between the raw film and 600 °C-annealed film.

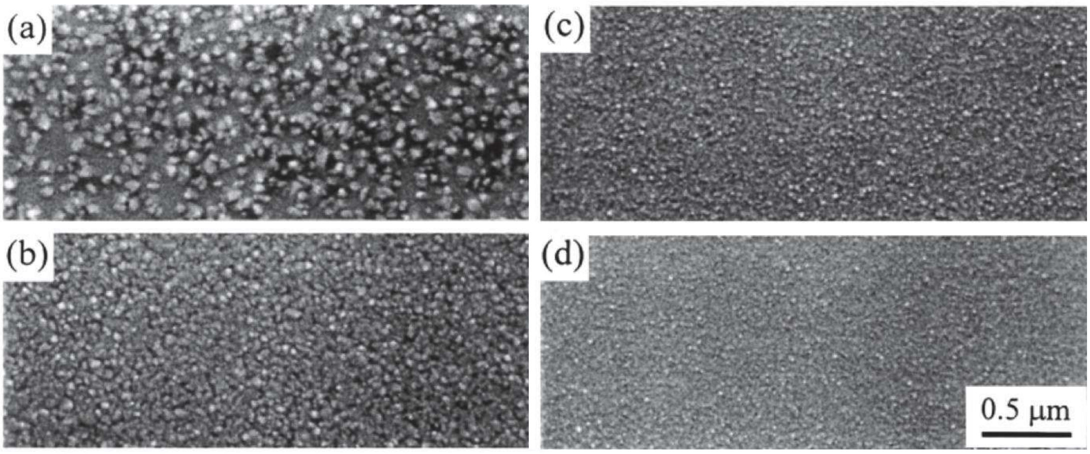

Fig. 1-39 SEM surface images of PECVD TiO_2 film deposited at 450 °C for 60 min with RF power of (a) 50 W, (b) 75 W, (c) 125 W and (d) 150 W. [25]

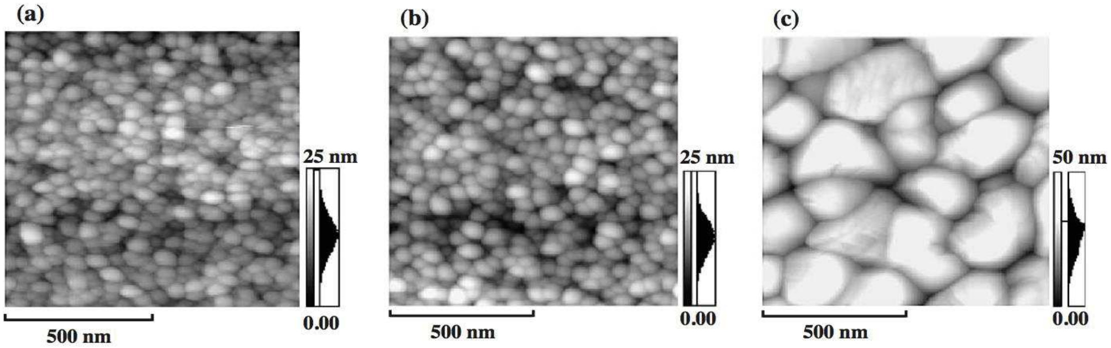

Fig. 1-40 AFM images of TiO_2 films: (a) PECVD as-grown film, (b) 600 °C-annealed film and (c) 900 °C-annealed film. [178]

Wu and et al. have investigated a seeding effect of substrate on plasma deposition in 2011. [179] PECVD TiO_2 deposited at 200 °C from mixing gases TTIP + N_2 + O_2 on virgin silicon and on NiO_x-seeded-silicon were prepared in the work, whose images are presented in Figure 1-41(a) and (b) respectively. PECVD procedure was working with a total pressure 0.4 mbar and RF power 100 W. Seeding NiO_x was attached to silicon through electron-beam evaporation followed by oxidation treating under oxygen. The seeding interface was observed in SEM cross-section scanning as notified with black arrows in Figure 1-41(b). Post-thermal treatment from 300 to 700 °C was done for TiO_2 samples on both seeded and non-seeded substrates in Wu's work. Minimal crystallization temperature to anatase was found in post-annealing at 400 °C for TiO_2 film on virgin silicon. TiO_2 film on seeded silicon (NiO_x/Si) has developed a partial anatase structure with diffraction peak (101) by XRD, but very weakly, when post-heating to 300 °C.

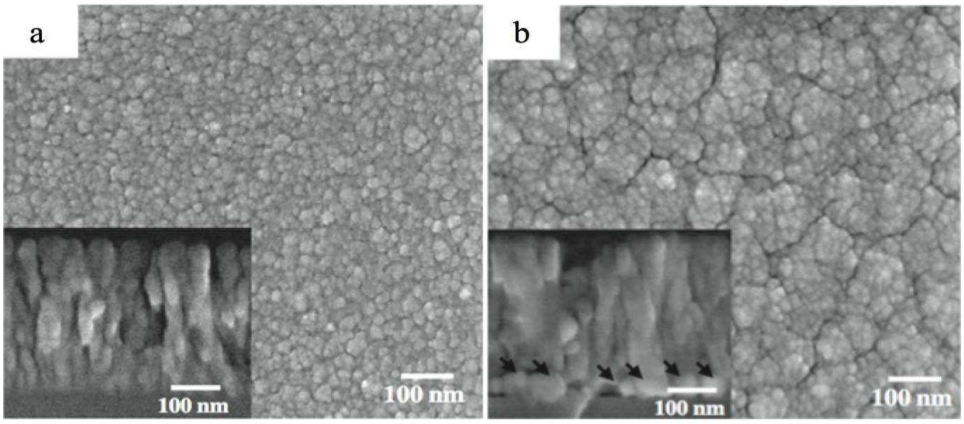

Fig. 1-41 SEM images of PECVD TiO_2 film on (a) virgin Si and (b) on NiO_x seeded Si deposited at 200 °C and 100W and post-annealed at 400 °C. [179]

In some other works, a bias voltage has been applied on the bottom electrode in PECVD reactor in order to further reduce deposition temperature when forming anatase TiO_2 films. Yet the method is not applicable for all materials since it is impossible to maintain a bias voltage on insulators such as polymeric substrate. In addition, in case of using "soft" substrates there is a risk of damaging the surface due to strong ion bombardment and/or consecutive local increase of temperature. [29, 30] Nevertheless, bias voltage has been proven to decrease preparing temperature of anatase TiO_2 in PECVD process.

Srivatsa et al. have obtained anatase materials in form of various three-dimensional nanostructures rather than a continuous film by applying a bias voltage of -150 V in PECVD. [180] The TiO_2 grains were deposited at 40 °C from working gases TTIP + Ar + O_2 with total pressure equal to 0.3 – 1.0 mbar and using RF power 60 W. Later on, Li et al. imposed lower bias voltage at 0, -10 or -50 V when depositing TiO_2 films from reactant gases TTIP + O_2 in PECVD process. [28] Ion energy corresponding to the applied bias was 5, 35 or 75 eV respectively. Substrate was heated at around 100 °C and working pressure was 0.004 mbar in the reactor.

RF power coupled to inductively coupled plasma (ICP) source of intensity 400 W was performed and corresponding plasma power on substrate was 0 – 12 W. Cross-section and surface SEM images on the films made with and without bias voltages have been exhibited in Figure 1-42. Anatase structure was found in both 0 V and -10 V biased thin films, meanwhile mixed anatase and rutile structure was observed in the -50 V biased sample according to XRD investigation. Deposited TiO_2 films have been modeled with three-layer structure base on an optical ellipsometry measurement: dense layer, gradient layer and top layer in the films.

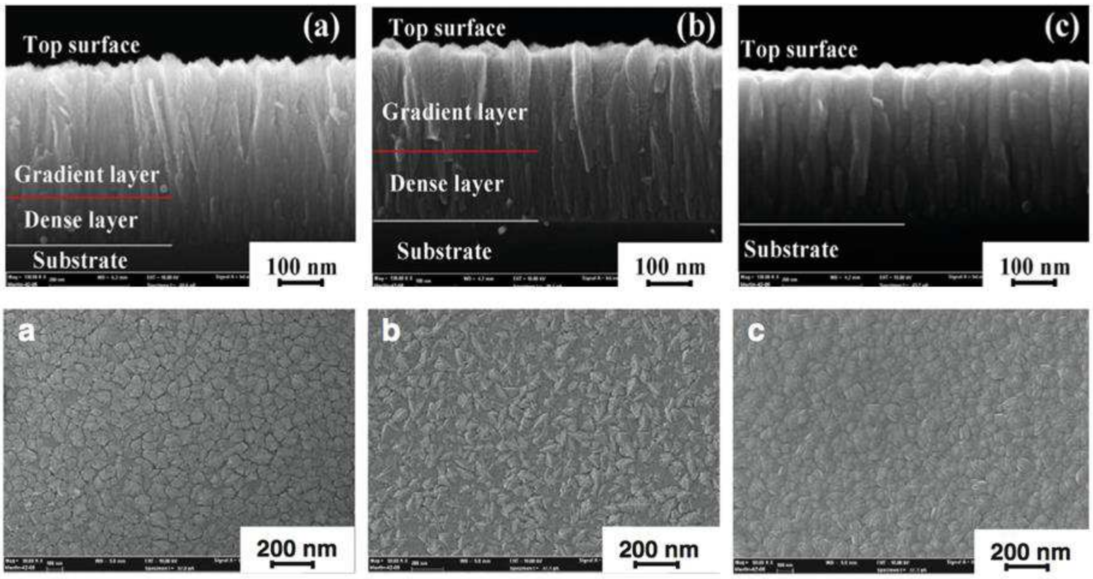

Fig. 1-42 SEM cross-section images (up) and surface images (bottom) of TiO_2 films deposited in PECVD process with bias voltage (a) 0, (b) -10 V and (c) -50 V. [28]

In addition, PECVD procedure makes it possible to dope heteroatoms in TiO_2 thin film by simply adding dopant gas source in the reactor. For instance, nitrogen-doped TiO_2 layer could be synthesized just by adding N_2 or NH_3 gas to the plasma reactor. [103-106, 163] TiO_2 doped with nitrogen atoms (as electron acceptor) would introduce lower electronic levels in conduction band and consequently the band gap is narrowed with the midgap levels. As a result, absorbance of TiO_2 could shift from ultraviolet (UV) to visible band and solar energy is efficiency to initiate photocatalysis AOP treatment. Romero et al. have prepared N-doped TiO_2 thin films from reactant gases TTIP + N_2 + O_2 in 2009, whose SEM images of the prepared materials are shown in Figure 1-43. [104]

Applied PECVD apparatus was coupled with microwave (MW) 2.45 GHz plasma discharge under electron cyclotron resonance (ECR) condition. MW-ECR PECVD can produce high plasma density and sustain at very low pressure. The doped films were deposited at 250 °C under total pressure 0.005 mbar (4×10^{-3} Torr) and power 400 W. Crystalline anatase was found in as-deposited films without post-annealing. Varying the nitrogen composition ratio from 17% to 88%, N-dopant TiO_2 films of band gap value 3.14 eV and 2.8 eV were respectively obtained.

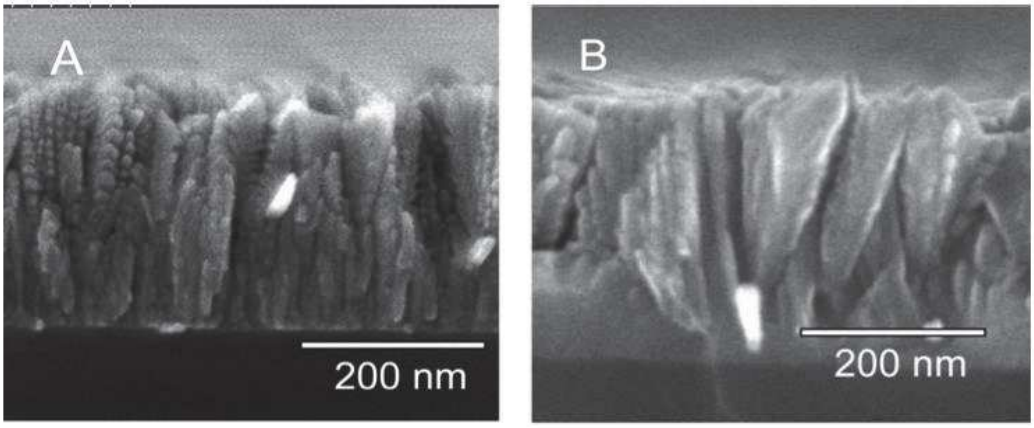

Fig. 1-43 SEM images of N-doped TiO_2 films deposited at 250 °C and 400 W in MW-ECR PECVD with N_2 composition ratio (A) 17% and (B) 88%. [104]

Moreover, MW-ECR equipped PECVD set-up has also been carried out to directly deposit anatase film in some other works by Borras et al. [181-184] and Szymanowski et al. [185] respectively. According to Borras' study, it is found that a homogeneous dense TiO_2 layer as "a critical thickness" was formed first and then porous TiO_2 layer was deposited on top in continuous plasma deposition development. They considered that micro-columnar porous TiO_2 layer has lately developed only after the critical thickness was formed. In the same author's work, substrate temperatures were experimented from 25 – 250 °C in MW-ECR PECVD process and 250 °C was determined as optimized parameter regarding to porous microstructure and morphology of anatase TiO_2 films.

Lastly, atmosphere pressure PECVD has also been studied in recent research for depositing materials including TiO_2 films. Since the operation is under ambient conditions, the reactor is easily simplified and enlarging the capacity is promising to large-surface deposition. However, more complex composition and much higher pressure in the process may reduce the quality of films in terms of impurities, stress, morphology and microstructure in comparison to vacuum plasma deposition. Only very few results on TiO_2 materials produced from atmospheric pressure PECVD (AP-PECVD) have been reported currently. And the photocatalytic performance of AP-PECVD TiO_2 materials can be even rarely studied. An example of atmospheric PECVD TiO_2 films deposited at 275 °C with pulse repetition of plasma discharge (10 and 50 Hz) are presented in Figure 1-44. [186]

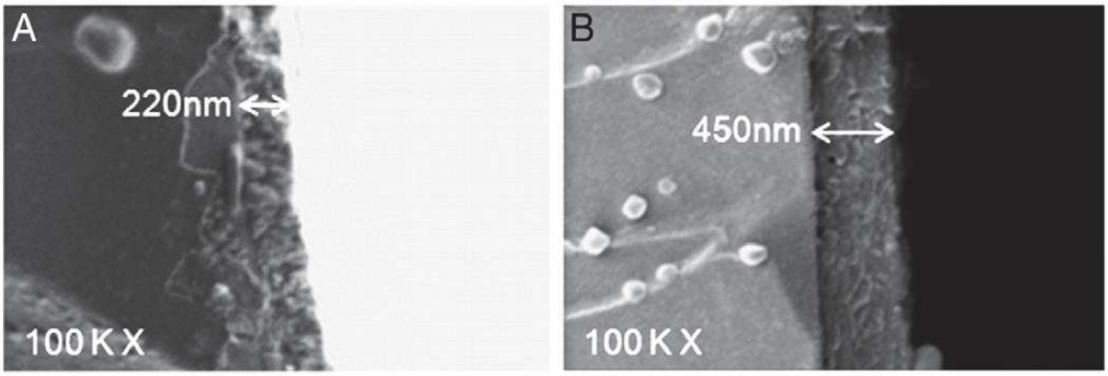

Fig. 1-44 SEM image of atmospheric PECVD TiO_2 deposited at 275 °C with a pulse repetition rates (a) 10 Hz and (b) 50 Hz. [186]

2.3 Conclusion

PECVD is an advanced chemical vapor deposition (CVD) technique assisted with electric power to the reactant gases. A major strength of PECVD process is that the target material could be deposited at lower substrate temperature in contrast to conventional CVD method. It could be explained as in the ionized plasma gas phase, thermal/plasma decomposition of the precursor could occur at lower temperature. Both inorganic (e.g. Si, Si_xN_y and SiO_2) and polymerized films have been obtained with PECVD method reported in recent studies.

According to the literature, silicon- or glass-supported TiO_2 films have been deposited either as amorphous phase or crystalline phase in many PECVD approaches summarized in Tables 1-12 to 1-14 including 1) with/without post-annealing, 2) using RF or MW power discharge, 3) with ICP plasma source, 4) under ECR condition, 5) applying vacuum or room pressures and 6) using pulsed discharge or not. For as-deposit amorphous TiO_2 films, post-annealing treatment (> 400 °C) has been applied to develop crystallite structure in the films. As-grown TiO_2 film was found in anatase phase deposited at minimal PECVD substrate temperature $T_s =$ 450 °C using RF power 100 W. Otherwise, seeding the substrate prior to PECVD synthesis has possibly reduced T_s to 300 °C, though the obtained crystalline structure in film was very inadequate.

On the other hand, applying bias voltage during PECVD process has reduced the temperature of anatase formation to 250 °C, yet continuous TiO_2 films were only obtained in some cases for instance with inductively coupled plasma (ICP) coupled PECVD. In other biased depositions, TiO_2 of three-dimensional nanostructures instead of a layer were obtained. PECVD using microwave (MW) power of 2.45 GHz in electron cyclotron resonance (ECR) condition has reduced T_s as low as to 100 °C when forming anatase films. But it should be noted that MW-ECR PECVD device operates at much higher discharge power (higher than 100 W) in comparison to RF PECVD. Applying a typical RF PECVD approach (without ECR or pulse repetition), no work has reported preparing temperature of anatase film below 400 °C. Whatever the plasma conditions may be, these are unsuitable for thermal-sensitive substrates, due to too high substrate temperature, post-heating temperature, discharge power and/or bias voltage.

The main challenge of this PhD thesis is to deposit anatase thin film using a PECVD process as a one-step method (or eventually completed with a post-annealing treatment), in operating conditions suitable for any kind of substrate including polymers. That means that no bias-voltage and no discharge power higher than 100 W are aimed at. Moreover substrate and/or post-annealing temperatures should be as low as possible, ideally lower than 250°C, and if not possible, competitive with regard to temperatures reported in the literature, that is lower than 400°C.

Table 1-12 RF PECVD depositing TiO_2 thin films (without post-annealing treatment).

Ref	TiO_2 thin films	Substrate	PECVD conditions				Crystallization temp.
			Working gases	Working pressure	Substrate temp. T_s	Electric power	
[187]	Amorphous TiO_2	Glass	[a] TTIP + Ar + O_2 TTIP + N_2 + O_2	0.6 mbar (60 Pa)	120 – 250 °C	RF 100 – 500 W	-
[25]	Anatase TiO_2	Silicon	TTIP + N_2 + O_2	0.37 mbar (37 Pa)	450 °C	RF 100 W	T_s = 450 °C (weakly crystalline)
[188]	Anatase TiO_2	Glass	TTIP + Ar + O_2	-	300, 400 °C	RF 5 W	T_s = 300 °C
[189]	Anatase TiO_2	[b] Silica powder	TTIP + He + O_2 TTIP + He + Ar + O_2	-	250 °C	RF 350 W	T_s = 250 °C
[8]	Anatase TiO_2	Glass Silicon	TTIP + O_2	0.2 mbar (20 Pa)	40, 300 °C	RF 20 W Bias: -50 V	T_s = 300 °C
[28]	Anatase TiO_2	Silicon	TTIP + O_2	0.004 mbar (0.4 Pa)	90 – 140 °C	[c] RF 400 W Bias: -50 V	T_s ~ 100 °C
[180]	[d] TiO_2	Si	TTIP + Ar + O_2	0.5 mbar (50 Pa)	Room temp. (25 °C)	RF 60 W Bias: -150 V	T_s = 25 °C
[190]	Anatase TiO_2	Silicon	TCl_4 + O_2 TCl_4 + Ar + O_2	0.13 mbar (13.33 Pa)	135 °C	Pulsed RF 200 W	T_s = 135 °C
[186]	Anatase TiO_2	Glass	TCl_4 + O_2	Atmosphere (1 bar)	275 °C	Pulse (50 kHz)	T_s = 275 °C

Note: [a] TTIP: titanium tetraisopropoxide, [b] silica powder: in PECVD circulating fluidized bed reactor, [c] RF 400 W: equipped with an inductively coupled plasma (ICP) source, [d] TiO_2: in 3D-structured nanoparticles rather than a deposited thin film.

Table 1-13 MR-ECR PECVD depositing TiO_2 thin films without post-annealing treatment.

Ref	TiO_2 thin films	Substrate	PECVD conditions				Crystallization temp.
			Working gases	Working pressure	Substrate temp. T_s	Electric power	
[183]	Anatase TiO_2	Silicon	TTIP + Ar + O_2	0.005 mbar (4×10^{-3} Torr)	250 °C	[a] MW-ECR 400 W	$T_s = 250$ °C
[104]	Anatase TiO_2	Silicon Quartz	TTIP + N_2 + O_2	0.005 mbar (4×10^{-3} Torr)	250 °C	MW-ECR 400 W	$T_s = 250$ °C
[185]	TiO_2	Glass	TCl_4 + O_2	0.005 mbar (4×10^{-3} Torr)	250 °C	MW-ECR 400 W	$T_s = 250$ °C
[191]	Anatase TiO_2	Silicon	TTIP + N_2+ O_2	-	-	MW-ECR	-

Note: [8] MW-ECR: microwave electron cyclotron resonance with 2.45 G.

Table 1-14 PECVD as-deposit TiO_2 thin films with post-annealing treatment.

Ref	TiO_2 thin films	Substrate	PECVD conditions				Post-annealing T_p	Crystallization temp.
			Working gases	Working pressure	Substrate temp. T_s	Electric power		
[192]	Anatase/rutile TiO_2	Silicon	TTIP + Ar + O_2	-	200 °C	RF 60 W	400 °C	$T_p = 400$ °C
[193]	Anatase TiO_2	Silicon	[a] TE + O_2	-	350 °C	RF 300 W	500 °C	$T_p = 500$ °C
[178]	Anatase TiO_2	Silicon	TTIP + Ar + O_2	1.33 mbar (133 Pa)	350 °C	RF 100 W	600, 900 °C	$T_p = 600$ °C (very weakly crystallized at 350 °C)
[26]	TiO_x:OH	-	TTIP + O_2	-	200 °C	-	300 – 700 °C	$T_p = 400$ °C
[179]	TiO_x:OH	Silicon [b] NiO_X/Si Quartz	TTIP + N_2 + O_2	0.4 mbar (40 Pa)	200 °C	RF 100 W	300 – 600 °C	$T_p = 400$ °C

Note: [a] TE: titanium (IV) ethoxide and [b] NiO_x/Si: NiO_x-seeded (20 nm thick) silicon made from e-beam evaporation and oxidation process.

Chapter II Experimental details

This chapter presents the operating conditions for the preparation and characterization of TiO_2 thin films. It is divided into three parts. The first part is dedicated to the preparation of materials including PECVD deposition, post-annealing and seeding approach. The second and third parts are related to implemented methods for the characterization of films in terms of physico-chemical (part 2) and functional (part 3) properties.

1 Preparation of supported TiO_2 thin films

In a first step, PECVD operating conditions have been experimented and optimized in order to deposit TiO_2 coating on different mechanical supports including dense and porous ones. As no anatase structure could be obtained for deposition temperature lower than 250°C, a post-thermal treatment has been envisaged and optimized in terms of temperature and time required for crystallization. In parallel, seeding the substrate with crystal nuclei before deposition has been investigated with the aim of getting anatase directly through the PECVD deposition step.

1.1 Deposition of films by PECVD method

1.1.1 PECVD set-up

The PECVD system used in this study was typically composed of four main parts: the precursor and gases sources, the reaction chamber (i.e. the deposition chamber), the power generator and the pumping system, as notified on the photo and schematic graph of PECVD apparatus (excluding the pumping system) in Figure 2-1 and Figure 2-2, respectively. Each constitutive part of the PECVD system is detailed below.

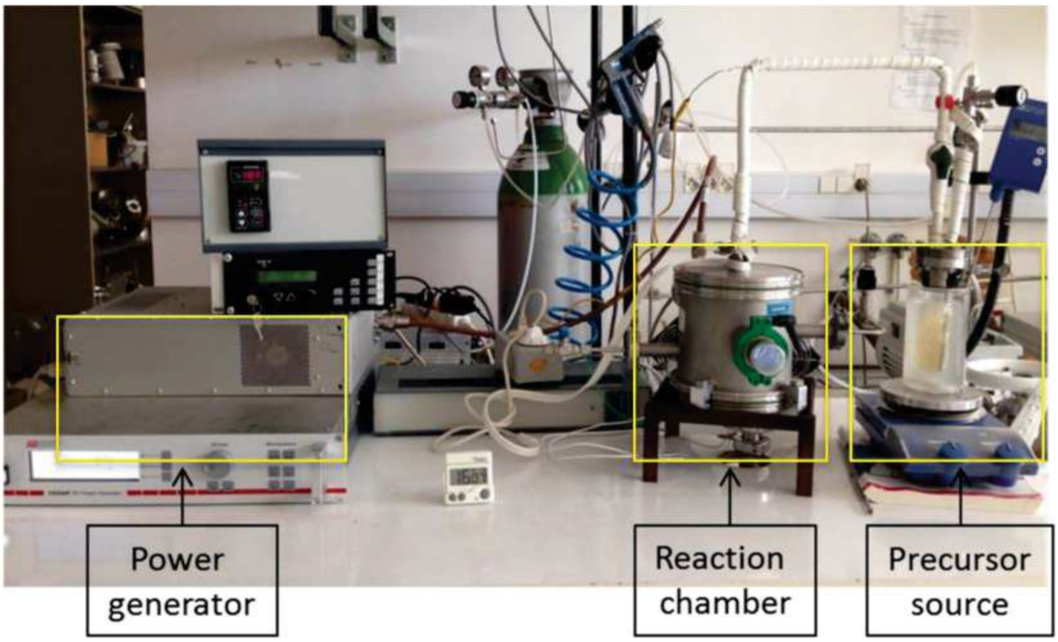

Fig. 2-1 Photo of the PECVD apparatus.

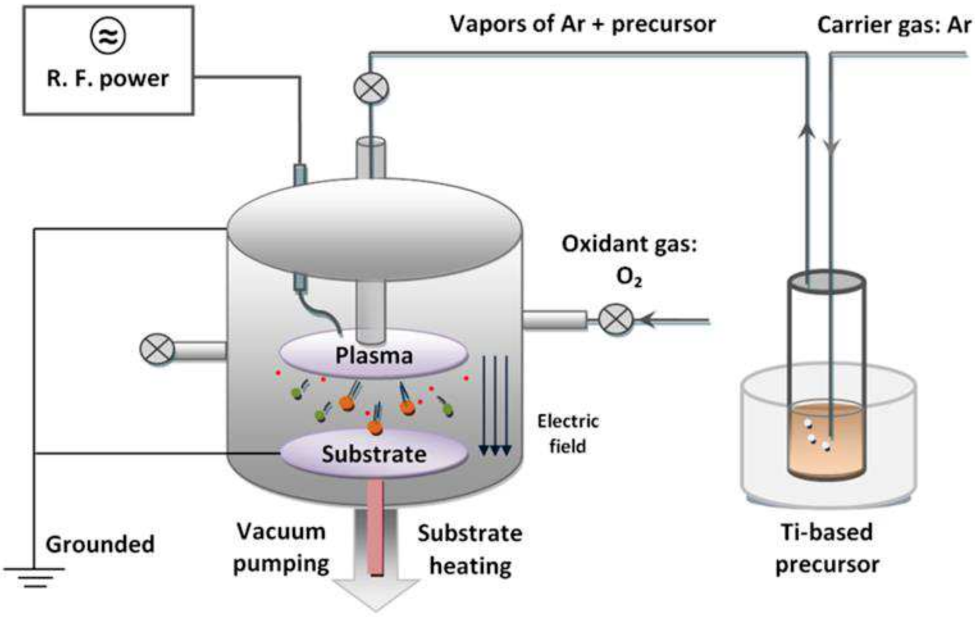

Fig. 2-2 Schematic graph of the PECVD apparatus.

Precursor and gases sources

The liquid metal-organic precursor contained in a sealed glass was held in an oil bath heated at 80 °C and stirred with Magnetic Stirrers from KA®, WERKE GmbH & Co. KG (Germany). Fluxes of argon and oxygen were regulated with a mass control unit of ROD-4MB, HORIBA (Japan). The inert argon (argon) was bubbling in liquid precursor as a carrier gas. The gas line connecting precursor source and reaction chamber was wrapped with circular coil of 220V Desostat-1D, L.LEGALLAIS (France) so that the line could be heated at 100 °C to avoid any precursor condensation in the pipe. Indeed, condensation causes pipe blockage, which can destabilize vacuum condition and produce TiO_2 powder falling down on the substrate. A thermal couple of Series 988, WATLOW (USA) was inserted between the coil and the pipe monitoring the actual temperature on the gas line. Oxygen was introduced as oxidant gas through an individual pipe directly connected to side of the reaction chamber.

Reaction chamber

The reaction chamber was a 10 liters steel cylinder equipped with a pressure gauge and two horizontal parallel plate electrodes. The pressure gauge (600 series/Baratron®, MKS Instruments GmbH (Germany)) was employed to investigate the pressure inside reaction chamber in real-time. The bottom electrode (diameter 10 cm) was used as the substrate holder. It was connected to a heating device from Eurotherm (France) heating up to 600°C. Bottom electrode (diameter 10 cm) and body of the chamber were grounded. The upper electrode (diameter 10 cm) was coupled to the power generator via metallic wires. One hole has been drilled in the center of the upper electrode, as a showerhead form, in which the carrier gas and precursor were injecting.

Power generator

R.F. power generator (CESAR^{TM} 136, Advanced Energy Industries Inc., USA) coupled with a matching box (RF navio, Advanced Energy Industries Inc., USA) was connected to the upper electrode on top of the chamber. A Teflon tube was needed to electrically separate the powered upper electrode from the grounded chamber.

Pumping system

The bottom of the reaction chamber was connected to a pumping system composed of a cold trap and a primary pump (Adixen, Pfeiffer Vacuum GmbH (Germany)). The cold trap placed between the deposition chamber and the pump enabled to retain the non-reactive species during the deposition process. The primary pump had two different roles: exhausting atmospheric gases and vapors (down to around 1 Pa) before the deposition step, and maintaining the required plasma pressure during the deposition process.

1.1.2 Precursor and substrates

Titanium tetra-isopropoxide (TTIP, $Ti(OCH(CH_3)_2)_4$) from Sigma-Aldrich (Germany) has been chosen as the metal-organic precursor to synthesize TiO_2. Chemical structure of TTIP molecule is given in Figure 2-3. TTIP is an effective precursor and less toxic than titanium chloride ($TiCl_4$), which is another common precursor for producing TiO_2. Hydrolysis of TTIP is easily taking place when it is in contact with water or air humidity. Therefore, filling TTIP liquid to the precursor tank and sealing the container was operated in a vacuum glove box workstation. The glove box was controlled at pressure of 1 mbar with water concentration < 1.2 ppm and oxygen concentration < 1 ppm. Afterwards, the sealed container was connected to the plasma reactor and kept in oil thermal bath.

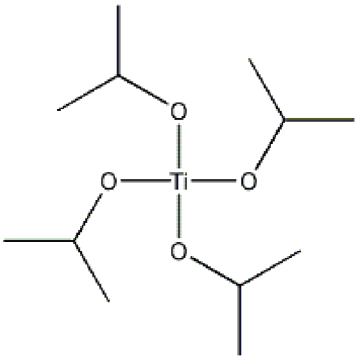

Fig. 2-3 Chemical structure of TTIP precursor.

In the literature, thermal decomposition of TTIP molecule has been analyzed in a CVD chamber coupled with mass spectrometry detection. [175] Propene (gas phase), water (gas phase) and titanium dioxide (solid phase) were found as the three main products from the reaction. Isopropanol was also observed as intermediate from hydrolysis and self-fragmentation of TTIP compound as written in Reaction 2-1 and Reaction 2-2. Isopropanol is further dissociated to water and propene as given in Reaction 2-3. Eventually, generalized reaction of TTIP breaking down to TiO_2, H_2O and C_3H_6 is summarized in Reaction 2-4.

Hydrolysis of TTIP:

$$Ti\ (OCH\ (CH_3)_2)_4\ (g) + 2\ H_2O\ (g) \rightarrow TiO_2\ (s) + 4\ (CH_3)_2CHOH\ (g) \qquad (2\text{-}1)$$

Break-down of TTIP:

$$Ti\ (OCH\ (CH_3)_2)_4\ (g) \rightarrow TiO_2\ (s) + 2\ C_3H_6\ (g) + 2\ (CH_3)_2CHOH\ (g) \qquad (2\text{-}2)$$

Isopropanol to propene:

$$(CH_3)_2CHOH\ (g) \rightarrow H_2O\ (g) + C_3H_6\ (g) \qquad (2\text{-}3)$$

Overall reaction:

$$Ti\ (OCH\ (CH_3)_2)_4\ (g) \rightarrow TiO_2\ (s) + 2\ H_2O\ (g) + 4\ C_3H_6\ (g) \qquad (2\text{-}4)$$

In a PECVD process, electron collision to molecules and ion-molecule interactions are also important. Yet no specific study has been reported on TTIP decomposing pathways (possibly of subsidiary interaction/reaction) in PECVD process.

Mechanical support was mounted on the bottom electrode for plasma deposition. Dense substrates such as silicon wafer and glass slide were applied to support TiO_2 thin film for characterization purpose. Silicon-supported TiO_2 layers were characterized for their chemical composition, morphology, wettability and crystalline structure and glass-supported TiO_2 layers were studied for band gap energy. Self-cleaning property of TiO_2 deposited on silicon were investigated following the Pilkington protocol. On the other hand, porous substrates such as ceramic and glass were used to fabricate functionalized membranes after optimized PECVD conditions have been established from the characterization stage. The applied dense and porous substrates are listed in Table 2-1.

Porous Anodisc (from Sigma-Aldrich) and porous ceramic disks (from Fraunhofer) are in round shape with a diameter of 47 mm. Anodisc is 0.1 mm thick and has a mean pore size equal to 250 nm. Ceramic disks are 1 mm thick with an asymmetric porous structure (Figure 2-4). They are composed of a macroporous support with a mean pore size of 2.5 µm and of a top layer with a smaller mean pore size. Two types of ceramic disks, characterized by top layers with two different mean pore sizes, 100 nm (Figure 2-4) and 800 nm, were used. The choice of two different ceramic supports is directly related to the wish to get two different geometries of titania materials. Indeed, two different kinds of TiO_2 coatings were deposited on them as: a continuous micrometer thick layer on 100 nm pored surface and a nanometer thick thin skin-coverage on 800 nm pored surface.

Table 2-1 Applied substrates to support TiO_2 thin films in PECVD process.

Dense substrate	Porous substrate
Si (100) wafer, MEMC (Korea)	Whatman® Anodisc 47, Sigma-Aldrich (Germany)
Borosilicate glass, Pyrex (France)	Ceramic Al_2O_3 disk, Fraunhofer (Germany)
Quartz glass	Mat of borosilicate glass fibers, Hollingsworth & Vose (USA)

A mat of borosilicate glass fibers (from H&V, USA) is another porous substrate that needs to be cut into a circle with 47 mm diameter to fit into the membrane cell. Thickness of the fiberglass mat is 0.4 mm and means pore size is 2.7 µm. Information about the porous substrates are summarized in the Table 2-2. Anodisc 47 support was used in preliminary synthesis to check TiO_2 morphology grown on porous surface. Ceramic Al_2O_3 disk and glass fiber were coated with TiO_2 materials and then tested in photodegradation diffusion cell and pilot plants.

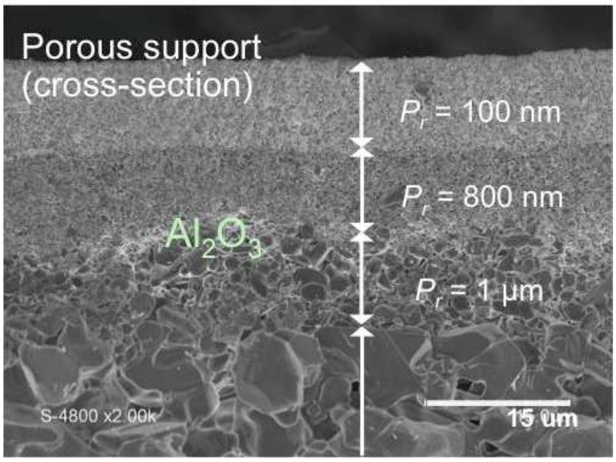

Fig. 2-4 Asymmetric porous alumina ceramic disk (from Fraunhofer) used as the support for PECVD TiO_2 thin film.

Table 2-2 Physical properties of the porous substrates.

Porous substrate	Mean pore size	Thickness	Diameter
Whatman® Anodisc	250 nm	0.1 mm	47 mm
Ceramic Al_2O_3 disk	Top-layer 100 nm Top-layer 800 nm	1 mm	47 mm
Mat of borosilicate glass fibers	2.7 µm	0.4 mm	-

Substrate surface was cleaned with ethanol and dried with air blowing before being mounted in the reactor. It was placed in the center on the bottom electrode just under the precursor inlet hole. Thermal-stable tape was used to fix the substrate on the edge.

1.1.3 Plasma deposition protocol and operating conditions

The plasma deposition protocol is presented in Table 2-3. Once the substrate fixed on the bottom electrode, all temperatures (oil bath, lines, substrate holder) and limit pressure in the reactor achieved, precursor and gases were introduced in the reaction chamber. Once the precursor and gases pressures stabilized, the RF power generator was switched on at the required power for the suitable duration depending on the targeted deposition thickness.

Table 2-3 Plasma deposition protocol.

1 Fill the precursor

- **Pour TTIP liquid in to container in Gloves Workstation**
- **Seal the container well**
- **Connect the precursor container to the reactor**

2 Prepare the reactor

- **Wrap the bottom electrode with aluminum paper**
- **Fix the substrate in the center of bottom electrode**
- **Connect the upper electrode, Teflon tube and the reactor**
- **Measure the distances from the top to the upper and bottom electrodes**
- **Close the reactor and start pumping to vacuum condition**

3 Start heating

- Heat the oil bath (precursor) to 80 °C
- Heat the gas carrier line to 100 °C
- Heat the substrate holder to target temperature
- Cool the trap with liquid nitrogen

4 Introduce gases

- Open valves and inject argon and precursor vapor to the reactor
- Open valves and inject oxygen to the reactor

5 Plasma on

- Switch on RF power generator
- Select ‘‘real mode’’ and input the intensity value
- Increase the tune capacity (C_T) to 99.5 %
- Reduce the load capacity (C_L) to 8.5 %
- Push the ‘‘on’’ button to initialize the plasma and start depositing
- Refill liquid nitrogen to cool the trap each 5 min
- Push the “off” button to stop the plasma

6 End the process

- Stop argon and oxygen gases
- Stop pumping and wait till minimal pressure
- Stop heating
- Open the reactor and collect TiO_2 sample
- Clean the reactor and trap

As RF power is on, gaseous molecules would be excited, ionized, dissociated and fragmented. Species such as hot electrons, radicals, ions and neutrals are typically formed in the plasma. Some transition of the electrons results in photon emission and thus the plasma is normally brightly illuminating. A photo of the PECVD reactor chamber obtained during a deposition process is displayed in Figure 2-5. The whitely plasma can be observed through the window glass.

A few points on an appropriate PECVD operation have to be declared. For instance, heating the gas lines constantly before gases inlet and until all the gases are stopped is very important to keep the pipes clean from condensation. The order of opening and closing gas valves (for argon and oxygen) should be correctly followed so that the liquid precursor would not be in contact to vacuum or oxygen directly. In addition, when applying the real mode on power generator, capacitances have to be adjusted in order to reduce the reflected intensity.

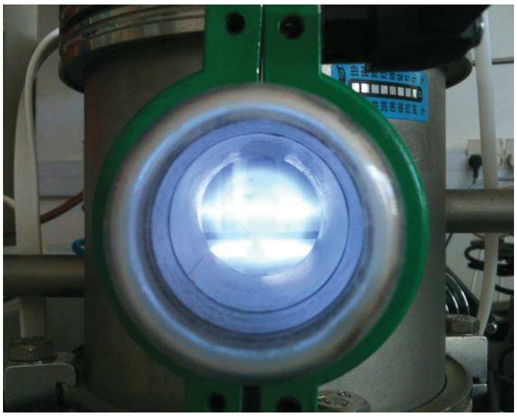

Fig. 2-5 Photo of the working PECVD reactor chamber.

PECVD operating conditions include: 1) thermal factors such as temperatures of substrate, precursor and gas line, 2) pressure factors such as partial pressure of Ar + TTIP and of O_2, 3) real electric power, 4) reactor configuration and 5) deposition duration. Detailed PECVD parameters for TiO_2 deposition are given in Table 2-4. Certain operating factors have been varied in order to study their effect on TiO_2 film growth on silicon.

Table 2-4 Controlled PECVD parameters in TiO_2 preparation.

Temperatures	**Pressure**	**RF power**	**Plasma dimension**	**Deposition duration**
Substrate temp. $T_s = 50 – 250°C$	Vacuum pressure $P_0 = 0.01$ mbar (1 Pa)	Real power $W_{real} = 50 – 65$ W	Electrode diameter $D_e = 10$ cm	$t = 3 – 40$ min
Precursor temp. $T_{oil} = 80°C$	Argon + TTIP pressure $P_{Ar + TTIP} = 0.155, 0.185, 0.225$ mbar		Plasma distance $d_P = 2.0, 2.5, 3.0$ cm	
Gas line temp. $T_{line} = 100°C$	Oxygen pressure $P_{O2} = 0.17$ mbar			

Substrate temperature (T_s) is important for surface reaction and surface diffusion/migration kinetics. It was varying from 50 to 250 °C in the studied PECVD process. Temperature of the oil bath (T_{oil}), that is the precursor temperature, was kept at 80 °C and temperature of the gas line (T_{line}) was maintained at 100 °C in the process.

The gas partial pressures were used instead of gas flow rates because millimeter valves were used in the gas line instead of flow meters to control the input gas flows. Partial pressure of Ar + TTIP ($P_{Ar+TTIP}$) and partial pressure of O_2 (P_{O2}) were calculated according to Equation 2-5 and 2-6 with knowing P_0 (initial limit pressure in the deposition chamber), P_1 (argon + TTIP partial pressure) and P_2 (total pressure once oxygen introduced). The influence of both P_{O2} (varying from 0.15 to 0.19 mbar) and $P_{Ar+TTIP}$ (equal to 0.155, 0.185 or 0.225 mbar) on the deposit chemistry and thickness homogeneity was studied.

Partial pressure of argon and precursor (Ar + TTIP):

$$P_{Ar+TTIP} = P_1 - P_0 \qquad (2\text{-}5)$$

Partial pressure of oxygen:

$$P_{O2} = P_2 - P_1 \qquad (2\text{-}6)$$

where P_0 is the initial limit pressure in the deposition chamber, P_1 is the pressure on ce argon and TTIP introduced and P_2 is the pressure after addition of oxygen.

RF power is the energy source to produce the weakly ionized plasma in PECVD process so that TiO_2 solid nanoparticle is eventually deposited on a surface. Forward electric power was supplied from the generator, whereas the reactor reflected some and only part of the power was enforced to the reactor. Then the real power can be known as written in Equation 2-7. Two different real powers equal to 50 W and 65 W were applied in this study.

Real power intensity:

$$W_{real} = W_f - W_r \qquad (2\text{-}7)$$

where W_{real} is the real power on upper electrode, W_f is the forward power supplied by generator and W_r is the reflected power from the chamber.

Reactor configuration, the space between two electrodes in particular, affects the geometry of the plasma phase and consequently the properties of the deposited films. Diameter of both electrodes (D_e) was 10 cm and the distance between them (d_p) was 2 – 3 cm adjusted by replacing a Teflon joint tube of different length. The distance from the reactor top to the bottom electrode (d_2) and the distance from the top to upper electrode (d_1) were measured. As a result, the plasma pathway length (i.e. electrode distance) was obtained by the first distance minus the second one as given in Equation 2-8. The influence of the plasma distance (equal to 2.0, 2.5 or 3.0 cm) on deposits chemistry and thickness homogeneity was studied.

Plasma distance:

$$d_p = d_2 - d_1 \tag{2-8}$$

where d_p is the length of plasma pathway, d_1 is the distance from the chamber top to upper electrode and d_2 is the distance from chamber top to bottom electrode.

Three different deposition durations were applied: 15, 20 and 40 min in the case of TiO_2-coating layer on silicon, quartz and porous ceramic substrates. On the other hand, four different deposition durations equal to 3, 5, 7 and 10 min was experimented on porous ceramic support (with 800 nm mean pore size) for TiO_2-skin coverage coating.

As a summary, all the TiO_2 samples prepared in this thesis work are presented in Table 2-5 listing the substrate material, substrate temperature, plasma conditions and deposition duration. Groups of sample B 1-5, ZJ 1-9 and M 1-4 (on silicon) were dedicated for PECVD optimization studies. Samples Q 1-3 were made on transparent quartz for light transportation study. Samples sS 1-2 were made on seeded silicon for crystallization process during post-annealing treatment. Samples M100, M800, LF100 and LF800 were PECVD prepared TiO_2-ceramic composite membranes having different formates of TiO_2 coating on the porous ceramic support.

Table 2-5 List of all the TiO_2 thin films prepared in this Ph.D work.

TiO_2 sample	Substrate	Substrate temperature (°C)	Ar+TTIP pressure (mbar)	Plasma distance (cm)	RF power (W)	Deposi- -tion duration (min)
B 1-5	Silicon	50 100 150 200 250	0.15	3	60	15
ZJ 1-9	Silicon	150	0.155, 0.185, 0.225	2 2.5 3	50	20
M 1-4	Silicon	150	0.225	2 3	50 65	20
Q1-3	Quartz	150	0.225	3	50	7 15 20
sS 1-2	Seeded silicon	150 250	0.225	3	50	50
M100	Porous ceramic (P_r=100nm)	150	0.225	3	50	20
M800	Porous ceramic (P_r=800nm)	150	0.225	3	50	7
LF100	Porous ceramic (P_r=100nm)	150	0.225	2	50	20 40
LF800	Porous ceramic (P_r=800nm)	150	0.225	2	50	20 40

Plasma deposition is a dynamic process in which the working pressures and electric powers are fluctuating along with deposition time. Reactor pressure and discharged power were recorded every minute when preparing TiO_2 thin films. Recorded values in the case of a TiO_2 film deposited in optimized synthesis conditions (determined from films properties – see chapter 3) are given in Table 2-6. It is observed that reaction pressure surged up in the first a few seconds the plasma was just initiated and followed with a fast dropping. After about 2 minutes, working pressure slowly climbed up due to collision and reaction in the gas phase.

Eventually, the total pressure stabilized roughly in the last a few minutes. As deposition going on, real power to the reactor was always fixed and forward power continuously increased since reflection from the chamber was keeping enhanced. The increased reflect power can be explained by more solid materials was attached to the upper electrode during deposition process. Constant real power intensity with a lower forwarding power is desired because carbonization of the precursor compound could be weakened.

Table 2-6 Dynamic reaction pressure and electric power in an optimal PECVD process.

Duration (min)	**Reaction pressure (mbar)**	**Forward power (W)**	**Reflected power (W)**	**Real power (W)**
0.1	0.590	130	80	50
2	0.490	96	46	50
4	0.483	112	62	50
6	0.490	120	70	50
8	0.495	130	80	50
10	0.506	134	84	50
12	0.520	138	88	50
14	0.524	139	89	50
16	0.516	140	90	50
18	0.516	145	95	50
20	0.516	147	97	50

1.2 Crystallization by post-annealing

As-grown TiO_2 films obtained from the mentioned PECVD protocol was obtained in amorphous phase. Since crystalline TiO_2 (anatase phase) is the most photocatalytic efficient form, great efforts were made to find temperature threshold in TiO_2 phase transformation from amorphous to anatase. Post-annealing the deposited films was operated in the furnace of VULCAN® 3-130, DETSPLY International (USA). Heating temperature, heating/cooling speed and dwelling time (i.e. staying duration) were programed on the furnace. Heating rate 1.0 °C min^{-1} and cooling rate 10 °C min^{-1} was applied in the most post-thermal treatments, whereas, slower heating speed 0.5 °C min^{-1} was experimented to investigate potential effect on crystallization. Post-annealing process was studied in two situations: 1) as a function of increased temperatures from 300 to 700 °C and 2) as a function of dwelling time at fixed 300 °C.

1.2.1 Post-annealing as a function of temperature 300 – 700 °C

First of all, TiO_2 thin film grown on silicon was synthesized with the optimized PECVD protocol. The sample was mounted in a high-temperature X-ray diffraction apparatus (X'pert Pro, Pan Analytical) that contained a compacted furnace. Silicon-supported TiO_2 thin film was heated from 100 to 700 °C with a heating rate 1 °C min^{-1}; at the meantime, X-ray diffraction measurement was taking place at each 100 °C increased temperature. The minimal temperature of crystallization was found in the continuous heating manner. Detail on diffraction measurement is to be explained in a following session 2.2.3 in this chapter.

In addition, four other samples of TiO_2 thin films on silicon were prepared under the optimized PECVD conditions. One sample was kept as deposited, the other three were heated to 300, 400 and 500 °C respectively in the furnace. Heating and cooling steps were kept in rates of 1.0 and 10 °C min^{-1}. No staying duration was applied to all the samples after reaching the target temperature. The heating programs are given in the Figure 2-6.

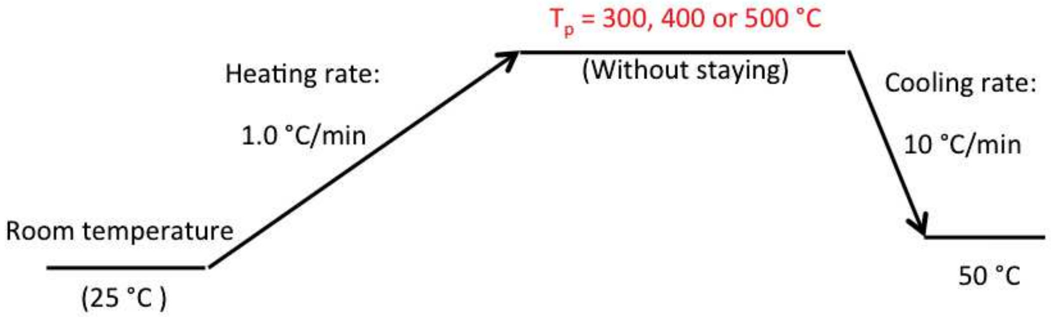

Fig. 2-6 Post-heating TiO_2 samples at T_p equal to 300, 400 or 500 °C.

Afterwards, room temperature XRD analysis was carried on the post-annealed TiO_2 samples to examine whether crystalline structure has been formed. In addition, a slower heating rate 0.5 °C min^{-1} was applied on heating a fifth sample at 300 °C with other conditions constant in order to investigate the possibility of crystallization at 300 °C without staying time.

1.2.2 Post-annealing as a function of duration at 300 °C

Post annealing TiO_2 deposit on silicon with dwelling time (i.e. staying duration) was devoted to further investigate the possibility of crystallizing at 300 °C that was not achieved without any staying time. Three samples have been were synthesized with the optimal PECVD protocol. Each of them was post-heated at 300 °C in the furnace independently with various hours.

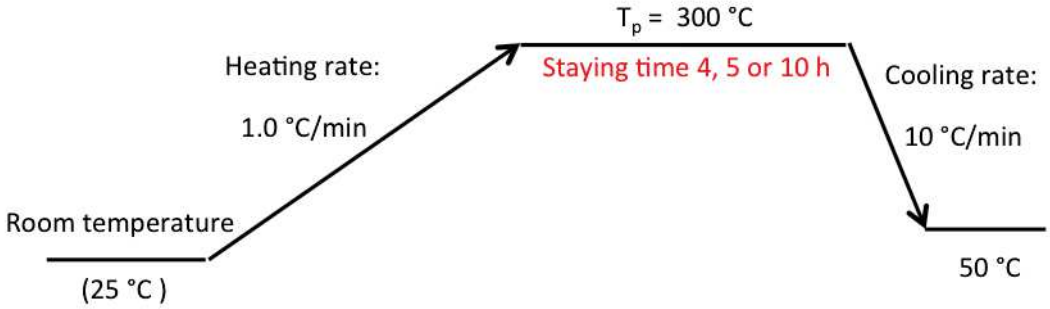

Fig. 2-7 Post-annealing TiO_2 thin films at 300 °C with 4, 5 and 10 h.

Heating and cooling speed was the same as previously at 1.0 and 10 °C min^{-1} aspect. The first sample was heated at 300 °C for 4 hours, the second one for 5 hours and the third one for 10 hours individually. Heating programs are illustrated in Figure 2-7. Room temperature XRD characterization was then carried out to examine to determine whether crystalline structure has been developed at lower temperature 300 °C due to a longer duration.

Furthermore, post-annealing another TiO_2 sample at even lower heating temperature 275 °C was experimented in the furnace. Heating and cooling steps were the same as previous at 1.0 and 10 °C min^{-1} and stabilization at 275 °C was prolonged as long as 24 hours. It was to prove whether 300 °C was the minimal temperature threshold for TiO_2 thin film crystallization, or if 275°C could be enough.

1.3 Seeding approach prior to PECVD process

Seeding substrate with anatase nuclei before PECVD deposition was aimed at reducing thermal energy required in TiO_2 crystallization process. Coupling concept of seeding and depositing is illustrated in Figure 2-7. A crystal nuclei attached surface is considered to potentially promote crystallization at lower surface temperature. The possible effect was first examined during plasma deposition process with substrate temperature at 150 °C and 250 °C. The effect on crystallization was secondly examined during post-annealing process at 300 °C.

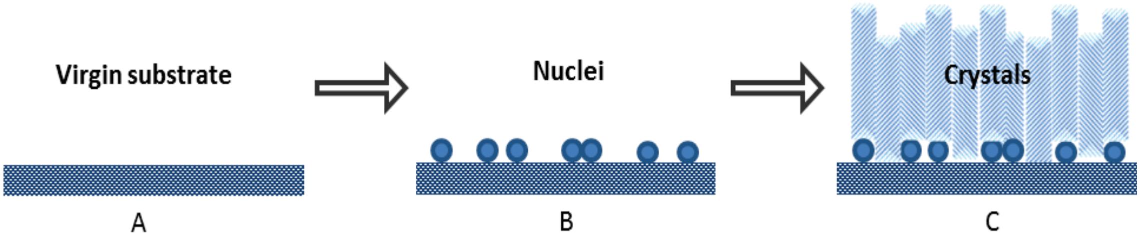

Fig. 2-8 Concept of using seeded substrate for PECVD TiO_2 deposition.

1.3.1 Seeding the substrate by sol dip-coating

The anatase sol for seeding substrate was basic hydrosol S5-300B provided by Millennium Inorganic Chemicals (France). Anatase solution was prepared by diluting the original sol in ammonia buffer at pH 11.5 with a ratio 1:7.5. After sufficient mixing for 4 hours, a piece of virgin silicon was vertically dipped into the solution with a homemade mechanical device. Sinking speed 5 cm min^{-1} and immersion time 20 seconds were set constantly. Withdrawing velocity was experimented with 1, 3 and 5 cm min^{-1} respectively to attach a seeding layer of proper thickness and dispersion on silicon. After one step of dipping, the wetted silicon pieces were vertically dried in air for one night. And then they were heated at 250 °C for 24 hours and then at 450 °C for another 24 hours in the furnace to remove organic solvent. Heating rate and cooling rate were 5 and 10 °C min^{-1} respectively. The preparation routine was adapted from a previous work of depositing anatase on porous ceramic using sol-gel method published by A. Ayral.[14]

Surface hydrophilicity is essential to provide a homogeneous dispersion of sol on silicon with dip-coating approach. 800 °C-annealed silicon was prepared in the furnace so that an oxidized surface was maintained in order to improve its surface wettability in comparison to the virgin silicon (100) wafer. Seeding approach was carried out on the annealed silicon substrate with the same dip-coating process described as previously.

Homogeneity of crystal nuclei dispersion on silicon surface is the key point to obtain a fully seeded-substrate that is to be mounted in PECVD reactor. Adhered anatase on both virgin and annealed silicon was witnessed with confocal Raman spectroscope. The seeded surface was also observed in the coupled microscope. Moreover, the seeding layers were observed in cross-sectional SEM images.

1.3.2 PECVD TiO_2 deposition on the seeded substrate

The best seeded-silicon and virgin silicon (as witness substrate) were fixed on the bottom electrode in PECVD reactor. TiO_2 thin films were deposited upon them under optimal plasma deposition conditions. In the case of seeded-substrate, two deposition experiments were particularly studied with substrate temperature at both 150 °C and 250 °C. It is more likely that TiO_2 deposit might be crystallized due to stronger seeding activity at higher surface temperature. A substrate temperature higher than 300 °C was not intended in the thesis work by applying PECVD process because post-thermal treatment would be carried out equal to or above 300 °C after all.

As-deposit TiO_2 thin films on seeded and non-seeded silicon (both prepared at 150 and 250 °C) were examined with XRD and Raman spectroscope right after PECVD process. Afterwards, the four samples went through the analysis in high-temperature XRD heating at 300 °C. Measurement duration at 300 °C lasted for 6 hours on each sample. Diffraction pattern was recorded each other half an hour at 300 °C. Phase transformation from amorphous TiO_2 to anatase was traced as function of heating duration and compared on the effect of seeding surface and deposited temperature.

2 Characterization on physico-chemical properties of TiO_2 films

Physico-chemical properties of TiO_2 thin films investigated in this study are morphology, surface wettability, chemical composition, crystalline structure, porosity, density and band gap energy. Fourier transformed infrared spectroscope (FTIR) and energy dispersion X-ray (EDX) were employed to analyze chemical bonding and elemental composition in the films. Scanning electron microscope (SEM) imaged the microstructure in the films. Water contact angle (WCA) examined TiO_2 surface hydrophilicity with or without the effect of UV irradiation. X-ray diffraction (XRD) and Raman spectroscope were applied to investigate the crystal structure in annealed films. X-ray reflectivity (XRR) and ellipsometry spectroscope (EP) were experimented and modeled to calculate film porosity. Optical absorbance measured in UV/Vis spectroscopy was plotted to determine the band gap energy of synthetic TiO_2 film on glass. Moreover, thermal analysis on heat transfer and weight loss was carried out for prepared TiO_2 materials by heating in the range 25 – 1000 °C.

2.1 Morphology, Chemistry, surface wettability and crystal structure (SEM, FTIR, EDX, WCA, XRD and Raman)

Morphology

Morphology of TiO_2 layer (amorphous and anatase) on silicon was inspected in scanning electron microscope (SEM), Hitachi S4800 (Japan). Samples were cut into suitable size and then horizontally and vertically mounted on SEM substrate holder for surface and cross-sectional scanning. The cut edge for cross-sectional purpose should be sharp and fresh. Each sample was metallized with Pt plasma pre-treatment for 40 seconds before inputting to the SEM sample chamber. Electron beam of energy 10-100 kV was shooting on the sample so that proportional magnified images were produced. Microstructure of the thin film was observed in surface and cross-section images. Thickness of TiO_2 layer was measured in SEM cross-sectional image, which was bearing 10% instrumental error. Furthermore, microstructure of as-deposit and annealed TiO_2 film (for the same sample) was compared in SEM images to check whether the post-annealing caused structure change or defect.

Chemistry

PECVD TiO_2 deposit on silicon was analyzed with FTIR, 710 Nicolet (France), as well as the corresponding post-annealed ones. The infrared absorbance spectrum of silicon-supported TiO_2 thin film was recorded in the wavenumbers range 400 – 4000 cm^{-1}, with an automatic subtract of silicon background in the Omnic program. Vibration due to O-H bond of adsorbed surface water, organic bond C-C and inorganic bond Ti-O was observed in infrared spectra. Normalized absorbance intensity of Ti-O vibration at wavenumber 450 cm^{-1} was calculated by dividing the measured intensity (from FTIR spectrum) with the film thickness. By comparing normalized intensity (independent of thickness) of samples made from different PECVD conditions, the sample with the richest Ti-O abundance was found and accordingly the optimal deposition parameters were determined. Infrared spectra of amorphous and anatase film (from the same sample) were recorded and difference was observed. In addition, chemical elements in the as-deposit film were analyzed in energy dispersion X-ray (EDX), Hitachi S4800 (Japan) from 0 – 10 keV. Elements and relevant atom ratio were estimated from EDX spectrum.

Surface wettability

Homemade water contact angle (WCA) device coupled with CCD detector was employed to study surface wettability of TiO_2 film with or without effect of UV illumination. Surface of both amorphous and anatase films on silicon was studied. In darkness, a droplet of pure water (from Millipore) with volume 0.6 ml was dropping from a syringe onto the film and immediately a photo of the TiO_2-water interface was captured by detector camera. Five positions on the surface were analyzed and thus an average contact angle was obtained for each sample. The photos were analyzed in a graphic program to measure and fit the solid-liquid contact angles. Afterward, the same sample was placed under a UV lamp of intensity 30 W m^{-2} at wavelength 355 nm for 20 minutes. The same WCA measurement as previous was made on the illuminated TiO_2 surface immediately after UV treatment. Mean water contact angle on irradiated and non-irradiated TiO_2 surface (for the same sample) was compared and the photo-induced hydrophilicity phenomenon was investigated. Difference of wettability between amorphous and crystalline surface was also compared.

Crystalline structure and crystallite size

Crystalline phase of post-annealed TiO_2 film was examined with X-ray diffraction (XRD) of X'pert Pro, Pan Analytical (Netherland) by matching the measured pattern to the database. Effect of PECVD substrate temperature and post-annealing temperature on crystal formation in the films was evaluated in the patterns. TiO_2 layer deposited on seeded-silicon was also studied in diffraction analysis. Incident X-ray was emitted from Cu Kα at wavelength 0.154 nm. XRD operational power was 40 kV and 20 mA and measuring angle 2θ was from 20 – 60 ° with a rotating speed 0.028 ° s^{-1}. In a result, one XRD recording on one TiO_2 sample took 25 minutes.

Crystallite size was estimated according to Scherrer equation as given in Equation 2-9, with knowing peak width in XRD pattern. For instance, by measuring the full-width at half maximum $\Delta(2\theta)_{FWHM}$ at $2\theta = 25.3$, crystal dimension D in the anatase TiO_2 film can be know from the below equation.

Scherrer equation:

$$D = \frac{0.9\,\lambda}{B\,cos\theta} \qquad (2\text{-}9)$$

where 0.9 is a constant (for sphere shape crystal), λ is the wavelength of incident X-ray (0.154 nm), θ is the incident angle and B is the radius value related to$\Delta(2\theta)_{FWHM}$ and instrumental resolution.

The radius value *B* as:

$$B = \sqrt{\Delta(2\theta)^2_{FWHM} - \Delta(2\theta)^2_{res}} \qquad (2\text{-}10)$$

where $\Delta(2\theta)_{FWHM}$ is full-width at half maximum at 2θ in diffraction pattern and $\Delta(2\theta)_{res}$ is instrumental resolution (equal to 0.09 for the applied XRD apparatus).

In addition, Raman spectroscope (from Jobin-Yvon Confocal Labram 1B) provided complementary characteristic spectrum on crystal structure. The confocal Raman spectroscope was coupled with Olympus BX40 microscope. TiO_2 anatase has fingerprint Raman scattering with incident light. Red laser of intensity 100 mW at wavelength 647.1 nm was emitted from Ar/Kr to stimulate molecular vibration in the sample. A detection network 1800 lines nm^{-1} for scattered light was chosen in a measuring window 150 – 800 cm^{-1}. Sensor CCD 30-11 (1024 × 256 pixels) was coupled to the Raman spectroscope for imaging on sample surface with a magnified lens ×100 times. As-grown and annealed TiO_2 films on silicon were examined in Raman spectroscope to confirm the anatase structure. Moreover, seeding layer on silicon and TiO_2 on seeded-silicon (as described in session 1.3 in this chapter) were also investigated with vibrational spectroscope. It is more feasible to analyze very thin anatase layer with confocal Raman spectroscope than with XRD.

2.2 Porosity and band gap energy (XRR, EP and UV/Vis)

Porosity

Porosity in the TiO_2 film on silicon was not directly measured with nitrogen adsorption/desorption method due to the limitation of material quantity inherent to thin film. Density of the film was modeled from X-ray reflectivity (XRR) fitting using X-ray diffractometer D5000, Siemens (Germany). The density of synthetic TiO_2 film was compared to the density of dense TiO_2 material and therefore the percentage of void volume was calculated as given in the Equation 2-11.

Porosity of thin film:

$$P = \frac{1/\rho_1 - 1/\rho_2}{1/\rho_1} \times 100\% \qquad \text{(2-11)}$$

where ρ_1 is the density of PECVD TiO_2 film and ρ_2 is the density of dense TiO_2 as a reference.

Porosity, thickness and refractive index of the thin film could also be modeled in optical ellipsometry spectroscope (EP) and XRR measurement with the methods described in one previous work of the group [194]. Light of energy in the range 1.2 – 4.5 eV was incident on TiO_2 surface with a spot area 3 cm^2. Polarization of the reflected electromagnetic wave was detected and calculated. A few mathematics laws were applied and modified to fit the measured data in the program. An example of Cauchy law is given in Equation 2-12.

$$n\,(\lambda) = B + \frac{C}{\lambda^2} \qquad \text{(2-12)}$$

where n is refractive index, λ is the wavelength, B and C are the equation coefficients.

Band gap energy

Band gap energy (E_g) of semiconductor has been explained in the first chapter. The band gap of PECVD TiO_2 thin film on glass was studied with optical measurement. Borosilicate glass (Pryex) and quartz were applied as the transparent substrates. Optimal PECVD conditions were operated to prepare TiO_2 films on glass with deposition duration as 7, 15 and 20 minutes so that various thicknesses were obtained. Post-annealing at 400 °C was carried out in the furnace to produce anatase phase. Amorphous and anatase films on glass were analyzed with UV/Vis spectroscope V-570, JASCO from Serlabo Technologies (France). Absorbance, transmittance and reflectance data were collected from wavelength 200 to 700 nm.

In general, the relation between the absorption coefficient (k) and the frequency (v) is described in Equation 2-14. [195]

$$khv = A(hv - E_g)^n \qquad (2\text{-}14)$$

where k is absorption coefficient, h is Planck constant, v is frequency, A is a constant, E_g is the band gap energy and n is index as: $n = 1/2$ for direct band gap and $n = 2$ is for indirect band gap.

Direct band gap:

$$khv = A(hv - E_g)^{1/2} \qquad (2\text{-}15\text{-}A)$$

Indirect band gap:

$$khv = A(hv - E_g)^2 \qquad (2\text{-}15\text{-}B)$$

where v is the frequency, E_g is the band gap energy, h is the Planck constant, k is the absorption coefficient and A is a constant.

It is commonly considering that TiO_2 amorphous and anatase are both indirect band gap, that is the inter-band transition between VB and CB is with non-straightforward vector. On the other hand, rutile TiO_2 is normally concerned having direct band gap. For the case of direct (n =1/2) and indirect band gap (n = 2), the Equation 2-14 can be adapted as in Equation 2-15-A and 2-15-B. The cut-of absorption wavelength can be found in UV/Vis absorbance spectrum and E_g would be determined by plotting $(khv)^n$ along with hv (n value is according to the type of band gap) in the cut-off region.

2.3 Investigation on phase transformation from amorphous TiO_2 to anatase (TGA-DSC and HT-XRD)

Thermal analysis heating the optimal TiO_2 sample from 100 to 1000 °C in the air was carried out. Heat transfer was measured in Thermo-Gravimetric Analysis (TGA), meanwhile, weight loss was detected in Differential Scanning Calorimetry (DSC) with equipment of SDT 2960 Simultaneous DSC-TGA, TA Instruments (US). Heating speed in DSC-TGA measurement was 1 °C min^{-1} and the minimal sample weight required by the thermal analysis was 10 mg. Three TiO_2 thins films were deposited on silicon in PECVD processes and the as-deposit material was collected by scrapping. Change of heat flux and sample weight was caused as heating when endothermic/exothermic reaction and carbonization occurred in crystallization process.

In parallel, high-temperature X-ray diffraction (HT-XRD) of X'pert Pro, Pan Analytical (Netherland) was applied to track the crystallization evolution by heating TiO_2 from 100 to 700 °C. Incident X-ray and measuring parameters were the same as the room temperature XRD method (described in session 1.2 in this chapter). An in-situ furnace is compacted under the sample holder in the diffractometer. Heating program used in HT-XRD analysis is illustrated in Figure 2-9. Heating and cooling rate were controlled as 1 and 10 °C min^{-1} respectively. XRD measurement took place at each increased 100 °C and the measurement lasted 25 minutes each time. Appearance and development of diffraction peaks (related to crystal faces) were observed when the measuring temperatures increased.

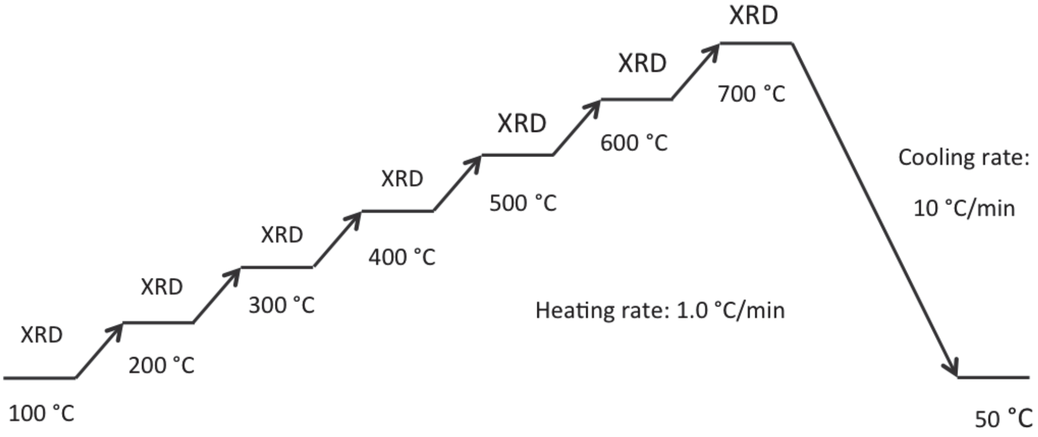

Fig. 2-9 High-temperature X-ray diffraction (HT-XRD) heating program.

3 Characterization on functional properties of TiO_2 films

Anatase TiO_2 thin films have been synthesized in PECVD process combined with post-annealing. After their physico-chemical properties were characterized, functional photocatalytic activity was assessed with various methods. The assessments included self-cleaning surface test (Pilkington protocol) for silicon-supported TiO_2 samples and diffusion test and membrane performance for ceramic-supported TiO_2 samples. Effect of preparation conditions (substrate and post-annealing temperatures) on photoactive efficiency was compared in “static” Pilkington test. Optimal anatase films on porous ceramic were examined in diffusion cell and pilot plants with “dynamic” conditions. UV source, model compound, initial concentration and applied pressure were investigated as variable parameters in the different tests.

3.1 Photocatalytic activity measurement in “static” conditions

Pilkington protocol was published in a patent, in which a fatty acid (stearic acid) was attached to TiO_2 surface and the adhered wax-like acid was removed from the surface under UV illumination. [196] Quantity of stearic acid remained on the surface was analyzed in infrared absorbance spectra as a function of UV illuminating duration.

3.1.1 Model compound, TiO_2 film and UV lamp

Stearic acid, from Sigma-Aldrich (Germany), was used as the model compound in self-cleaning surface test. Chemical structure of stearic acid (IUPAC name octadecanoic acid) is given in Figure 2-10. Molecular formula of stearic acid is $CH_3(CH_2)_{16}CO_2H$ with molar mass 284.48 g mol^{-1}, density 847.0 kg m^{-3} and boiling point 376.1 °C. 0.25 g powder of stearic acid was diluted in 100 ml methanol and the solution of concentration 8.8×10^{-3} mol L^{-1} was prepared.

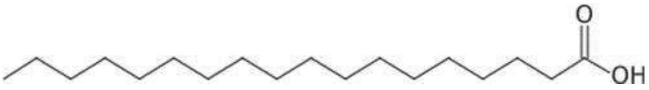

Fig. 2-10 Chemical structure of stearic acid.

PECVD TiO_2 films were deposited on silicon at substrate temperature at 50, 150 and 250 °C with other parameters kept constant. Post-thermal treatment was made at 400 °C so that anatase could be formed in the films. Virgin silicon and TiO_2-coated silicon were dipped into the prepared stearic acid solution ($c = 8.8 \times 10^{-3}$ mol L^{-1}) manually with hands. They were immersed in the solution for a few seconds and then drew out afterward. The wetted samples were dried in the air and then white wax-like stearic acid was adhered on the surface. Such organic compound attached silicon and TiO_2 surfaces were ready for self-cleaning experiment.

UV source was provided from four tubular CLEO compact lamps from Philips (Netherland) arrayed in a Eurosolar box. The lamp emits highly concentrated radiation in the range 300 – 400 nm, whose emission spectrum is presented in Figure 2-11 (provided by the lamp manufacturer). Total irradiation intensity of the new furnished UV lamp was 50 W m^{-2} with a main peak at wavelength 355 nm.

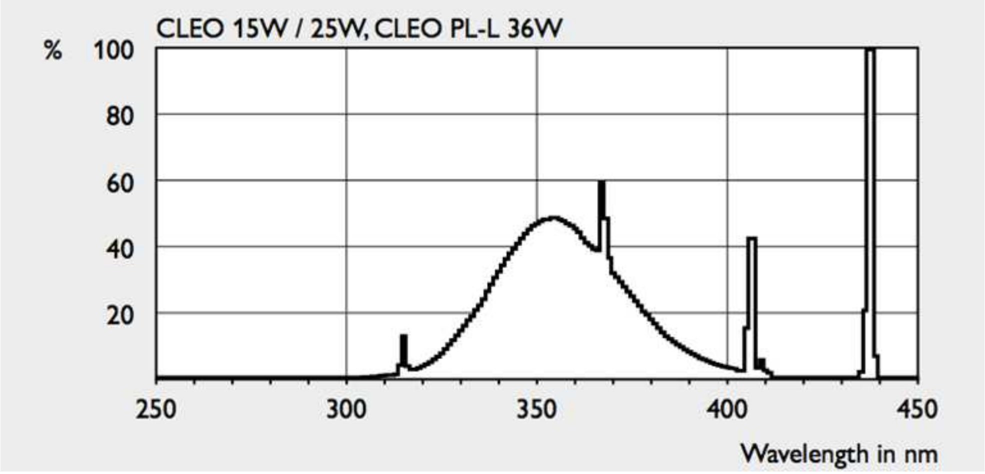

Fig. 2-11 Emission spectrum of the UV source (CLEO fluorescent lamp).[197]

A photo of the CLEO compacted lamp (arrayed in a box) is displayed in Figure 2-12. Since the tubular lamps would be aged by long-term use, irradiation intensity in the real-time could be measured by a radiometer of UVICURE®, Electronic Instrumentation and Technology (USA) that is shown on the left hand in the photo.

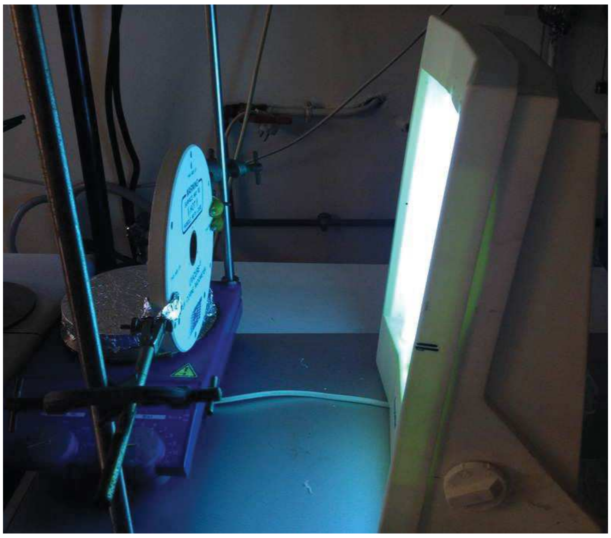

Fig. 2-12 Photo of CLEO compacted lamp with its irradiation intensity measure by a radiometer.

3.1.2 Pilkington test

Pilkington protocol was established to evaluate UV illuminated TiO_2 surface's photodegradation capability on the selected model compound stearic acid. Stearic acid has an

18-carbon chain and is rich in C-H bond that can be characteristically detected in infrared spectroscopy. The organic molecules were immobilized on TiO_2 surface by dip coating in stearic acid solution ($c = 8.8 \times 10^{-3}$ mol L^{-1}). The assessment protocol is graphically depicted in Figure 2-13. It is a simple method since the analysis is done by a fast infrared absorbance measurement on the solid surface. The dip-coated sample was placed under the UV lamp with distance 30 cm. With each 10-minute UV irradiation the dip-coated sample was analyzed in FTIR (with the same operation as described in session 1.2 in this chapter). Infrared absorption spectra were recorded from wavenumber 500 to 4000 cm^{-1} along with illumination duration. Eventually, the amount of stearic acid molecules remained on TiO_2 surface was proportionally analyzed and compared according to the infrared spectra.

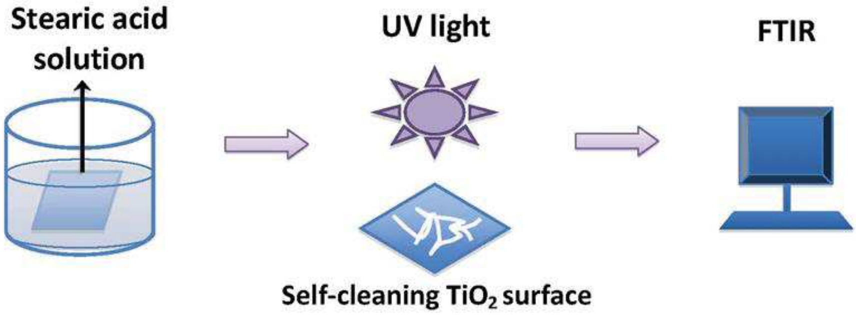

Fig. 2-13 Schematic presentation of Pilkington test.

In principle, intensity of C–H vibration (specified wavenumber 2800 – 3000 cm^{-1}) detected in FTIR is proportional to the number of stearic acid molecules present on the sample surface. The peak area at wavenumber 2800 – 3000 cm^{-1} was integrated in Omnic program. Decline of the C-H band area (A) was quantified as a function of UV irradiation time. Then photodegradation rate (R_{ST}) of stearic acid by illuminated TiO_2 was determined as in Equation 2-16.

Photodegrading conversion rate (R_{ST}):

$$R_{ST} = (1 - \frac{A_t}{A_0}) \times 100\% \qquad (2\text{-}16)$$

where t is the UV irradiation duration, A_0 is the initial peak area of C-H vibration (2 800 – 3000 cm^{-1}) in FTIR spectrum and A_t is the studied peak area at time t.

Photodegradation efficiency was compared on silicon-supported TiO_2 samples made from PECVD processes with substrate temperatures at 50, 150 and 250 °C, all being post-annealed at 400 °C. Effect of preparation condition on self-cleaning property has been figured out from Pilkington experiment results.

3.2 Photocatalytic activity measurement in “dynamic” conditions

PECVD TiO_2 deposits on porous substrates were studied in diffusion cell to examine their photo-activity in liquid phase. Diffusion process was caused by differential concentration without any pressure applied. Photoreaction was taking place at the mean time when organic molecules were diffusing through TiO_2-coated porous membrane.

3.2.1 Model compound, TiO_2-coated membrane, diffusion cell and UV lamp

Methylene blue (MB), a blue dye compound (IUPAC name 3,7-bis(dimethylamino)-phenothiazin-5-ium chloride), was used as the model compound in diffusion test. Molecular formula of MB is $C_{16}H_{18}ClN_3S$ and its molar mass is 319.85 g mol^{-1}. Its chemical structure is presented in Figure 2-14. MB molecules in water have a characteristic absorbance at wavelength 665 nm.

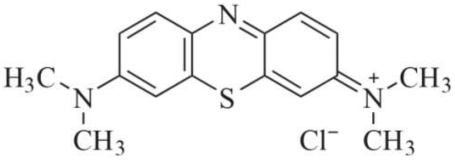

Fig. 2-14 Chemical structure of methylene blue (MB).

Ceramic disks with diameter 47 mm and thickness 1 mm, supplied from Fraunhofer (Germany), were applied as the porous substrate to support TiO_2 thin films.

The diffusion cell was constructed of feed and reception compartments. TiO_2-coated membrane was separating the two compartments in the between. The photoactive surface was faced to the reception side, to which the UV source was applied. Schematic presentation of the diffusion test is illustrated in Figure 2-15. The two compartments were both under atmosphere and no differential pressure applied. The solute MB molecules diffused through the functionalized membrane from the feed solution (higher concentrated) to the accepting solution (lower concentrated), meanwhile photoreaction occurred on the reception side with UV irradiation.

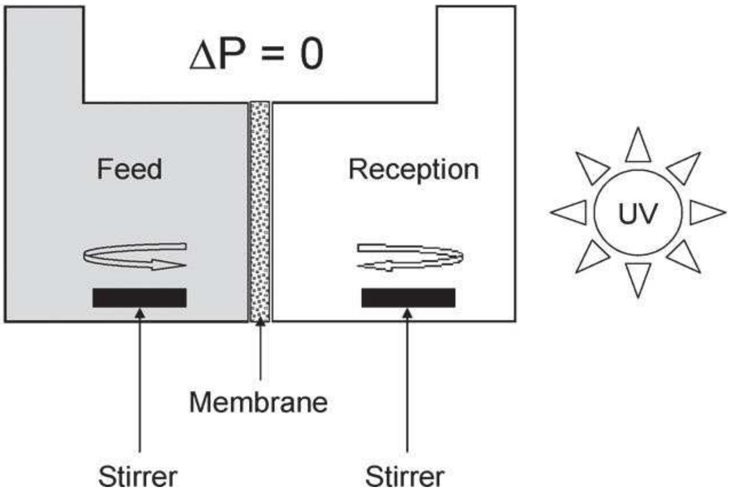

Fig. 2-15 Configuration of the diffusion cell. [14]

The employed UV lamp is the same one as described in Pilkington test (seen in session 3.1 in this chapter). Yet four new tubular CLEO compact lamps, from the same manufacturer (Philips, Netherland), were replacing the aged ones. Radiometer UVICURE® from Electronic Instrumentation and Technology (USA) was used to measure the real-time intensity of the new fluorescent lamps, which was found at 55 W m^{-2} (with main peak at wavelength 355 nm).

3.2.2 Diffusion test

Mother solution of MB of concentration 1×10^{-3} mol L^{-1} was prepared with dissolving 0.0320 g MB powders in 100 ml water (from Millipore). By diluting the mother solution, a series of solution with concentration 1×10^{-6}, 2×10^{-6}, 4×10^{-6}, 6×10^{-6}, 8×10^{-6} and 1×10^{-5} mol L^{-1} were derived. Absorbance spectrum of MB solution (c = 1×10^{-5} mol L^{-1}) was measured with UV/Vis spectroscope and maximum absorption intensity was found at wavelength 665 nm. Calibration curve was made by plotting the aspect absorption intensity (at 665 nm) as a function of concentration of the diluted solutions (from 10^{-6} to 10^{-5} mol L^{-1}).

Light interaction in a material is explained in Lambert-Beer law as given in Equation 2-17, where light transmission (T) is related to concentration of solution. When absorbance (A) is defined as $-ln(I/I_0)$ as written in Equation 2-18, A is in a linear relationship with concentration

(C) as expressed in Equation 2-19. With this principle, MB concentration was calculated from the UV/Vis absorbance intensity (determined with UV/Vis spectrometry V-570, JASCO, at 665 nm corresponding to the maximum absorbance by MB) with knowing the calibrated linear relationship slope.

Lambert-Beer law:

$$Tsm. = \frac{I}{I_0} = e^{-\varepsilon l C} \tag{2-17}$$

$$Abs. = -ln(\frac{I}{I_0}) = \varepsilon l C \tag{2-18}$$

where I_0 and I are the intensity of incident and transmitted light, *Tsm.* is the transmittance, *Abs.* is the absorbance, ε is the molar extinction coefficient, l is the light path length and C is the solution concentration.

Then,

$$C = \frac{Abs.}{k} \tag{2-19}$$

where C is the solution concentration, *Abs* is the absorbance and k is the factor as $k = \varepsilon l$.

In order to characterize the photocatalytic activity of TiO_2-Al_2O_3 composite membrane M100 and M800 in diffusion conditions, degradation tests using methylene blue (MB) in water solution were performed in a lab-scale diffusion cell. TiO_2-coated membrane was integrated in middle of the diffusion cell with photoactive layer facing to the reception side. The ceramic support was also tested under the same conditions to check the self-photolysis contribution.

The diffusion cell (seen in the photo of Figure 2-16) consisted of two borosilicate glass tanks of volume 90 mL separated with the flat membrane of membrane surface area equal to 12.56 cm^2. As a remark, it can be noted that borosilicate glass cuts most of the radiation under 400 nm and, considering the emission spectrum (Figure 2-11), better performance could be expected using a quartz cell (or a source emitting at higher wavelength, as a solar simulator).

The feed tank contained the aqueous solution of MB ($C_0 = 10^{-4}$ mol /L); the reception tank was initially filled with pure water. After a first stage with a contact time of one day in order to saturate the pore surface in the membrane with adsorbed organic molecules, the feed and reception tanks were replaced by fresh aqueous solution and pure water respectively. Starting time ($t = 0$) was accounted immediately. Equivalent duration of alternative period of 1 h in the absence of UV irradiation and of 1 h in the presence of UV irradiation was operated. Increase of organic concentration in the reception tank can be caused by diffusion in the un-irradiated period, whereas, decrease of the concentration can be found due to photo-degradation in spite of continuous diffusion transport. The UV irradiation was applied at a distance of 20 cm from the anatase-coated side of the membrane placed in contact with the reception solution. UV specific power and wavelength were 35 W m^{-2} and 365 nm, respectively.

Fig. 2-16 Photos of the diffusion test with UV lamp off (up) and on (bottom).

Three samples of TiO_2 layer (a few µm thick) coated ceramic membrane were prepared from optimal PECVD process combined with post-annealing. They were examined in the diffusion test using MB feed solution of initial concentration 1×10^{-4} mol L^{-1}. Two samples of TiO_2 skin (hundreds of nm thick) coated ceramic membrane were also investigated in the same way. Each of the samples was tested three to four times to investigate reproducible performance.

3.3 Material and method for membrane performance in photocatalytic membrane reactor (PMR)

Membrane performance in terms of permeation ability and photocatalytic property has been investigated performing dynamic tests (differential pressure ΔP in the range 0.1 – 1.0 bar) with TiO_2-coated ceramic membranes integrated in a PMR process. Two kinds of PMR were used. In the first configuration (lab-scale) implemented at ITM-CNR (University of Calabria, Rende, Italy), 60 mL solution was circulated in the loop of the PMR system with permeation returning to the feed. In the second configuration (pilot-scale) implemented at IEM (University of Montpellier, France), 3 L solution was running in the PMR system with permeation separating away from the system.

Before any photocatalytic performance test, volume flux of water J_{water} (L m^{-2} s^{-1}) through the prepared membrane was measured at different pressure ΔP as calculated in Equation 2-20:

Water flux through the membrane:

$$J_{water} = \frac{V_{water}}{\Delta t \times S} \qquad (2\text{-}20)$$

where J_{water} is flux of water through the membrane, V_{water} is the permeated volume of water (V = 0.05 L), Δt is the duration measured for 0.05 L water flowing through and S is the membrane surface area (S = 0.126 m^2).

3.3.1 Lab-scale PMR (ITM-CNR)

Acid orange 7 (AO7) from Sigma-Aldrich (Germany), IUPAC name sodium 4-[(2E)-2-(2-oxonaphthalen-1-ylidene)hydrazinyl]benzenesulfonate, has been chosen as the model compound in the lab-scale PMR test. Molecular formula of AO7 is $C_{16}H_{11}N_2NaO_4S$ and its molar mass 350.32 g mol^{-1}. Its chemical structure is presented in Figure 2-17. Absorbance spectrum of AO7 molecules in water was recorded with UV/Vis spectroscopy and maximum absorbance intensity was found at wavelength 485 nm. Calibration was made by plotting absorbance intensity at 485 nm as function of concentration of AO7 solution (from 10^{-6} to 10^{-5} mol L^{-1}).

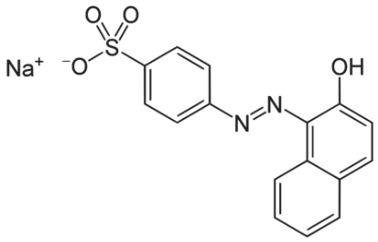

Fig. 2-17 Chemical structure of acid orange 7 (AO7).

Membrane cell was homemade and it was built with cross-flow configuration as shown in Figure 2-18. It was fitted for membrane disk with diameter 47 mm and thickness 1 mm. A window made of quartz with diameter 35 mm was fixed on the top of the cell to access UV source. Due to coverage of O-ring on membrane for sealing purpose, the active surface of membrane (in contact to the solution) was of diameter 40 mm.

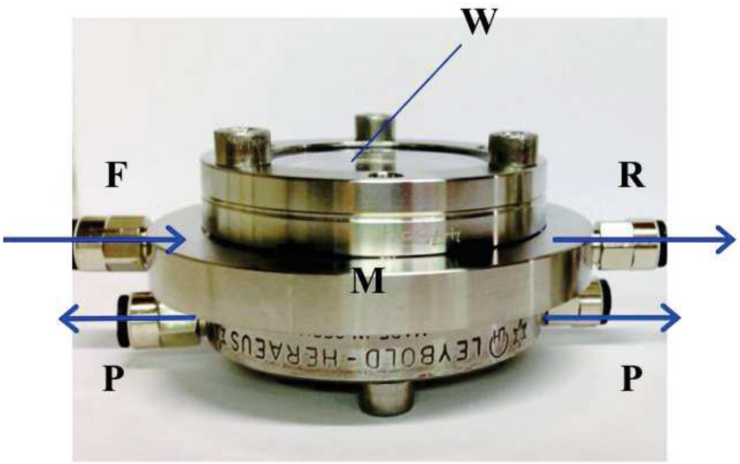

Fig. 2-18 Photo of membrane cell used in the pilot-scale unit, with a quartz window (W), the flat membrane disk (M) with the titania-coated side on the feed side (F), the retentate (R) and the permeate (P) returned to the feed container.

A graphic presentation and a photo of the lab-scale PMR are shown in Figure 2-19 and Figure 2-20. Teflon tubes were used as the solution flowing and connecting between the feed and reactor compartments. A peristaltic pump was employed for solution circulation avoiding external contaminant to the aqueous solution. Both retentate and permeate were recycle to the feed tank as a cycling loop. The dead-end loop was designed because permeability flux through the membrane was fast. Transmembrane pressure (ΔP) could be increased with a valve on Teflon tube. UV lamp was placed on the top of the membrane cell just on top of the glass window. Photodegradation measurement started as the UV lamp being switched on. In total initial volume of 60 mL was used as the feed and sampling solution of 1.5 mL was taken from he feed tank every 10 minutes. The solution was analyzed with its absorbance at λ = 485 nm in UV/Vis spectrometry. The analyzed solution was wasted then. Mass balance is considered throughout the process lasting for 2 hours.

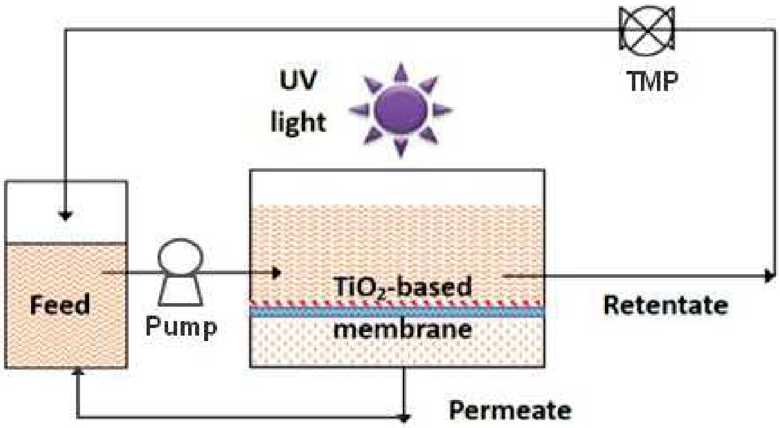

Fig. 2-19 Lab-scale PMR with permeation circulating in the loop.

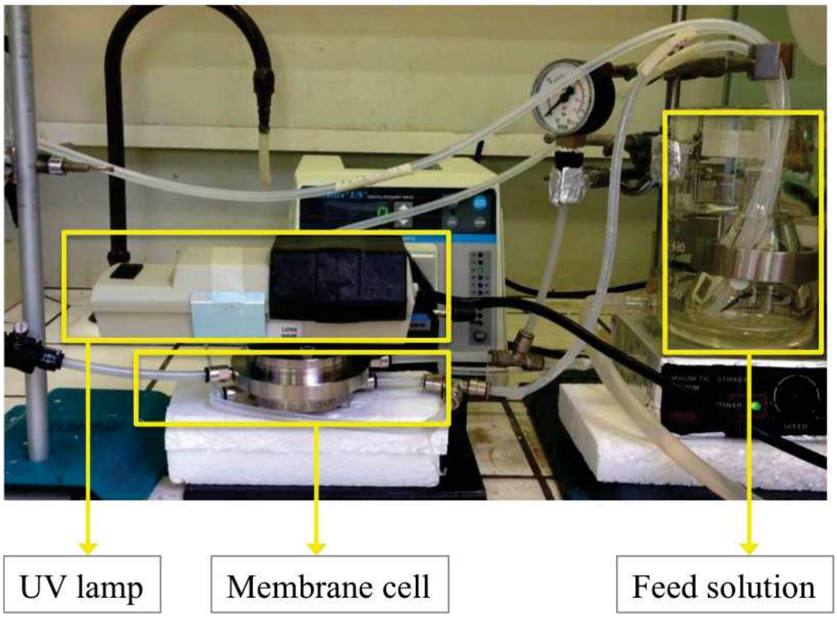

Fig. 2-20 Photo of the lab-scale PMR apparatus with a dead-end cycling.

An alternative configuration of the membrane cell was worked with TiO_2 layer in contact with the feed solution as schematically presented in Figure 2-21. The applied pressure on membrane surface of TiO_2 layer could increase sorption capacity on the photoactive layer as in Langmuir's adsorption model. Products and by-products from the organic solute's photodegradation can exist in the permeate flow. In the experiment, retention and permeation solutions are both circulated back to the feed tank (being stirred all the time) throughout the photodegradation test.

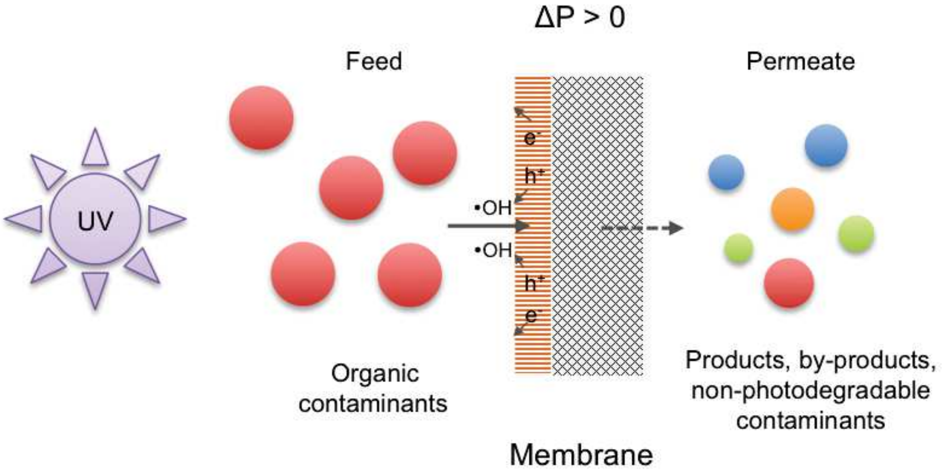

Fig. 2-21 Configuration of TiO_2 photoactive coating in contact with feed solution in photocatalytic membrane reactor (PMR).

Two types of UV source with intensity either 4 W or 500 W were studied in the PMR operation. The low power (4 W) compact UV lamp from UVP (Germany) emits wavelength at 254 nm, 365nm or a combination of both wavelengths. This lamp is lightweight and safe for free hand use. In the experiment, it was placed on contact to the top of membrane cell parallel to the quartz window. The distance between the lamp and TiO_2 surface on membrane was 5 cm. The high-intensity 500 W lamp was form Helios Italquartz srl (Italy), having models as Zs (UVA emission at 360 nm and ozone free) and Zp (including UVA, UVB and UVC emission). The high-intensity lamp had to be operated in a sealed chamber for security reason. The distance between the lamp and membrane was 30 cm.

TiO_2-Al_2O_3 composite membranes LF100 and LF800 were prepared in PECVD process by Master internship student Li, F. Membrane LF100-a and LF100-b were deposited on alumina support of pore size 100 nm with deposition equal to 20 and 40 min respectively. Membrane LF800-a and LF800-b were deposited on alumina support of pore size 800 nm with deposition equal to 20 and 40 min respectively. First of all, water permeance was measured in the lab-scale unit using 60 mL deionized water with constant circulation speed 40 mL min^{-1} at pressure 0.3, 0.5 and 0.7 for M100 membranes and at 0.05, 0.10 and 0.15 bar for LF100 and

LF800 membranes. Then the photodegradation test was operated using 60 ml AO7 solution of initial concentration $C_0 = 1\times10^{-4}$ mol L^{-1} as the feed for each test in lab-scale unit.

By considering the mass balance of AO7 solute (in mol), the remaining amount of AO7 in the feed tank (M_t) can be known as in the Equation 2-21 taking account of the concentration in the feed tank (C_i) and the extrated solution volume (V_i).

The amount of AO7 in the mixing feed tank:

$$M_t = C_i\left(V_0\text{-}\sum V_i\right)+\sum C_i V_i \qquad (2\text{-}21)$$

where C_i is measured concentration of AO7 solution in the feed tank (well-mixed) at instant UV irradiation time (when t = 0 initially $C_0 = 1\times10^{-4}$ mol/L), V_0 is the initial volume of AO7 feed solution (V_0 = 60 ml), and V_i is the extracted sampling volume of AO7 solution (separated from feed tank) at instant time (V_i = 1 mL).

Accordingly, photodegradation rate of AO7 (R_{AO7}) by can be calculated with comparing initial amount and the amoung at instant illumination time as given in Equation 2-22.

Photodegrading conversion rate of AO7 (R_{AO7}):

$$R_{AO7} = \left(1-\frac{M_t}{M_0}\right)\times 100\% \qquad (2\text{-}22)$$

where M_0 is the initial amount of AO7 (mol) in the feed solution and M_t is the total amount of AO7 (mol) in the mixed feed solution at instant UV irradiation time (M_t is know from mass balance calculation in the system as described in Equation 2-21).

The feed tank was kept in a water thermal bath whose temperature was constantly maintained. The peristaltic pump controlled feeding flow rate at 30, 40 and 50 mL min^{-1} and its effect on membrane performance was studied. TMP was experimented from 0.05 to 0.70 bar and its effect on photodegradation efficiency was also evaluated. TMP at 0.3, 0.5 and 0.7 bar was applied when using TiO_2-layer (a few μm thick) coated membrane. TMP at 0.05, 0.10 and 0.15 bar was applied when using TiO_2-skin (hundreds of nm thick) coated membrane. No higher pressure was operated in the membrane process to avoid breaking up the prepared membranes due to the rigidity of ceramics.

In parallel, another model compound, phenol (from Sigma-Aldrich) was tested in the same lab-scale PMR using TiO_2-Al_2O_3 composite membranes LF100 and LF800, which were deposited with 20 and 7 min on alumina support of pore size 100 nm and 800 nm respectively. Phenol has molecular formula C_6H_5OH and molar mass of 94.11 g mol^{-1}; its chemical structure is given in Figure 2-22. PMR operational procedure on feed volume, flow rate and TMP was the same as using AO7 as model compound. However, sampling volume of phenol solution was 0.75 mL each time and quantitate analysis was carried out in high performance liquid chromatography (HPLC).

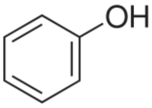

Fig. 2-22 Chemical structure of phenol.

Phenol concentration in aqueous phase was measured by HPLC, Aligent 1100 Series Instrument (Germany) using a GEMINI C18 column by UV absorbance at wavelength 254 nm. The mobile phase consisted of acetonitrile/water/acetic acid solution (volume ratio 50/49/1) feed to a flow rate of 1.0 mL min^{-1}. The column pressure was 140 bar and injection volume was 20 μL. Calibration curve was made by plotting HPLC-UV absorbance at 254 nm as a function of phenol concentration from 10^{-5} to 10^{-4} mol L^{-1}.

In addition, total organic carbon (TOC) was measured for both cases using AO7 and phenol as model compound in liquid phase. The initial and end solutions (each 10 mL) of PMR process were analyzed in TOC aimed at investigating the mineralization degree in the photocatalytic process. The tubes for solution flowing in the loop were tested with Teflon and Nylon materials in order to avoid carbon contaminant.

3.3.2 Pilot-scale PMR (IEM-UM)

Continuous experiments on membranes M100 and M800 were performed in dynamic conditions under applied pressure using a homemade tangential filtration pilot plant with the specific membrane surface area 12.56 cm^2 with that of the diffusion cell (discussed in session 3.2.2). The circulation speed of liquid in the filtration loop was fixed at 2 m s^{-1} by means of a circulation pump. Configuration of membrane implantation in the pilot cell is schematically presented in Figure 2-23 with photoactive TiO_2 layer implanted with a contact to permeate solution. In the experiment, retentate solution is circulated back to the feed tank but the permeation solution would be flowing separately away from the feed source.

By performing such reactor configuration, organic solutes that could pass through the porous membrane could be mineralized into final products as water and carbon oxide due to photocatalysis effect with UV illuminating. Yet low-level polluted solution is normally required as the feed using this configuration since the contact time between transported organic contaminants and TiO_2 surface is instant as the permeate is flowing away from the loop.

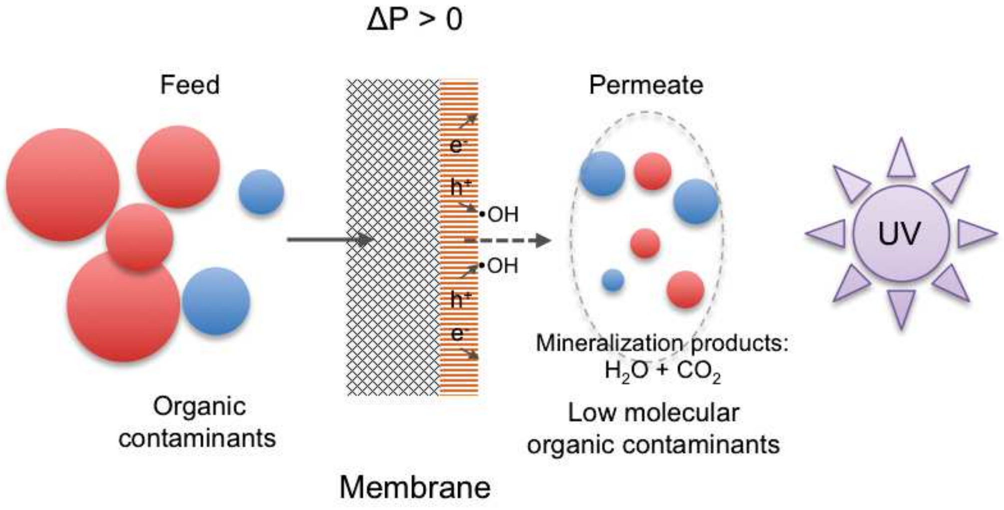

Fig. 2-23 Configuration of TiO_2 photoactive surface in contact with permeate solution in photocatalytic membrane reactor (PMR).

Model compound (methylene blue), TiO_2-Al_2O_3 composite membranes and UV lamp consisted in the pilot-scale unit were the same ones used in the previous diffusion test (seen in session 3.2.1 in this chapter). Configuration of the cross-flow membrane cell used in the pilot is schematically presented in Figure 2-24.

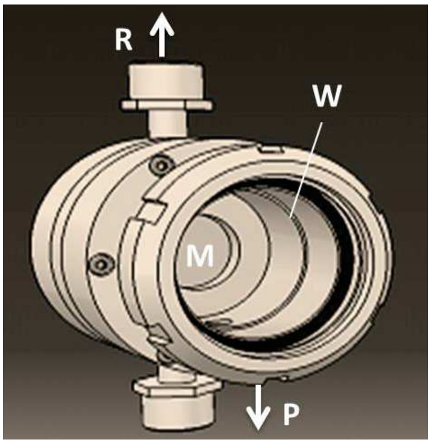

Fig. 2-24 Membrane cell of the pilot-scale unit, with a borosilicate window (W), the flat membrane disk (M) with the titania-coated side on the permeate side, the retentate (R) returned to the feed tank in the pilot loop, and the permeate (P) extracted with the tube from the membrane cell.

Schematic presentation and a photo of the pilot-scale PMR are both given in Figure 2-25 respectively. A vertically positioned membrane cell was implanted since the feed tank and metal tubes for liquid flowing were constructed in a up-and-down streaming configuration. The pilot set-up was more space-saved in this arrangement. Compressed air was introduced to the feed tank to increase the pressure in the closed system. Transmembrane pressure (TMP) worked from 0.25 to 0.75 bar in the experiment (no higher due to the risk of breaking the ceramic membrane). Retentate was recycled to the feed while permeate was separated apart.

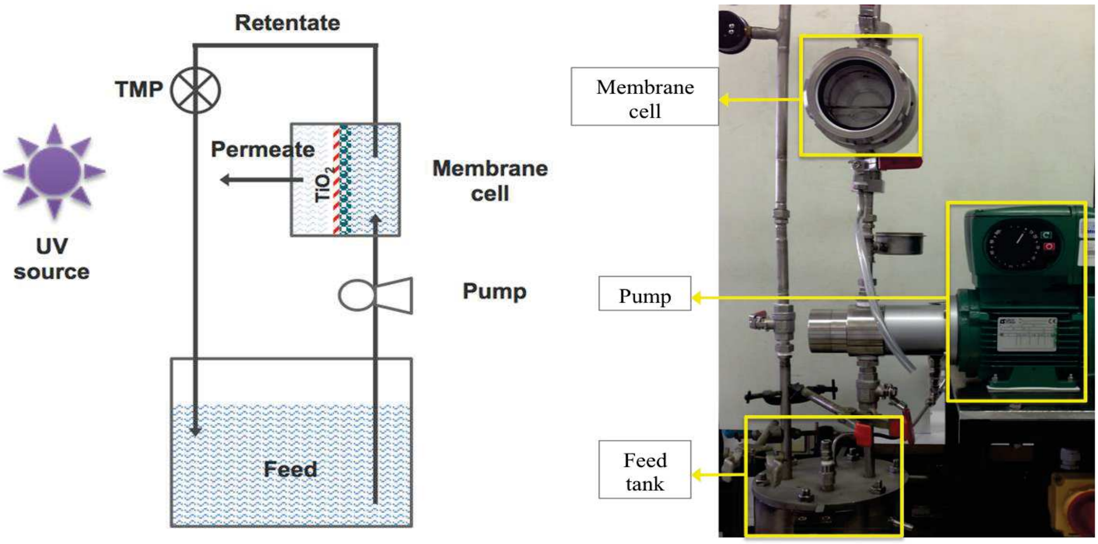

Fig. 2-25 Pilot-scale PMR: schematic graph (left) and photo (right).

Both membrane types of M100 and M800 were experimented in the pressure-dirven photocatalytic membrane process using the pilot-scale unit. First of all, pure water permeance through the membranes was measured under pressure from 0.25 to 0.75 bar. Then the photodecomposition tests were operated with the CLEO UV lamp with a distance 20 cm to the membrane cell's window glass. 2.5 L feed solution for each running test. Initial concentration of MB feed solution $C_0 = 3.2 \times 10^{-7}$ and $C_0 = 1.25 \times 10^{-7}$ mol L^{-1} has been respectively used for membrane M100 and M800 with constant $\Delta P = 0.25$ bar in the process. UV illumination is continuously supplied from the permeate side. Concentration of the permeate solution (C_{pilot}) was analyzed each 5 minutes with the solution absorbance at λ = 485 nm. One photodegradation test completed when 2.5 L feed solution consumed up. Three repetition tests for one membrane were made to prove performance stability. And for each type of the TiO_2-coated membranes, duplicate samples were examined in the PMR process to confirm on reproducibility.

In the dynamic conditions, concentration of MB in the feed (C) leading to a complete photodegradation is equal to δ_{MB} over water flux (J_{water}) as $C = \delta_{MB}/J_{water}$, where δ_{MB} parameter is known from the diffusion experiment. Then the expected photodegradation ratio (R_{Exp}) can be assumed with comparing C and C_0 (initial concentration in the pilot) as described Equation 2-23.

Expected photodegradation rate (R_{Exp}):

$$R_{Exp} = \frac{C}{C_0} \times 100\% = \frac{\delta_{MB}/J_{water}}{C_0} \times 100\% \tag{2-23}$$

where R_{Exp} is the expected photodegradation rate of MB, C_0 is the concentration of MB feed in the pilot and C is theoretical concentration dependent on δ_{MB} parameter (photodegrading capacity of the membrane) and J_{water} is the water flux through the membrane at ΔP.

In the experiment using the pilot-scale unit, photodegrading performance was evaluated on membranes M100 and M800. The experimental degradation rate of MB (R_{MB}) by the illuminated membranes was obtained as Equation 2-24.

Experimental photodegrading conversion rate (R_{MB}):

$$R_{MB} = \left(1 - \frac{C_{piLot}}{C_0}\right) \times 100\% \tag{2-24}$$

where R_{MB} is the measured conversion rate in the pilot, C_0 is MB initial concentration of the feed in the pilot and C_{pilot} is measured concentration of permeated MB solution through the membrane under continuous UV irradiation.

Information on all the UV lamps used in the photocatalytic tests is summarized in Table 2-7. Radiance intensity (referring the amount of photons emitted per unit surface area) from the powered UV lamp was measured with a radiometer at a distance corresponding to the distance between lamp and glass window on the membrane cell.

Table 20-7 Summary of UV lamp parameters (applied in the experiments).

UV lamp	Radiance intensity (measured by radiometer in lab)	Radiating wavelength	Manufacturer
CLEO compact UV lamp	50 W m^{-2}	355 nm	Philips (Netherland)
UV polymeration equipment Zp	760 W m^{-2}	180 nm – visible	Helios Italquartz srl (Italy)
UV polymeration equipment Zs	760 W m^{-2}	360 nm	Helios Italquartz srl (Italy)
Compact UV lamp	18 W m^{-2}	365 nm or 254 nm	UVP (Germany)

On the basis of the experimental details presented in this chapter, physico-chemical and functional properties of the films have been investigated. Films properties will be presented and discussed in the following chapters.

Chapter III Physico-chemical properties of TiO_2 material

PECVD preparation approach of amorphous TiO_2 thin film has been optimized with substrate temperature (T_s), partial pressure of argon + precursor, plasma distance and RF power intensity. Characterization of the synthesis material is explained in this Chapter. Phase transformation of TiO_2 from amorphous to anatase is attained by post-annealing treatment, which has been decided with the crystallization kinetic analysis.

1 Optimization on PECVD operating conditions

Plasma deposition process was initiated to prepare TiO_2 thin film using the PECVD apparatus presented in chapter 2. First, substrate temperature (T_s = 50 – 250 °C) was studied with its effect on TiO_2 deposition rate. For this study, partial pressure of argon and precursor ($P_{Ar+TTIP}$), partial pressure of oxygen (P_{O2}), RF discharge power and deposition duration (t_d) were maintained constant. Secondly, $P_{Ar+TTIP}$ was enhanced and t_d was prolonged in order to increase deposited TiO_2 thickness. Parallel, the influence of $P_{Ar + TTIP}$ and plasma distance (d_p) on Ti-O abundance and thickness homogeneity was investigated. Finally, optimized parameters T_s, $P_{Ar+TTIP}$ and d_p in PECVD process have been determined.

1.1 Effect of substrate temperature (T_s)

Amorphous TiO_2 thin film was obtained as substrate temperature T_s restrained below 250 °C in our applied PECVD process. Preliminary depositions were made with varying T_s (50 – 250 °C) when the other synthesis parameters kept as constant as possible. Partial pressure of argon + precursor ($P_{Ar+TTIP}$) was maintained in the range 0.15 – 0.16 mbar (fluctuating slightly) and partial pressure of O_2 (P_{O2}) was maintained at 0.17 mbar. Electric RF power was slightly fluctuating in the range 60 – 65 W (with a fixed forwarding power equal to 250 W). Plasma distance (d_p), adjusted by the distance between the upper and bottom electrode, was maintained at 3 cm. With these mentioned PECVD operating conditions, TiO_2 films were deposited on silicon substrate and noted as samples B1 – B5 (seen in Table 3-1).

Table 3-1 PECVD operating conditions for samples B1 – B5 (TiO_2 on silicon substrate).

Sample No.	Substrate temp. T_s (°C)	Partial pressure $P_{Ar+TTIP}$ (mbar)	Partial pressure P_{O2} (mbar)	RF Power (W)	Plasma distance d_p (cm)
B1	50	0.150 mbar	0.17	62	3
B2	100	0.162 mbar	0.17	63	3
B3	150	0.151 mbar	0.17	61	3
B4	200	0.163 mbar	0.17	61	3
B5	250	0.163 mbar	0.17	63	3

A photo of the five deposited TiO_2 samples is presented in Figure 3-1. Each sample was cut straight in the centerline for SEM cross-sectional scanning for thin film's morphology observation and thickness measurement.

Fig. 3-1 Photo of silicon-supported TiO_2 thin films (from B1 to B5) made at PECVD T_s = 50, 100, 150, 200 and 250 °C respectively.

In order to examine the thickness uniformity, cross-sectional SEM analysis was carried out along the straight centerline from the left end to the right end. Thickness was notified in SEM spot by spot with each 0.2 cm scanning (in total 4 cm length as the deposition diameter). Exemplified SEM images (taken around the center position) of sample B1, B3, B4 and B5 are presented in Figure 3-2. It is apparent that PECVD TiO_2 deposit has micro-columnar structure. Moreover, uniformed TiO_2 cluster in dimension ca. 10 nm (estimated from SEM) is observed as consisting block in the thin films. The porosity of PECVD TiO_2 thin film, inherent to the columnar microstructure, is certainly advantageous for catalytic membrane application in terms of large specific surface and high permeability.

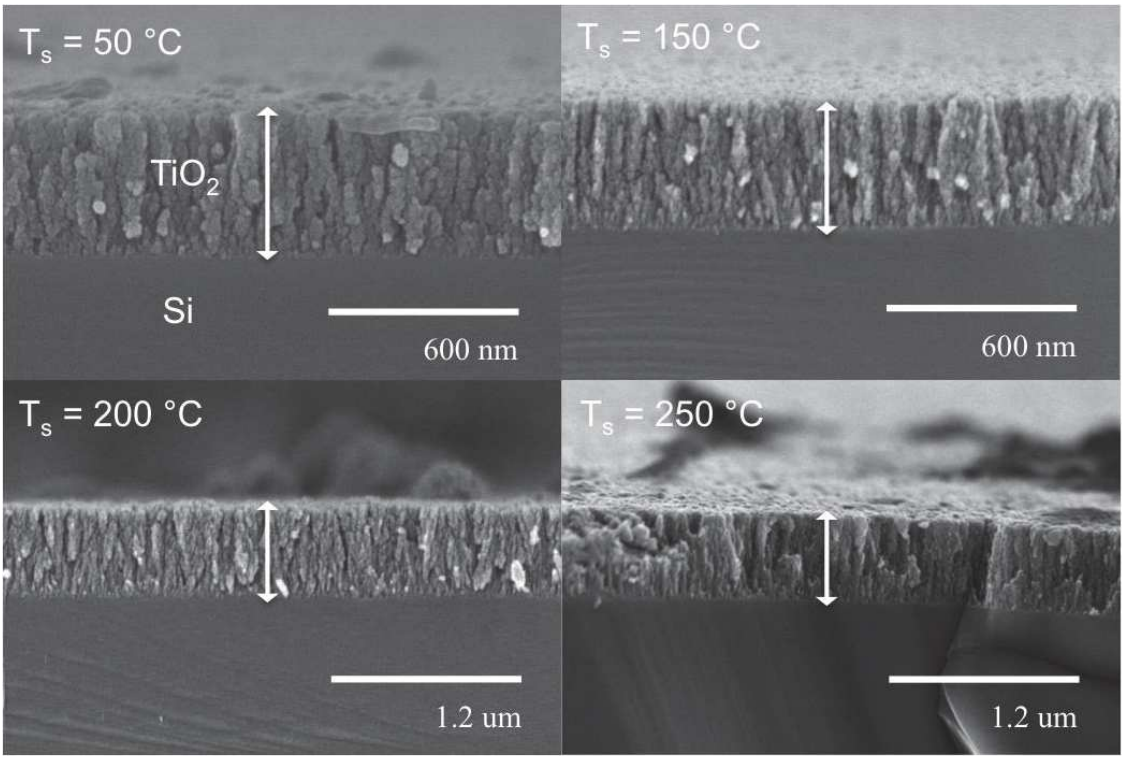

Fig. 3-2 TiO_2 thickness measured in cross-sectional SEM investigation for samples B1 to B5 deposited at different substrate temperatures from 50 to 250 °C.

Thickness profile of TiO_2 (on surface of diameter equal to 4 cm) is plotted along with the coordinate of the substrate coordinate as presented in Figure 3-3, where the coordinate position at 2 cm is the center of the substrate. It can be seen that the deposition thickness is symmetric as consistent to observation in the photo of the samples (shown in Figure 3-1). Due to the geometry of gas inlet from a drilled hole in upper electrode, TiO_2 layer was deposited thicker in the center (just under the gas entrance) and thinner surrounding the edge (toward to the outlet of the reactor). Moreover, TiO_2 grew faster on surface at higher T_s (200 and 250 °C) than that at lower T_s (50 and 150 °C). However, thickness variance (on depositing surface 12.56 cm^2) obtained at higher T_s was larger than that of lower T_s as seen in Figure 3-3. The best thickness uniformity and has been attained for sample B3 made at PECVD T_s = 150 °C in comparison to the other samples including B4 and B5.

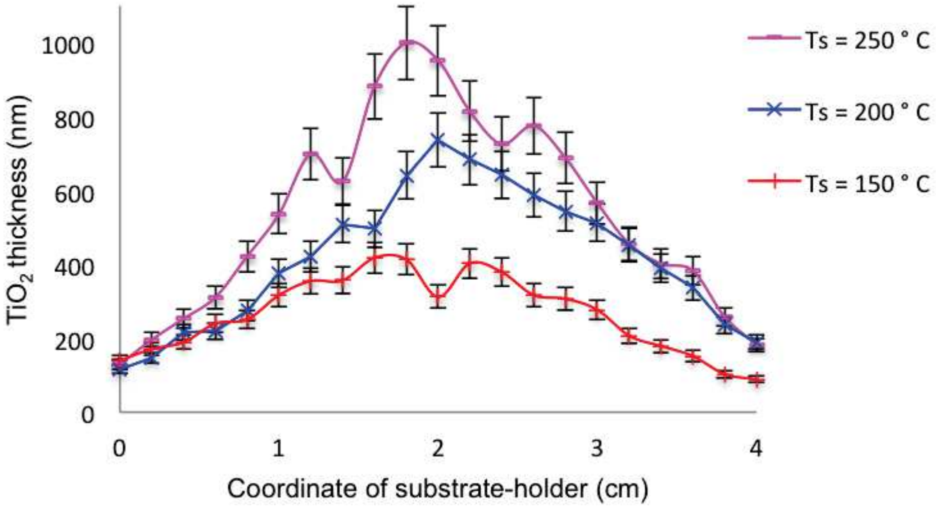

Fig. 3-3 Thickness profile of TiO_2 thin films versus the coordinate of substrate (at 2cm is the center of the electrode) prepared with PECVD T_s from 150 – 250 °C (the bars indicating SEM instrumental error for thickness measurement).

Mean thickness is known by averaging the profiled thickness values of each sample and the results of B1 to B5 are listed in Table 3-2. The standard deviation (given in percentage) is indicated nest to the mean thickness as a notification for thickness homogeneity. In the same table, TiO_2 deposition rate (nm min^{-1}) known by dividing the thickness by deposition duration (equal to 15 minutes in this study) is also given.

Table 3-2 TiO_2 film growing rate at different PECVD T_s (50 – 250 °C).

Sample No.	**Substrate temp. T_s (°C)**	**Mean TiO_2 thickness (nm)**	**TiO_2 deposition rate (nm min^{-1})**
B1	50	277 (± 20%)	18.4
B3	150	266 (± 20%)	17.7
B4	200	415 (± 23%)	27.7
B5	250	536 (± 25%)	35.7

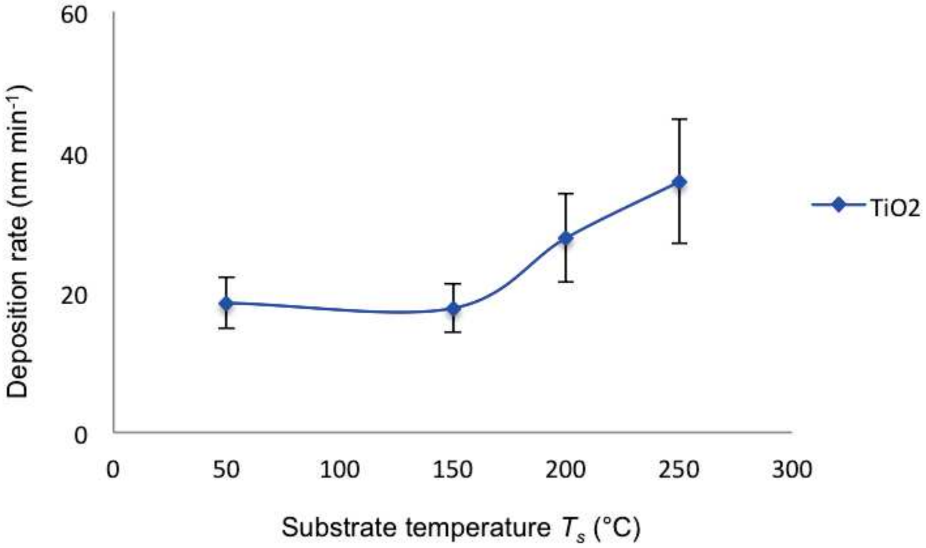

Fig. 3-4 Deposition rate at various substrate temperatures in the PECVD process (the bars indicating for the standard deviation of thickness on deposited surface 12.56 cm^2).

TiO_2 grew in a velocity more or less than 18 nm min^{-1} (± 20%) in both case of T_s = 50 and 150 °C, whereas, the deposition rate increased to 28 nm min^{-1} (± 23%) at 200 °C and 36 nm min^{-1} (± 25%) at 50 °C. The deposition is generally accelerated yet less averagely when T_s is increased in the range of 50 – 150 °C as the aspect deposition rate (with standard deviation indicated) presented in Figure 3-4.

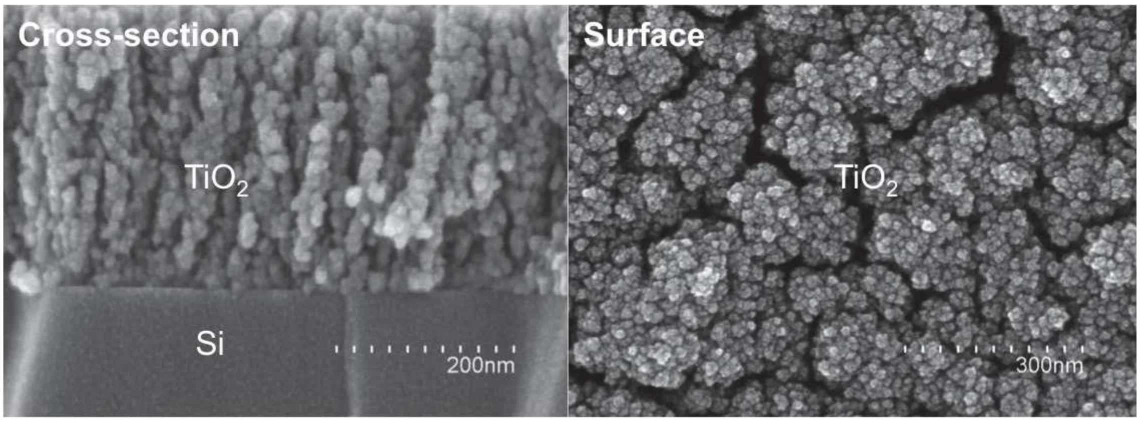

Fig. 3-5 Morphology of PECVD TiO_2 deposit on silicon substrate at T_s = 150 °C (sample B3): SEM cross-section (left) and surface (right) images.

Zoomed SEM images of the sample B3 (deposited at T_s = 150 °C) both from the side view and the top view are displayed in Figure 3-5. Micro-columnar porous structure and the uniform TiO_2 nanoparticles are clearly observed the presented images. Regarding to the reasonable deposition rate and the smoothest thickness of sample B3, T_s = 150 °C has been determined as the optimal substrate temperature in the following PECVD studies.

1.2 Influence of partial pressure ($P_{Ar+TTIP}$) and plasma distance (d_p)

PECVD parameters including partial pressure $P_{Ar+TTIP}$ and plasma distance d_p affect the density of gaseous molecule and ion energy distribution in the reactor. In another word, the stability of plasma process and properties of deposited film have been studied with modifying these two conditions. Accordingly, samples ZJ1 – ZJ9 of TiO_2 deposit on silicon were prepared by varying $P_{Ar+TTIP}$ (0.155, 0.185 and 0.225 mbar) and d_p (3.0, 2.5 and 2.0 cm), and maintaining other PECVD parameters constant as indicated in Table 3-3. Thickness profile (from SEM investigation) and chemical composition (from FTIR analysis) of theses samples has been analyzed and will be discussed in the following two sections in this session.

Table 3-3 PECVD conditions (varying $P_{Ar+TTIP}$ and d_p) for TiO_2 samples ZJ1 – ZJ9 (on silicon substrate).

Sample No.	**$P_{Ar+TTIP}$ (mbar)**	**Plasma distance d_p (cm)**	**Substrate temp. T_s (°C)**	**Deposition duration (min)**	**RF Power (W)**	**P_{O2} (mbar)**
ZJ1	0.155	3.0	150	20	50	0.17
ZJ2	0.185	3.0	150	20	50	0.17
ZJ3	0.225	3.0	150	20	50	0.17
ZJ4	0.155	2.5	150	20	50	0.17
ZJ5	0.185	2.5	150	20	50	0.17
ZJ6	0.225	2.5	150	20	50	0.17
ZJ7	0.155	2.0	150	20	50	0.17
ZJ8	0.185	2.0	150	20	50	0.17
ZJ9	0.225	2.0	150	20	50	0.17

1.2.1 Effect on thickness homogeneity and deposition rate

Thickness profile of samples ZJ1 – ZJ9 was studied by cross-sectional SEM, operated on deposition centerline spot to spot every 0.5 cm along total length 4 cm (deposition diameter) similar as described in session 1.1. Mean thickness averaged from the film profile is presented in Table 3-4, where standard deviation (in percentage) on depositing surface 12 cm^2 is given in embrace. With variable $P_{Ar+TTIP}$ and d_p and constant T_s (150 °C), RF power (50 W) and duration (20 min), deposited TiO_2 films have thickness in the range 0.5 – 3.5 µm. Thickness deviation varies from ± 7% to ± 35% from one sample to another sample, presenting the deposition homogeneity.

Table 3-4 Mean thickness of samples ZJ1 – ZJ9 (TiO_2 film on silicon substrate) prepared with variable $P_{Ar+TTIP}$ and d_p.

d_p / $P_{Ar+TTIP}$	**3.0 cm**	**2.5 cm**	**2.0 cm**
0.155 mbar	0.75 µm (± 14%)	0.559 µm (± 13%)	0.816 µm (± 35%)
0.185 mbar	0.492 µm (± 14 %)	1.275 µm (± 14%)	1.775 µm (± 30%)
0.225 mbar	1.290 µm (± 7%)	2.880 µm (± 21%)	3.497 µm (± 28%)

It can be seen that the best homogeneity (with the least deviation ± 7 %) was obtained for sample ZJ3 (with the highest $P_{Ar+TTIP}$ and longest d_p), whereas the worst homogeneity (with the largest deviation ± 35 %) was depicted on sample ZJ 7 (with the lowest $P_{Ar+TTIP}$ and shortest d_p). TiO_2 deposition rate (i.e. thickness/ deposition duration) of samples ZJ1 – ZJ9 is plotted in Figure 3-6 with the error bar indicating for thickness deviation so that effect of $P_{Ar+TTIP}$ and d_p on layer homogeneity and deposition rate would be obvious.

As shown in Figure 3-6, higher argon flux leads to faster TiO_2 growth rate due to the increased number of TTIP vapor molecules (driven by argon flux) in the chamber. Shorter plasma distance results in thicker deposits due to the same reason at the scale of the inter-electrodes space (nevertheless this effect is not obvious in the case of the lowest argon flux giving the lowest TTIP concentration whose influence on the film growth rate is certainly slightly dependent on the plasma volume).

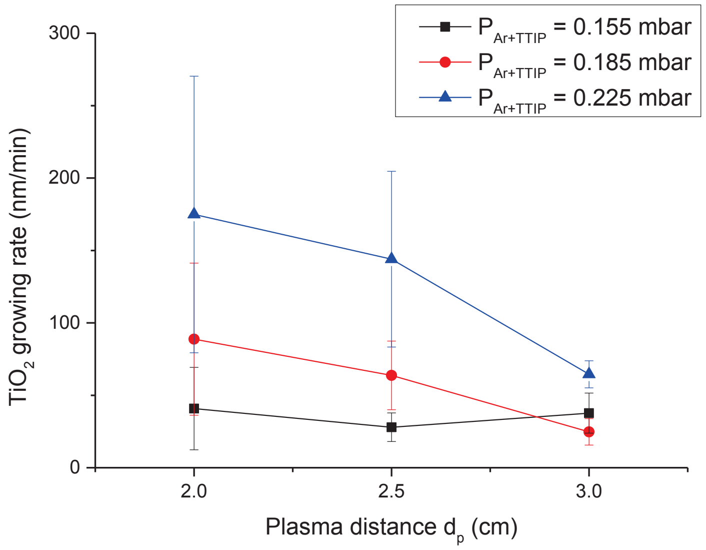

Fig. 3-6 Effect of pressure $P_{Ar+TTIP}$ and plasma distance d_p on TiO_2 deposition rate.

It is interesting to find out that TiO_2 film uniformity greatly depends on the plasma pathway length. Indeed, a longer plasma distance (d_p) produces a smoother layer. It can be explained that a better dispersion of precursor (especially in horizontal scope) would be achieved when the inter-electrode space is wider, since there is more time for molecules to diffuse through the gas phase.

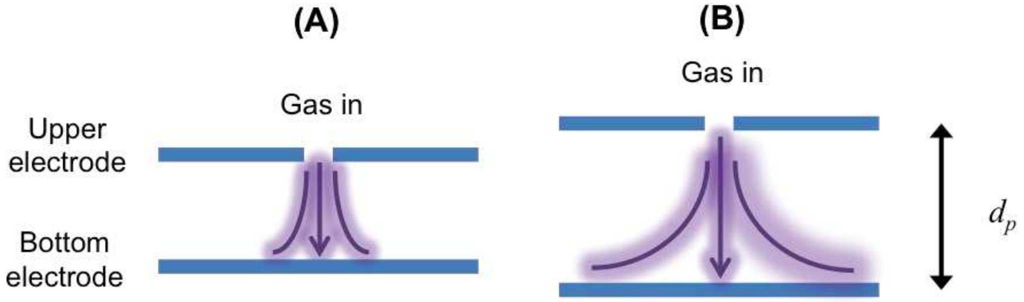

Fig. 3-7 Schematic presentation on gas diffusion through short (A) and long (B) inter-electrode plasma distance (d_p) in PECVD reactor.

A schematic presentation of gaseous molecule diffusion from the gas-in entrance of upper electrode to the substrate at bottom electrode is given in Figure 3-7. The violet shadow in the figure represents a plasma illumination in PECVD process. In addition, the reason for argon flux playing a less substantial role on deposition rate when d_p is long is that a larger space allowing small difference on density change and more time for molecules to diffuse-in and diffuse-out.

1.2.2 Effect on Ti-O abundance per unit volume in the film

Chemical composition of the prepared films at different $P_{Ar+TTIP}$ and d_p has been examined by infrared vibrational spectroscopy. FTIR spectrum of the sample ZJ3 is displayed in Figure 3-8 as one example considering the sample of the smoothest thickness. As seen in infrared spectrum, broad absorbance bands around 3200 and 1600 cm^{-1} are majorly contributed by O-H stretching and H_2O bending vibrations (water molecules are absorbed on the surface). Possible C-H vibration might be overlapped in these broad bands, which could be caused by organic residues originated from the organic precursor. O=C=O vibration (from CO_2 in the air) at 2300 cm^{-1} is observed since the analysis is has been performed in atmosphere.

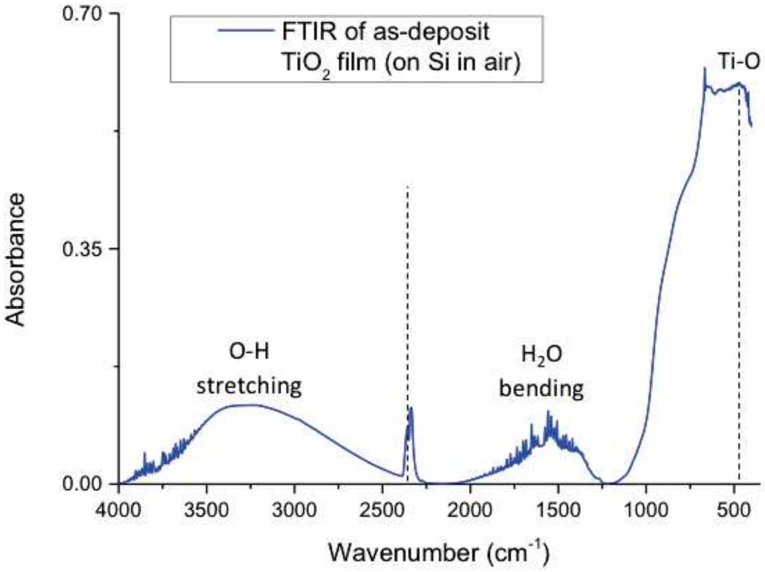

Fig. 3-8 FTIR spectrum of silicon-supported amorphous TiO_2 film (sample ZJ3).

Skeletal Ti-O vibration is detected below wavenumber 1000 cm^{-1}. One study reported that amorphous TiO_2 had characteristic absorption at 730 cm^{-1} (shoulder peak), 520 cm^{-1} (strong peak) and 340 cm^{-1} (strong peak). [198] In our work, a shoulder peak at ca. 700 cm^{-1} and another more intense peak at ca. 500 cm^{-1} have been observed in the PECVD amorphous TiO_2 thin film (seen in Figure 3-8).

The absorbance intensity at 450 cm^{-1} was compared among the samples ZJ1 – ZJ9 from the spectra recorded at the central spot of each deposition, where the thickness was measured in previous SEM study. The wavenumber 450 cm^{-1} is found with a characteristic peak for the annealed TiO_2 samples of anatase phase (will be further explained later). Normalized absorbance intensity at 450 cm^{-1} has been obtained by treating the measured absolute intensity with a factor proportional to TiO_2 thickness. Such factors for samples ZJ1-ZJ9 are listed in Table 3-5.

Consequently, the thickness-independent Ti-O vibration can be compared as plotted in Figure 3-8. It can stand for Ti-O abundance per unit volume in the synthetic film, since absorbance intensity of light is proportional to the number of molecules. So the highest normalized absorbance indicates the richest Ti-O density among samples ZJ1 – ZJ9.

Table 3-5 Normalized absorbance intensity (at 450 cm^{-1}) of TiO_2 thin films prepared with different PECVD parameters of $P_{Ar+TTIP}$ and d_p.

d_p / $P_{Ar+TTIP}$	**3.0 cm**	**2.5 cm**	**2.0 cm**
0.155 mbar	0.818	1.255	2.057
0.185 mbar	1.805	2.037	1.080
0.225 mbar	4.658	1.646	0.756

As presented in Figure 3-9, $P_{Ar+TTIP}$ and d_p have apparent influence on Ti-O abundance in the deposited film (reflected from absorbance at characteristic wavenumber 450 cm^{-1}). With low partial pressure $P_{Ar+TTIP}$ = 0.155 mbar, a small decline of Ti-O composition is discovered when elongating d_p from 2 to 3 cm. In contrast, with high $P_{Ar+TTIP}$ = 0.225 mbar Ti-O composition surged up when extending d_p to 3 cm. With medium $P_{Ar+TTIP}$ = 0.185 mbar, increase of Ti-O composition is found when extending d_p to 2.5 cm and saturation state is then reached when continuously enlarging d_p to 3 cm. It can be explained that decomposition is the rate-limiting step when the pressure is high, whereas, the reactant density is the rate-limiting step when the pressure is low.

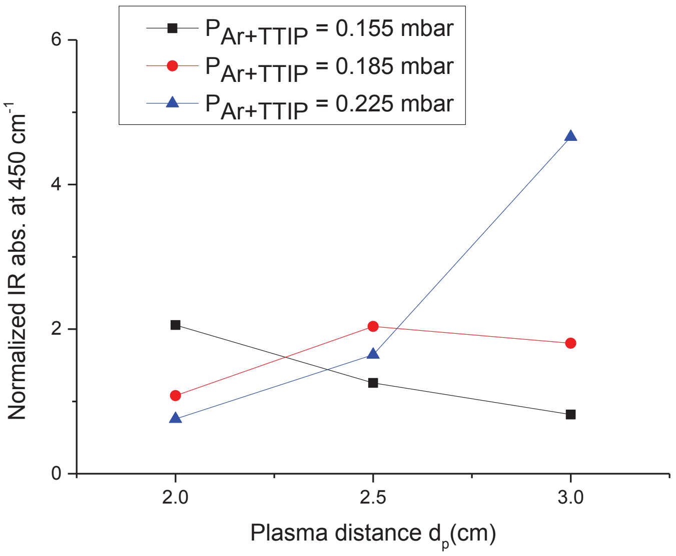

Fig. 3-9 Comparison of Ti-O abundance in thin films by normalized infrared absorbance (at 450 cm^{-1}) of TiO_2 samples ZJ1 – ZJ9.

There is an outstanding increase of Ti-O per unit volume for sample ZJ3 produced with $P_{Ar+TTIP}$ = 0.225 mbar and d_p = 3.0 cm. It is reasonable that denser TiO_2 can be docked when $P_{Ar+TTIP}$ is higher, leading to a larger amount of precursor vapor molecules in the gaseous phase. On the other hand, longer d_p allows more time for decomposition of precursor TTIP and thus organic residues (from the metal-organic precursor) is eliminated from being entrapped in the film. Wider inter-electrode space (i.e. longer d_p) also allows more scope for precursor to diffuse and react in gas phase before reaching the substrate. Eventually, $P_{Ar+TTIP}$ = 0.225 mbar and d_p =3 cm, leading to the richest Ti-O composition can be considered as the optimal PECVD operating conditions, which is consistent with the previous thickness study (session 1.2.1).

1.3 Effect of electric RF power

Radio frequency (RF) power has been applied with real intensity either at 50 W (when working with forwarding power 150 W) or 65 W (working with forwarding power at 200 W). RF power discharge of 50 and 65 W has been studied here to examine its influence of TiO_2 properties, as well as to explore the stability thorough the whole PECVD process.

At the meantime, plasma distance (d_p) was tested again either equal to 2 or 3 cm in order to confirm the configuration effect on Ti-O abundance in the film. As summarized in Table 3-6, samples M1 and M2 were synthesized with 50 W using d_p equal to 2 and 3 cm, respectively. Samples M3 and M4 were made with 65 W using d_p equal to 2 and 3 cm, respectively. Other PECVD parameters were kept constant as T_s = 150 °C, $P_{Ar+TTIP}$ = 0.225 mbar, P_{O2} = 0.17 mbar and t = 20 min as in the optimal protocol.

Table 3-6 PECVD operating conditions for TiO_2 samples M1 – M4 (on silicon).

Sample No.	RF power (W)	Plasma distance d_p (cm)	$P_{Ar+TTIP}$ (mbar)	P_{O2} (mbar)	Substrate temp. T_s (°C)	Deposition duration (min)
M1	50	2	0.225	0.17	150	20
M2	50	3	0.225	0.17	150	20
M3	65	2	0.225	0.17	150	20
M4	65	3	0.225	0.17	150	20

SEM images of samples M1 – M4 are displayed in Figure 3-10. Cracked TiO_2 surface is observed on M1 and M3 when applying short d_p = 2 cm with both power intensity 50 and 65 W. Yet there is no such problem for M2 and M4 when applying d_p = 3 cm. It can be explained that stronger ion density and/or ion bombardment causes intensive stress in the film since the inter-electrode space is small, which leads to the surface cracking.

Thickness profiles of TiO_2 layers of samples M2 and M4 (deposited with constant d_p 3 cm and RF power equal to 50 and 65 W) are plotted in Figure 3-11. At this time, half of deposition in diameter was measured experimentally (from SEM) and the other half was mirrored in symmetry. Mean thickness is obtained as 3.8 µm (± 21%) for sample M2 (deposited with RF power 50 W) and 2.6 µm (± 25%) for sample M4 (RF power 65 W). It is clear that supplying a lower electric RF power equal to 50 W produces a thicker TiO_2 layer.

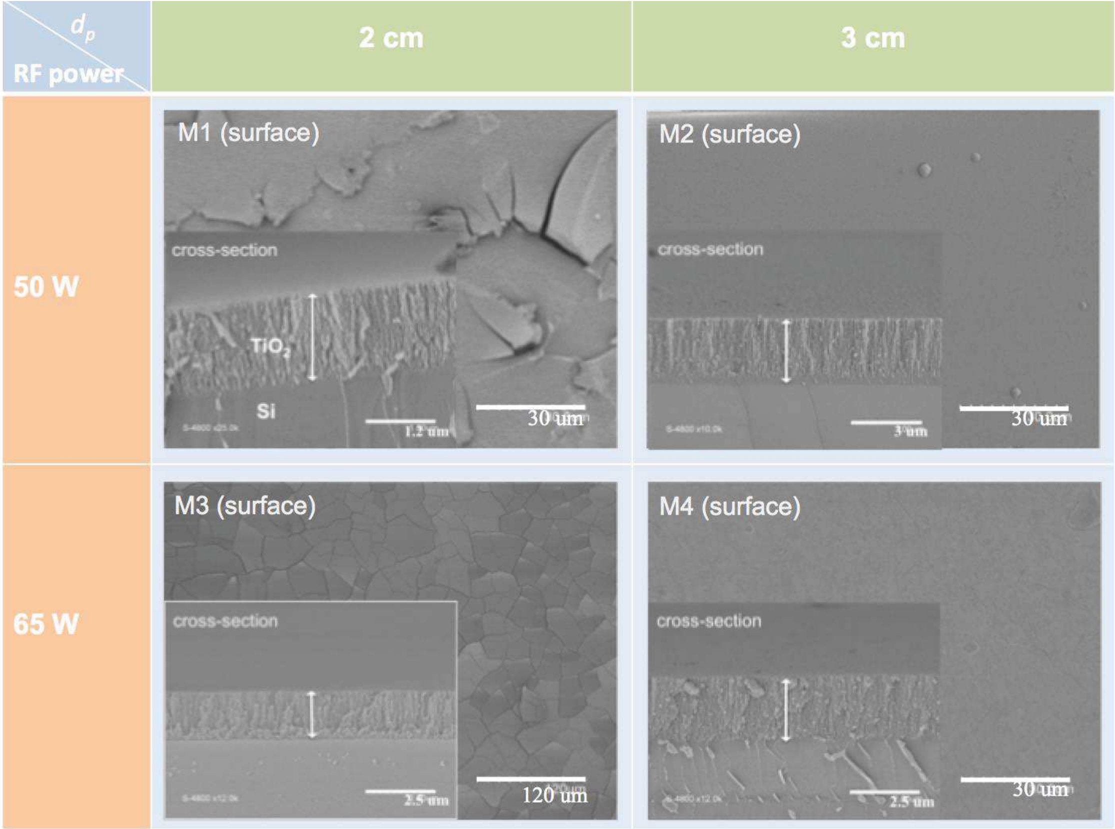

Fig. 3-10 SEM images of samples M1 – M4 (TiO_2 on silicon) prepared with RF power 50 and 65 W and plasma distance 2 and 3 cm.

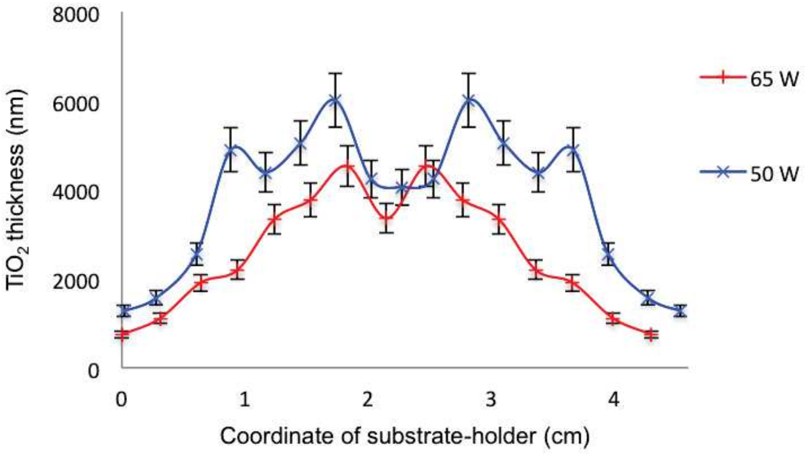

Fig. 3-11 Thickness profile of TiO_2 samples prepared with constant d_p = 3 cm and RF power equal to 50 and 65 W respectively (measured by SEM of 10% instrumental error indicated with the bars).

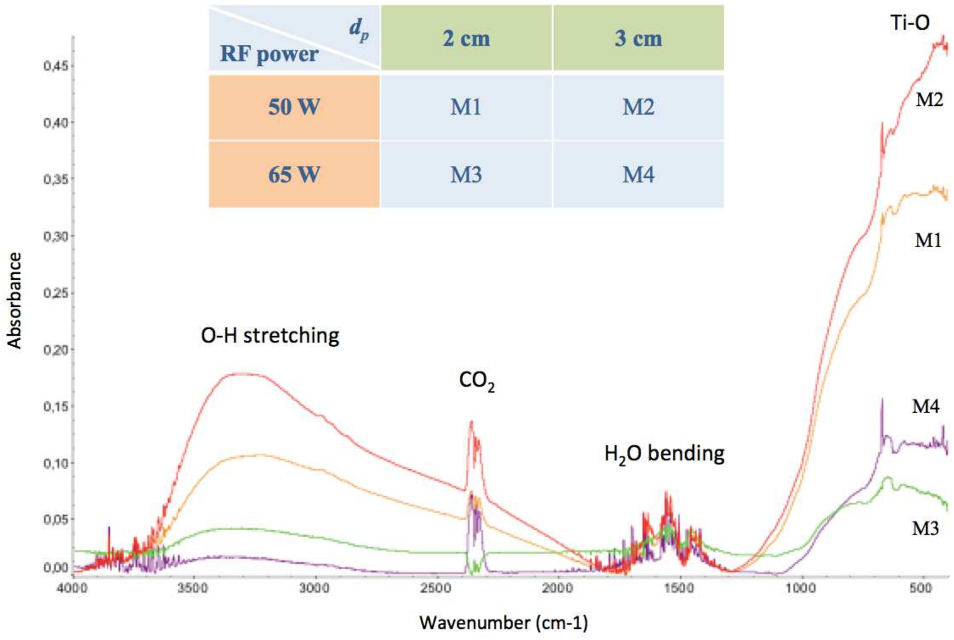

Fig. 3-12 Normalized FTIR spectra (independent from the thickness) of TiO_2 thin films deposited on silicon as samples M1 – M4.

In addition, chemical composition of samples M1 – M4 was examined by FTIR; the corresponding normalized infrared spectra are presented in Figure 3-12. Apparent difference on normalized vibrational absorbance in the range 700 – 500 cm^{-1} (thickness irrelevant) can be witnessed in the figure. Samples M1 and M2 (obtained at 50 W) have more intensive Ti-O abundance than that of M3 and M4 (obtained at 65 W). Besides, applying the same power intensity, sample made with longer d_p = 3 cm has more Ti-O composition than that of d_p = 2 cm. Eventually, power = 50 W and d_p = 3 cm is figured out as the optimized conditions for preparing the sample with the richest Ti-O abundance per unit volume (sample M2).

Concerning the stability PECVD process lasting as long as 20 min, the RF power discharge of intensity 50 W (from a fixed forwarding power 150 W) is preferred over 65 W (from forwarding power 200 W). Indeed, dynamic plasma process could go through more sparkling at 65 W during reaction and/or deposition process. In addition, more severe carbonization of precursor occurred in the gas-in tube at 65 W maybe due to higher gas temperature, which could cause blockage in the gas pathway.

In a summary, optimization work of preparing amorphous TiO_2 thin films in PECVD process has been studied. It is found that optimal substrate temperature T_s is equal to 150 °C leading to a reasonable deposition rate and good thickness homogeneity. Further on, partial pressure of argon and precursor $P_{Ar+TTIP}$ = 0.225 mbar (controlled by argon flux) and plasma distance d_p = 3 cm (i.e. inter-electrode distance) have been determined as optimal values for good thickness uniformity and rich Ti-O abundance. In addition, 50 W (obtained from forwarding power 150 W) has been identified as optimized RF power able to maintain stable plasma process with less carbonization of precursor. Partial pressure of oxygen P_{O2} = 0.17 mbar and deposition duration t = 20 minutes appear as satisfying complementary PECVD parameters.

2 Optimization of post-annealing conditions to develop crystallized films

It has been reported that crystalline TiO_2 material could be deposited spontaneously only when T_s was heated above 450 °C in PECVD process. [25] In our work, optimal T_s = 150 °C has been chosen to prepare TiO_2 films in regarding to feasibility for thermal-sensitive substrate. As the as-grown TiO_2 films were found all in amorphous phase in the work, post-annealing treatment on as-deposit sample was carried out in a furnace in order to crystallize TiO_2 film. The post-thermal treatment was studied both along with increased temperatures (200 – 700 °C) and along with heating duration (1 – 6 h) at 300 °C. In the end, seeding substrate was experimented to investigate its activity on phase transation from amorphous to crystallized phase post-annealing at 300 °C.

2.1 Film crystallization as a function of temperature (T_p)

High-temperature X-ray diffraction (HT-XRD) analysis in the range 200 – 700 °C was made on one optimal silicon-supported TiO_2 film. The heating process is set as non-stop mode with heating rate 1 °C min^{-1}. X-ray diffraction pattern was recorded in-situ on the heated TiO_2 sample with every increased 100 °C. Each XRD measurement took 25 minutes to complete. HT-XRD patterns in the range 200 – 700 °C on the same sample are displayed in Figure 3-13.

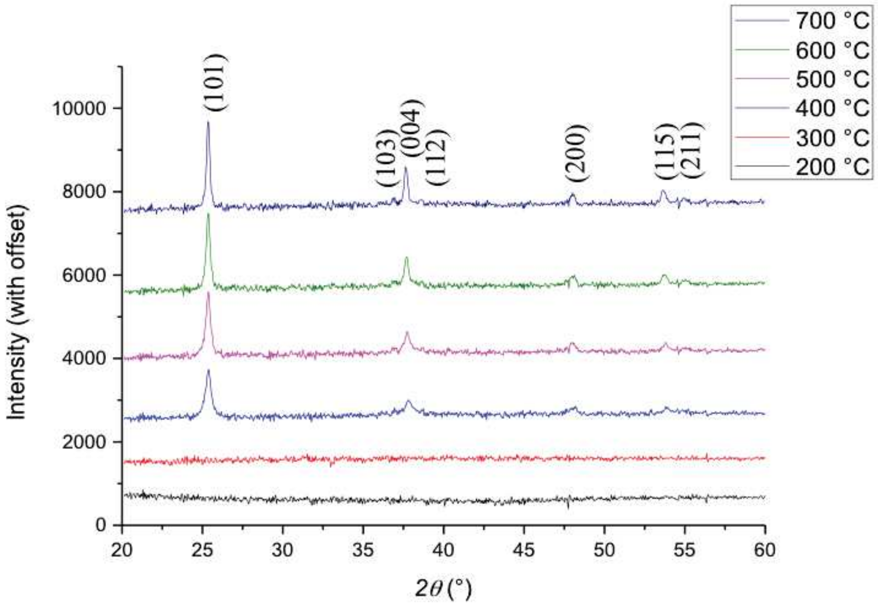

Fig. 3-13 High-temperature XRD analysis heating from 200 to 700 °C on silicon-supported TiO_2 thin film.

It is clear that crystallization is observed in TiO_2 film for post-annealing temperature at least equal to 400 °C in HT-XRD analysis. In another word, T_p = 400 °C is the critical temperature for crystallization when as in non-stop heating mehod. The developed crystalline structure was found as anatase phase by matching the diffracted pattern to the database (Anatase TiO_2 phase, JCPDS No. 89–4921). The main diffraction peaks of anatase phase at 2θ = 25.4°, 37.9°, 48.1°, 54.0° and 55.1° have been detected on the 400 °C-annealed TiO_2 film, which represent the crystal planes of anatase (101), (004), (200), (115) and (211) respectively. Enhancement of the peak intensity undergoes gradually when T_p continues to increase from 400 till 700 °C. It implies that the development of anatase crystallinity has taken place due to higher heating temperature. Moreover, pure anatase phase was maintained in TiO_2 film by heating as high as 700 °C. In some other work, it is reported that rutile sometimes has been formed when post-annealing above 600 °C was carried out. [14]

On the other hand, as-grown TiO_2 material (on silicon) was scrubbed away from the substrate for thermal analysis in the range 25 – 1000 °C. About 10 mg TiO_2 powder was collected from three optimized PECVD as-deposit samples. The amorphous TiO_2 powder went through thermo-gravimetric analysis (TGA) and differential scanning calorimetric (DSC) analysis by heating it to 1000 °C in the air (with heating rate 1 °C min^{-1}). Weight-loss curve was measured from TGA by tracking the mass of sample. Heat-flow curve was recorded from

DSC by comparing the heat exchange between the sample and reference. The two curves have been measured at the meantime and are presented in Figure 3-14.

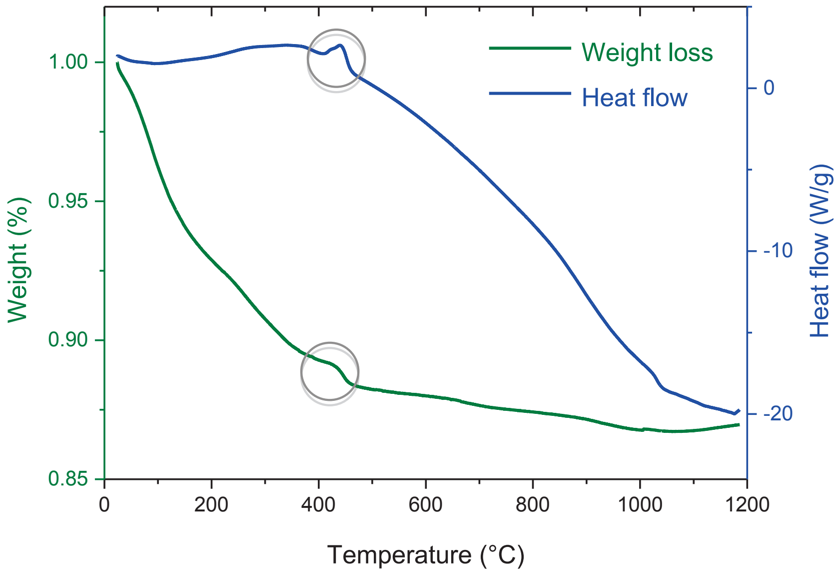

.

Fig 3-14 Thermal analysis by heating as-deposit amorphous TiO_2 material from 25 to 1000 °C.

As seen in Figure 3-14, the heat-flow curve (in blue color) witnesses an exothermic peak at 400 – 450 °C (highlighted with a grey circle). It is supposed as relevant to TiO_2 phase transition from amorphous to crystalline structure. When atoms are rearranging from random to organized positions they would release energy in heat since it is exothermic process when the entropy is reduced. At the meantime, the weight-loss curve (in green color) detects a secondary loss of mass at 400 – 450 °C (highlighted with a grey circle) that follows the first weight reduction (about 10% drop). Remove of the weight by heating below 450 °C should be mainly caused by dehydration, dehydroxylation and removal by oxidation of residual organics in the synthetic film. A secondary weight loss (a very small amount) occurring at 450 °C could be explained by further release of 'internal' organic residues entrapped in Ti-O framework. The liberation of "deep" trapped organic groups was realized simultaneously when crystallization took place. The organic residues in the film were generated from the metal-organic precursor TTIP during PECVD reaction.

2.2 Film crystallization as a function of heating duration (t_p)

Great efforts have been made to discover the possibility to crystallize TiO_2 film below 400 °C. At first, T_p was reduced to 300 °C and staying duration at 300 °C was prolonged to a few hours in post-annealing treatment. High-temperature XRD (HT-XRD) analysis was made at T_p = 300 °C lasting for 6 hours (with heating rate 1 °C min^{-1}) on one optimal silicon-supported TiO_2 film. HT-XRD patterns have been recorded in-situ on the heated TiO_2 sample each an hour for 6 h at 300 °C; the results are presented in Figure 3-15. As seen in the figure, anatase phase (main crystal face (101) at 2θ = 25.4°) was successfully developed at lower T_p = 300 °C with a cost of longer duration till 5 hours. Further on, the (101) peak continued to rise apparently from the 5th to 6th hour heating at 300 °C representing the development of crystallinity in the film as a function of heating duration.

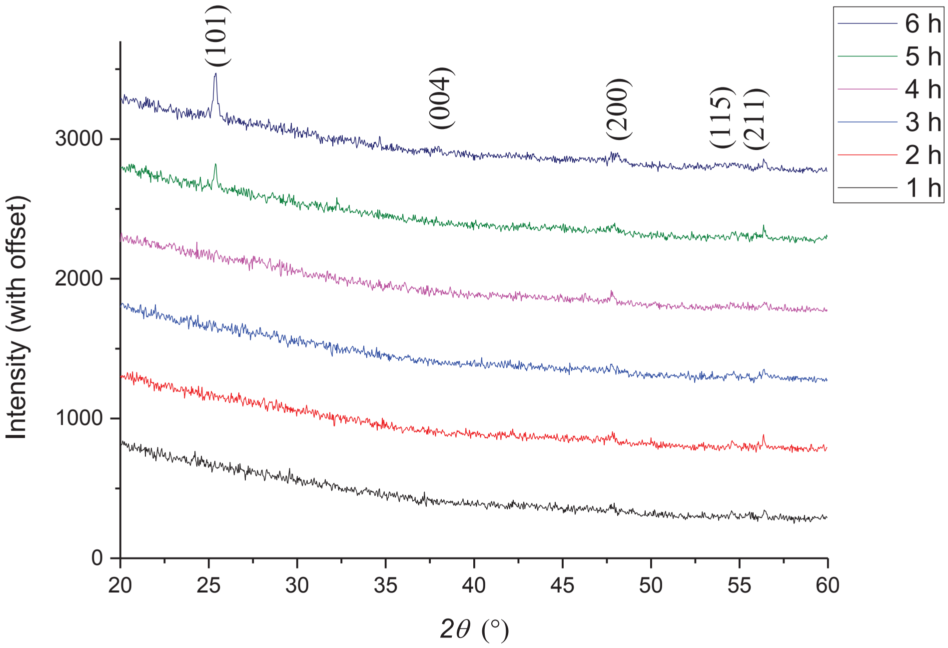

Fig. 3-15 High-temperature XRD analysis heating silicon-supported TiO_2 thin film at 300 °C with duration till 6 h.

A complementary experiment on post-annealing treatment at 300 °C (with heating rate 1 °C min^{-1}) for 5 hours was carried out on one optimal TiO_2 film (on silicon) in a separate furnace, followed with a cooling step to room temperature (with cooling rate 10 °C min-^{1}). Room temperature XRD analysis was made on the as-deposit TiO_2 film and the annealed same sample; results are presented in Figure 3-16. It confirms the previous result that formation of crystalline anatase structure has been succeeded by annealing at 300 °C within 5 hours staying. It is noted that diffraction peaks of silicon substrate sometimes can be detected due to the thin thickness of TiO_2 layer as presented in Figure 3-15. Diffraction peaks of anatase (101) and (004) at aspect 2θ = 25.4° and 37.9° have been indicated in the figure to be distinguished from silicon peaks.

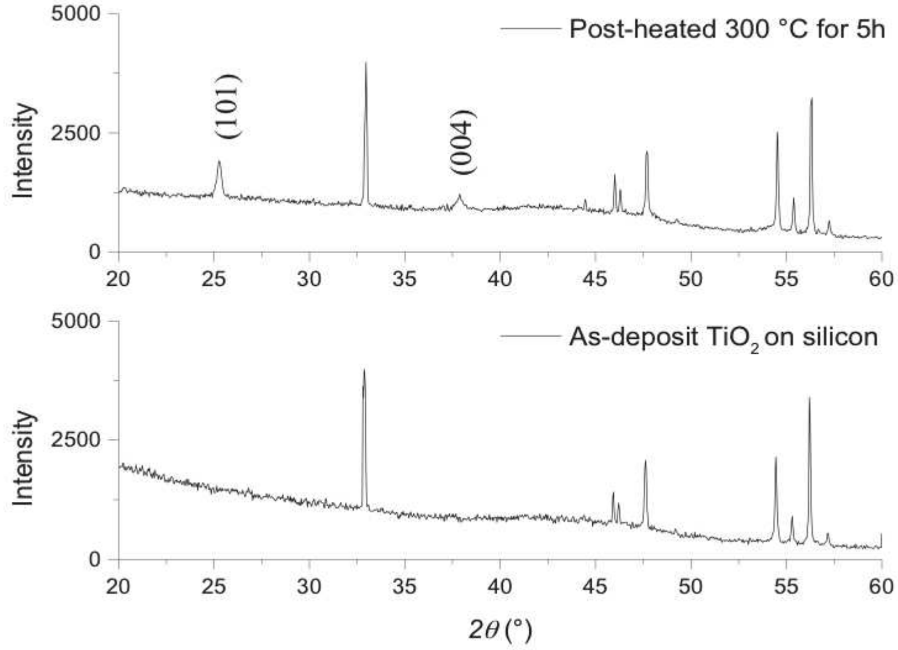

Fig. 3-16 XRD analysis on as-deposit and 300 °C-annealed TiO_2 film deposited on silicon substrate.

Possibility of improving crystallization of the optimal TiO_2 film at 300 °C was studied by prolonging to even longer as 10 h with a heating rate 1 °C min^{-1} and then a cooling rate 10 °C min^{-1}. Room temperature XRD patterns of both the as-deposit and 300 °C-annealed film (for 10 h) are compared in Figure 3-17.

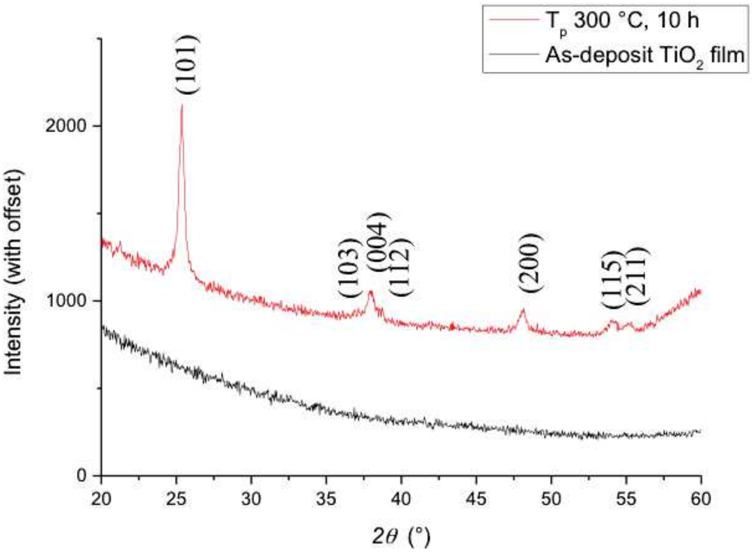

Fig. 3-17 XRD on as-deposit and 300 °C-annealed TiO_2 film (heated for 10 hours).

The anatase structure is more fully developed when heating at 300°C for 10 hours (Figure 3-17) in contrast to the film heated at 300°C for 5 hours (Figure 3-16). Main anatase peaks (101), (004), (200), (115) and (211) at 2θ = 25.4°, 37.9°, 48.1°, 54.0° and 55.1° have all been detected in the case of longer staying time of 10 hours at 300°C. Besides, another optimized TiO_2 sample (on silicon) was heated at 275°C for 24 hours but no crystal structure has been found. It suggests that the lowest critical crystallization temperature for the synthetic TiO_2 film is 300°C within 5 hours staying and that a longer staying (e.g. 10 hours) develops a better crystallinity structure.

2.3 Seeding effect on phase transformation

A seeding layer was obtained by dip-coating the silicon substrate in sol solution that has been mixed for 1 or 3 h. SEM images of the seeded-silicon substrate are presented in Figure 3-18. According to the surface image, it is clear that 3-h stirred solution produced better dispersion of seeds on silicon surface than that of 1-hour stirred one did. Sol aggregation is formed on surface for the short-term 1 h mixed solution, whereas, well-suspended anatase nanoparticles have been spread on surface from long-term 3 h mixed solution. Thickness of the seeding layer is estimated ca. 60 – 70 nm as notified in the cross-sectional SEM images of Figure 3-18.

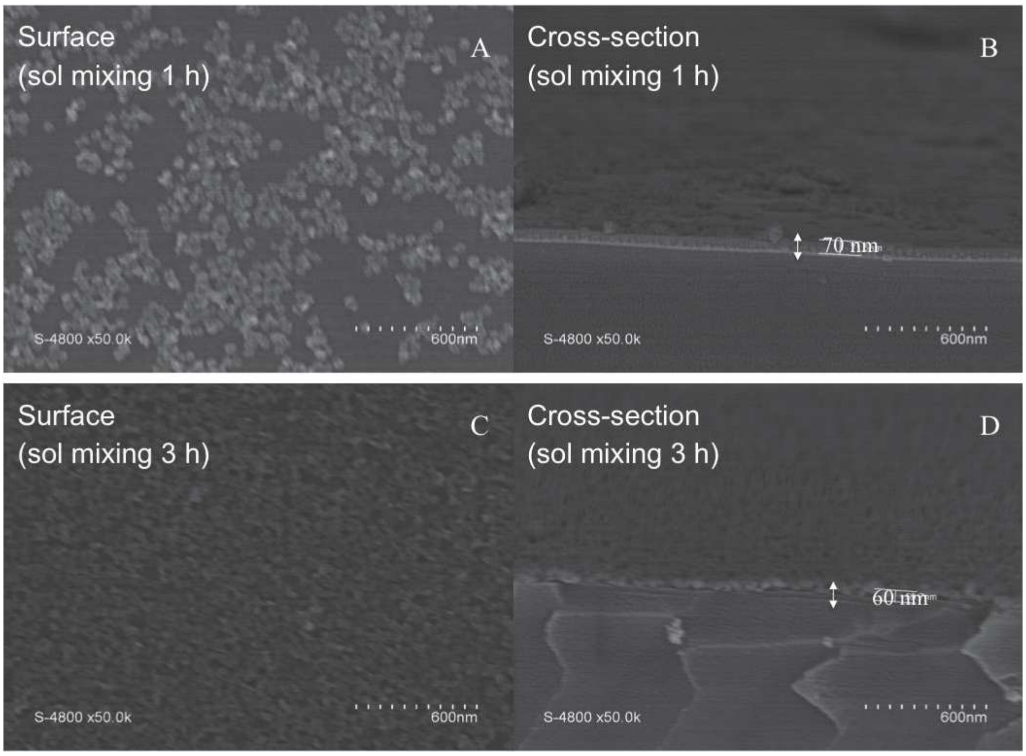

Figure 3-18 SEM images on nuclei seeded-silicon dip-coated from the anatase sol being mixed for 1 hour (A and B) and 3 hours (C and, D).

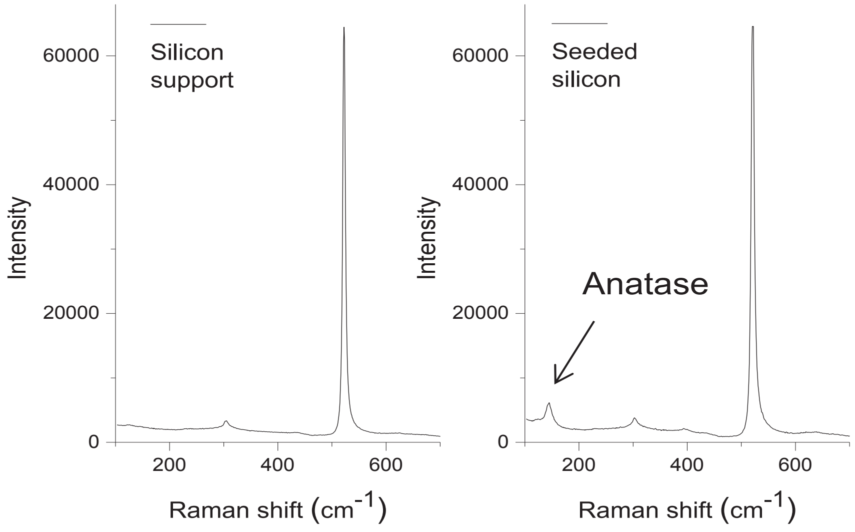

Figure 3-19 Proof of anatase seeding layer: Raman spectra of silicon (left) and seeded-silicon (right).

The nature of seeding layer was examined by vibrational Raman spectroscopy. The analysis spectroscopy has a confocal function coupled with a microscope making it less limited to the very thin thickness. Raman spectra of virgin silicon and seeded-silicon (better dispersed sample from 3-h mixed solution) are presented in Figure 3-19. It proves that anatase layer was successfully seeded on the surface, as anatase TiO_2 has the characteristic Raman scattering at 150 cm^{-1} according to the literature. [116]

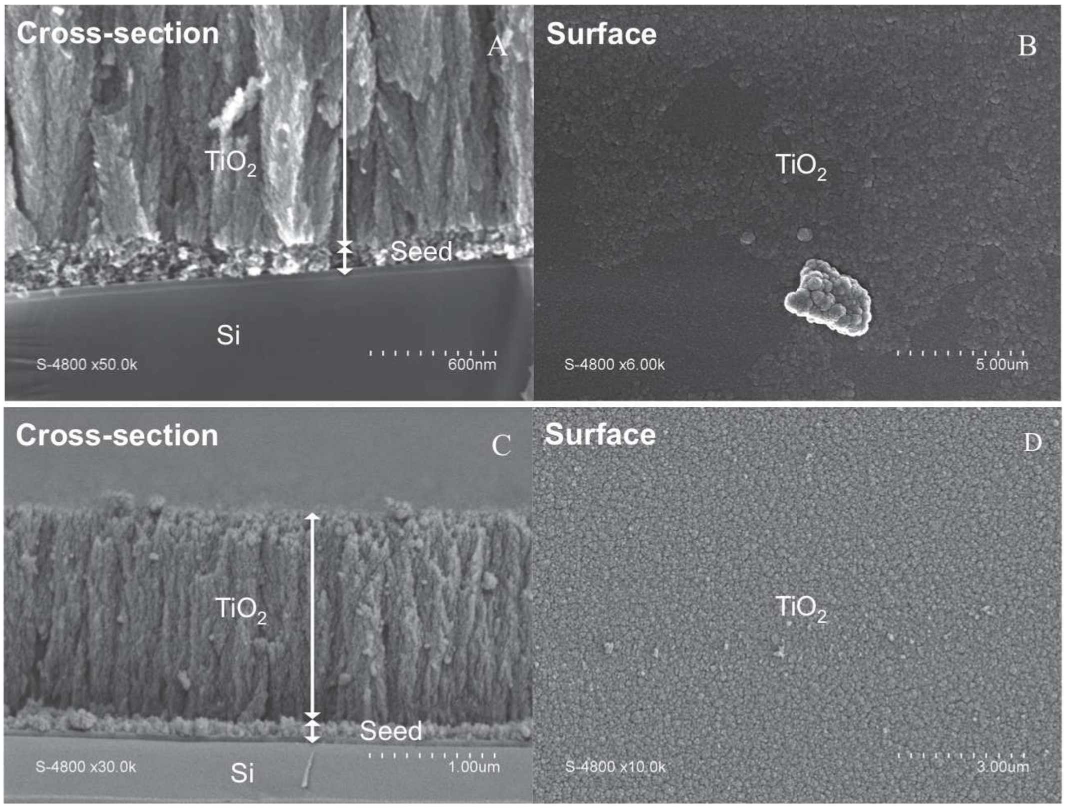

Fig. 3-20 SEM images of the optimal TiO_2 deposit on seeded-silicon substrates that were dip-coated from 1-hour stirred sol (A and B) and 3-hour stirred sol (C and D).

After seeding preparation, PECVD TiO_2 was deposited on the seeded-silicon as well on bared silicon as a controlled experiment. SEM images of TiO_2 deposit on seeded-silicon (both made from 1-h and 3-h mixed solution) are given in Figure 3-20. Seeding layer of thickness less than 100 nm is observed for both situations at the interface between TiO_2 deposit and the silicon surface as presented in the figure. However, for the former case (preparing the sol with 1 h stirring) less uniformed seeding was observed in global scanning. That is the seeds were thick or think or even in absence on the substrate according to cross-sectional scanning. And on the surface, seeds with aggregated grains were also observed for the case using inadequately mixed sol solution.

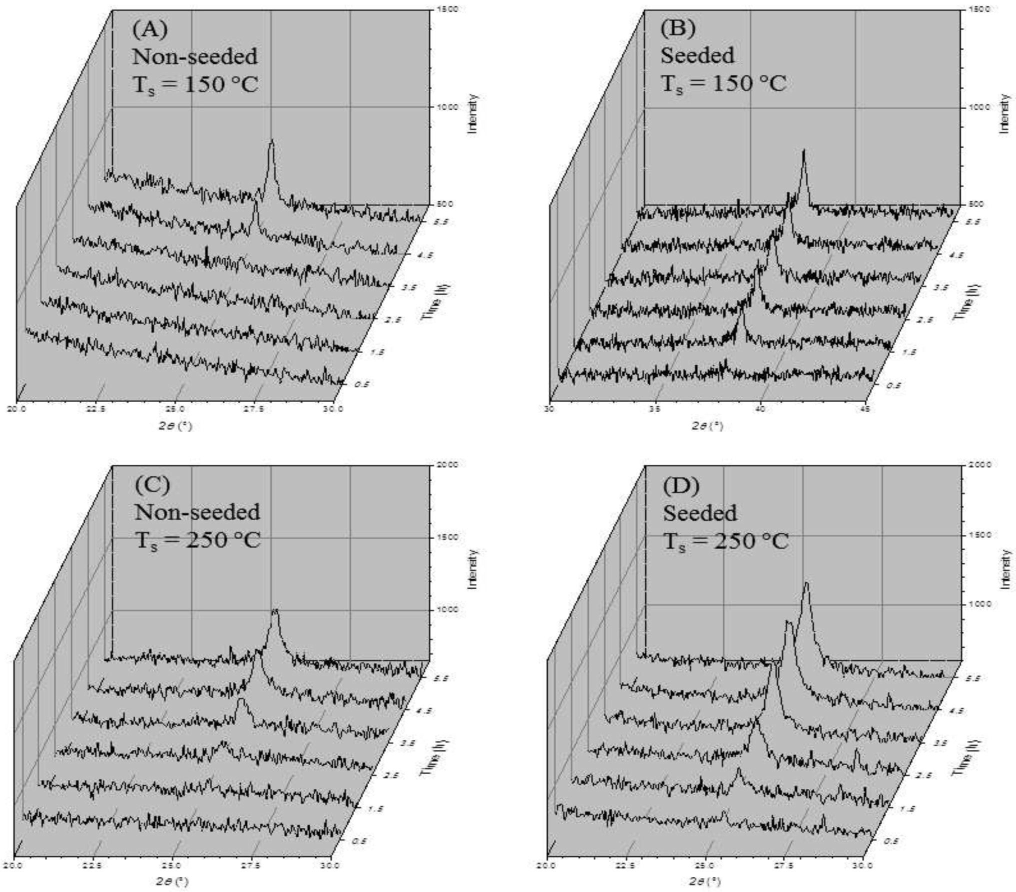

Fig. 3-21 Crystallization kinetics with seeding-effect: high-temperature XRD analysis (heated at 300°C lasting 6 h) of TiO_2 thin films on silicon deposited at T_s = 150 and 250°C (A and C) and on seeded-silicon at T_s = 150 and 250°C (B and D).

High-temperature XRD (HT-XRD) heating at 300°C lasting for 6 h was made on both TiO_2 deposits on silicon and seeded-silicon (obtained with T_s = 150°C in optimized PECVD process) to track crystallization kinetics with presence of seeding effect. It is seen in Figure 3.21-A that anatase peak (101) at 2θ = 25.4° appears since 4.5 h heating at 300°C for TiO_2 deposit on silicon, which confirms on the previous result in section 2.2. With the presence of nuclei layer, acceleration on TiO_2 crystallizing on seeded-silicon was found since 1.5 h at 300°C (Figure 3.21-B). Yet another anatase crystal face (004) at 2θ = 37.9° has appeared since 1.5 h in this case, while peak (101) at 2θ = 25.4° was unchanged along with time (not presented in the figure). It implies that the seeding layer may not only accelerate phase transition but also change crystallizing habit depending on the underneath seeds.

In addition, higher PECVD substrate temperature (T_s = 250°C) has been operated for TiO_2 deposition on seeded-silicon as well. It is more likely that stronger seeding activity could occur at higher surface temperature. High-temperature XRD operated at 300°C for 6h has also been made on the two samples (T_s = 250°C) as shown in Figure 3.21-C and D. Appearance of both XRD peaks (101) at 2θ = 25.4° and (004) at 2θ = 37.9° has been observed on TiO_2 deposits on silicon and seeded-silicon when T_s = 250°C. Yet only peak (101) is presented in the figure for showing the evolution kinetics. TiO_2 crystallization was accelerated from 3.5 to 1.5 h at 300°C due to seeding nuclei when T_s = 250°C in PECVD process. On the other hand, T_s = 250°C enables saving 1 h of crystallization of TiO_2 on silicon post-annealing at 300°C in comparison to that of T_s = 150°C in PECVD process.

As a conclusion, as-deposit TiO_2 film on silicon (T_s = 150°C) has been crystallized into anatase phase by post-annealing either at 400°C without staying or at 300°C with more than 4.5 h staying. Crystallization of TiO_2 film on silicon can be saved by 1 h post-heating at 300°C when T_s has been increased to 250°C in PECVD process. Moreover, seeding nuclei present on silicon surface accelerates phase transition to 1.5 h by post-heating at 300°C no matter T_s = 150 or 250°C in PECVD procedure. Above all, concerning fully degree of crystallization and removal of organic residues in the film the optimized post-thermal treatment has been decided as 400°C for 3 hours for fabrication of photocatalytic membrane.

3 Structural properties of the optimal TiO_2 thin film

Microstructure of supported TiO_2 thin film and crystal size in the annealed-film was characterized by SEM and XRD respectively. Photo-induced surface wettability of TiO_2 surface was examined with water contact angle measurement. Band gap energy (E_g) of TiO_2 thin film (deposited on glass in this case) was obtained from optical measurement. Porosity and refractive index of the synthesis thin film have been studied with XRR and ellipsometry spectroscopy analysis.

3.1 Morphology, crystal structure and photo-induced hydrophilicity

Microstructure of both amorphous and anatase TiO_2 thin films was investigated in SEM with their images presented in Figure 3-22. No structural damage due to post-annealing was found and the anatase film maintained the porous micro-columnar morphology by comparing as-deposited and post-annealed samples. Yet the anatase surface shows slight integration effect after being heated at 400°C as presented in the surface image of Figure 3-22 (right). Some tiny gaps on surface is observed for the annealed thin film maybe due to dehydroxylation, release of organic residues and crystallization by heating.

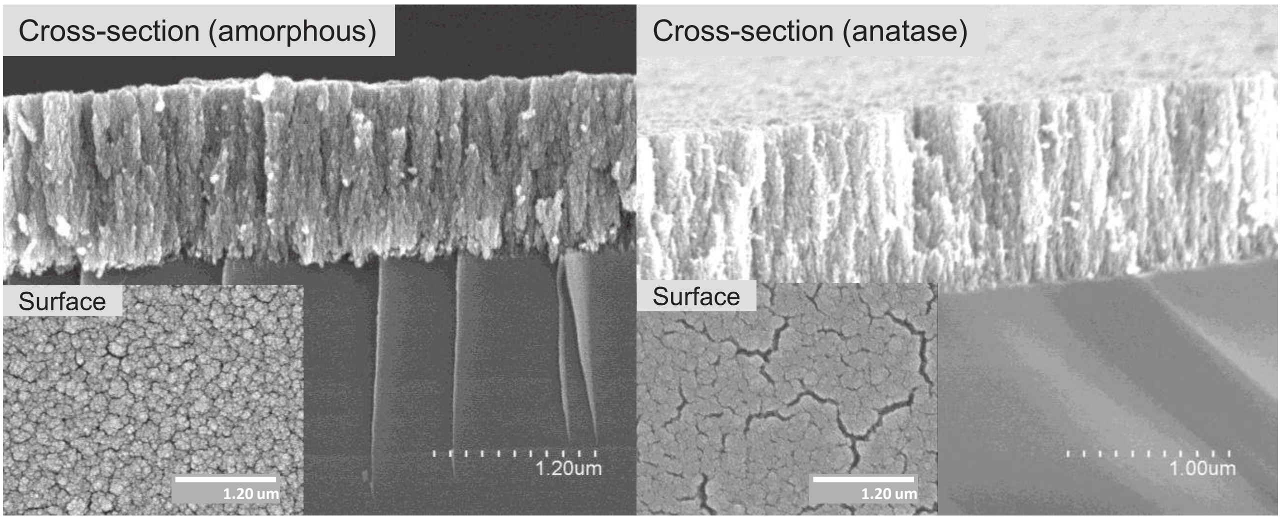

Fig. 3-22 SEM images on the optimal TiO_2 amorphous (left) and anatase (right) thin film on silicon substrate.

FTIR spectra of the optimal amorphous and anatase TiO_2 thin films are compared in Figure 3-23. Reduction absorbance of O-H stretching band for anatase film should be caused by water evaporation and remove of organic residues due to post-annealing treatment at 400°C. Characteristic shoulder peak at 700 cm^{-1} is observed for both amorphous and anatase phases, whereas, a sharp peak at 450 cm^{-1} is only clearly witnessed for the anatase film. [198]

In addition, the chemical elements existing in the as-deposit thin film were analyzed by EDX as the spectrum presented in Figure 3-24. Silicon has strong signal since the X-ray penetrate the thin film and then to the silicon substrate. Carbon is detected in the film due to entrapped organic residues from the precursor. And the atom ratio between titanium and oxygen is found roughly as 1:2.5 before post-annealing.

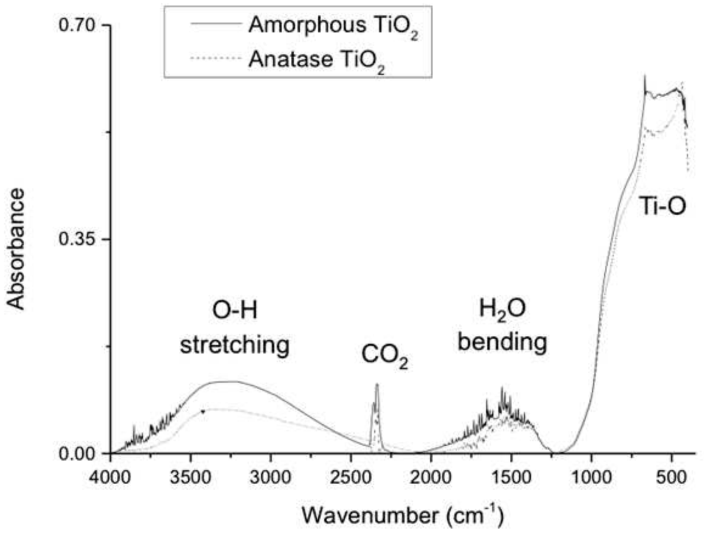

Fig. 3-23 FTIR spectra of as-deposit and 400°C-annealed TiO_2 film (deposited on silicon substrate).

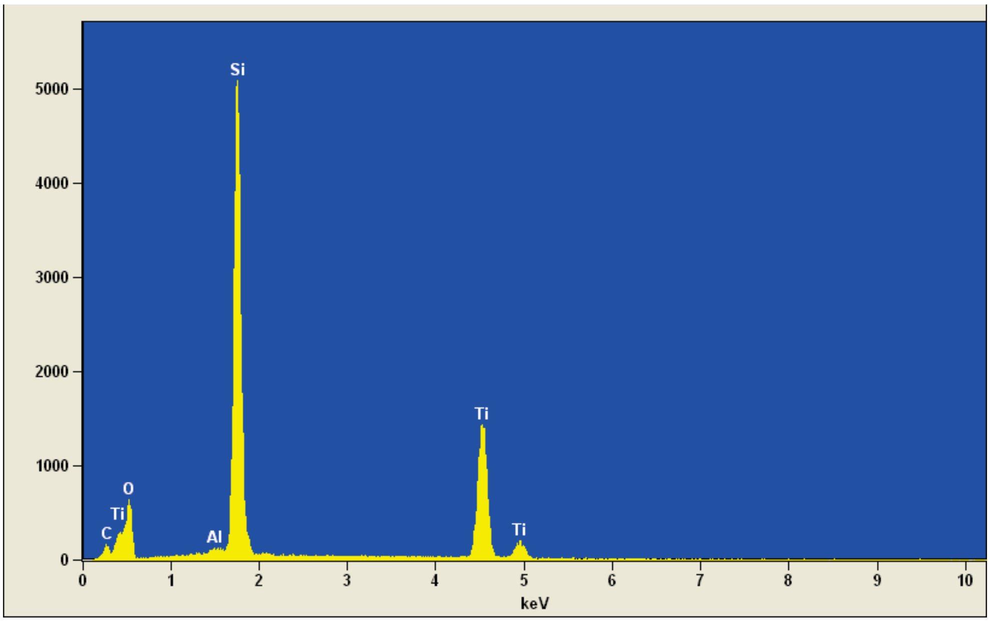

Fig. 3-24 EDX spectrum of as-deposit TiO_2 thin film on silicon substrate indicating the existed elements in the synthesis film.

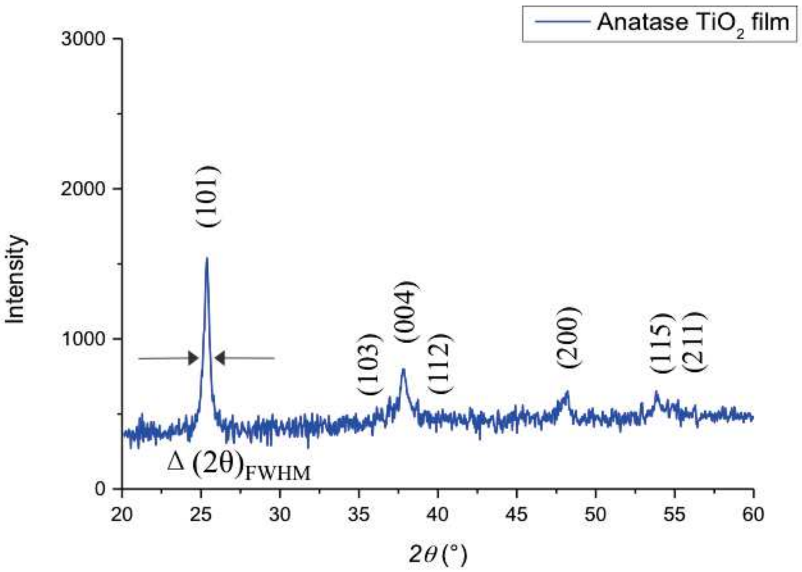

Fig. 3-25 XRD pattern of the optimal anatase TiO_2 thin film (on silicon).

Crystalline size of TiO_2 nanoparticles in the anatase film is calculated with Scherrer equation (as explained in Equation 2-9 in Chapter II) when knowing XRD peak width. XRD pattern of the optimal anatase TiO_2 film (supported on silicon) is presented in Figure 3-25. The width of peak (101) at $2\theta = 25.4°$ is measured as $\Delta(2\theta)_{FWHM} = 0.407°$ (as indicated between the two arrows in the figure). According to Scherrer equation, TiO_2 crystal size in the film is estimated approx. as 20 nm.

Photo-induced hydrophilicity phenomenon has been witnessed on anatase TiO_2 surface in the work. Water contact angle was measured on the optimal amorphous and anatase TiO_2 film (deposited on silicon) with or without the effect of UV irradiation. Photos of the water droplet on TiO_2 surface are presented in Figure 3-26. It can be seen that amorphous TiO_2 surface is generally hydrophobic whatever irradiation is applied. Contact angle of water φ on amorphous TiO_2 in dark is 66° and 61° without and with UV illumination, respectively, as notified in Figure 3.26-A and-B.

On the other hand, anatase TiO_2 surface shows a more hydrophilic surface with contact angle equal to 29° in dark (37° reduced comparing to the amorphous surface). With a period of UV illumination (within 20 min), the contact angle goes down to 10° on the anatase surface. Such photo-caused super-hydrophilicity can be explained with one proposed mechanism that oxygen vacancy in anatase surface is generated under UV source and it can be replaced by hydroxyl group from H_2O and thus the surface becomes more hydrophilic. [40]

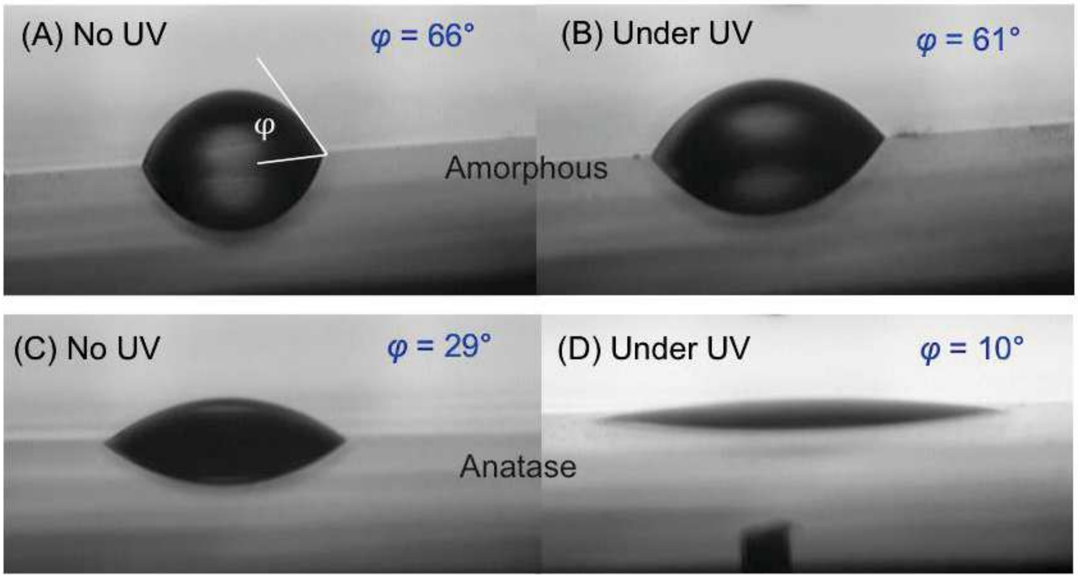

Fig. 3-26 Water contact angle (φ) on TiO_2 amorphous (A), irradiated amorphous (B), anatase (C) and irradiated anatase (D).

3.2 Band gap energy (E_g)

Band gap energy (E_g) is an important property of photocatalytic material relevant to photoelectrical transition and catalytic efficiency. E_g is defined as the energy difference between two electronic levels: valence band (VB) and conduction band (CB). E_g can be calculated from the optical measurement based on the light-and-matter interaction. In the work, UV/Vis spectroscopy and ellipsometry spectroscopy have been carried out to study E_g of the synthetic TiO_2 thin films on substrate.

3.2.1 UV/Vis spectroscopy analysis on E_g

For UV/Vis absorbance analysis, TiO_2 was synthesized on quartz substrate with the optimized PECVD conditions as listed in Table 3-7. Samples Q1, Q2 and Q3 of TiO_2 films with different thickness have been deposited on the transparent substrate within deposition duration as 7, 15 and 20 minutes in order to study TiO_2 thickness effect on light transportation through the film.

Table 3-7 PECVD conditions for preparing TiO_2 samples Q1, Q2 and Q3 (on quartz).

Sample No.	**Deposition duration (min)**	**Partial pressure $P_{Ar+TTIP}$ (mbar)**	**Partial pressure P_{O2} (mbar)**	**RF power (W)**	**Plasma distance d_p (cm)**	**Substrate temp. T_s (°C)**
Q1	7	0.225	0.17	50	3	150
Q2	15	0.225	0.17	50	3	150
Q3	20	0.225	0.17	50	3	150

Mass of the glass substrate m_1 (before PECVD process) and mass of TiO_2-deposited glass m_2 (after PECVD process) were measured in thermal mass balance respectively, in which the temperature was controlled so that humilidity was kept in the same level relevant to water absorbed on TiO_2 surface. Consequently, mass of the as-deposit TiO_2 film m_3 could be known by deducting m_2 with m_1. TiO_2 mass per unit surface for sample Q1, Q2 and Q3 was obtained by dividing m_3 with glass surface area. Results are presented in Table 3-8. Thickness of TiO_2 film (also given in the table) was theoretically obtained with knowing deposition rate and deposition duration.

Table 3-8 Mass and thickness of TiO_2 thin film deposited on quartz for samples Q1, Q2 and Q3.

Sample No.	**[a] Mass of as-deposit TiO_2 film (amorphous)**	**[b] Thickness of TiO_2 film (amorphous and anatase)**
Q1	0.6 g m^{-2}	0.5 μm
Q2	3.0 g m^{-2}	1.0 μm
Q3	4.0 g m^{-2}	1.3 μm

[a] Mass of as-deposit TiO_2 film : experimental values obtained from thermal-controlled balance and [b] Thickness of TiO_2 film: theoretical values calculated by multiplying the average deposition rate (R = 65 nm min^{-1}) and the deposition duration (t = 7, 15 and 20 min).

Lambert-Beer law describes light-matter interaction when the light is passing through the matter. In principle, more intensity of light can be absorbed with larger amount of molecules in the film and there can be up-limit thickness that light can pass through. Absorbance spectra of amorphous and anatase films are presented below.

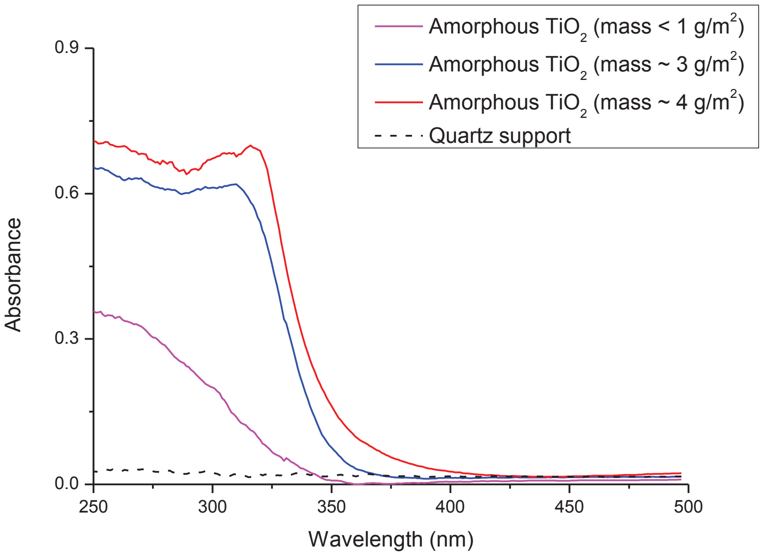

Fig. 3-27 Light absorbance of as-deposit amorphous TiO_2 films deposited on quartz.

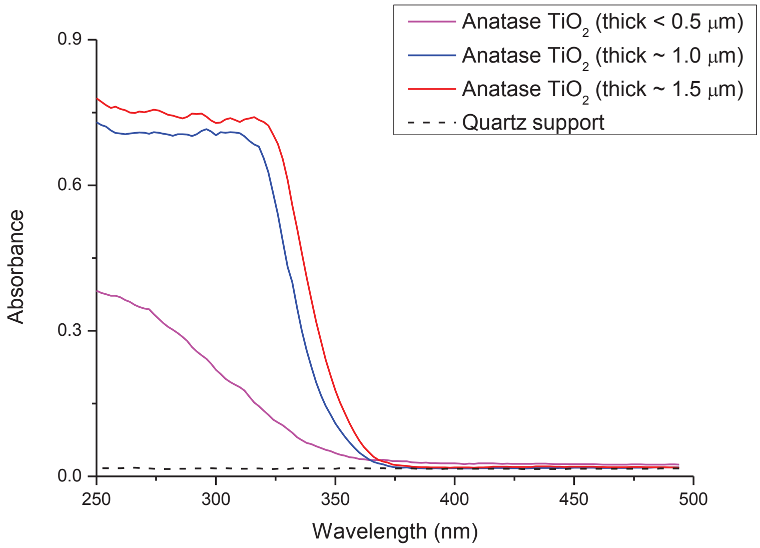

Fig. 3-28 Light absorbance of 400°C-annealed anatase TiO_2 films deposited on quartz.

Light absorbance of bared quartz and TiO_2-deposited quartz was analyzed in UV spectroscopy in the range 250 – 500 nm; spectra are given in Figure 3-27. Maximum absorbance intensity the cut-off edge approx. wavelength 350 nm is found as 0.4, 0.65 and 0.7 for 7, 15 and 20-min deposited samples Q1, Q2 and Q3 (with deposited TiO_2 mass per unit surface ca. 0.6, 3.0 and 4.0 g m^{-2}) respectively.

Q1, Q2 and Q3 samples were then annealed at 400°C and the anatase phase was form. Since the mass of the anatase film could be different from the as-deposit form due to removal of organic residues (as known from the previous TGA thermal analysis), theoretical thickness values (multiplying average deposition rate and deposition duration) are indicated hereby. Relevant UV spectra of the anatase Q1, Q2 and Q3 samples are plotted in Figure 3-28. Very similarly, the intensity of absorbance is proportional to the anatase film thickness. Slight change of absorption cutting-off edge has been caused after crystallization as seen in the figure.

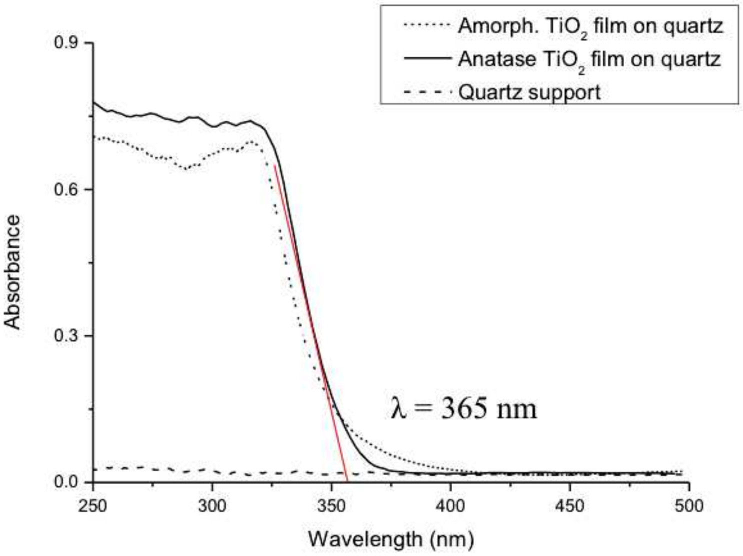

Fig. 3-29 Absorbance of light by sample Q3 of TiO_2 film on quartz both in amorphous and anatase phase.

Sample Q3 (20-minute deposit) absorbs the largest energy of incident light (in UV band $\lambda <$ 350 nm) in comparison to the other samples Q1 and Q2. UV spectra of sample Q3 of both amorphous and anatase phases are compared in Figure 3-29. It is found for sample Q3 that the cut-off absorbance wavelength (λ) is 350 nm for amorphous and 365 nm for anatase by fitting in the cut-off region. Fitting curve (in red) and absorbance λ value is illustrated for the anatase TiO_2 film in the figure.

According to the Equation 2-14 (chapter 2), indirect type E_g of amorphous and anatase TiO_2 can be obtained by plotting $\sqrt{kh\upsilon}$ as a function of $h\upsilon$ as presented in Figure 3-30. The transformed curve $\sqrt{kh\upsilon}$ v.s. $h\upsilon$ is often referred as Tauc plot. [195] Extrapolating the linear fitting at the cut-off region to zero leads to determination of E_g value. As a result, band-gaps equal to 3.31 and 3.30 eV were found for the optimal amorphous and anatase TiO_2 film respectively.

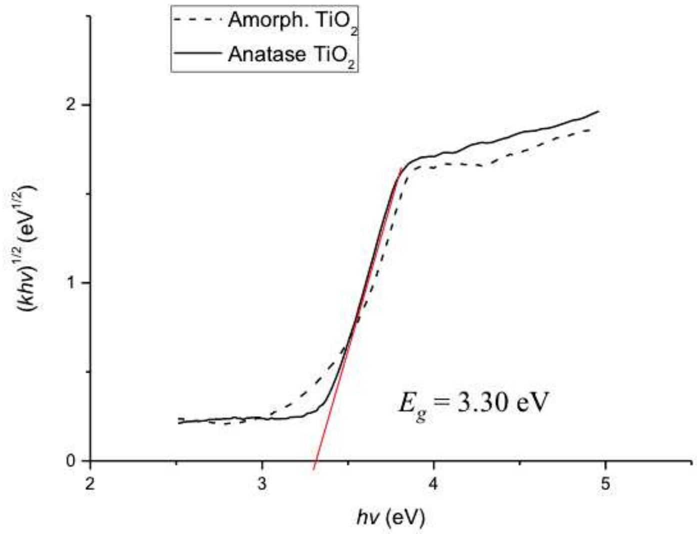

Fig. 3-30 Determination of band gap of TiO_2 film on quartz with Tauc plot.

In addition, light transmittance and reflection have also been measured on glass-supported anatase TiO_2 films (with 7, 15 and 20-minute deposition duration) in UV/Vis spectroscopy in the range 200 – 800 nm. Total mass of TiO_2 film (on glass surface area 3 cm^2) is less than 1 mg for 7-minute deposited sample and is approx. 1 and 3 mg for 15- and 20-minute deposited samples, respectively. The transmittance and reflection curves are presented in Figure 3-31 and Figure 3-32, respectively. It can be found that more oscillation of transmitted and reflected light is produced when film becomes thicker (e.g. the 20-minute deposit TiO_2 sample). It is reasonable that complex interaction between light and matter could occur as the multiple layers are formed.

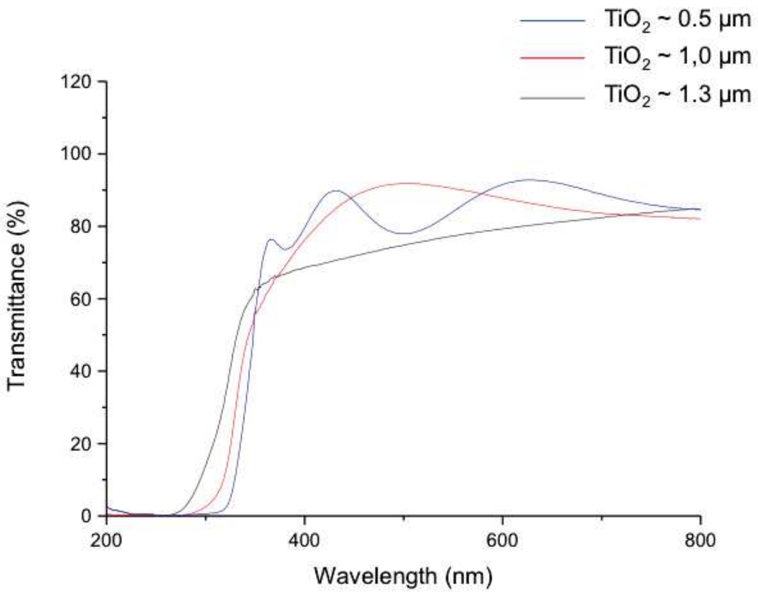

Fig. 3-31 Transmittance of light through glass-supported anatase TiO_2 films of different thickness (deposited with 7, 15 and 20 minutes).

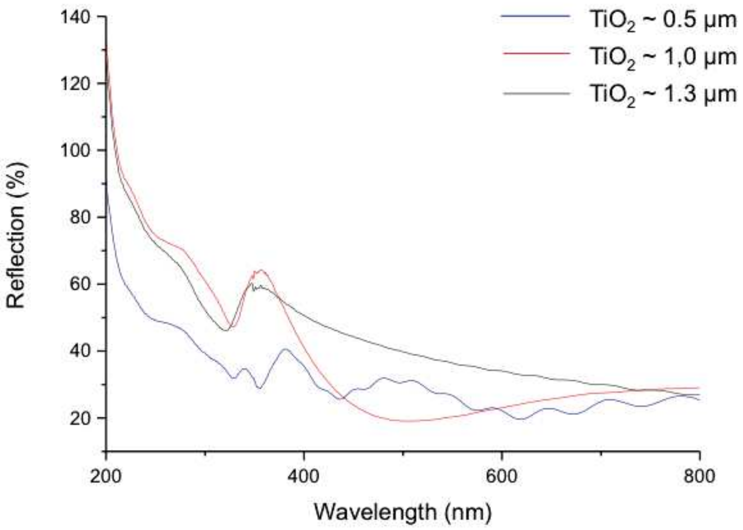

Fig. 3-32 Reflection of light from glass-supported anatase TiO_2 films of different thickness (deposited with 7, 15 and 20 minutes).

3.2.2 Ellipsometry spectroscopy analysis on E_g

In ellipsometry spectroscopy analysis a light beam (ellipse with a ~ 10 mm and b ~ 3 mm) is employed on the optimal anatase TiO_2 film (on silicon). Polarization parameters (α and β) in the reflected light from the film are measured and regressed with various possible models.

Three positions on TiO_2 surface were analyzed in ellipsometry spectroscopy, which are indicated in the photo of Figure 3-33 as spots 1, 2 and 3. The reason is that layer singularity and thickness are essential factors in simple modeling application on measured data.

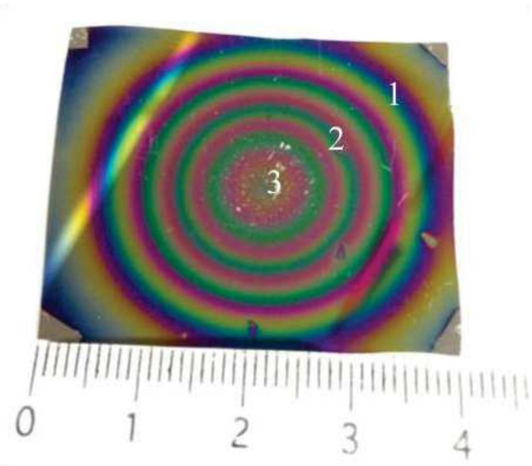

Fig. 3-33 Photo of the optimal anatase TiO_2 film (on silicon) for ellipsometry spectroscopy analysis on three spots (marked as 1, 2 and 3).

At spot 1 (thinner TiO_2 deposition) a single layer model was used to calculate film thickness and E_g, whereas, at spots 2 and 3 (thicker TiO_2 deposition) a two-layers model (of bulk and surface layers) was attempted to simulate roughness. Several regressed models such as Cauchy law (most-often used in literature for TiO_2 layer), Bruggeman law (to estimate porosity) and Forouhi law (to estimate E_g in some papers) have been tested in our study on the measured polarized angles in the range 1.24 – 3.50 eV (i.e. NIR + visible + UV). However, good fitting has only been achieved on spot 1 on edge of the deposition where TiO_2 layer is relatively thin. Reliable fitting on spot 2 and 3 was not succeeded due to large thickness variation and surface roughness, especially on spot 3 where the light diffusion is important.

Cauchy dispersion law (Equation 2-12 in Chapter II) was applied in the range 1.25 – 3.50 eV (i.e. NIR + visible + UV) to fit the measured data on spot 1 of the anatase TiO_2 film. Polarization parameters α and β measured (in violet color) from experiment and the corresponding fitting curves by Cauchy law (in green color) are presented in Figure 3-34. As a result, it is obtained that thickness of TiO_2 film is 181 nm and refractive index (at 633 nm) is n = 1.953 (with fitting goodness $R^2 > 0.99$) on spot 1. At the meantime, band gap energy is modeled as E_g = 3.15 eV (R^2 = 0.94) on the same spot of the anatase film, where TiO_2 thickness is relatively thin (181 nm).

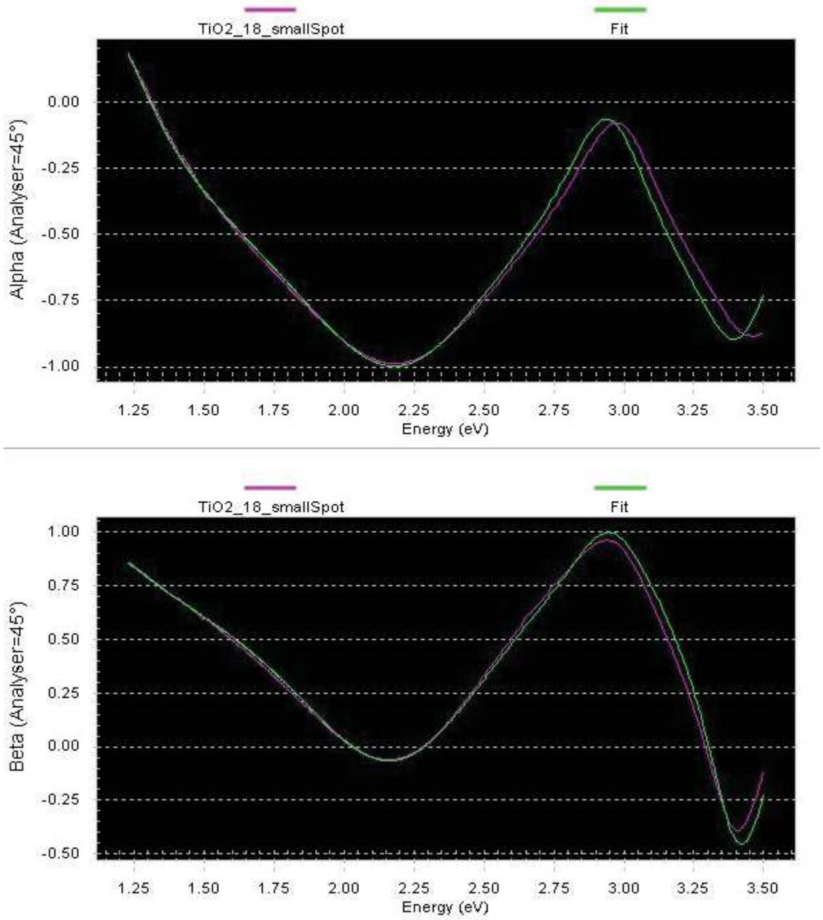

Fig. 3-34 Ellipsometry spectroscopy measurement curve (in violet) and the fitting curve (in green) to calculate thickness and E_g of the anatase TiO_2 film (on silicon).

3.3 Porosity

Porous column-like microstructure was discovered by SEM observation of PECVD TiO_2 film (session 3.1). However, the film porosity could not been directly measured with common techniques including N_2 adsorption/desorption method limited by the film's thin thickness. In the work, ellipsometry spectroscopy and X-ray reflectivity have been experimented to investigate on the porosity in the deposited film.

Ellipsometry spectroscopy analysis on the anatase TiO_2 thin film (at spot 1 as seen in the photo of Figure 3-33) has been modeled with Bruggeman law (for mixture of TiO_2 and void) to estimate porosity. Polarization parameters (α and β) of the reflected light has been well fitted in range 0.124 – 3.10 eV (i.e. NIR + visible) with the applied mathematics law. In a result, the percentage of void volume in the film is found as $v = 46$ % (with fitting goodness

$R^2 = 0.99$) and refractive index of the sample is $n = 1.959$ (at 633 nm). It should be noted that the obtained void percentage (45.8 %) in the film is relevant to TiO_2 thickness of 180 nm. The optical analysis on thicker TiO_2 layer was not succeeded in rational fitting.

In addition, X-ray reflectivity analysis on the anatase TiO_2 film (at spot 3 as seen in the photo of Figure 3-33) was carried on. In the Figure 3-35, the measured reflectivity curve (in red) and the fitting curve (in green) are presented. With knowing the incident X-ray wavelength (0.154 nm) and assuming film thickness of TiO_2 (2000 nm), density of the PECVD anatase film is obtained as $\rho = 2.52$ g cm^{-3} by modeling program.

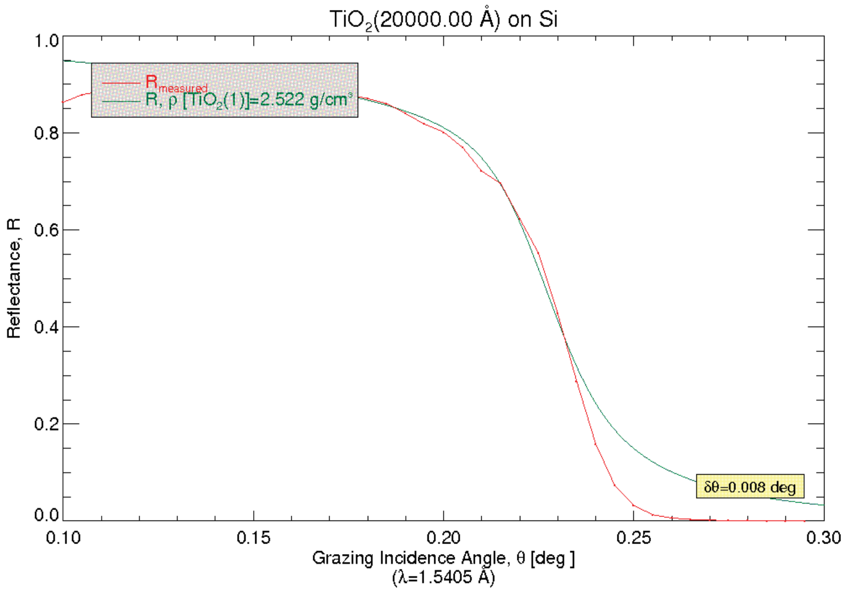

Fig. 3-35 X-ray reflectivity measured curve (in red) and fitted curve (in green) to estimate porosity in the anatase TiO_2 film (on silicon).

By knowing the density, percentage of void volume (v) in the synthetic anatase film is calculated as in Equation 2-11 (Chapter 2). Porosity (i.e. the void in the film) is obtained as $v = 33.3\%$ by comparing the density of PECVD anatase film ($\rho = 2.52$ g cm^{-3}) and the density of dense anatase material ($\rho_0 = 3.78$ g cm^{-3}).

It should be noted that porosity of PECVD anatase film is thickness dependent by comparing the value obtained at spot 1 (thick) and spot 3 (thin) as illustrated in Figure 3-33. It is found that void percentage $v = 33$ % (obtained from X-ray reflectivity) on central position of TiO_2 film (~ 2 µm thick) and $v = 46$ % (obtained from ellipsometry spectroscopy study) on edge position of TiO_2 film (~ 180 nm thick).

4. Conclusion

Chemical bonding in the deposited film (a few micrometers thick) was observed in FTIR spectrum at characteristic at wavenumber 450 and 700 cm^{-1} for anatase TiO_2 material; in addition, existing chemical elements of Ti and O atoms were proved in EDX spectrum. Micro-columnar structure and thickness of the film have been witnessed and measured in SEM. Crystalline phase was determined as anatase for the 400°C-annealed thin film with XRD analysis, with nanocrystal size ca. 20 nm according to XRD peak width. Apparent density of the synthesis anatase TiO_2 film was known as 2.52 g cm-^{3} from XRR measurement and accordingly the porosity of film could be estimated as 33% by comparing it to dense anatase material. Photo-induced wettability on anatase surface was proved with reduction of water contact angle from 29° to 10° due UV exposure. Band gap energy (E_g) of the optimally prepared anatase film was found at 3.30 eV base on optical absorbance measurement. The studied physico-chemical properties of the optimal anatase TiO_2 film (on dense support including silicon and quartz) are summarized in Table 3-9. They could affect photocatalytic activity and membrane permeability, which will be discussed in the following chapter.

Table 3-9 Summary on physico-chemical properties of optimal PECVD TiO_2 deposit.

Physico-chemical properties	**PECVD TiO_2 thin film**
Crystalline phase	Anatase
Morphology	Micro-columnar
Mean thickness	1.3 – 3.8 µm
Crystallite size	20 nm
Band gap energy E_g	3.30 eV
Apparent density	2.52 g cm^{-3}
Porosity (thickness dependent)	33.3 % (1.5 µm thick)
Water contact angle	29° (in dark) 10° (with UV)

Chapter IV Photocatalytic and permeation properties of TiO_2 material

PECVD TiO_2 thin films were deposited on dense (e.g. silicon) and porous (e.g. alumina ceramic) substrates and went through different assessments of their photocatalytic activity. Photos of TiO_2 on silicon wafer and TiO_2 on ceramic disk are presented in Figure 4-1. After post-annealing at 300 or 400 °C, the photocatalytic efficiency of the anatase films were investigated using some organic solute (as model compound) in water solution under certain UV irradiation condition.

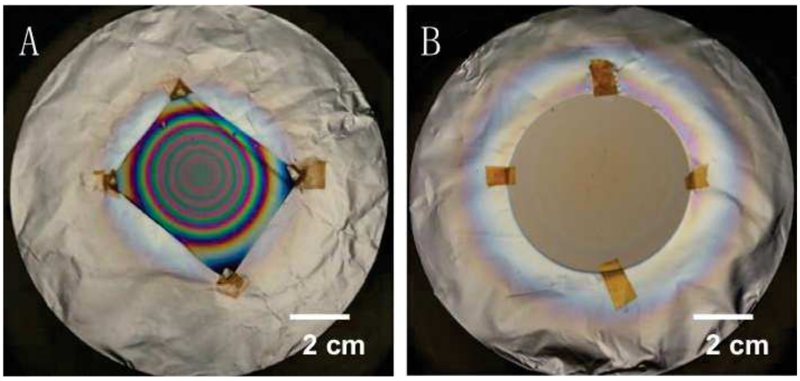

Fig. 4-1 Photos of silicon-supported TiO_2 thin film (A) for Pilkington assessment and alumina-supported TiO_2 thin film (B) for membrane performance test.

Surface self-cleaning property of dense-Si-supported TiO_2 was examined with a standardized assessment method: Pilkington protocol (Part 1 of the chapter). Photoactivity of porous-Al_2O_3-supported TiO_2 was investigated in a diffusion cell with organic solute being diffusing through and photo-reacted under interval UV illumination (Part 2 of the chapter). Then photocatalytic and permeation performance of porous-Al_2O_3-supported TiO_2 was explored in membrane reactor in two configurations: 1) TiO_2 layer and UV source facing the permeate solution in a pilot-scale unit and 2) TiO_2 layer and UV source facing the feed solution in a lab-scale unit (part 3 of the chapter).

1 Photocatalytic activity of PECVD TiO_2 thin film (on silicon) in static condition

Photocatalytic activity of anatase TiO_2 thin film deposited on silicon wafer was evaluated from patented Pilkington method as described in chapter 2.

An example of time-resolved FTIR spectra of stearic acid adhered on anatase TiO_2 surface with UV irradiation is given in Figure 4-2. Photodegradation of stearic acid is witnessed as the reduction of vibration band ν(C-H) of stearic acid molecule (wavenumber from 2800 – 3000 cm^{-1}) along with UV irradiating (35 W m^{-2}, λ = 355 nm) duration equal to 0, 20, 40 and 60 minutes.

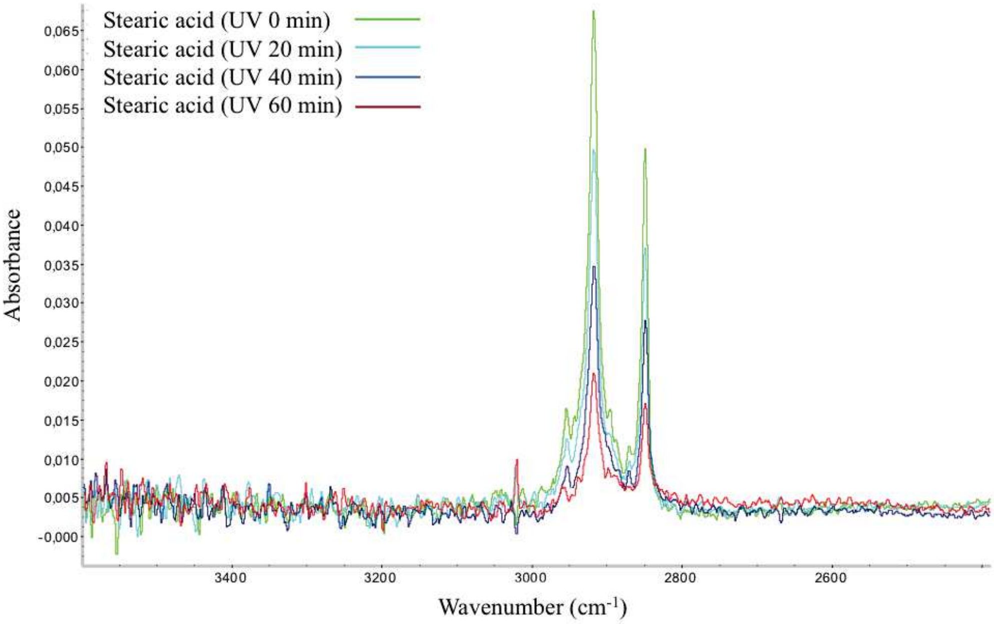

Fig. 4-2 Time-resolved FTIR spectra of photodegraded stearic acid caused by UV irradiated TiO_2 thin film deposited on silicon.

1.1 Effect of PECVD substrate temperature

Photodegradation rates of stearic acid related to anatase TiO_2 layers deposited at different substrate temperatures (T_s = 150 and 250 °C) are plotted along with irradiation time in Figure 4-3. It can be seen that all the anatase films (deposited at different T_s and then post-annealed at the same T_p) have evident photocatalytic effectiveness on decomposing stearic acid within 80-min UV illumination. The used UV lamp had a polychromatic spectrum and an irradiance of 35 W m^{-2} (measured with the UV radiometer at the bottom level of the Petri box). This UV irradiation is corresponding to 1×10^{-4} mol of photon s^{-1} m^{-2}. In the case of PECVD at T_s = 50 °C, R_{ST} caused by the anatase surface rises up to 70% at 80 min irradiation. In the case of PECVD T_s caused by R_{ST} observed on the corresponding anatase thin films reaches 90 – 100% at the same irradiation time, which is representative of almost completely self-cleaning surface. Less impurity (e.g. organic residues) entrapped in TiO_2 layer in PECVD process at higher substrate temperature could explain the better photocatalytic efficiency of the thin film deposited at higher T_s.

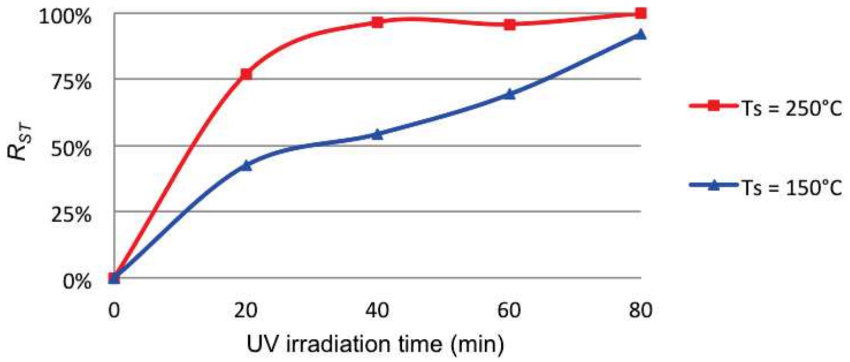

Fig. 4-3 Effect of PECVD substrate temp. (T_s) on photodegraded rate (R_{ST}): on 300 °C -annealed TiO_2 thin films prepared at T_s = 150 °C and 250 °C.

1.2 Effect of post-annealing temperature

Post-annealing at T_p = 300 °C (for 10 h) and T_p = 400 °C (for 1 h) was carried out on TiO_2 thin films prepared at the same PECVD substrate temperature T_s = 150 °C. Pilkington test results of R_{ST} from the anatase TiO_2 thin films obtained from two different post-annealing conditions and the amorphous film in the absence of post-annealing are presented in Figure 4-4. In general, anatase films have effective R_{ST} (up to 100%) in contrast to amorphous film (approx. 25%) at 80 min irradiation.

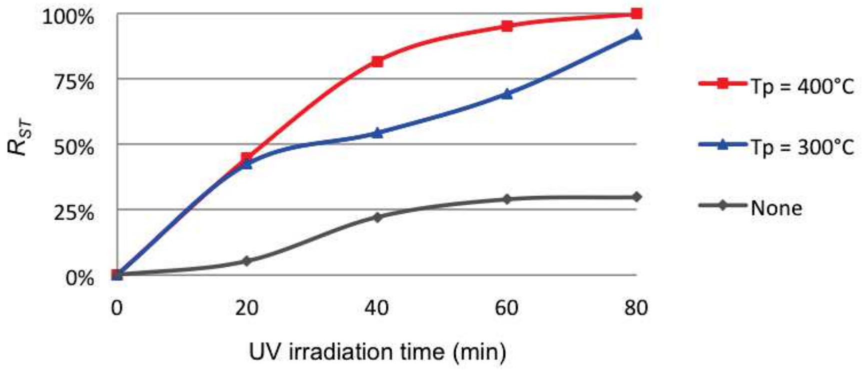

Fig. 4-4 Effect of post-annealing temp. (T_p) on photodegraded rate (R_{ST}): 300 °C and 400 °C-annealed and non-annealed TiO_2 thin films prepared at substrate temp. 150 °C.

Moreover, anatase film annealed at 400 °C (for 1 h) has improved photocatalytic efficiency since 40 min irradiation in comparison to anatase film annealed at 300 °C (for 10 h). A possible reason is that higher post-annealing temperature could have led to higher degree of crystallinity in the film and to a more thorough removal of impurity.

At the mean time, uncoated silicon was examined with Pilkington test as a controlled experiment, whose result of R_{ST} is compared to that of anatase-coated silicon (TiO_2 deposited at T_s = 150 °C and then post-annealed at T_p = 400 °C) as shown in Figure 4-5. Deduction of stearic acid due to self-photolysis and/or evaporation caused by irradiation/thermal effect is investigated in the controlled test on uncoated silicon.

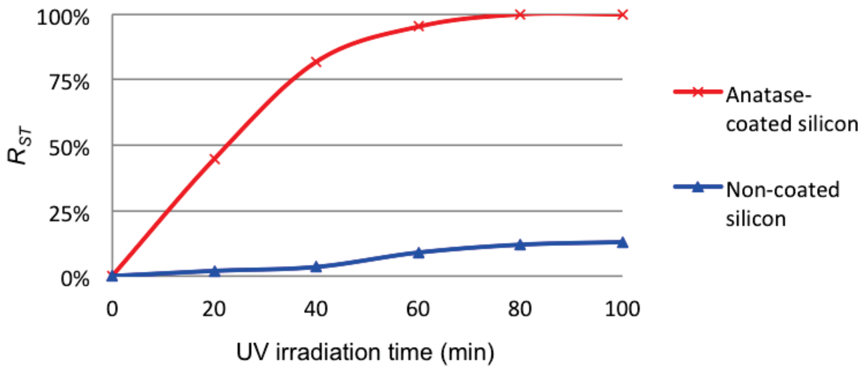

Fig. 4-5 Self-cleaning surface on anatase-coated silicon (complete removal of stearic acid) in contrast to the controlled experiment on the non-coated silicon.

Figure 4-5 shows that no significant degradation is observed on the uncoated substrate after 100 min of UV irradiation, whereas degradation is complete after 80 min for the anatase-coated silicon wafer and 50 min are required to reach a degradation rate of 90%. Very similar MB photodegradation rates are reported in the literature whatever the type (purely ceramic or mixed with polymer, doped or not) and geometry (film, wire, tube, fiber etc.) of titania membrane may be. [31, 126, 127, 199-201] The specific power of the UV device used, 35 W m^{-2}, is close to that used in paper referenced [202] 32 W m^{-2}, for the photocatalytic characterization of titania layers prepared at high temperature by conventional CVD method. For such dense layers (with stearic acid only adsorbed at the external surface), a degradation rate of 90% was observed after a time of UV irradiation ranging from 4 to 28 min as a function of the deposition conditions [202]. In another paper from our group dedicated to mesostructured anatase layers prepared by sol-gel route and exhibiting a very high photocatalytic activity [119] the same degradation rate requires an irradiation time of 10 s but with a 11 times larger irradiation power (380 W m^{-2}).

2 Photocatalytic activity of PECVD TiO_2 thin film (on alumina) in diffusion condition

In order to characterize the photocatalytic activity of anatase-coated ceramics in diffusion conditions, methylene blue (MB) as model compound in aqueous solution was studied in a lab-scale diffusion cell. UV/Vis absorbance spectrum of MB in water was measured and a maximum absorbance was found at λ = 665 nm as shown in Figure 4-6.

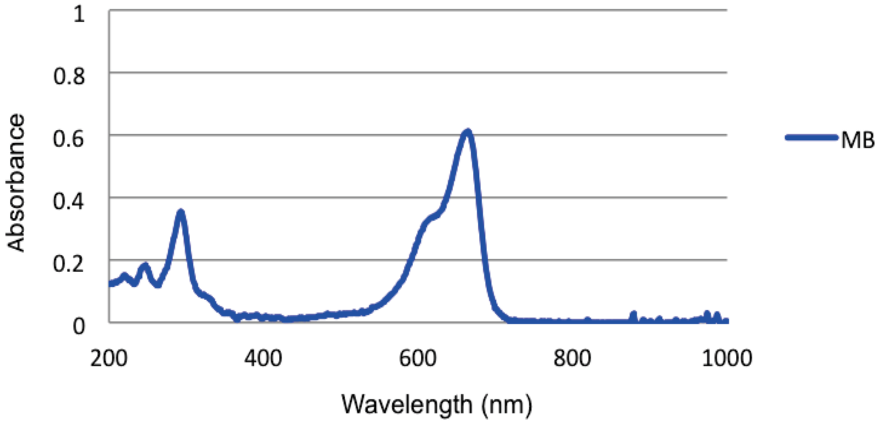

Fig. 4-6 UV/Vis absorbance spectrum of MB compound in water ($C = 1\times10^{-5}$ mol L^{-1}).

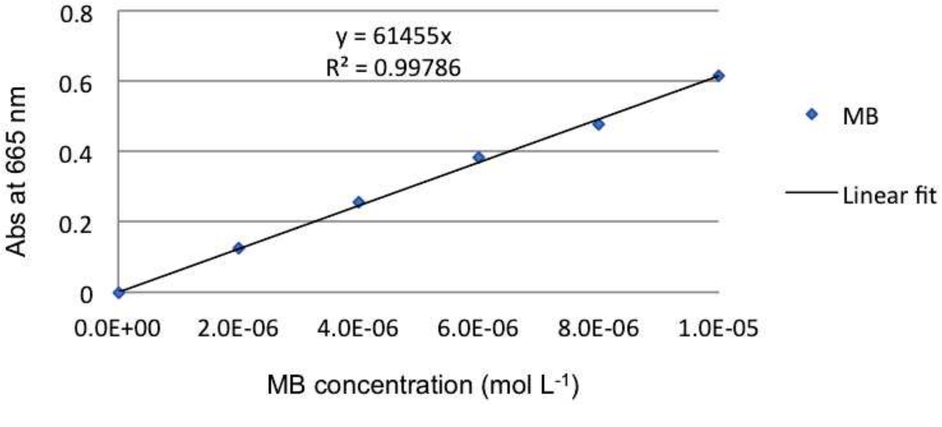

Fig. 4-7 Calibration curve of absorbance of MB at λ = 665 nm (in water) versus concentration.

A calibration curve was first established in order to determine the MB concentration in the reception tank (in the range 10^{-6} – 10^{-5} mol L^{-1}). The measured absorbance value of MB at λ = 665 nm was plotted as a function of $C = 2\times10^{-6}$, 4×10^{-6}, 6×10^{-6}, 8×10^{-6} and 1×10^{-5} mol L^{-1} as presented in Figure 4-7. A linear fitting is acquired as calibration curve $y = 61455x$ (R^2 = 0.998), where y is absorbance at λ = 665 nm and x is concentration. Accordingly, concentration of MB in the reception tank from the diffusion experiment is calculated from the measured absorbance values.

The diffusion test described in chapter 2 was first implemented using a filter disk (from Millipore: diameter 30 mm, thickness 0.41 mm and mean pore size 2.3 μm) as a reference separator between the feed tank (filled with MB solution of $C_0 = 1\times10^{-4}$ mol L^{-1}) and reception tank (filled with initially pure water). The amount of diffused MB per unit area (mol m^{-2}) was measured by the concentration in the reception tank versus diffusing time as presented in Figure 4-8. The flux (J) is known from the slope of linear fitting on diffusivity curve as $J = 2.35\times10^{-8}$ mol m^{-2} s^{-1}. Diffusion coefficient (D_i) of MB in water was calculated $D_i = (J \times d)/C_0$, where d is the thickness of separator (d = 0.41 mm) and C_0 is the initial concentration. Consequently, we have $D_i = 9.64\times10^{-11}$ m^2 s^{-1} for MB molecules in pure water in the case of initial feed $C_0 = 1\times10^{-4}$ mol L^{-1}.

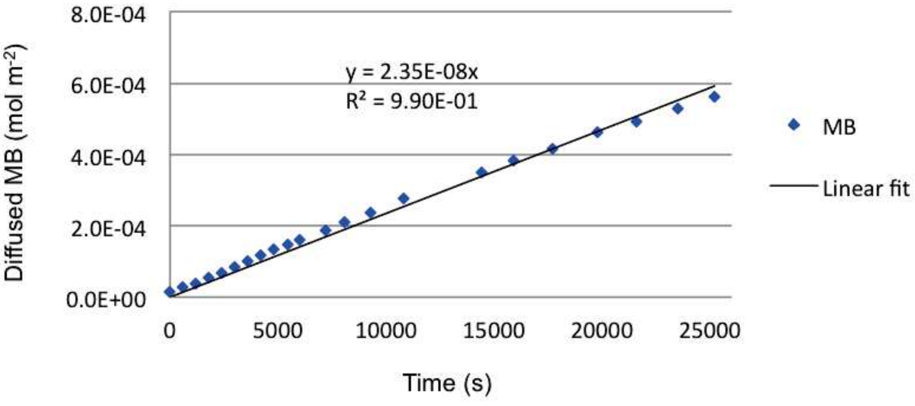

Fig. 4-8 Measurement on diffusion coefficient (D_i) of MB compound in water.

2.1 Morphology and catalytic efficiency of TiO_2-layer coating (M100)

Photodegradation tests in the diffusion cell were first performed on membrane M100. Microstructure of M100 and its support are presented in SEM images of Figure 4-9. As mean thickness of TiO_2 layer is d layer μm (± 7%) and mean pore size of the support (in the top layer) is Pr = 100 nm, then we have $d \geq$ 100 nm, thP_r for this coating format for preparing TiO_2-Al_2O_3 composite membrane M100. Porosity of the columnar-like thin film is approx. 33% (modeled from XRR) and TiO_2 crystal dimension is approx. 20 nm (known from XRD).

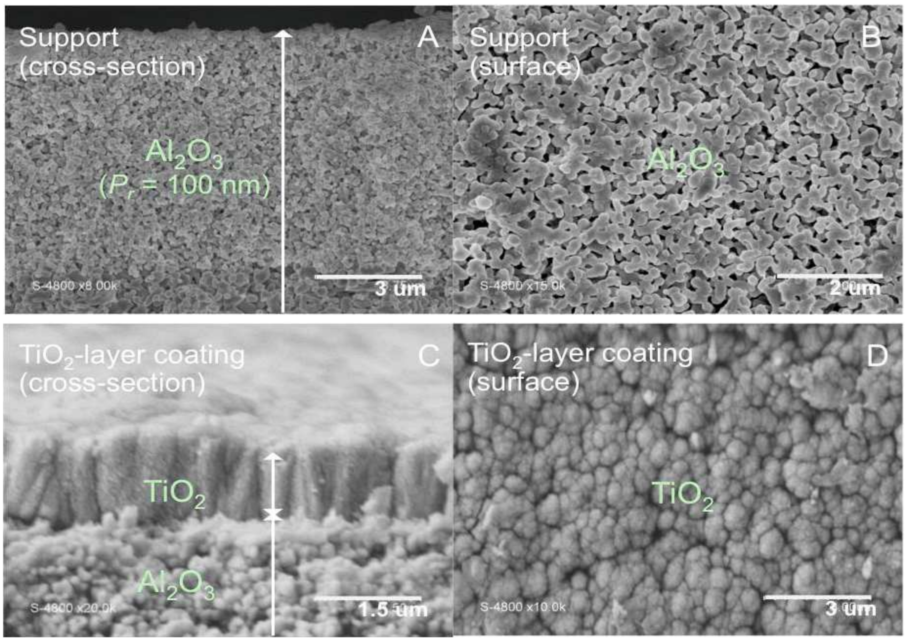

Fig. 4-9 SEM images of membrane M100 (C and D) and the support (A and B).

The amount of transported MB through M100 in the absence of UV irradiation along with 8 h is plotted in Figure 4-10. Following, the diffusion test was carried on the same membrane with interval UV irradiation each another hour. Three repetition "diffusion + irradiation" tests were made and displayed as 1st, 2nd and 3rd test in Figure 4-10.

Except the periods of alternated UV irradiation, MB concentration in the reception tank versus time increases in agreement with Fick's law. Moreover, it could be proved that the mass balance in solution (feed and reception) is correctly respected, thanks to the initial saturation of the membranes surface. During the irradiation times, a decrease of MB concentration is observed in the reception tank. In some cases, the final concentration at the end of the irradiation period is lower than the initial concentration at the beginning of the previous period with UV. This result indicates that the destroyed amount of MB is larger than that crossing the membranes by diffusion. From the change of slope corresponding to the UV irradiation periods, it is possible to evaluate δ_{MB}, the quantity of destroyed MB per unit time and per unit membrane surface area. [14]

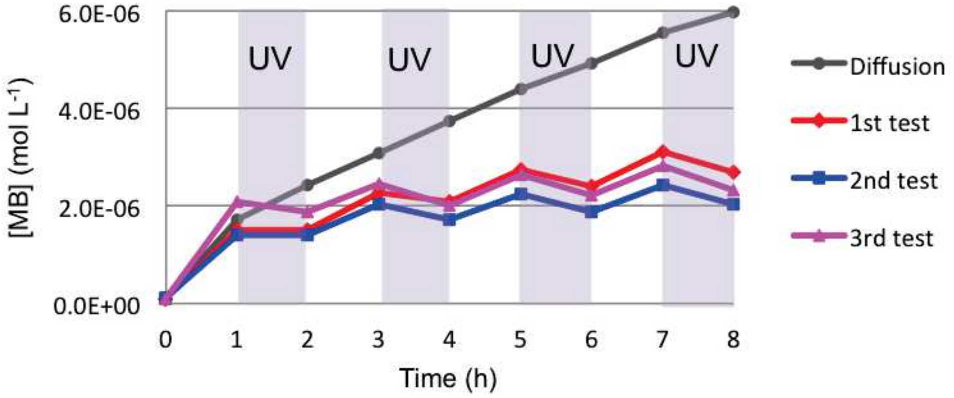

Fig. 4-10 Diffused MB through membrane M100 in the absence of UV irradiation (grey) and with periodic UV irradiation each an hour (colored).

The quantity of photodegraded MB solute per unit time and per unit area (δ_{MB}) is determined with the method presented in Figure 4-11. Due to the low evolution of solute concentration in the reception tank during short periods of few hours, the applied linear interpolation by extrapolating the previous diffusion rate are well acceptable.

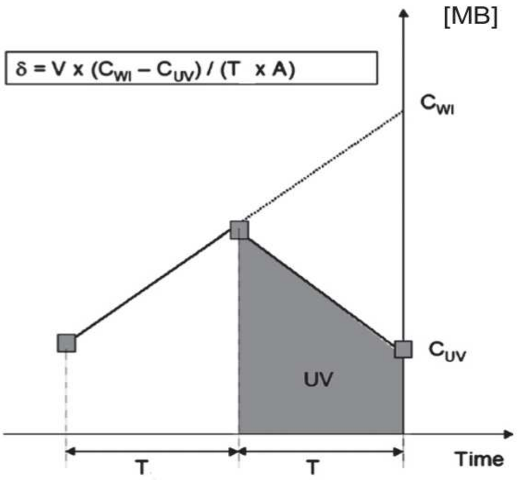

Fig. 4-11 Calculation of δ_{MB} (quantity of destroyed MB per unit time and per unit surface area): V is the liquid volume in the reception tank ($V = 0.09$ L), C_{UV} is MB concentration measured in the presence of UV irradiation, C_{WI} is MB concentration without irradiation (theoretical value), T is duration with UV irradiation ($T = 1$ h) and A is the membrane surface area ($A = 1.26\times10^{-3}$ m^2). [14]

Table 4-1 Values of δ_{MB} (quantity of photodegraded MB solute per unit time and per unit membrane area) related to membrane M100 (TiO_2-layer coating).

Time (h)	**δ_{MB} (mol/m^2 s)**		
	1st test	**2nd test**	**3rd test**
1 - UV off	-	-	-
2 - UV on	1.99×10^{-8}	1.85×10^{-8}	3.21×10^{-8}
3 - UV off	-	-	-
4 - UV on	1.34×10^{-8}	1.40×10^{-8}	1.48×10^{-8}
5 - UV off	-	-	-
6 - UV on	1.43×10^{-8}	1.28×10^{-8}	1.52×10^{-8}
7 - UV off	-	-	-
8 - UV on	1.67×10^{-8}	1.37×10^{-8}	1.56×10^{-8}
Average	1.61×10^{-8}	1.48×10^{-8}	1.94×10^{-8}

As a result, δ_{MB} is calculated in the presence of UV irradiation (50 W m^{-2}, 355 nm) and the results from the three repetition tests are listed in Table 4-1. An average photodegradation capacity is found in the magnitude of $\delta_{MB} = 2 \times 10^{-8}$ mol m^{-1} s for TiO_2-layer coating membrane M100.

Similar degradation test was performed using ceramic support alone in order to prove the absence of autophotolysis contribution. By comparing the evolutions of permeated concentration through uncoated ceramic and TiO_2-coated ceramic (M100) under periodic UV irradiation as shown in Figure 4-12, there is no self-photolysis effect observed due to the applied UV lamp. It is also found that the diffusion rate through the support differs that through M100, which could be explained specific sorption and/or interaction of Al_2O_3-MB and TiO_2-MB. Surface hydrophilicity of Al_2O_3 and TiO_2 could also be taken into account for inorganic-organic interaction in aqueous circumstance.

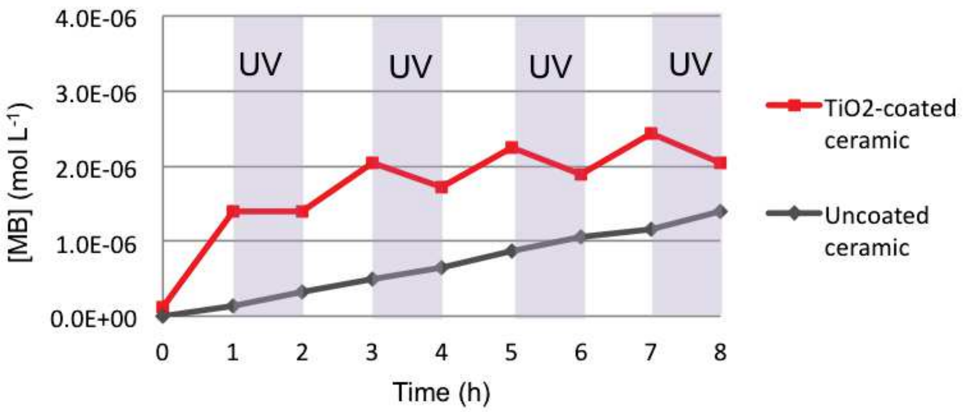

Fig. 4-12 “Diffusion + irradiation” tests on membrane M100 and the support alone proving the absence of self-photolysis.

2.2 Morphology and catalytic efficiency of TiO_2-skin coating (M800)

TiO_2-skin coating on alumina support (of top-layer pore size P_r = 800 nm) was achieved by shortening PECVD duration. To obtain TiO_2 coverage but without pore blockage on the support, deposition durations of 3, 5, 7 and 10 min were respectively experimented in PECVD process. SEM surface investigation are exhibited in Figure 4-13: inadequate TiO_2 coverage is observed for 3 and 5-min deposition (A and B); a properly covered surface with TiO_2 is seen on 7-min deposition (C) and excessive coverage is found on 10-min deposition (D). Theoretical thickness of TiO_2 coverage can be calculated with knowing the average deposition rate as 65 nm min^{-1} with the optimized PECVD operating conditions.

Eventually, 7 min was determined in PECVD process to prepare membrane M800 with TiO_2-skin coating (theoretical thickness ~ 450 nm). SEM images of the membrane M800 and the alumina support are presented in Figure 4-14.

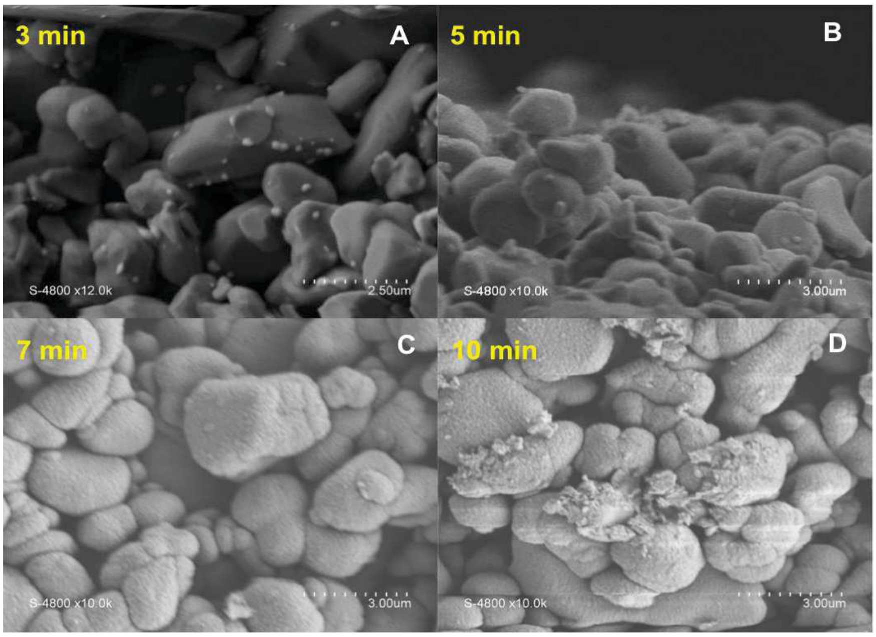

Fig. 4-13 SEM surface images of TiO_2 skin-covering on ceramic with variant PECVD deposition duration: (A) 3 min, (B) 5 min, (C) 7 min and (D) 10 min.

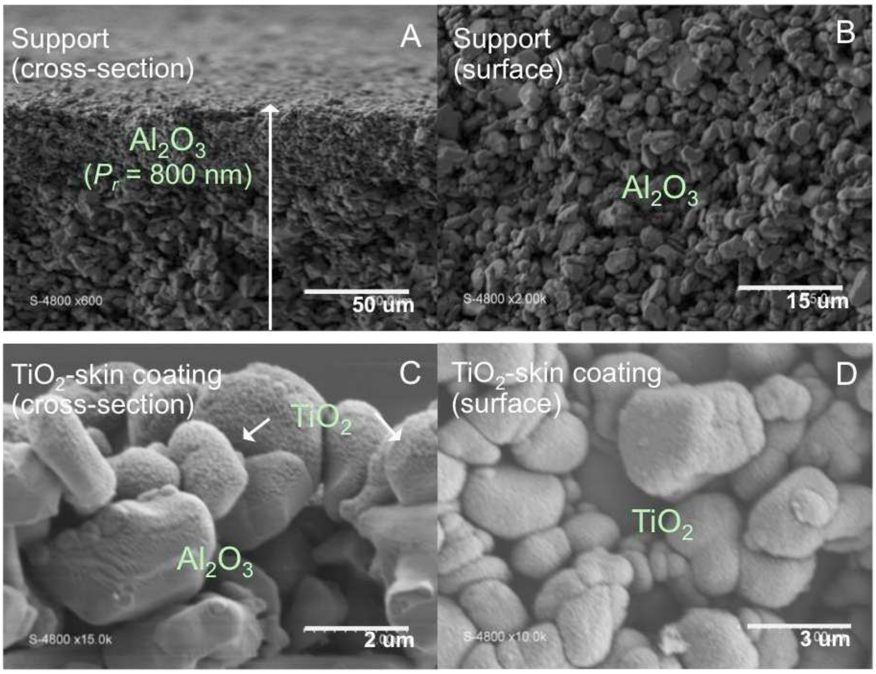

Fig. 4-14 SEM images of membrane M800 (C and D) and the support (A and B).

MB in aqueous solution transported through the TiO_2-skin coating membrane M800 was measured as in the method described in previous section in the absence of UV irradiation (increased MB concentration in reception tank due to concentration gradient) and in the presence of periodic UV irradiation every another hour (change of MB concentration in reception tank due to competition between diffusion and photodegradation rates). Results of the diffusion test and repeated tests on “diffusion + irradiation are summarized in Figure 4-15.

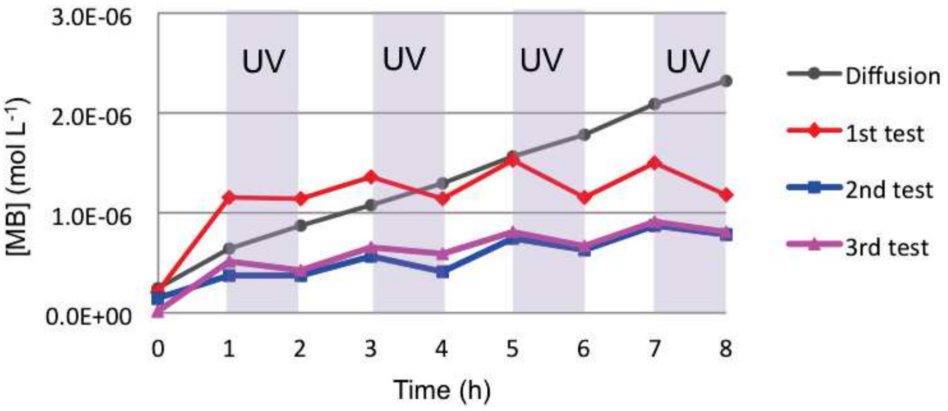

Fig. 4-15 Diffused MB through membrane M800 in absence of UV irradiation (grey) and with periodic UV irradiation each one hour (colored).

Quantity of photodegraded MB solute per unit time and per unit surface area (δ_{MB}) is calculated with the same method previously explained. Averaged δ_{MB} values of of TiO_2-skin coated M800 membrane in the presence of periodic UV irradiation (50 W m^{-2}, 355 nm) are listed in Table 4-2. The result of average photodegrading capcity of membrane M800 is close to 1×10^{-8} mol m^{-2} s^{-1}.

Table 4-2 Values of δ (the quantity of photodegraded MB solute per unit time and per unit membrane area) caused by membrane M800 (TiO_2-skin coating).

Time (h)	**δ_{MB} (mol/m^2 s)**		
	1st test	**2nd test**	**3rd test**
1 - UV off	-	-	-
2 - UV on	1.38×10^{-8}	3.28×10^{-8}	8.80×10^{-9}
3 - UV off	-	-	-
4 - UV on	6.33×10^{-9}	5.04×10^{-9}	4.22×10^{-9}
5 - UV off	-	-	-
6 - UV on	1.10×10^{-8}	6.57×10^{-9}	5.04×10^{-9}
7 - UV off	-	-	-
8 - UV on	9.45×10^{-9}	5.04×10^{-9}	4.93×10^{-9}
Average	1.01×10^{-8}	1.24×10^{-8}	5.75×10^{-9}

At the mean time, the same photodegradation test was made on the support of M800 in diffusion conditions with the same UV operation. As shown in Figure 4-16, self-photolysis effect is excluded on the relevant support alone.

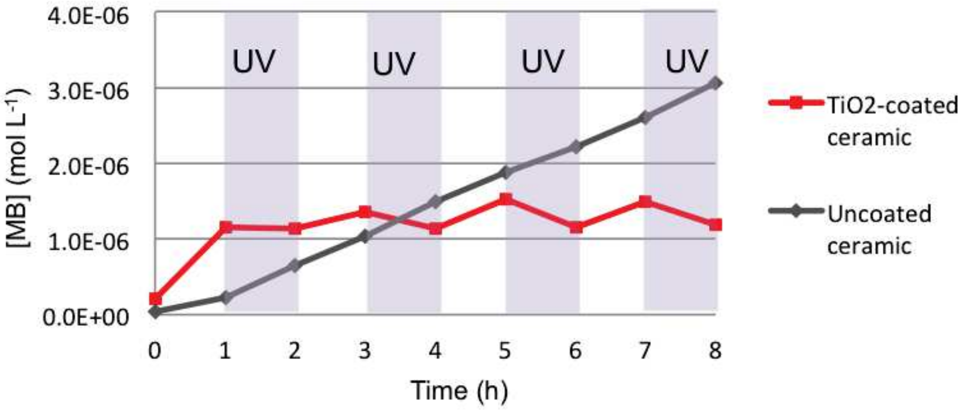

Fig. 4-16 “Diffusion + irradiation” tests on membrane M800 and its support proving the absence of self-photolysis.

In a summary, average values of δ_{MB} over three cycles under UV source (50 W m^{-2}, 355 nm) are 2×10^{-8} mol m^{-2} s^{-1} and 1×10^{-8} mol m^{-2} s^{-2} for membrane M100 and M800 respectively.

These values are in the same order of magnitude as those previously measured for titania membranes prepared by sol-gel route in our group [14] or for Ag-titania-polymer composite membranes in a very recent paper. [203] Moreover, these values are two orders of magnitude higher than those measured for ceramic supports alone (2.4×10^{-10} mol s^{-1} m^{-2} and 3.6×10^{-10} mol s^{-1} m^{-2} for supports with 100 nm pore size and 800 nm pore size respectively), which proves that supports do not contribute to the photodegradation.

3 Photocatalytic activity of PECVD TiO_2-based membrane in dynamic condition

By applying pressure in the membrane process, catalytic performance of TiO_2-based membrane has been investigated in dynamic condition in two different membranes reactors: one is placing photoactive TiO_2 surface in contact with permeate solution (pilot-scale unit) and the other is with feed solution (lab-scale unit).

3.1 Configuration with photoactive TiO_2 layer toward the feed (pilot-scale unit)

As described in chapter 2, pure water permeance through TiO_2-Al_2O_3 composite membranes was first measured. The water permeance was determined from the volume flux of water (J_{water}) versus the transmembrane pressure (ΔP) as presented in Figure 4-17 and Figure 4-18 for membrane M100 and M800 respectively. For each membrane type, more than three duplicated membranes were prepared and examined in water permeation test. In general, reproducible permeating performance was observed.

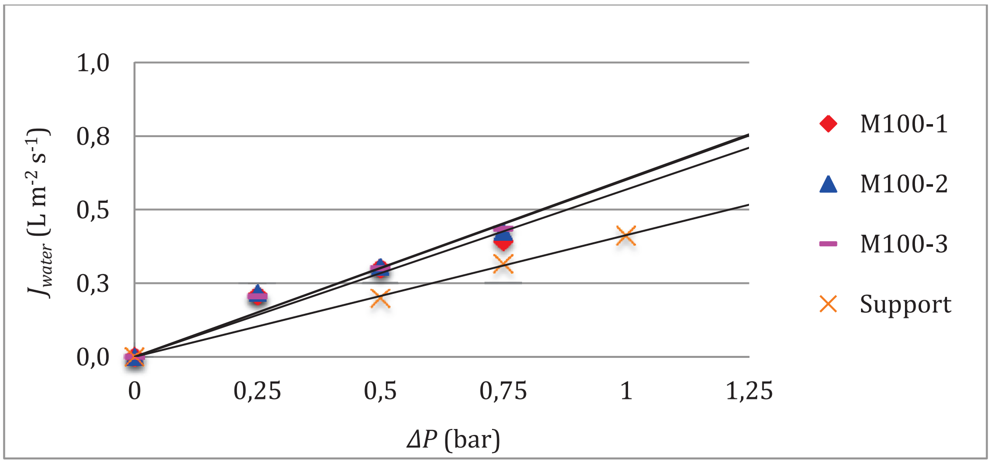

Fig. 4-17 Water flux through three duplicated M100 membranes (with TiO_2-layer coating).

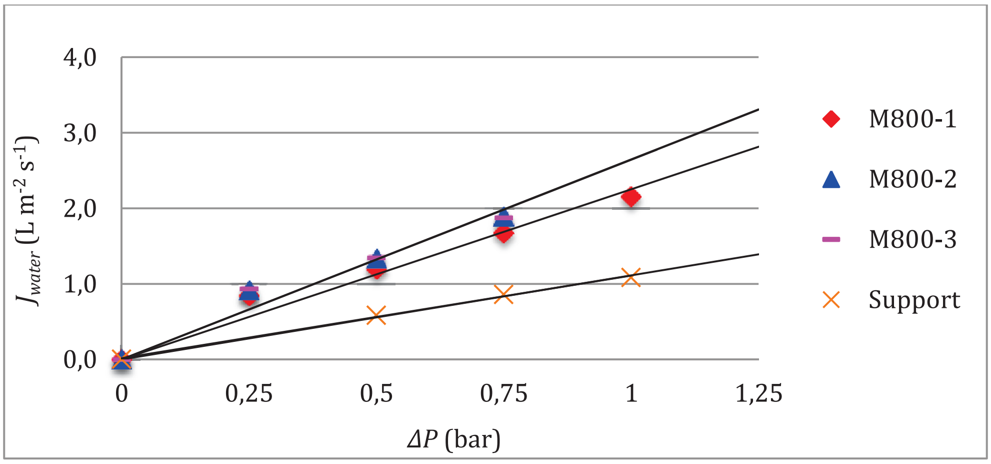

Fig. 4-18 Water flux through three duplicated M800 membranes (with TiO_2-skin covering).

Water permeance was measured as 0.38 L m^{-2} s^{-1} bar^{-1} (i.e. 1368 L m^{-2} h^{-1} bar^{-1}) and 1.89 L m^{-2} s^{-1} bar^{-1} (i.e. 6804 L m^{-2} h^{-1} bar^{-1}) for M100 and M800, respectively. Such values of water permeance are among the highest reported in the literature for many kinds of titania membranes. [127, 199-201, 204] A higher flow permeance of the M800 is obtained due to higher mean pore size of the support and absence of a denser top layer. Indeed, as shown previously, in the case of M100, the anatase film is in the form of conform top layer, whereas in the case of M800, the anatase material is not an entire layer but a skin-coverage.

In the case of M100, the water permeance is slightly higher than that of the support alone (0.41 L s^{-1} m^{-2} bar^{-1}) maybe due to hydrophilicity of the additional anatase layer. In the case of M800, the water permeance is almost twice higher than that of the support alone (1.11 L s^{-1} m^{-2} bar^{-1}), certainly due to the pronounced hydrophilic nature of the anatase material (water contact angle equal to 29° as measured for a plasma film deposited on silicon wafer in a previous paper by our group. [31] As a comparison, the water contact angle of a naturally oxidized silicon is in the range 60-70°. [205]) On the other hand, PECVD coating could have plasma etching effect on the substrate that increases a general porosity in the substrate. For instance the porosity was discovered as 44.5% and 36.8% for M100 and its support with mercury porosimetry method. In both cases, the permeation ability of membranes has been clearly demonstrated.

Table 4-3 Calculating the expected photodegradation ratio of MB (C/C_0) according to the measured δ_{MB} (from diffusion condition) and water flux J (at $\Delta P = 0.25$ bar).

Membr. type	δ_{MB} (mol m^{-2} s^{-1})	ΔP (bar)	J_{water} (L m^{-2} s^{-1})	$C = \delta_{MB}/J_{water}$ (mol L^{-1})	C_0 in pilot (mol L^{-1})	Expected C/C_0
M100-1	2×10^{-8}	0.25	0.15	1.33×10^{-7}	2.50×10^{-7}	53%
M100-2	2×10^{-8}	0.25	0.18	1.11×10^{-7}	2.50×10^{-7}	44%
M800-1	1×10^{-8}	0.25	0.9	1.25×10^{-8}	1.25×10^{-7}	10%
M800-2	1×10^{-8}	0.25	0.8	1.11×10^{-8}	1.25×10^{-7}	9%

As UV lamp being switched on, concentration in the permeation flow (C_{pilot}) was analyzed each 5 min in 60-min operation. The experimental values of photodegradation rate R_{MB} measured on M100 and M800 membranes are presented in Figure 4-19.

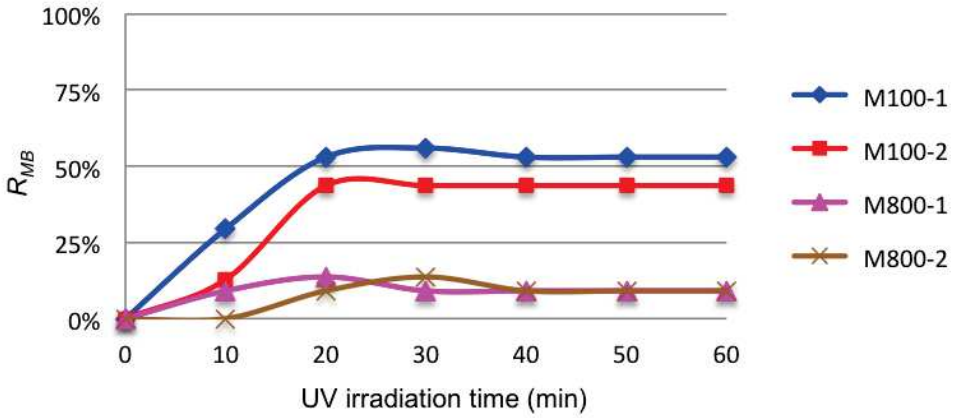

Fig. 4-19 Measured photodegradation R_{MB} on membranes M100 (duplicated) and M800 (duplicated) in the pilot-scale unit with constant UV irradiation (50 W/m^2, 355 nm).

The first 20-min R_{MB} was not constant due to the geometry of pilot cell that permeate compartment has 50 mL remaining solution (without being photodegraded) to run out of the unit. After consumption of the remained permeation solution (in 20 min), constant reduced concentrations were found in the permeating flow because of photocatalysis process with continuous UV illumination. Membrane M100 performed about 5 times higher photocatalytic efficiency than that of M800, which could be caused by slower transmembrane flowing speed and larger δ_{MB} of M100. It was observed that approx. 50% of MB molecules in water has been degraded by M100 membranes from feed concentration 3.2×10^{-7} mol L^{-1} at transmembrane pressure 0.25 bar. Whereas for M800 membrane, it was found that approx. 10% of MB molecules was destroyed from the feed of concentration 1.25×10^{-7} mol L^{-1} at the same pressure.

As displayed in Figure 4-20 and Figure 4-21, the experimental results of photodegrading capacity of M100 and M800 respectively are in very good accordance with expected values (Table 4-3). It proves the absence of defects on membranes and pilot-scale unit. Moreover, reproducible performance was maintained on duplicate membranes of each coating format under the same pilot operation.

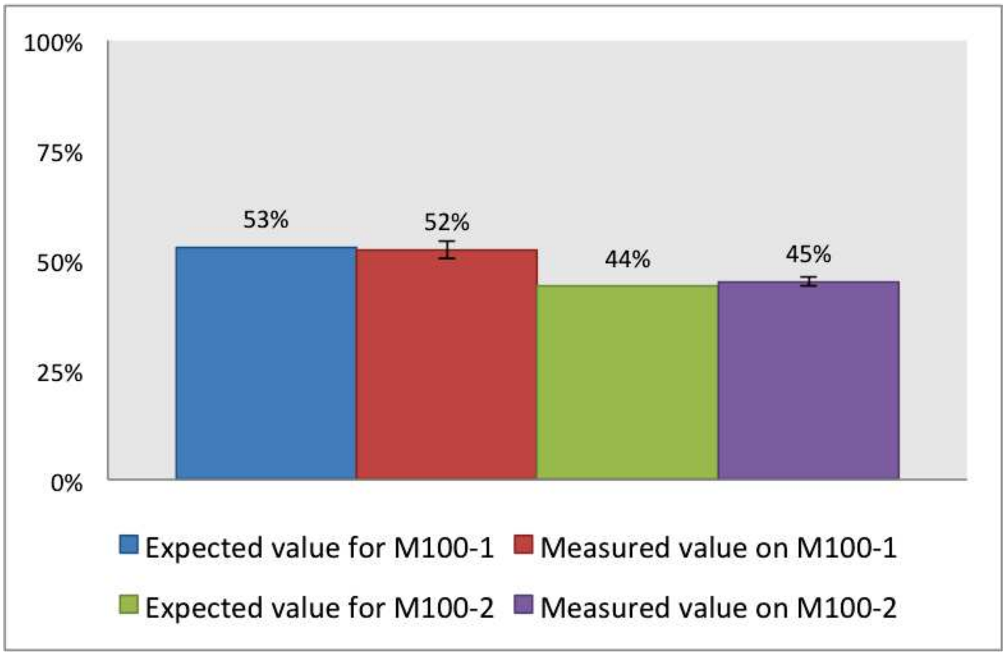

Fig. 4-20 Expected and experimental R_{MB} values on duplicate membrane M100-1 and M100-2 with UV irradiation (50 W m^{-2}, 355 nm).

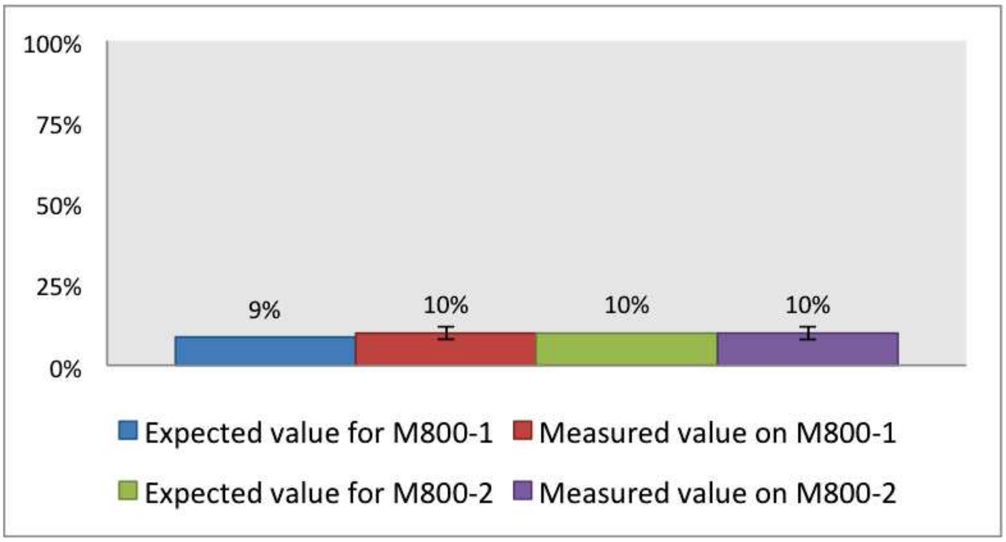

Fig. 4-21 Expected and experimental R_{MB} values on duplicate membrane M800-1 and M800-2 with UV irradiation (50 W m^{-2}, 355 nm).

3.2 Configuration with photoactive TiO_2 layer in contact with feed (lab-scale unit)

As described in chapter 2, model compound acid orange 7 (AO7) and phenol have been used as due compounds in the lab-scale membrane reactor configured with photo-active TiO_2 layer to the feed. UV lamp either of low intensity 4 W (at $\lambda = 254$ nm or $\lambda = 365$ nm) or of high intensity 500 W (UVA emission from 360 nm) has been employed as the irradiation source to study their effect on membrane's photocatalytic efficiency.

3.2.1 Acid orange 7 as degraded model compound

UV absorbance spectrum from wavelength 200 – 500 nm of prepared AO7 solution is presented in Figure 4-22, where a maximum absorbance wavelength was found at 485 nm. Following, the calibration curve of AO7 absorbance at $\lambda = 485$ nm versus concentration of AO7 solution is plotted in Figure 4-23.

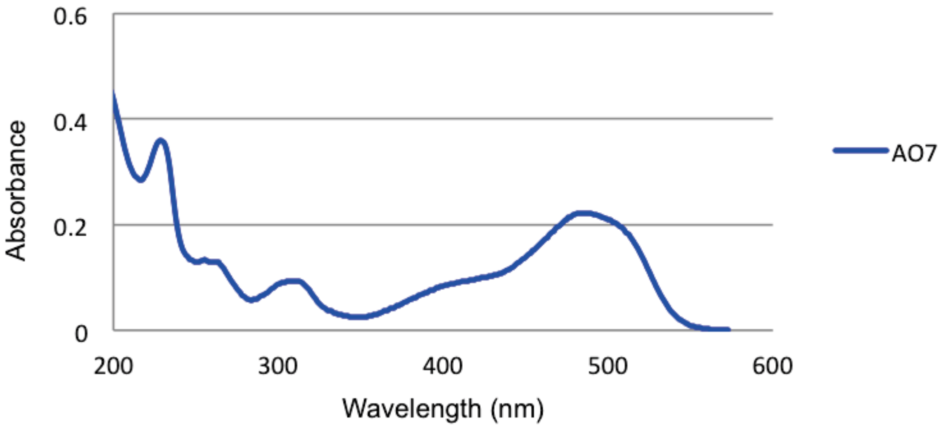

Fig. 4-22 UV absorbance spectrum of AO7 compound in water ($C = 1\times10^{-5}$ mol L^{-1}).

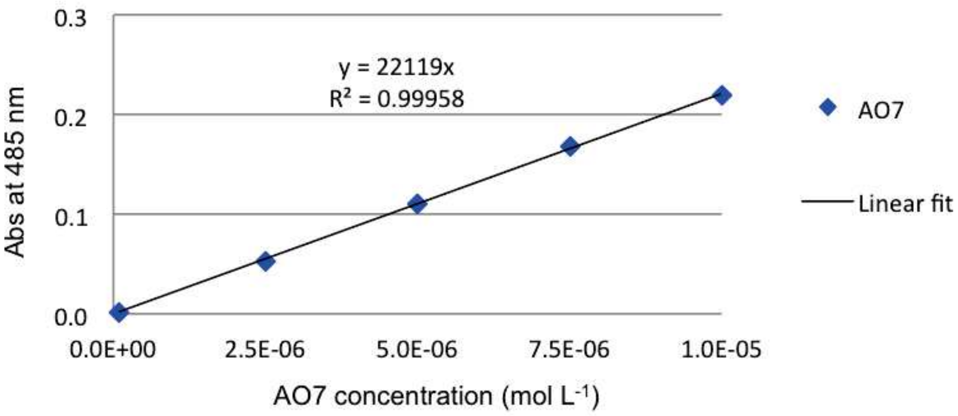

Fig. 4-23 Absorbance of AO7 at λ = 485 nm (in water) versus concentration.

Membranes LF03, LF04 and LF05 were prepared by an intership student (Li, F.) with PECVD duration 10, 15 and 20 min respectively on porous ceramic of top-layer *Pr* = 800 nm. Water permeation through the membrane LF04 and its support is plotted out versus pressure as in Figure 4-24. It is consistently found out that TiO_2-skined ceramic has almost twice higher water permeance than that of the ceramic alone.

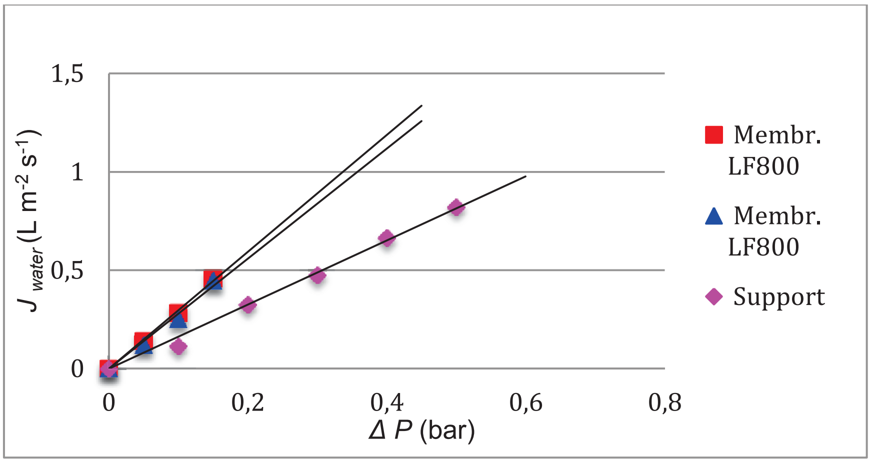

Fig. 4-24 Water flux through membrane LF04 and its support in the lab-scale unit.

3.2.1.1 Effect of PECVD condition

Membranes LF100 were 100 nm pore-sized supports coated with TiO_2 layer with deposition duration equal to 20 min (LF100-a) and 40 min (LF100-b). On the other hand, membranes LF800 were 800 nm pore-sized supports coated with TiO_2 layer with deposition duration equal to 20 min (LF100-a) and 40 min (LF100-b). Photocatalytic performances of AO7 dye by membrane LF100 and LF800 using high intensity 500 W UV lamp are presented in Figure 4-25 and Figure 4-26 respectively.

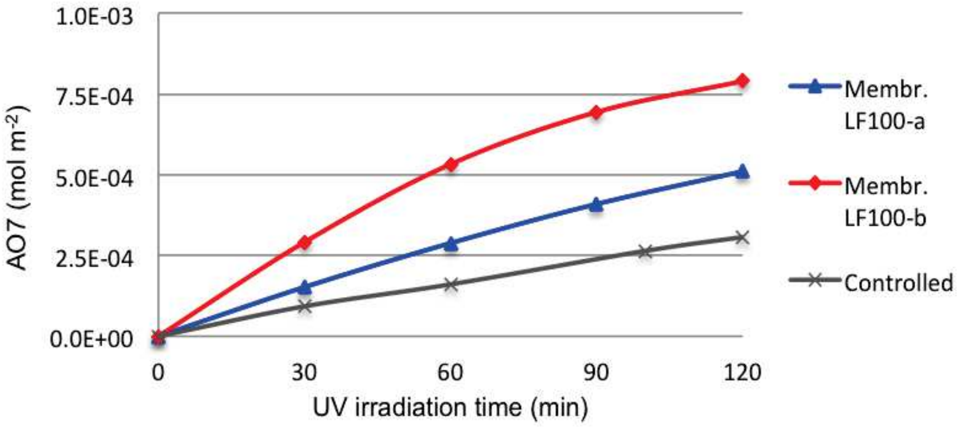

Fig. 4-25 Effect of deposition duration on photodegraded AO7 per unit surface area (mol m^{-2}) for membrane LF100-a (20-min deposition), LF100-b (40-min deposition) and the support (controlled) using 500 W UV lamp of Zp-type emission (including UVA, UVB and UVC).

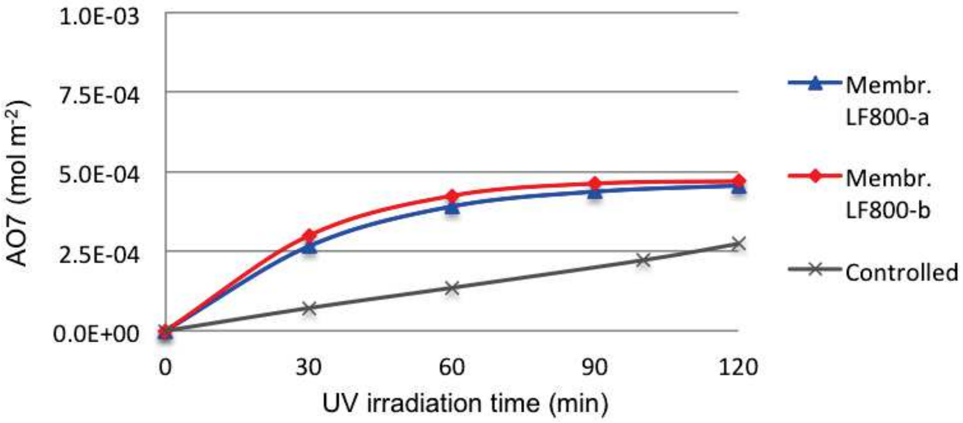

Fig. 4-26 Effect of deposition duration on photodegraded AO7 per unit surface area (mol m^{-2}) for membrane LF800-a (20-min deposition), LF800-b (40-min deposition) and the support (controlled) using 500 W UV lamp of Zp-type emission (including UVA, UVB and UVC).

Thicker TiO_2 layer (made with longer deposition duration) has improved the photodegradation rate of AO7 in the first cast of membrane LF100 (as seen in Figure 4-25), however such effect is not observed in the second case of membrane LF800 (as seen in Figure 4-26).

3.2.1.2 Effect of UV irradiation

UV lamp devices of high intensity (500 W) and low intensity (4 W) have been experimented and studied with their effect on photodegradation efficiency. The 500W UV lamp has option of Zp-type emission including UVA, UVB and UVC (from 180 nm to visible range) and of Zs-type emission including UVA (from 360 nm) . The 4 W UV lamp has alternative emitting wavelength either 365 nm or 264 nm. The lab-scale unit was operated with membrane LF800 and its support (as controlled experiment) using AO7 dye solution of initial concentration 1×10^{-5} mol L^{-1} and volume 60 mL. Circulation speed 30 ml min^{-1} and transmembrane pressure 0.1 bar have been maitained in the membrane process.

Both lamp devices were tested on membrane LF800 for degrading aqueous AO7 dye, whose results are presented in Figure 4-27 and Figure 4-28 respectively. As seen in Figure 4-27, 500 W lamp illuminated LF800 membranes shows almost complete decomposition of AO7 (up to 95%, i.e. degraded solute per unit area equal to 5.0×10^{-4} mol m^{-2}) within 2 h with both emission types of Zp and Zs. The self-photolysis effect (as the controlled) with the support alone presents almost triple degradation degree (ca, 17%) under broader irradiation spectrum (Zp type) than that under the only UVA spectrum (Zs type).

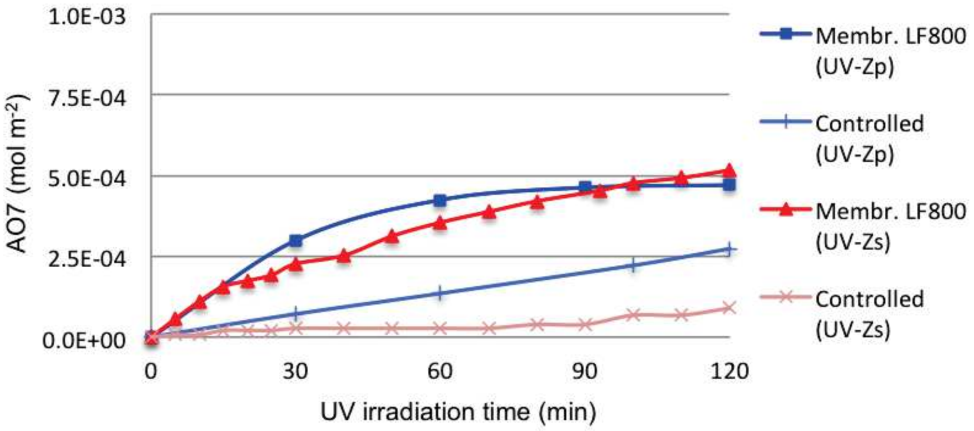

Fig. 4-27 Effect of irradiation spectrum on on photodegraded AO7 per unit surface area (mol m^{-2}) for membrane LF800 and the support (controlled) using 500 W UV lamp with alternative emission of Zp-type (UVA, UVB and UVC) and Zs-type (UVA).

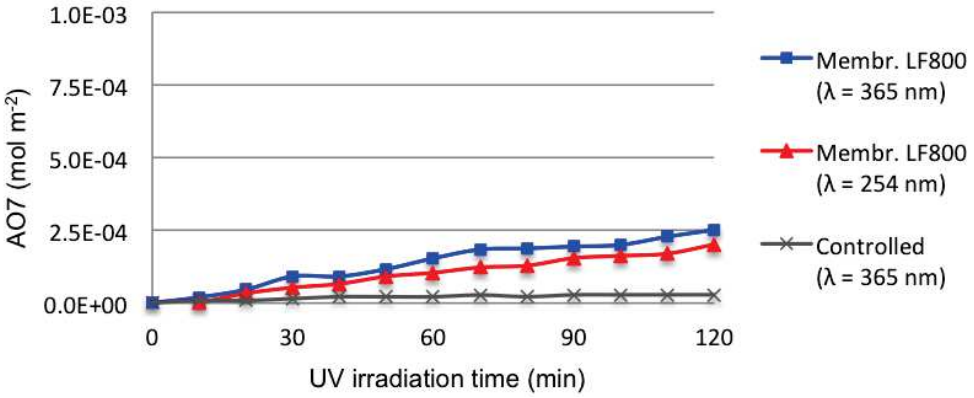

Fig. 4-28 Effect of irradiation wavelength on photodegraded AO7 per surface area (mol m^{-2}) for membrane LF800 and its support alone (as controlled) using 4 W powered-UV lamp with alternative emission λ = 365 nm or λ = 254 nm.

By replacing the 500 W UV lamp with the 4 W one (Figure 4-28), self-photolysis has been significantly reduced as less than 5% of AO7 was degraded within 2 h in the absence of photocatalytic layer. On the same membrane LF800, UV emission at λ = 365 nm caused a slightly enhanced degradation rate 54% (i.e. destroyed AO7 per unit area as 2.5×10^{-5} mol m^{-2}) in contrast to emission at λ = 254 nm with degradation rate 45% (i.e. 2.0×10^{-5} mol m^{-2}).

In a summary, photodegradation efficiency has been improved less than 10 times from 2.5 × 10^{-5} mol/m^2 (with 4 W UV irradiation) to 3.5 × 10^{-4} mol/m^2 (with 500 W UV lamp) by increasing more than 100 times of irradiation intensity. The 500 W lamp with Zs-type emission (only UVA) could be the best option of the studied devices in terms of the fastest photoreaction kinetics and a very low self-photolysis effect, yet the operation of this lamp needs to be done with more cares due to peronsal protection from the high irradiation.

3.2.1.3 Effect of dynamic conditions in membrane process

Membrane LF05 was planted in the lab-scale membrane cell and the pressure-driven membrane process was operated in the same way as mentioned previously in terms of AO7 feed solution and high-intensity UV Zs type emission (UVA from 360 nm). In many number of successive photodegradation experiments, variant transmembrane pressure of 0.05, 0.10 and 0.15 bar and flowing speeds of 20, 30 and 40 mL/min were carried out in the membrane process. Corresponding photodegradation rates of AO7 under the aspect dynamic conditions were respectively recorded along with irradiation duration 2 h.

At a fixed flowing speed of 30 mL/min in the system, transmembrane pressures ΔP equal to 0.05, 0.10 and 0.15 bar resulted in generally similar catalytic effectiveness on membrane LF05 as shown in Figure 4-29. At the end of 2.5 h irradiation, photodegradation rate reached close to 85%, 85% and 90% at ΔP = 0.05, 0.10 and 0.15 bar, respectively. The reaction efficiency is faster when applied pressure is higher as could been observed for the evolution curve recorded at 0.15 bar. Moreover the amount of decomposed solute per unit membrane area is 5.9 × 10^{-4} mol/m^2 at the highest-pressure condition. It could be explained by Langmuir model of adsorption that higher pressure (or concentration) leads to larger adsorbing capacity before the saturation of monolayer sorption.

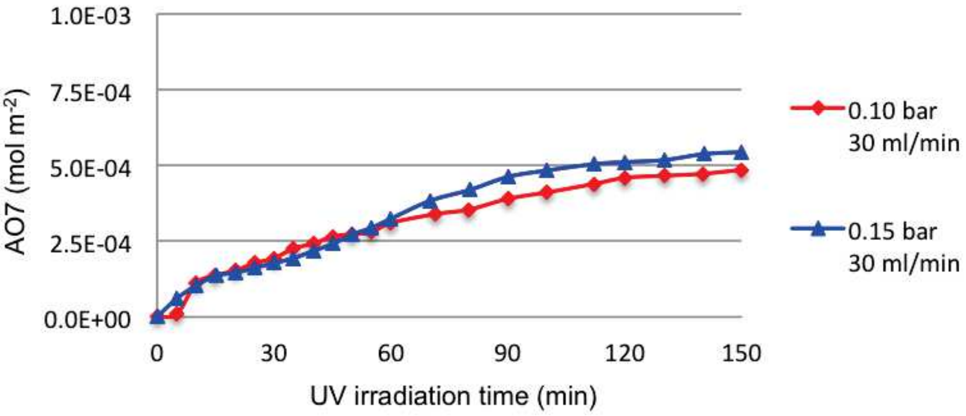

Fig. 4-29 Effect of transmembrane pressure (0.10 and 0.15 bar) on photodegraded AO7 per unit surface area (mol m^{-2}) for membrane LF800 with fixed circulation speed 30 ml min^{-1} under 500 W-powered UV Zs-type emission (UVA).

On the other hand, obtained photodegradation evolutions versus irradiation time were measured at fixed ΔP = 0.10 bar with variant flowing speeds of 20, 30 and 40 mL min^{-1}. Results of photodegradation rates are displayed in Figure 4-30. Degraded rates of 90%, 86% and 82% have been observed on the same membrane at 2-h irradiation with circulating speeds of 20, 30 and 40 mL min^{-1} respectively. The slower feed flowing speed sweeping on membrane surface has resulted in faster catalytic efficiency. Moreover, the amount of decomposed aqueous AO7 per unit membrane area is 8 × 10^{-8} mol m^{-2} s^{-1} at the lowest circulation speed. The contacting time between the solute and TiO_2 active sites could be maintaining longer when the horizontal flowing is slower. Close values of photodegradation rate of AO7 (R_{AO7}) as 90.2% and more than 90% within 2 h reaction time were found in the individual work of Zhang et al. using TiO_2 hollow fiber membrane [206] and Bai et al. using $SrTiO_3/TiO_2$ fibers modified cellulose acetate membrane [207, 208]. In Zhang et al.'s work, initial AO7 solution of volume 20 ml and concentration 20 mg L^{-1} (i.e. 5.7 × 10^{-5} mol L^{-1}) was used in the membrane process operating at transmembrane pressure 0.9 bar and circulation speed 40 ml min^{-1} (with a relatively slow water flux through the membrane at 12.2 L m^{-2} h^{-1} comparing to our results). In Bai et al.'s work, initial concentration of AO7 solution 50 mg L^{-1} (i.e. 14.3× 10^{-5} mol L^{-1}) and similarly slow water flux 10 L m^{-2} h^{-1} at 1.5 bar was maintained during the tests. In addition, Mendret et al. used TiO_2/Al_2O_3 composite membrane and found an optimal pH = 4 for photodegrading aqueous AO7 with reaction rate as 15.6 µmol L^{-1} min^{-1}, whose membrane having permeability coefficient close to ours as high as 1200 L m^{-2} h^{-1} [209, 210].

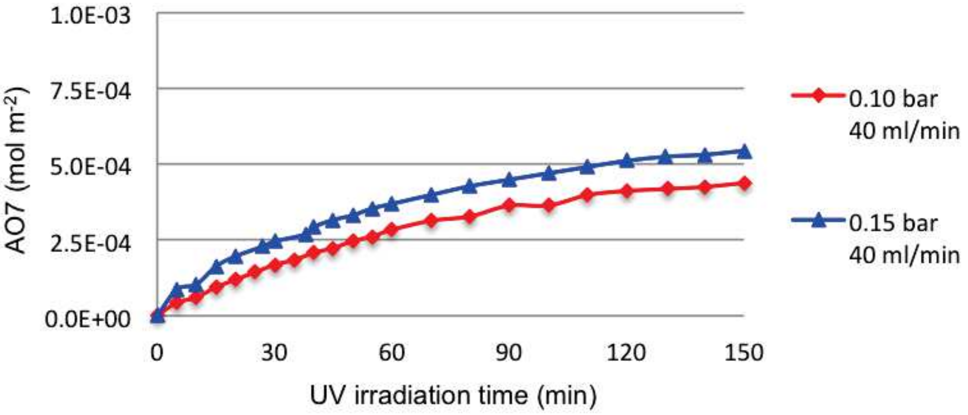

Fig. 4-30 Effect of transmembrane pressure (0.10 and 0.15 bar) on photodegraded AO7 per unit surface area (mol m^{-2}) for membrane LF800 with fixed circulation speed 40 ml min^{-1} under 500 W-powered UV Zs-type emission (UVA).

3.2.2 Phenol as degraded model compound

Phenol (C_6H_6O) has been used as the dye compound for the characterization of membrane M100, using a 4 W-powered UV irradiation at λ = 365 nm. Concentration of phenol in aqueous solution was analyzed with HPLC-UV method. An example of HPLC-UV analysis on phenol solution is given in Figure 4-31. Retention time of phenol in the applied HPLC method was found at 4.7 min. Absorbance at wavelength 254 nm was measured at each retention time and thus concentration of phenol solution was calculated from calibration curve.

Adsorption of phenol on membrane M100 and the support along has been carried out at 37 °C. The adsorbed phenol per unit volume within 100 min is presented in Figure 4-32. It is consistently found that the porous support itself could have larger adsorbing capacity for organic solute as the previous work on sorption of AO7 compound. As explained previously, different wettability of alumina and anatase TiO_2 surfaces.

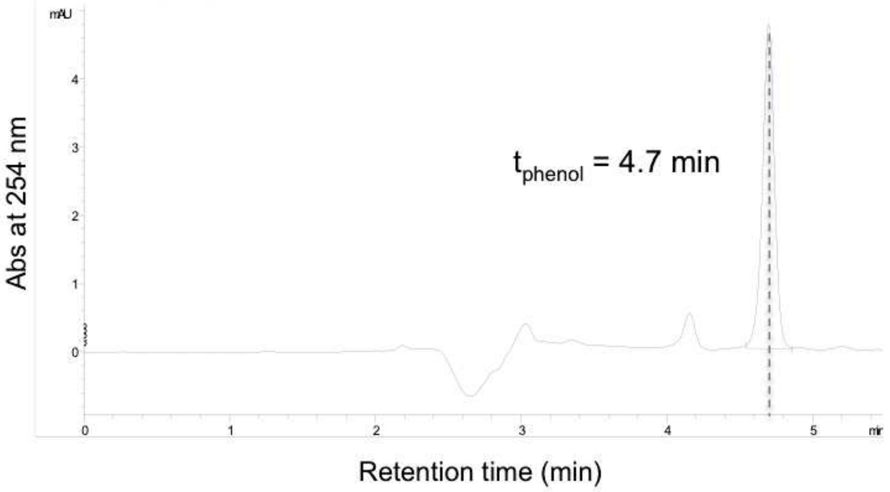

Fig. 4-31 HPLC-UV analysis on phenol in aqueous solution.

Photodegradation experiment was carried out using phenol solution of initial concentration 1× 10^{-4} mol/L (10 times higher than the case of AO7 compound in previous work) and in the volume 65 mL. Low intensity 4 W-powered lamp with emission at λ = 365 nm was applied as the UV source in the test. The feed tank was maintained at 24 and 37 °C as the reaction temperature, whose results on the amount of degraded phenol by the membrane M100 is given in Figure 4-32. Transmembrane pressure was studied at 0.3, 0.5 and 0.7 bar at constant circulation speed 40 mL min^{-1} with the corresponding degraded number of phenol is given in Figure 4-33.

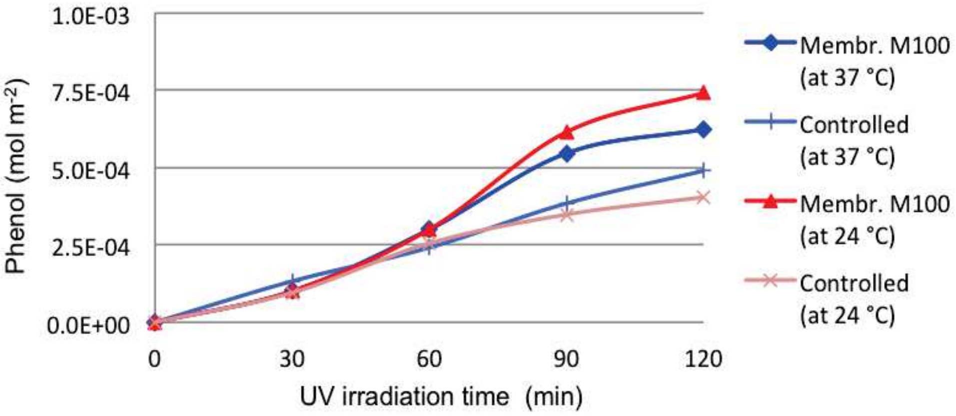

Fig. 4-32 Degraded phenol at different reaction temperature of 24 °C and 37 °C operated at the same transmembrane pressure 0.7 bar.

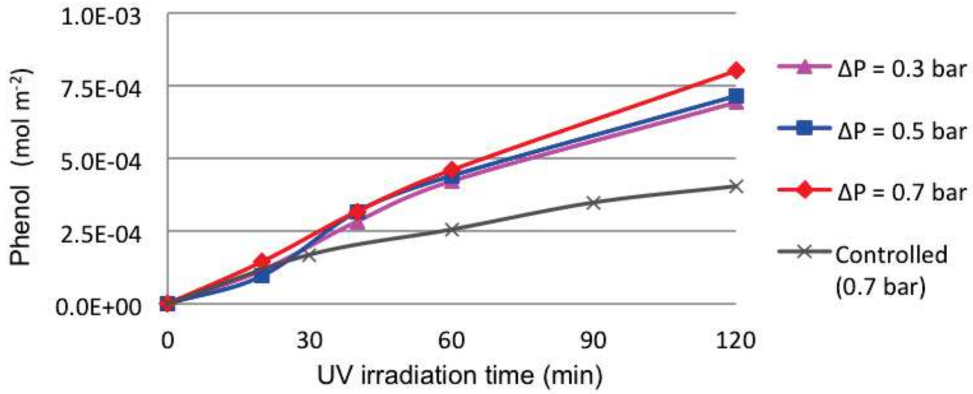

Fig. 4-33 Degraded phenol at different transmembrane pressure at 0.3, 0.5 and 0.7 bar operated at the same temperature 24 °C.

The controlled experiment was made on the alumina support alone and it was found that 12% of phenol could be degraded at 2 h without applying coated TiO_2 layer. Combined with the coated anatase TiO_2 layer, almost twice higher photodegradation rate of phenol, equal to 20% (i.e. destroyed phenol per membrane surface area equal to 1.1×10^{-7} mol m^{-2} s^{-1}) was observed than that of the support alone at $\Delta P = 0.7$ bar. It was pointed out in Yang et al.'s work that photodegradation of phenol by TiO_2 modified polymer membrane was 32.5% at longer-lasting 6 h irradiation time using initial phenol solution of volume 200 mL and concentration 10 mg L^{-1} (i.e. 1×10^{-4} mol L^{-1}) [211]. In another work of Djafer et al. it was found the degrading rate of the organic solute (including phenol) in the range of $0.8 - 3.8 \times 10^{-8}$ mol m^{-2} s^{-1} using TiO_2/Al_2O_3 composite membrane [14].

Reaction kinetic constant k (min^{-1}) reflects how fast a reaction is taking place. We compare the kinetic performance of composite TiO_2/Al_2O_3 membranes M100, M800 and LF03 using different pollutant organic compounds and UV lamps in PMR reactors, as listed in Table 4-4. Assuming that the photocatalytic process is a first-order kinetic reaction for the first 10 min, we could simply know the k (min^{-1}) according to the equation $ln(C/C_0) = -kt$, where C and C_0 are the instant and initial concentration in the liquid phase and t is UV irradiation time. Membrane M100 is characterized by a k (min^{-1}) = 0.041 close to that reported in literature for a TiO_2/Al_2O_3 membrane prepared from atmospheric plasma spray (APS) method having k (min^{-1}) = 0.076 when degrading the same MB compound in water [147].

Table 4-4 Photocatalytic reaction kinetic constant *k* (min^{-1}) of composite TiO_2/Al_2O_3 membranes prepared with PECVD method in this work. (MB: methylene blue and AO7: acid orange 7)

Membrane	Reaction kinetics *k* (min^{-1})	Polluant compound in water	UV irradiation
M100	0.041	MB (3×10^{-7} mol L^{-1})	355 nm, 50 W m^{-2}
M800	0.010	MB (1.25×10^{-7} mol L^{-1})	355 nm, 50 W m^{-2}
LF03	0.017	AO7 (1×10^{-5}mol L^{-1})	360 nm, 760 W m^{-2}
LF03	0.007	AO7 (1×10^{-5}mol L^{-1})	365 nm, 18 W m^{-2}
M100	0.017	Phenol (1×10^{-4}mol L^{-1})	365 nm, 18 W m^{-2}

As a summary, lab-scale unit with membrane's photoactive surface in contact with feed solution and pilot-scale unit with the active surface in contact with permeate solution have been both experimented. Degraded model compounds including MB, AO7 and phenol were used to investigate photocatalytic performance of membrane M100 and membrane LF04. Moreover, UV sources of options different intensity and emitting wavelengths were tested their effect on photodegradation reaction. Further on, the dynamic conditions as transmembrane pressure and circulation speed were examined in the testing membrane process.

4 Modeling of sorption and photocatalyzed reaction process

4.1 Modeling of sorption experiments

To identify independently the sorption parameters of membrane the sorption experiments in batch system has been carried out as described in chapter 2.

4.1.1 Mathematical descriptions

Two mathematical models have been developed. The first one is neglecting the effect of diffusion in body of membrane the second one is taking the effect of diffusion into account. These models have been used for evaluation of adsorption rate constants and sorption capacities.

Adsorption model 1

This model is neglecting external and internal mass transfer and accounting the infinite diffusion rate inside the membrane body (including the TiO_2 layer and Al_2O_3 porous support). Under these assumptions the concentration of i-th component in liquid phase inside of porous structure of membrane is equal to the concentration in tank and no concentration gradient in liquid phase is present.

The mass balance equation for i-th component in the tank can be written as:

$$V\frac{dc_i}{d\tau} = -V_{MS}\left[\frac{\delta_M\left(1-\varepsilon_M\right)}{\delta_M+\delta_S}\rho_M r_{ads}^M + \frac{\delta_S\left(1-\varepsilon_S\right)}{\delta_M+\delta_S}\rho_S r_{ads}^S\right] \tag{4-1}$$

where c_i denotes the concentration of i-th component in tank, V volume of tank , V_{MS} volume of membrane with support and τ time.

The mass balances for adsorption of i-th component in catalytic layer and support are given by following Equation 4-2 and Equation 4-3.

$$\frac{dq_i^M}{d\tau} = r_{ads}^M \tag{4-2}$$

$$\frac{dq_i^S}{d\tau} = r_{ads}^S \tag{4-3}$$

The initial conditions are: $q_i^S = 0$, $q_i^M = 0$, $c_i = c_{i0}$.

Adsorption model 2

This model is neglecting external mass transfer and only the effect of diffusion in both membrane layer and support is taken into account. The mass balance of i-th component in tank under this assumption can be described by equation 4-4:

$$V\ \frac{dc_i}{d\tau} = A_M \varepsilon_M D_{Mi} \left.\frac{\partial c_i^M}{\partial x}\right|_{x=0} - A_M \varepsilon_S D_{Si} \left.\frac{\partial c_i^S}{\partial x}\right|_{x=\delta_M+\delta_S} \tag{4-4}$$

The mass balance equations in porous photo-active layer contain mass transport by diffusion and adsorption on catalyst surface:

$$\frac{\partial c_i^M}{\partial \tau} = D_i \frac{\partial^2 c_i^M}{\partial x^2} - \frac{(1-\varepsilon_M)}{\varepsilon_M} \rho_M r_{ads}^M \tag{4-5}$$

$$\frac{\partial q_i^M}{\partial \tau} = r_{ads}^M \tag{4-6}$$

where D_i is diffusion coefficient of component i and is assumed constant along all axial coordinate x.

The mass balance equations in porous support is also accounting for mass transport by diffusion and adsorption on membrane support surface

$$\frac{\partial c_i^S}{\partial \tau} = D_i \frac{\partial^2 c_i^S}{\partial x^2} - \frac{(1-\varepsilon_S)}{\varepsilon_S} \rho_S r_{ads}^S \tag{4-7}$$

$$\frac{\partial q_i^S}{\partial \tau} = r_{ads}^S \tag{4-8}$$

The initial, boundary and interfacial conditions are as follow:

$$\tau < 0 : c_i^M = c_{i0}^M, c_i^S = c_{i0}^S, q_i^M = q_{i0}^M, q_i^S = q_{i0}^S$$

$$\tau \ge 0 : \qquad x = 0 : c_i^M = c_i$$

$$x = \delta_M : \varepsilon_M \frac{\partial c_i^M}{\partial x} = \varepsilon_S \frac{\partial c_i^S}{\partial x}$$

$$c_i^M = c_i^S$$

$$x = \delta_M + \delta_S : c_i^S = c_i$$

4.1.2 Results of sorption modeling

Calculation of sorption parameters is carried out with assumption that the membrane has been dried before immersing in the solution of the initial conditions. In an agreement with operated experiments the ideally mixed compartment with solution has been used. As mentioned above two models have been developed: 1) one neglecting internal diffusion in the body of membrane and 2) one accounting for internal diffusion in the body of membrane (support or TiO_2-coated support)

Adsorption model 1(neglecting internal mass transfer)

A) Calculation for adsorption on the support

Sorption capacity of the support, rate constant of adsorption (k_a) and desorption (k_d) for AO7 solute has been calculated. The values of these parameters have been obtained on the base of minimizing the sum of squares of deviation between the experimental and calculated (model) values.

It was calculated for both experiments carried out using initial concentrations 5×10^{-5} mol L^{-1} and 1×10^{-4} mol L^{-1}. The comparisons between experimental and calculated values for both situations ($C_0 = 5 \times 10^{-5}$ and 1×10^{-4} mol L^{-1}) are presented in Figure 4-34.

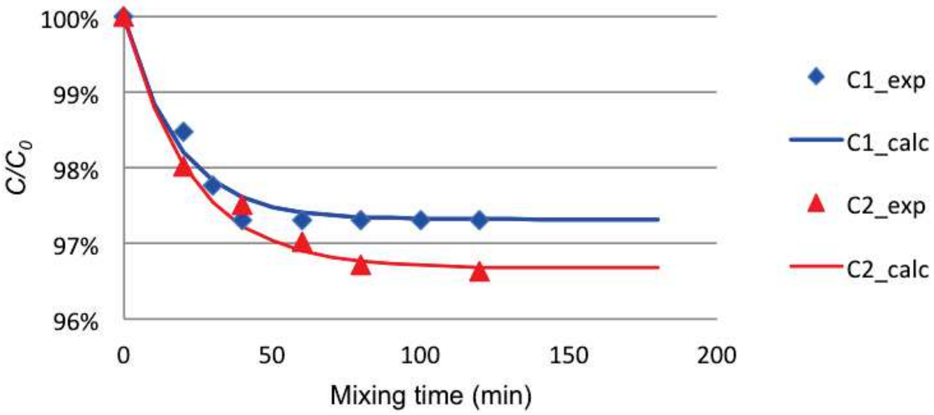

Fig. 4-34 Experimental and calculated data for AO7 adsorption on the porous support using initial concentrations $C_1 = 1 \times 10^{-4}$ mol L^{-1} and $C_2 = 5 \times 10^{-5}$ mol L^{-1}.

For all the continuous calculations on sorption (with effect of diffusion) and photodegradation experiments, we have used the estimated constants (Q_{sat}, k_a, k_d) obtained from the experiments as explained in Figure 4-35.

Table 4-5 Optimized constants for sorption on the porous support.

Bared support		
V (L)	0.005	
k_a (L mol^{-1} min^{-1})	**219.12**	
k_d (min^{-1})	**3.2812** $\times 10^{-2}$	
Q_{sat} (mol L^{-1})	**9.1576** $\times 10^{-5}$	
D_S (mm)	27	
δ_S (mm)	1	
V_S (L)	3.722×10^{-4}	
C_0 (mol L^{-1})	1×10^{-4}	5×10^{-5}
Θ_{eq}	0.3939	0.2440
C_{eq} (mol L^{-1})	9.7315×10^{-5}	4.8337×10^{-5}
K_{eq} (L mol^{-1})	6.6782×10^{3}	

Parameters in the Table 4-5 such as Θ_{eq}, C_{eq} and K_{eq} ($K_{eq} = k_a/k_d$) indicate the equilibrium surface coverage, equilibrium concentration of AO7 in solution and equilibrium constant of sorption respectively. The constants k_a, k_d and Q_{sat} in Table 4-5 are related with respect to the volume of solid material.

The reaction rate in form relevant to volume:

$$r^S[\text{mol/volume of solid/min}] = q^S_{A*}\left[k^S_a c^s_A\left(1-\frac{q^s_A}{q^S_{A*}}\right)-k^S_d\frac{q^s_A}{q^S_{A*}}\right] = q^S_{A*}\left[k^S_a c^s_A\left(1-\Theta^S_A\right)-k^S_d\Theta^S_A\right] = \\ = q^S_{A*}k^S_a\left[c^s_A\left(1-\Theta^S_A\right)-\frac{1}{K^S_{eq}}\Theta^S_A\right] \tag{4-9}$$

By comparing it with eq for description of reversible adsorption in model above, we have the reaction rate relevant to the weight of material:

$$r^s[\text{mol/weight of solid/min}] = k^S_{ads}\left[c^s_i\left(1-\frac{q^s_i}{q^S_*}\right)-\frac{1}{K^S_{ads}}\frac{q^s_i}{q^S_*}\right] = k^S_{ads}\left[c^s_i\left(1-\Theta^S_i\right)-\frac{1}{K^S_{ads}}\Theta^S_i\right] \quad (4\text{-}10)$$

By relating the Equations 4-9 and 4-10, we have:

$$\begin{gathered} r^S_{ads} = \frac{1}{\rho^S} r^S \\ k^S_{ads}\left[c^s_i\left(1-\Theta^S_i\right)-\frac{1}{K^S_{ads}}\Theta^S_i\right] = \frac{q^S_{A*}k^S_a}{\rho^S}\left[c^s_i\left(1-\Theta^S_i\right)-\frac{1}{K^S_{eq}}\Theta^S_i\right] \end{gathered} \quad (4\text{-}11)$$

We can find the relation between these constants as:

$$k^S_{ads}[L/g/\min] = \frac{q^S_{A*}k^S_a}{\rho^S} = q^S_* k^S_a \quad (4\text{-}12)$$

$$K^S_{eq} = K^S_{ads} \quad (4\text{-}13)$$

$$q^S_*[mol/g] = \frac{q^S_{A*}[mol/L]}{\rho^S[g/L]} \quad (4\text{-}14)$$

where ρ^S is density of solid in support. The same approach can be used for TiO_2 layer when recalculating constant between different units.

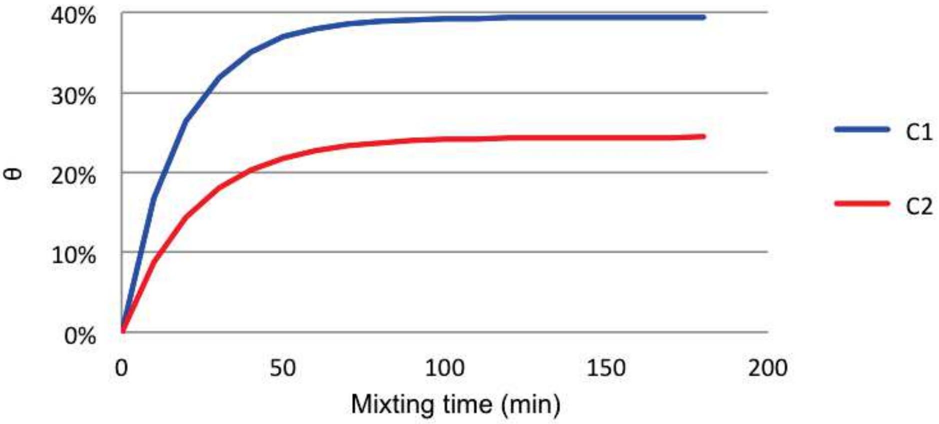

Fig. 4-35 Time dependency of surface coverage (θ) of adsorbed AO7 on porous support using initial concentrations $C_1 = 1 \times 10^{-4}$ mol L^{-1} and $C_2 = 5 \times 10^{-5}$ mol L^{-1}.

B) Calculation for adsorption on TiO_2-coated support

Comparing the adsorption results with barred support and TiO_2-coated support it is evident that during preparation of TiO_2-coated support the structural changes resulting in change of sorption properties of material take place. The sorption capacity of coated support is substantially lower. The decrease in the sorption capacity could be the consequence of support sintering process or/and partial covering of internal structure of support by deposited TiO_2 which seems to adsorb notably lower amount of AO7. There was carried out adsorption experiments with initial concentrations of AO7 solution 1×10^{-4} and 5×10^{-5} mol L^{-1}. With respect to the low adsorption capacity of TiO_2-coated support the changes in concentration of AO7 solution were close to the experimental error of measurement and cannot be used for parameter estimation. The decrease of amount of used solution with respect to volume of membrane could improve the sensitivity of experiment. But even decreasing the volume to the minimal value possible (5 mL) did not lead to an improvement. There were no independent data from adsorption measurements on TiO_2 layer unaffected by the porous support available therefor we have treated the TiO_2-coated support as "mixed materials" and we assumed mean values of adsorption related constants (Q_{sat}, k_a, k_d) identical for both materials.

The comparison of model and experimental data for LF100 membrane is shown on Figure 4-36. The model prediction is in good agreement with experimental data. The obtained constants are summarized in Table 4-6.

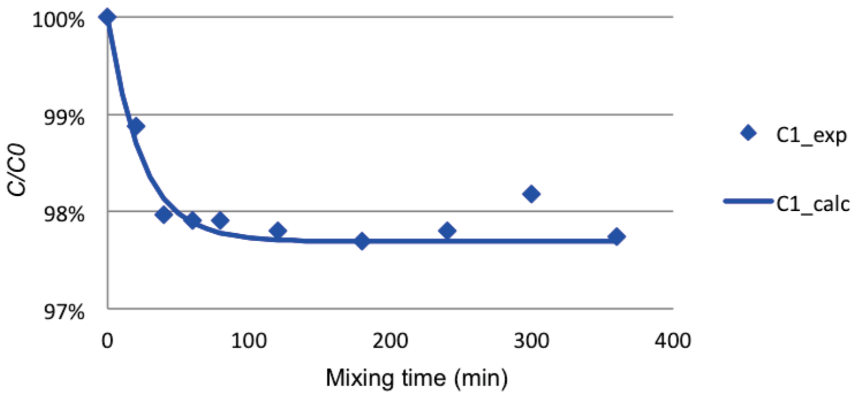

Fig. 4-36 Experimental and calculated data for AO7 adsorption on TiO_2-Al_2O_3 composite membrane LF100 using initial concentrations $C_1 = 1 \times 10^{-4}$ mol L^{-1}.

Table 4-6 Optimized constants for sorption on TiO_2-coated support.

TiO_2 layer + support	
V (L)	0.005
k_a ($L mol^{-1} min^{-1}$)	**219.12**
k_d (min^{-1})	**1.941** $\times 10^{-2}$
Q_{sat} ($mol L^{-1}$)	**5.910** $\times 10^{-5}$
D_S (mm)	27
δ_S (mm)	1
δ_M (μm)	1
V_{MS} (L)	3.722×10^{-4}
C_0 ($mol L^{-1}$)	1×10^{-4}
Θ_{eq}	0.5244
C_{eq} ($mol L^{-1}$)	9.769×10^{-5}
K_{eq} ($L mol^{-1}$)	1.1287×10^{4}

As already mentioned the sorption capacity of the coated support is lower than the barred one. This situation is also reflected in obtained values of sorption parameters as can be seen in the experiments using initial AO7 concentration 1×10^{-4} mol L^{-1}. The optimized values of saturation capacity and desorption rate constants for coated support are about of 60% and 65% coated support and barred one, respectively. The adsorption rate constant remains unchanged. The steady state concentrations of AO7 are close to each other in theboth cases, which result to higher steady state coverage in the case of coated support.

Adsorption model 2 (taking account internal mass transfer):

A) Calculation for adsorption on the support

The second model has been used for calculation of the effect of internal diffusion. Diffusion coefficient of AO7 molecules in pure water is known as $D_i = 5 \times 10^{-6}$ ($cm^2 s^{-1}$) from the experimental measurement carried out in our laboratory. There is comparison of experimental data and data calculated by model for pure support (Figure 4-34). Comparing the results of model accounting diffusion in internal structure of membrane (Figure 4-37) with results of the one neglecting this effect (Figure 4-34) there are almost negligible differences between the values of calculated time concentration profiles in reservoir.

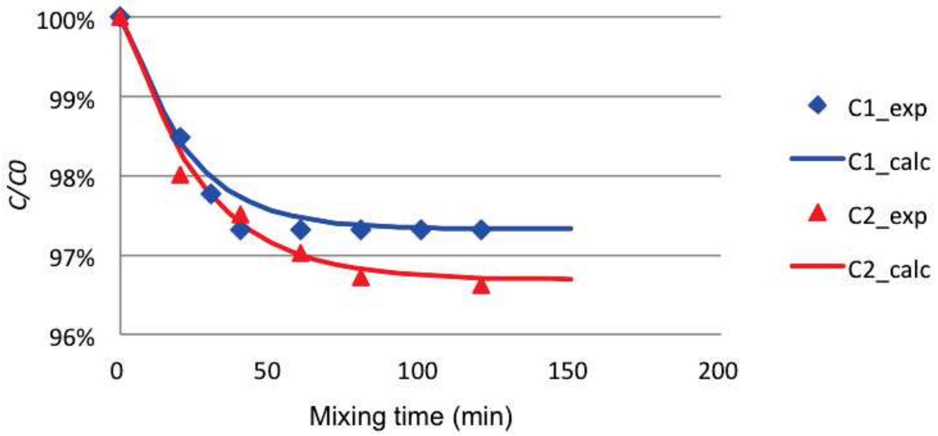

Fig 4-37 Experimental and calculated data of AO7 adsorption on the porous support by taking account diffusion coefficient of AO7 as $D_i = 5 \times 10^{-6}$ cm^2 s^{-1} and using initial concentrations $C_1 = 1 \times 10^{-4}$ mol L^{-1}and $C_2 = 1 \times 10^{-5}$ mol L^{-1}.

Using the mathematical model including the effect of diffusion the information about time changes of concentration and surface coverage profiles inside the porous structure can be obtained. The results of calculation of these profiles for experiment carried out with initial concentration of AO7 $C_1 = 1 \times 10^{-4}$ mol L^{-1} are presented in figures 4-38 and 4-39. The adsorption reaction in the initial stage of experiment is relatively fast with respect to the diffusion into the body of support and the concentration profile with minimum in centre of support is formed (Figure 4-38) as shown for the times 7, 14 and 29 min, respectively. The differences between concentration in the centre of support and at the boundaries of support are decreasing with increasing time and diminish when the steady state is reached (Figure 4-38). The surface coverage profiles have also minimum in the centre of support body but it is not pronounced as in the case of concentration in the liquid phase (Figure 4-39). The surface coverage is increasing with time and after 50 min of experiment the differences in concentration in the centre of support and at the boundaries is negligible.

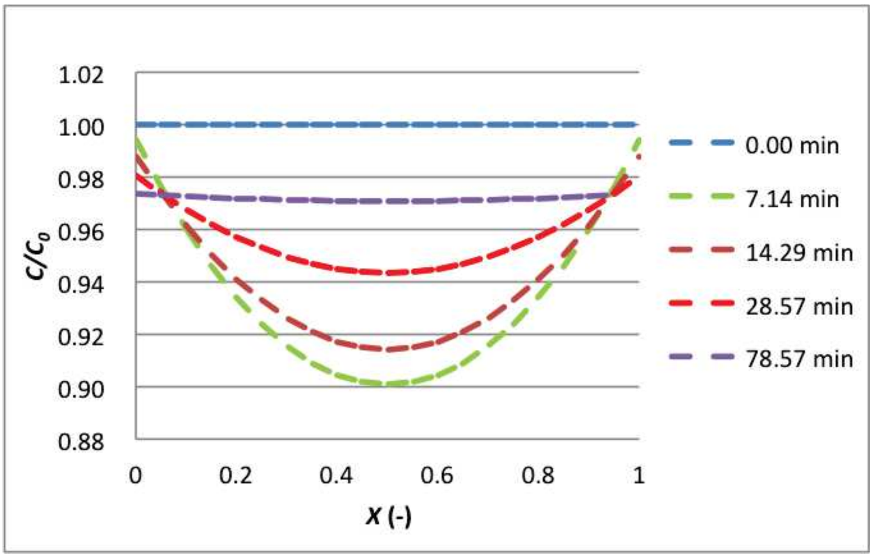

Fig. 4-38 Dimensionless concentration profiles of AO7 in liquid phase inside the porous structure of support as function of time. The symbol x denotes the dimensionless axial coordinate inside support. (Barred support, initial concentrations of AO7 $C_0 = 1 \times 10^{-4}$ mol L^{-1}, volume of AO7 solution 5 mL, diffusion coefficient of AO7 as $D_i = 5 \times 10^{-6}$ cm^2 s^{-1}).

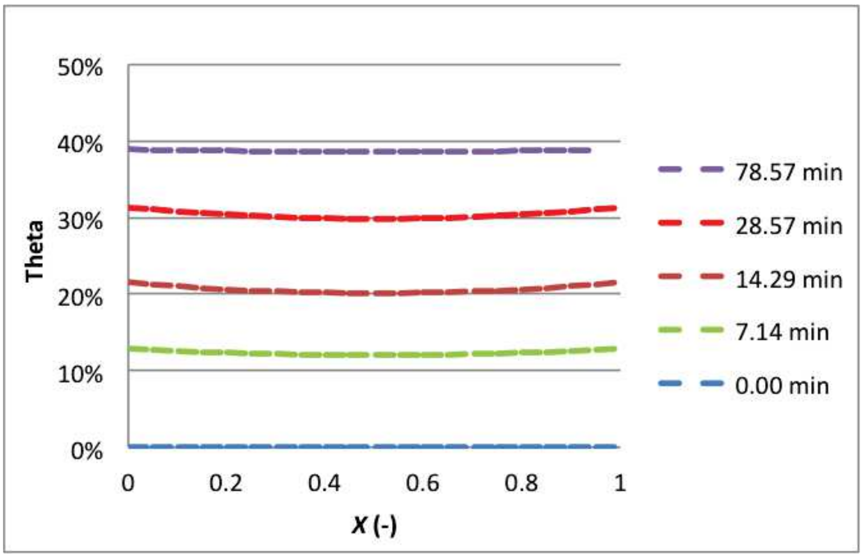

Fig. 4-39 Surface coverage (theta) profiles inside the porous structure of support as function of time. The symbol x denotes the dimensionless axial coordinate inside support. (Barred support, initial concentrations of AO7 $C_0 = 1 \times 10^{-4}$ mol L^{-1}, volume of AO7 solution 5 mL, diffusion coefficient of AO7 as $D_i = 5 \times 10^{-6}$ cm^2 s^{-1}).

B) Calculation for adsorption on TiO_2-coated support

Calculation on the data was made by considering a combination of support + TiO_2 layer with the relevant constants obtained from the previous calculation for this material. The results of these calculations are summarized on figures 4-40 and 4-41. The behaviour of concentration and surface coverage profiles are analogous to the ones in case of barred support with the exceptions that the higher surface coverage is reached at steady state and the maximal difference between concentrations in the centre and at boundaries is lower for TiO_2-coated support. The difference between the concentrations in the centre and boundaries is related to the ratio of adsorption rate and diffusion flux. When the rate of consumption of species by adsorption is higher with respect to the diffusion flux the difference increases as for the case of barred support.

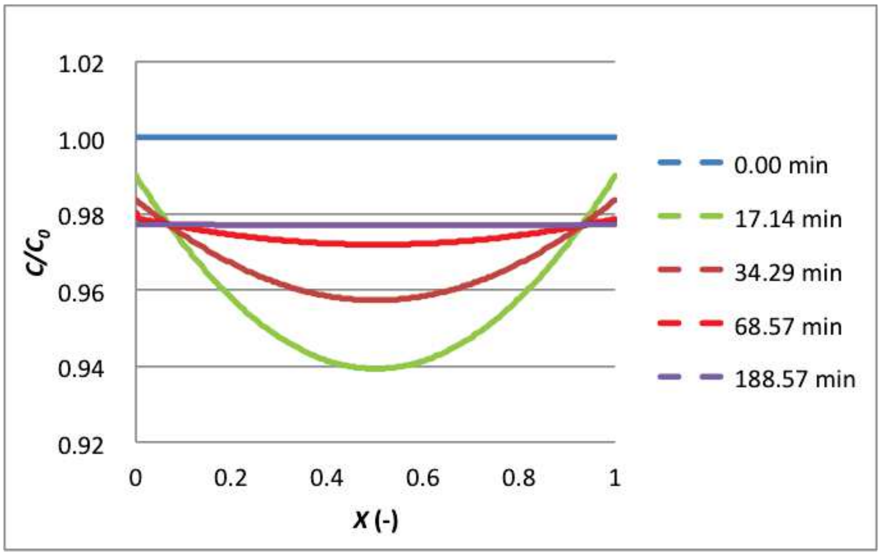

Fig. 4-40 Dimensionless concentration profiles of AO7 in liquid phase inside the porous structure of TiO_2-coated support as function of time. The symbol x denotes the dimensionless axial coordinate. (TiO_2-coated support, initial concentrations of AO7 $C_0 = 1 \times 10^{-4}$ mol L^{-1}, volume of AO7 solution 5 mL, diffusion coefficient of AO7 $D_i = 5 \times 10^{-6}$ cm^2 s^{-1}).

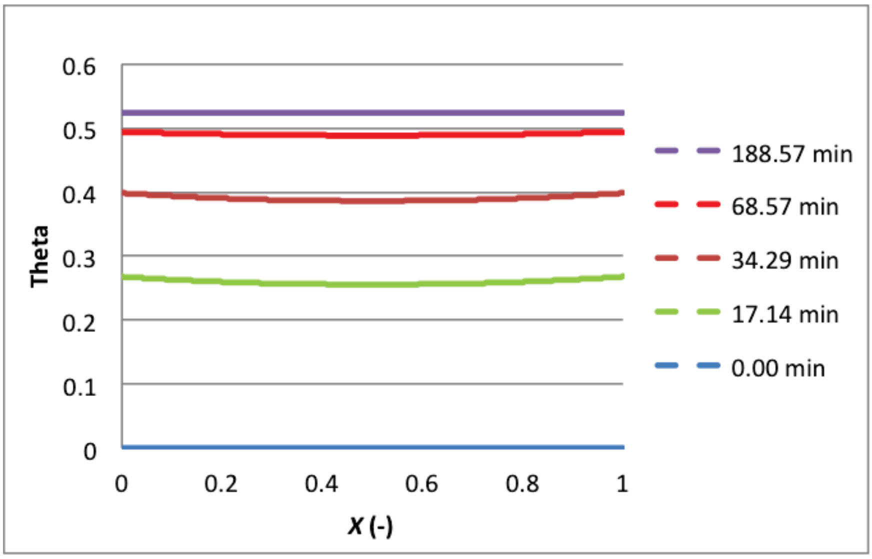

Fig. 4-41 Surface coverage (theta) profiles in the porous structure of TiO_2-coated support as function of time. The symbol x denotes the dimensionless axial coordinate in support. (TiO_2-coated support, initial concentrations of AO7 $C_0 = 1 \times 10^{-4}$ mol L^{-1}, volume of AO7 solution 5 mL, diffusion coefficient of AO7 as $D_i = 5 \times 10^{-6}$ cm^2 s^{-1}).

4.2 Modeling of photocatalytic experiments

General mathematical model has been developed taking into account experimental arrangement described in Chapter II. The schematic drawing of modelled system is shown in Figure 2-18 and Figure 2-24 of Chapter II.

4.2.1 Mathematical descriptions

The system consists of three mains parts 1) tubing, 2) tanks, and 3) photocatalytic cell with membrane. Equations for the individual parts are developed separately. The complete model comprises the equations for individual parts bounded through the boundary conditions. The changes of the temperature through the effects of chemical reactions, sorption, light, mixing etc. are neglected. The isothermal conditions are assumed in this study and the final model is based on mass balances only.

4.2.1.1 Mass balance of tubing

The tubing has been separated into three sections as follows:

1) Feed tube – connection of feed tank and photocatalytic reactor
2) Retentate tube – the outlet of retentate from photocatalytic reactor
3) Permeate tube – the outlet of permeate from photocatalytic cell

Dynamic model of isothermal plug flow reactor with axial dispersion and non-compressible fluid has been used to describe the individual tubes. Bulk homogeneous reactions in tube and surface reactions on the wall of tube are taken into account to the general form of equation. The surface reactions can be used to describe sorption of component on tube wall. This equation can be written as:

$$\frac{\partial c_i}{\partial \tau} = \frac{\partial}{\partial z}\left(D_{ax,i} \frac{\partial c_i}{\partial z} \right) - \frac{\partial \left(v c_i \right)}{\partial z} + \sum_j \nu_{ij}^b r_{b,j} + \frac{2}{r_t} \sum_j \nu_{ij}^s r_{s,j} \tag{4-15}$$

Where c_i denotes concentration of component I, τ time, z the axial coordinate, D_{ax} axial dispersion coefficient, v velocity, ν_{ij}^b stoichiometric coefficient in bulk reaction, r_b reaction rate of bulk reaction, r_t tube radius, ν_{ij}^s stoichiometric coefficient in surface reaction, and r_s reaction rate of surface reaction on the tube wall, respectively.

As has been verified experimentally, the reactions in the bulk phase and the adsorption on tube surface can be neglected. The equation can be rewritten in form:

$$\frac{\partial c_i}{\partial \tau} = \frac{\partial}{\partial z}\left(D_{ax,i} \frac{\partial c_i}{\partial z} \right) - \frac{\partial \left(v c_i \right)}{\partial z} \tag{4-16}$$

The initial and boundary conditions are:

$$\tau < 0, c_i = c_{i0}$$

$$z = 0 : c_i = c_i^0(\tau)$$

$$z = L_t : D_{ax,i} \frac{\partial c_i}{\partial z} = 0$$

where L_t is the length of tube and c_{i0} is initial concentration. The boundary conditions for individual tube are set appropriately in dependency of arrangement of experimental set-up and they are defined with details in summary table of model equations.

4.2.1.2 Mass balance of tanks

Feed tank (constant contribution) and permeate tank (depending on permeate fully or partially recycling back to the feed) are present in the lab-scale and pilot-scale photocatalytic membrane reactor (PMR) units.

1) Mass balance of feed tank

General mass balance equation of feed tank is also accounting homogeneous bulk reactions and the dynamic model of ideally mixed semi-batch tank reactor is used. To describe the different arrangement of experiments (with recycling permeate to the feed tank and the one with fully or partially separated permeate) the factor s_f is introduce to the equation. This factor defines the ratio of permeate recycled back to the feed tank. Then we have $s_f = 0$ for the case where no permeate recycling and $s_f = 1$ where all permeate recycling back to the feed tank. The mass balance equation of i-th component is given as:

$$V^{FT}\frac{dc_i^{FT}}{d\tau}+c_i^{FT}\frac{dV^{FT}}{d\tau}=s_f\dot{V}^Pc_i^P+\dot{V}^Rc_i^R-\dot{V}^Fc_i^{FT}+V^{FT}\sum_j \nu_{ij}^{FT}r_j^{FT} \qquad (4\text{-}17)$$

where the V^{FT} is the volume of feed tank, c_i^{FT}, c_i^P, c_i^R are the molar concentrations of component I in feed tank, permeate and retentate respectively. The symbols $\dot{V}^R, \dot{V}^P, \dot{V}^F$ denote the volumetric flows of retentate, permeate, and feed respectively. The reaction term $V^{FT}\sum_j \nu_{ij}^{FT}r_j^{FT}$ can be neglected because no reactions have been identified during blank experiments. Thus the final equation is given as:

$$V^{FT}\frac{dc_i^{FT}}{d\tau}+c_i^{FT}\frac{dV^{FT}}{d\tau}=s_f\dot{V}^Pc_i^P+\dot{V}^Rc_i^R-\dot{V}^Fc_i^{FT} \qquad (4\text{-}18)$$

The total mass balance of feed tank is described by following equation:

$$\frac{d(V^{FT}\rho^{FT})}{d\tau} = s_f \dot{V}^P \rho^P + \dot{V}^R \rho^R - \dot{V}^F \rho^{FT} \tag{4-19}$$

where ρ^R, ρ^{FT}, ρ^P are the densities of liquid in retentate, feed tank and permeate, respectively. Aqueous solution of low concentration of organic solute has been used in all experiments and isothermal conditions were assumed so that the change of densities with change of concentration of dye can be neglected and the Equation 4-19 can be rewritten to use volumetric flows only:

$$\frac{dV^{FT}}{d\tau} = s_f \dot{V}^P + \dot{V}^R - \dot{V}^F \tag{4-20}$$

The flow of permeate ($\dot{V}^P$) can be calculated based on water permeation measurements and is defined by equation below:

$$\dot{V}^P = \pi_w \left(p^R - p^P\right) = \pi_w \Delta p \tag{4-21}$$

where π_w is water permeance, p^R, p^P the pressure in retentate and permeate compartment respectively, and Δp identifies the cross-membrane pressure drop. The feed flow is defined by pump delivery.

The initial conditions for Equations 4-8 and 4-9 are defined by initial concentration of i-th component and amount of solution in feed tank as:

$$\tau = 0: \; V^{FT} = V_0^{FT}, c_i^{FT} = c_{i0}^{FT}$$

2) Mass balance of permeate tank

As for the derivation of mass balance equations for permeate tank, similar assumptions as given in the feed tank have been also used hereby. The mass balance of i-th component is then given in Equation 4-22 and total mass balance in Equation 4-23.

$$V^{PT}\frac{dc_i^{PT}}{d\tau} + c_i^{PT}\frac{dV^{PT}}{d\tau} = (1 - s_f)\dot{V}^P c_i^P \tag{4-22}$$

$$\frac{dV^{PT}}{d\tau} = (1 - s_f)\dot{V}^P \tag{4-23}$$

The initial conditions are described as:

$$\tau = 0: \; V^{PT} = V_0^{PT}, c_i^{PT} = c_{i0}^{PT}$$

4.2.1.3 Mass balance of photocatalytic cell

For the purpose of mathematical modeling, the photocatalytic cell has been divided into three sections:

1) Retentate compartment
2) Permeate compartment
3) Membrane (composite of the support + TiO_2 layer)

which are to be discussed one to one as following:

1) Mass balance of retentate compartment

The retentate compartment has been simulated as dynamic continuous stirred tank reactor to which the feed is input from feed tank and the retentate is removed. Part of the mixture also permeates through the membrane to the permeate side and it is controlled by setting cross membrane pressure drop. In the general form of the applied modeling it is assumed that the reactions can take place in homogenous phase. TiO_2 catalyst is assumed to be on the top of support and it is oriented in direction toward the retentate compartment. The external mass transfer resistance has been neglected and the near membrane surface concentration is equal to the bulk concentration in retentate compartment. The mass balance equation of i-th component is then given in Equation 4-24:

$$V^{RC}\frac{dc_i^{RC}}{d\tau} = \dot{V}^F c_i^F - \dot{V}^R c_i^R + A_M \varepsilon_M D_{Mi} \left.\frac{\partial c_i^M}{\partial x}\right|_{x=0} - \dot{V}^P c_i^M\Big|_{x=0} + V^{RC}\sum_j \nu_{ij}^{RC} r_j^{RC} \tag{4-24}$$

where c_i^{RC} introduces the concentration of i-th component in retentate compartment, V^{RC} the volume of retentate compartment, A_M the membrane area, ε_M the membrane porosity, D_{Mi} effective axial dispersion coefficient of i-th component in membrane, c_i^M concentration of i-th component in membrane and term $\sum_j v_{ij}^{RC} r_j^{RC}$ the contribution of bulk reactions in retentate compartment respectively.

Performed experimental test showed that the contribution of bulk reactions in retentate compartment can be neglected. Under this assumption the Equation 4-24 can be written in modified form of Equation 4-25.

$$V^{RC}\frac{dc_i^{RC}}{d\tau} = \dot{V}^F c_i^F - \dot{V}^R c_i^R + A_M \varepsilon_M D_{Mi} \left.\frac{\partial c_i^M}{\partial x}\right|_{x=0} - \dot{V}^P \left. c_i^M \right|_{x=0} \tag{4-25}$$

The total mass balance can be written as:

$$\dot{V}^F = \dot{V}^R + \dot{V}^P \tag{4-26}$$

The initial conditions of Equation 4-15 are defined as:

$\tau = 0:\ c_i^{RC} = c_{i0}^{RC}$

2) Mass balance of permeate compartment

The derivation of mass balance equation for permeate compartment is based on similar assumptions as in the case of retentate side and the final equation can be given in form:

$$V^{PC}\frac{dc_i^{PC}}{d\tau} = -\dot{V}^P c_i^{PC} - A_M \varepsilon_s D_{Si} \left.\frac{\partial c_i^S}{\partial x}\right|_{x=\delta_M+\delta_s} + \dot{V}^P \left. c_i^s \right|_{x=\delta_M+\delta_s} \tag{4-27}$$

where V^{PC} denotes volume of permeate compartment, c_i^{PC} the concentration of i-th component in permeate compartment, ε_s the porosity of support layer, D_{Si} effective axial dispersion coefficient in support layer, c_i^S the concentration of i-th component in fluid (liquid) phase in support, δ_M the thickness of photocatalytic layer, δ_S thickness of support. The initial conditions are given as:

$\tau = 0: \; c_i^{PC} = c_{i0}^{PC}$

3) Mass balance in photocatalytic membrane

The mass balance equations in porous photo-active layer contain mass transport by convection, dispersion as well as the adsorption and reaction on catalyst surface:

$$\frac{\partial c_i^M}{\partial \tau} = D_{Mi} \frac{\partial^2 c_i^M}{\partial x^2} - \overline{\mathrm{v}}_M \frac{\partial c_i^M}{\partial x} - \frac{(1-\varepsilon_M)}{\varepsilon_M} \rho_M r_{ads}^M \tag{4-28}$$

$$(1-\varepsilon_M)\rho_M \frac{\partial q_i^M}{\partial \tau} = (1-\varepsilon_M)\rho_M r_{ads}^M - (1-\varepsilon_M)\rho_M r_{dec}^M \tag{4-29}$$

where ε_M denotes membrane porosity, c_i^M the molar concentration of i-th component in fluid (liquid) phase, $\overline{\mathrm{v}}_M$ the local interstitial fluid velocity in membrane porous space, D_{Mi} the effective dispersion coefficient of i-th component, ρ_M the density of membrane solids catalyst, r_{ads}^M rate of adsorption, q_i^M concentration of adsorbed species i in solid catalyst, r_{dec}^M rate of photocatalytic decomposition of i-th component.

Rate of reversible adsorption of i-th component in photocatalytic membrane is given by:

$$r_{ads}^M = k_{ads}^M \left[c_i^M \left(1 - \frac{q_i^M}{q_*^M} \right) - \frac{1}{K_{ads}^M} \frac{q_i^M}{q_*^M} \right] \tag{4-30}$$

where k_{ads}^M stands for the rate constant of adsorption in membrane, K_{ads}^M the equilibrium constant of adsorption in membrane, q_*^M concentration of adsorption sites in membrane.

Rate of photocatalytic reaction (irreversible) is described:

$$r_{dec}^M = k_{dec}^M c_h \frac{q_i^M}{q_*^M} \tag{4-31}$$

where c_h is concentration of holes generated by photon flux.

Concentration of photo-generated holes is proportional to the light intensity [24]:

$$c_h = k_I I^a = k_I I_o^a \left(\exp[-\alpha x]\right)^a = k_I I_o^a \exp[-a\alpha x] \tag{4-32}$$

By substituting expression for the hole concentration into photocatalytic kinetics we have:

$$r_{dec}^M = k_{dec}^M k_I I_o^a \exp[-a\alpha x] \frac{q_i^M}{q_*^M} = \bar{k}_{dec}^M \exp[-\bar{\alpha} x] \frac{q_i^M}{q_*^M} \tag{4-33}$$

where

$$\bar{k}_{dec}^M = k_{dec}^M k_I I_o^a$$

$$\bar{\alpha} = a\alpha$$

The mass balance equations in porous support contain mass transport by convection, dispersion as well as the adsorption on support surface:

$$\frac{\partial c_i^S}{\partial \tau} = D_{Si} \frac{\partial^2 c_i^S}{\partial x^2} - \bar{\mathrm{v}}_S \frac{\partial c_i^S}{\partial x} - \frac{(1-\varepsilon_S)}{\varepsilon_S} \rho_S r_{ads}^S \tag{4-34}$$

$$(1-\varepsilon_S)\rho_S \frac{\partial q_i^S}{\partial \tau} = (1-\varepsilon_S)\rho_s r_{ads}^S \tag{4-35}$$

where ε_S denotes support porosity, c_i^S the molar concentration of component i in fluid (liquid) phase in support, $\bar{\mathrm{v}}_S$ the local interstitial fluid velocity in support porous space, D_{Si} the effective dispersion coefficient, ρ_S density of solid support, r_{ads}^S rate of adsorption, q_i^S concentration of adsorbed species i in support.

The rate of reversible adsorption of component i in support is given as:

$$r_{ads}^S = k_{ads}^S \left[c_i^s \left(1 - \frac{q_i^S}{q_*^S}\right) - \frac{1}{K_{ads}^S} \frac{q_i^S}{q_*^S} \right] \tag{4-36}$$

where k_{ads}^S stands for the rate constant of adsorption, K_{ads}^S the equilibrium constant of adsorption, q_*^S concentration of adsorption sites in support.

The initial, boundary and interfacial conditions are as following:

$$\tau < 0 : c_i^M = c_{i0}^M , c_i^S = c_{i0}^S , q_i^M = q_{i0}^M , q_i^S = q_{i0}^S$$

$$\tau \geq 0 :$$

$$x = 0 : c_i^M = c_i^{RC}$$

$$x = \delta_M : -\varepsilon_M D_{Mi} \frac{\partial c_i^M}{\partial x} + \varepsilon_M \overline{\text{v}}_M c_i^M = -\varepsilon_S D_{Si} \frac{\partial c_i^S}{\partial x} + \varepsilon_S \overline{\text{v}}_S c_A$$
$$c_i^M = c_i^S$$

$$x = \delta_M + \delta_S : -D_{Si} \frac{\partial c_i^S}{\partial x} = 0$$

where δ_M is the catalytic membrane thickness and δ_S the thickness of support.

4.2.2 Results of reaction modeling of AO7 decomposition

Data processing on experimental results of reaction is based on some estimation of constants in photocatalytic decomposition. The data from sorption experiments has been used for calculation in the reaction made in experiment. The k_{dec} was fitted in this case to describe the experimental data.

The above described model has been applied in processing of experimental data from photocatalytic decomposition of AO7 in arrangement with recirculation of retentate to the feed tank. The results obtained from fitting of independent sorption experiments have been used and the decomposition constant k_{dec} has been estimated from experimental measurements of photocatalytic decomposition.

The two experiments with slightly different initial concentration of AO7 carried out with the membrane LF04 have been simulated. The comparison of experimental and predicted data in the form of time dependency of dimensionless concentration is depicted on Figure 4-42. The calculated values of model curves are almost identical for these small differences in initial concentrations of AO7. The experimental and model data are in good agreement for optimized value of k_{dec}= 2.36 × 10^{-4} mol g^{-1} min^{-1}.

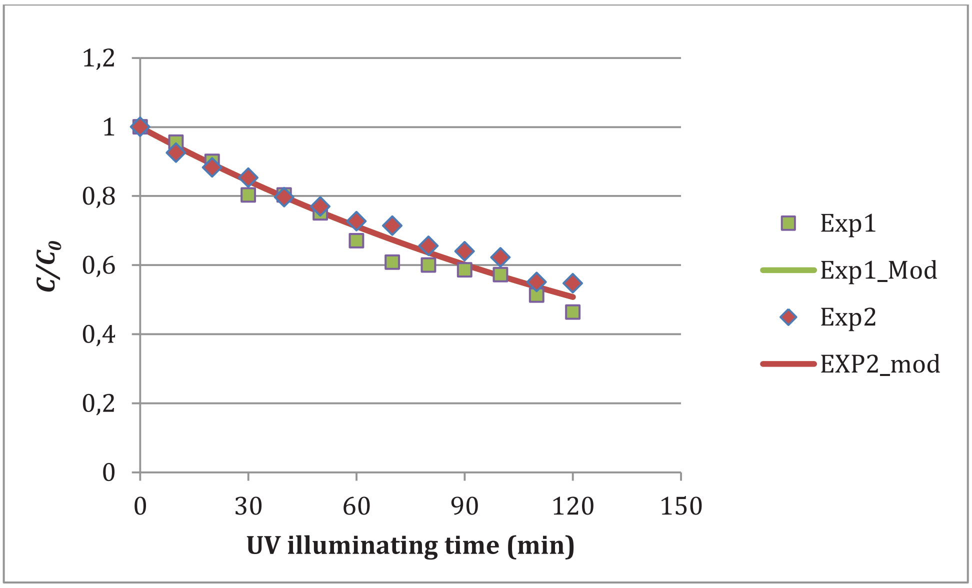

Fig. 4-42 Comparison of experimental and predicted data in process of AO7 decomposition.

As the additional results from this calculation the concentration profiles of AO7 in the liquid phase present in porous structure (Figure 4-43) and also surface coverage of solid phase (Figure 4-45) as the function of time are obtained.

The Figure 4-43 shows the overall concentration profiles. The predominant change of concentration is located in the TiO_2 layer, where the decomposition reaction takes place (Figure 4-43 and Figure 4-44). The change in concentration profile inside the porous support, where the adsorption reaction only is taken into account, is negligible. The change of concentration inside the support is pronounced only in the initial stage of experiment where the sorption of AO7 to unsaturated support is fast. The detail concentration profiles in TiO_2 layer (X=0-0.0005) for different experimental time are shown in Figure 4-44. The concentration inside porous structure is influenced by the concentration of AO7 in feed tank. With decreasing concentration of AO7 in feed tank the concentration profiles are shifting to the lower values. The decrease of feed tank concentration also influences the concentration gradient in TiO_2 layer. With decreasing concentration the concentration gradient decrease as the result lower rate of adsorption and decomposition of AO7.

Detailed profiles of surface coverage in TiO_2 layer and in support near the interface TiO_2 layer-support are demonstrated in Figure 4-45. The abrupt change in the coverage at the interface due to the decomposition reaction in TiO_2 layer is present. As the surface coverage is decreased by decomposition reaction taking place on the surface of TiO_2 the adsorption reaction only takes place on the support which is increasing the coverage. Comparing the differences at the interface they are decreasing with time as the rate of decomposition is decreasing.

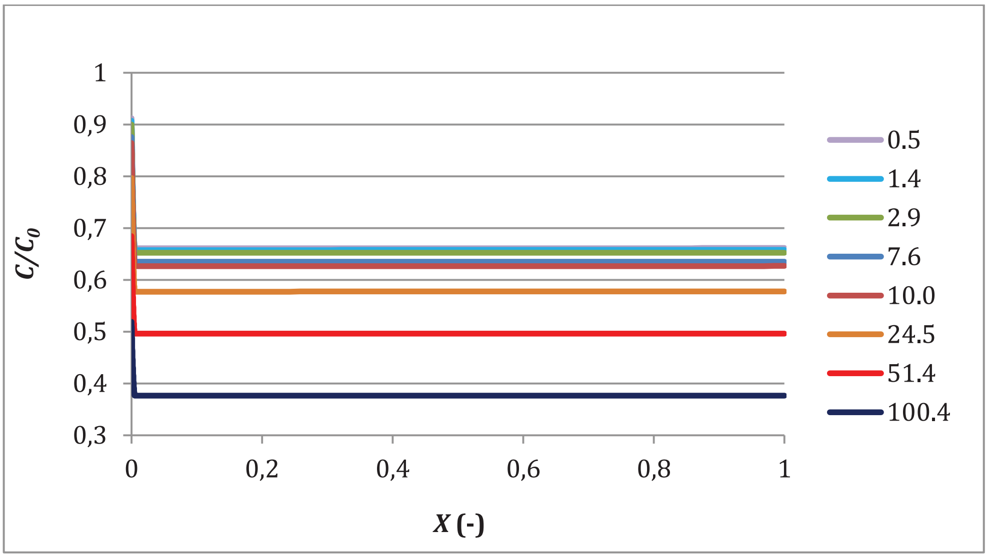

Fig 4-43 Dimensionless concentration profiles of AO7 as function of reaction time from 0.5 to 100.4 min.

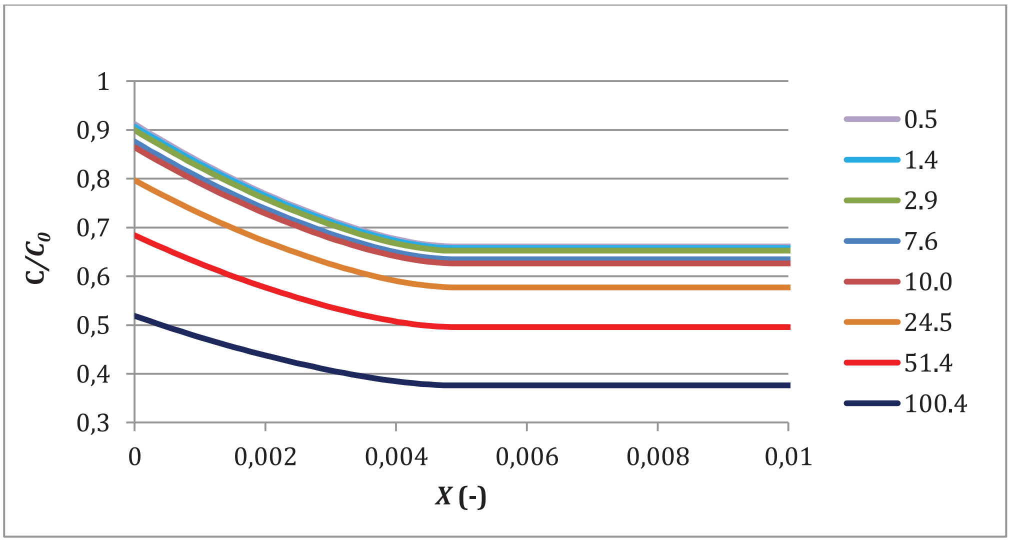

Fig 4-44 Dimensionless concentration profiles of AO7 as a function of time from 0.5 to 100.4 min – detail of TiO_2 layer (X = 0-0.0005) with support interface (support X > 0.0005).

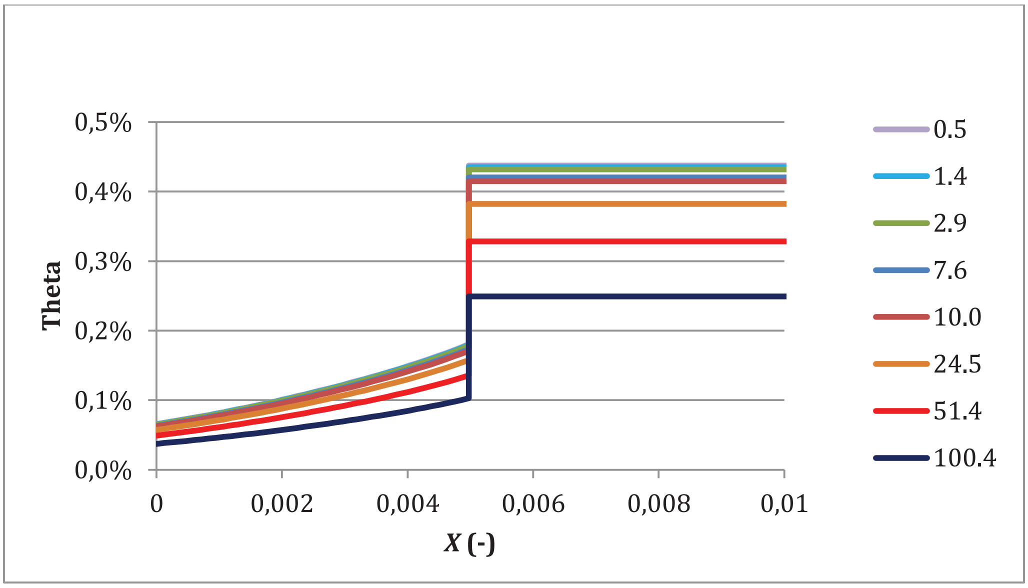

Fig. 4-45 Surface coverage profiles (theta) as a function of time from 0.5 to 100.4 min – detail of TiO_2 layer (X = 0-0.0005) with support interface (support $X > 0.0005$).

5. Conclusion

Modeling results have been obtained from mathematical calculation on the experimental results including two steps: adsorption of organic reactants on the TiO_2/Al_2O_3 composite membrane and reaction of the organic reactants on the composite membrane under UV illumination condition. The adsorption study contains the adsorbed model pollutant AO7 on uncoated porous Al_2O_3 support and on TiO_2-coated Al_2O_3 support (that is the composite membrane), yet the steady-state condition with no transmembrane pressure was operated in the petri dish for the adsorption measurement. There is almost negligible difference as found between the models neglecting and accounting the internal mass diffusion in the membrane body. In general, the adsorption capacity of AO7 compound by TiO_2 coated support was calculated as less than that of the uncoated support. It could be possibly due to the TiO_2 coating as denser top-layer after depositing and sintering processes. Equilibrium Surface coverage (θ) and equilibrium constant of sorption were estimated as 52.4% and 1.13×10^4 L mol^{-1} for the TiO_2/Al_2O_3 composite membrane.

Modeling on the photocatalytic reaction was based on mass balance calculation taking account the tubes, tanks and the membrane cell in the lab-scale PMR loop. The tubing has been considered through three parts as the feed tube, retentate tube and permeate tube. The tanks have been studied with mass balance in the feed tank and permeate tank. And the photocatalytic membrane cell was divided into retentate compartment, permeate compartment and the membrane body to analyze the mass balance of the organic pollutant AO7. By summarizing all the calculation, the modelled value was found in good agreement with experimental data for optimized M100 membrane having decomposition rate constant kdec= 2.36×10^{-4} mol g^{-1} min^{-1} for AO7 aqueous compound. According to the AO7 concentration profile, the changes of concentration inside the porous support, where the adsorption reaction only is taken into account, is negligible. With decreasing concentration in the feed tank the concentration gradient in TiO_2 layer was reduced; as a result lower rate of adsorption and decomposition of AO7 was oberved.

General conclusion and perspectives

The thesis is devoted to integrate TiO_2 photocatalysis process with membrane separation process aimed for degrading tedious organic pollution in water treatment technology. The work has been carried out first by design of TiO_2-based composite membrane, synthesis and optimization of anatase TiO_2 thin films, characterization of their main physico-chemical properties and investigation of the functional performance of TiO_2-coated membranes.

Plasma-enhanced chemical vapor deposition (PECVD) is a one-step method applied in the thesis to deposit amorphous TiO_2 thin film on different types of substrate at low temperature in comparison to CVD method. PECVD operating conditions in particular as substrate temperature (T_s), partial pressure of bring gas argon and precursor TTIP ($P_{Ar+TTIP}$), plasma distance (d_p) and RF power intensity (W_{real}) have been studied with their influence on deposition rate, Ti-O composite and thickness uniformity. Concerning a homogenous deposited thickness and a reasonable surface energy in plasma/reaction process $T_s = 150$ °C was decided based on the study of PECVD T_s from 50 – 250 °C. Moreover, $P_{Ar+TTIP} = 0.225$ mbar (0.155, 0.185 and 0.225 mbar studied) and $d_p = 3.0$ cm (2.0, 2.5 and 3.0 cm studied) were determined regarding to the richest Ti-O abundance and the smoothest thickness of the thin film. More amounts of precursor vapor and longer times for diffusion in the gas phase explain that the higher $P_{Ar+TTIP}$ and longer d_p could work as the optimal conditions. Since $W_{real} = 65$ W led to deposit with cracking surface due to stronger ion bombardment, $W_{real} = 50$ W was maintained in the optimal PECVD protocol.

Afterward, post-annealing as-deposit at 300 °C for minimal staying time 4.5 h or at 400 °C (no staying time needed) was proven being able to form crystalline anatase phase in as-deposit thin film on silicon substrate according to XRD analysis. Pure anatase phase was developed and maintained (no rutile or brookite phase was formed) by annealing the supported TiO_2 thin film from 300 to 700 °C. Crystallization annealing duration at 300 °C could be shortened from 4.5 h for TiO_2 on non-seeded silicon (made at $T_s = 150$ °C) to 1.5 h for TiO_2 on anatase-seeded silicon (obtained from sol dip-coating).

Chemistry of the amorphous and anatase TiO_2 thin films (deposited on silicon) has been interpreted from EDX and FTIR spectra. Chemical elements consisting of Ti, O, C, Si and Al were detected in the as-deposit film. Existence of C and Al could be originated from residues from the precursor (metal-organic compound TTIP) and alumina foil (protection wrap on the bottom electrode) during plasma/reaction process. Signal of element Si is due to penetration of incident X-ray through the thin film to silicon substrate as in EDX measurement. A shoulder absorbance peak at wavenumber 700 cm^{-1} due to vibration of Ti-O was observed in FTIR spectra of both amorphous and anatase films. Another sharp absorbance peak at wavenumber 450 cm^{-1} was found characteristic for the obtained anatase film.

Physico-chemical properties of the optimal TiO_2 thin film including crystalline structure, microstructure, density, porosity, band gap, and surface hydrophilicity have been characterized. It is found that the film has columnar alike microstructure in SEM scanning. Mean thickness of the optimal film was known to be 1.3 μm (± 7% in full-scale surface area 12.6 cm^2) with SEM cross-section analysis. Apparent density of the synthesized anatase layer was found as 2.52 g cm^{-3} by modeling XRR curve and accordingly the porosity (i.e. void volume percentage) was calculated as 33 % with knowing the density of dense anatase 3.87 g cm^{-3}. The cut-off absorbance by anatase thin film (supported on quartz) was found at 365 nm. Therefore, band gap energy (E_g, 1.3 μm thick layer) was obtained as 3.30 eV by applying Tauc plot on the UV/Vis absorbance spectrum, whereas E_g (180 nm thick layer) was known as 3.15 eV by regressing Cauchy law on EP measurement from 1.25 – 3.50 eV. Crystal faces of anatase phase (101), (004) and (200) at 2θ = 25.4°, 37.9° and 48.1° aspect were found in the XRD pattern of anatase film. Complementary Raman scattering signal at 150 cm^{-1} characteristic for anatase materials was also observed on the obtained anatase thin film. Water contact angle on anatase surface was reduced from 29° in darkness to 10° with 20-min UV irradiation, which verified photo-induced hydrophilicity property.

Functional performance of the silicon-supported anatase thin film as photocatalyst was examined with patented Pilkington assessment by self-removing stearic acid adhered on TiO_2 surface in air under UV irradiation (35 W m^{-2}, $\lambda = 355$ nm). At 50-min UV illumination photodegraded rate of stearic acid (R_{ST}) on anatase-coated silicon reached 90% and after 80 min UV stearic acid was completely removed. No significant degradation was observed on the uncoated substrate after 100 min of UV irradiation. The result is compared to a study of photocatalytic characterization titania layers prepared at high temperature by conventional CVD, in which UV device of intensity 32 W m^{-2} was used. For such dense layers (with stearic acid only adsorbed at the external surface), a degradation rate of 90% was observed after a time of UV irradiation ranging from 4 to 28 min relevant to deposition conditions [202]. In another paper from our group dedicated to mesostructured anatase layers prepared by sol-gel route and exhibiting a very high photocatalytic activity [119], the same degradation rate requires an irradiation time of 10 s but with a 11 times larger irradiation power (380 W m^{-2}).

Further on, anatase-coated porous alumina ceramics (i.e. the fabricated TiO_2 composite membrane) were tested in "static" condition under the effect of diffusion of the organic solute in water. Membranes M100 (TiO_2-layer thickness ≈ 1.3 μm) and M800 (TiO_2-skin thickness ≤ 0.5 μm) were made of PECVD anatase films on macroporous supports with deposition durations equal to 20 min and 7 min respectively. Photodegrading efficiency of methylene blue (MB) in water by periodically illuminated membranes M100 and M800 (UV source of intensity 50 W m^{-2}, $\lambda = 355$nm) was determined as δ_{MB}, the quantity of destroyed MB per unit membrane surface area and per unit time. The value of δ_{MB} was obtained by calculating the difference of diffused MB through the membrane either with or without UV irradiation. It has been found that δ_{MB} equal to 2×10^{-8} mol m^{-2} s^{-1} for M100 and 1×10^{-8} mol m^{-2} s^{-1} for M800. These results are in the same order of magnitude as those previously measured for titania membranes prepared by sol-gel route in our group [14] or for Ag-titania-polymer composite membranes in a very recent paper [203].

To follow up, the membranes were then tested in "dynamic" condition in the pressure-driven membrane process in constructed pilot-scale unit. Water permeability through membranes was first measured as 1800 L m^{-2} h^{-1} bar^{-1} and 8280 L m^{-2} h^{-1} bar^{-1} for M100 and M800 using the reactor configuration of TiO_2 surface in contact with permeate solution. With continuous UV illumination (50 W m^{-2}, $\lambda = 355$nm), membrane M100 performed about 5 times higher photocatalytic efficiency (about 50% degraded MB from initial $c_0 = 3.2 \times 10^{-7}$ mol L^{-1}) than that of M800 (about 10% degraded MB from initial $c_0 = 1.25 \times 10^{-7}$ mol L^{-1}) due to a slower water permeability (at transmembrane pressure $\Delta P = 0.25$ bar) and larger capacity δ_{MB} of membrane M100. The experimental degradation rates are in very good accordance with expected values (theoretically obtained from δ_{MB}), which proves the absence of defects on membranes and pilot-scale unit. The reproducible performance was maintained on duplicate membranes of each coating format of M100 and M800.

In parallel, influences of UV sources (power intensity and emission wavelength) and dynamic membrane process (transmembrane pressure and circulation speed) on photodegradation rate of acid orange 7 (AO7) and phenol were studied in lab-scale unit with the photocatalytic layer in contact with the feed solution contained in the circulation loop of the photocatalytic membrane reactor. With 4 W-powered UV irradiation for 2 h, destroyed AO7 per unit membrane surface area was found 2.5×10^{-5} mol m^{-2} at emission wavelength $\lambda = 365$ nm and 2.0×10^{-5} mol m^{-2} at alternative $\lambda = 254$ nm. With 500 W-powered UV irradiation (UVA emission from 360 nm) for 2 h, destroyed AO7 was found 3.5×10^{-4} mol m^{-2} by the same membrane that is 10 times higher than that of using the low-intensity lamp. Self-photolysis effect (uncoated ceramic support alone considered as non-photoactive) was found 2.8×10^{-6} mol m^{-2} (as 11% contribution to photodegradation) and 9.0×10^{-5} mol m^{-2} (as 26% contribution to photodegradation) under 4 W and 500 W UV irradiation, respectively. Process modeling (adsorption and photocatalysis reaction) was finally carried out from these available experimental outputs.

Taking benefit of the quantification of the photocatalytic performance of the prepared membranes with simplified membrane devices and with model organic molecule and of the modeling results, the next stage should be to evaluate the membrane applicability considering real urban or industrial waters and to scale-up of possible purification units.

In term of material engineering perspectives for the future research could be interested in depositing TiO_2 thin film with nitrogen dopant using additional N_2 or NH_3 in the PECVD reactor. The band gap energy (E_g) of N-doped TiO_2 can be narrowed since the non-metal atoms (N in this case) as electron acceptors reduce the minimal energy levels in the conduction band. Consequently, absorbance shift to the visible band can lead to solar harvesting in photocatalytic water treatment technology.

Another possible valuation field for the developed PECVD-deposited TiO_2 thin films could be their integration in multilayer systems enabling water splitting and selective hydrogen extraction.

Appendices

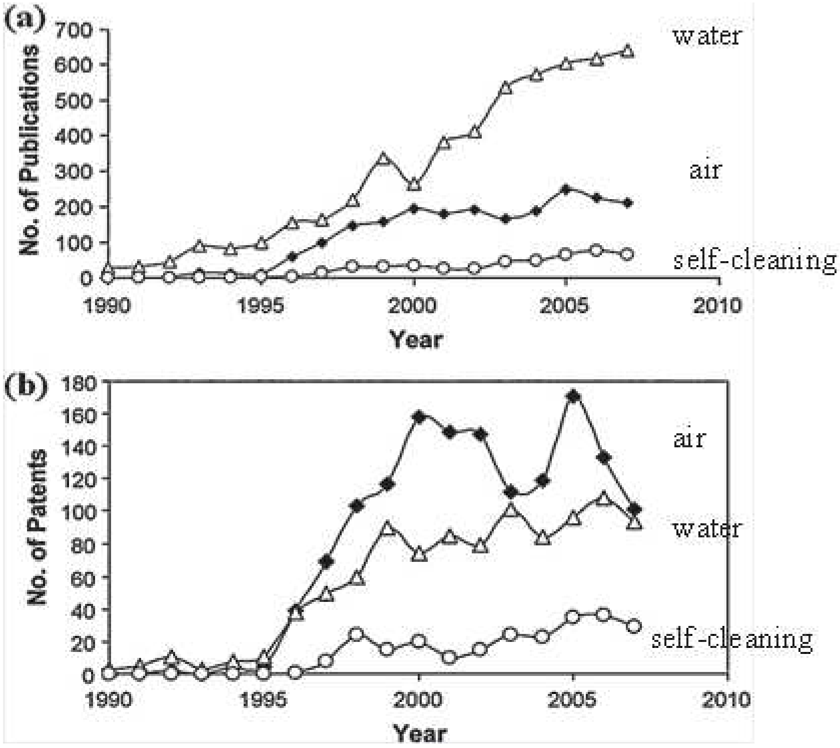

Appendix 1. Annual publications on TiO_2 photocatalysis with (a) scientific papers and (b) patens in water purification (ΔΔ), air purification (◆) and self-cleaning (○). [40]

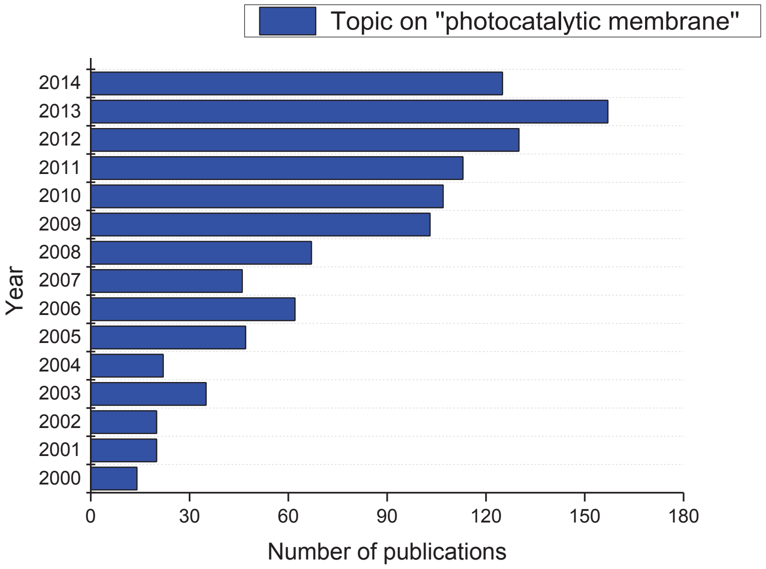

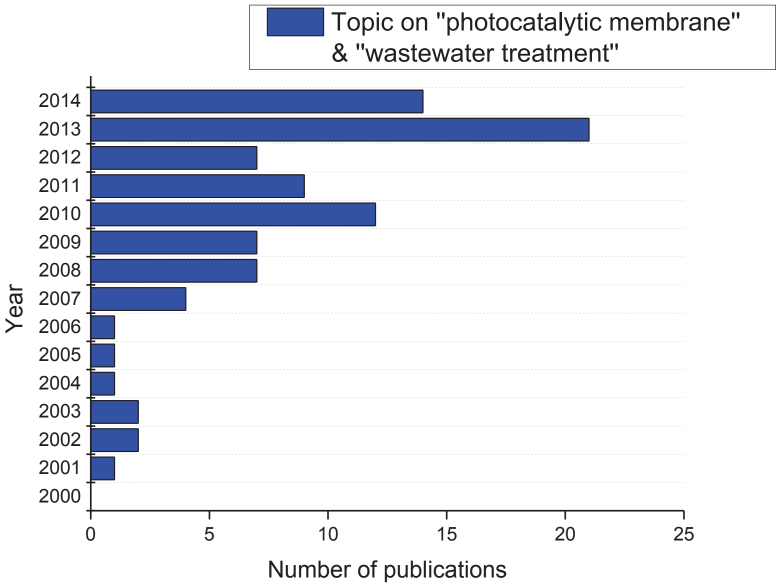

Appendix 2 Publications relevant to photocatalytic membrane and wastewater treatment from January 2000 to September 2014 (an online survey based on "web of science").

References

1. Tchobanoglous, G., Burton, L.F. and Stensel, H.D., *Wastewater Engineering: Treatment and Reuse* 2002: Metcalf & Eddy.
2. Glaze, W., Kang, J.W. and Chapin, H.D., *The Chemistry of Water Treatment Processes Involving Ozone, Hydrogen Peroxide and Ultraviolet Radiation.* J. Int. Ozone Assoc., 1987. **9**(4): p. 335-352.
3. Koppenol, W.H.a.L., F.J., *The oxidizing nature of the hydroxyl radical. A comparison with the ferryl ion (FeO2+).* J. Phys. Chem., 1984. **88**(1): p. 99-101.
4. Fujishima, A.a.H., K., *Electrochemical photolysis of water at a semiconductor electrode.* Nature, 1972. **238**: p. 37-38.
5. Al-Ekabi, H.a.S., N., *Kinetic studies in heterogeneous photocatalysis. 1. Photocatalytic degradation of chlorinated phenols in aerated aqueous solutions onver TiO2 supported on a galss matrix.* J. Phys. Chem., 1988. **92**(20): p. 5726-5731.
6. Grabowska, E., Reszczynska, J. and Zaleska, A., *Mechanism of phenol photodegradation in the presence of pure and modified-TiO2: A review.* Water Res., 2012. **46**(17): p. 5453-71.
7. Mozia, S., Toyoda, M., Inagaki, M., Tryba, B. and Morawski, A.W., *Application of carbon-coated TiO2 for decomposition of methylene blue in a photocatalytic membrane reactor.* J. Hazard. Mater., 2007. **140**(1-2): p. 369-75.
8. Hájková, P., Špatenka, P., Krumeich, J., Exnar, P., Kolouch, A., Matoušek, J. and Kočí, P., *Antibacterial effect of silver modified TiO2/PECVD films.* Europ. Phys. J. D, 2009. **54**(2): p. 189-193.
9. Nakano, R., Ishiguro, H., Yao, Y., Kajioka, J., Fujishima, A., Sunada, K., Minoshima, M., Hashimoto, K. and Kubota, Y., *Photocatalytic inactivation of influenza virus by titanium dioxide thin film.* Photochem. Photobio. Sci., 2012. **11**(8): p. 1293-1298.
10. Nakata, K.a.F., A., *TiO2 photocatalysis: Design and applications.* J. Photochem. and Photobio. C: Photochem. Rev., 2012. **13**(3): p. 169-189.
11. Ollis, D.F., *Integrating photocatalysis and membrane technologies for water treatment: A review.* Ann. N. Y. Acad. Sci., 2003. **984**: p. 65-83.
12. Mozia, S., *Photocatalytic membrane reactors (PMRs) in water and wastewater treatment. A review.* Sep. Purif. Tech., 2010. **73**(2): p. 71-91.
13. Athanasekou, C.P., Romanos, G.E., Katsaros, F.K., Kordatos, K., Likodimos, V. and Falaras, P., *Very efficient composite titania membranes in hybrid ultrafiltration/photocatalysis water treatment processes.* J. Membr. Sci., 2012. **392-393**: p. 192-203.
14. Djafer, L., Ayral, A. and Ouagued, A., *Robust synthesis and performance of a titania-based ultrafiltration membrane with photocatalytic properties.* Sep.Purif.Tech., 2010. **75**(2): p. 198-203.
15. You, S.J., Semblante, U.S., Luc, S.C., Damodara, A.R. and Wei, T.C., *Evaluation of the antifouling and photocatalytic properties of poly(vinylidene fluoride) plasma-grafted poly(acrylic acid) membrane with self-assembled TiO2.* J. Hazard. Mater., 2012. **237-238**: p. 10-19.
16. Hu, A., Zhang, X., Oakes, D. K., Peng, P., Zhou, N. and Servos, R.M., *Hydrothermal growth of free standing TiO2 nanowire membranes for photocatalytic degradation of pharmaceuticals.* J. Hazard. Mater., 2011. **189**(1-2): p. 278-285.
17. Zeng, Y., Cheng, G., Wen, M. and Wu, W., *Effect of external bias voltage and coating thickness on the photocatalytic activity of thermal sprayed TiO2 coating.* Prog. Org. Coat., 2007. **61**(2-4): p. 321-325.
18. Choi, H., Stathatos, E. and Dionysiou, D.D., *Sol–gel preparation of mesoporous photocatalytic TiO2 films and TiO2/Al2O3 composite membranes for environmental applications.* Appl. Cat. B: Envir., 2006. **63**(1-2): p. 60-67.

19. Vijayalakshmy, S.a.S., B., *Enhanced performance of dye-sensitized solar cells with TiO2 blocking layers and Pt counter electrodes prepared by physical vapor deposition (PVD).* Electrochim. Acta., 2014. **116**(0): p. 334-342.
20. Ragazzon, D., Farstad, M. H., Schaefer, A., Walle, L. E., Uvdal, P., Borg, A. and Sandell, A., *Growth of TiO2(B)(001) on Au(111) by chemical vapor deposition.* Surf. Sci., 2015. **633**: p. 102-108.
21. Kulisch, W., *Remote plasma-enhanced chemical vapour depoisiton with metal organic source gases: principles and applications.* Surf. Coat. Tech., 1993. **59**: p. 193-201.
22. Stroyuk, L.A., Kryukov, I.A., Kuchimii, Y.S. and Pokhodenko, D.V., *Quantum effects in semiconductor photocatalysis.* Theor. Exp. Chem., 2005. **41**(4): p. 207-228.
23. Agrios, G.A.a.P., P., *Recombination rate of photogenerated charges versus surface area: Opposing effects of TiO2 sintering temperature on photocatalytic removal of phenol, anisole, and pyridine in water.* J. Photochem. Photobio. A: Chem., 2006. **180**(1–2): p. 130-135.
24. Chen, D., Li, F and Ray, K.A., *Effect of mass transfer and catalyst layer thickness on photocatlaytic reaction.* AIChE J., 2000. **46**(5): p. 1034-1045.
25. Huang, S.S.a.C., J.S., *Comparison of the characteristics of TiO2 films prepared by low-pressure and plasma-enhanced chemical vapor deposition.* J. Mater. Sci.: Mater. Elec., 2002. **13**(2): p. 77-81.
26. Wu, C.Y., Chiang, B. S., Chang, S. and Liu, D. S., *Determination of photocatalytic activity in amorphous and crystalline titanium oxide films prepared using plasma-enhanced chemical vapor deposition.* Applied Surface Science, 2011. **257**(6): p. 1893-1897.
27. Srivatsa, K.M.K., Bera, M. and Basu, A., *Preparation of large surface area rutile titania crystals at room temperature by PECVD with applied d.c. bias.* Mater. Lett., 2008. **62**(20): p. 3527-3529.
28. Li, D., Carette, M., Granier, A., Landesman, J.P. and Goullet, A., *In situ spectroscopic ellipsometry study of TiO2 films deposited by plasma enhanced chemical vapour deposition.* Applied Surface Science, 2013. **283**: p. 234-239.
29. Lacoste, A., *PBII processing of dielectric layers: physical aspects limitations and experimental results.* Surf. Coat. Tech., 2001. **135**(2-3): p. 268-273.
30. Lacoste, A.a.P., J., *Processing considerations with plasma-based ion implantation of polymers: Theoretical aspects, limitations, and experimental results.* Nuc. Instr. Meth. Phys. Res. Sec. B: Beam Inter. Mater. Atom., 2003. **208**: p. 260-266.
31. Zhou, M., Roualdès, S., Zhao, J., Autès,V. and Ayral, A., *Nanocrystalline TiO2 thin film prepared by low-temperature plasma-enhanced chemical vapor deposition (PECVD) for photocatalytic applications.* Thin Solid Filmes, 2015. **accepted**.
32. *P/N junctions and band gaps*. 2011; http://solarcellcentral.com/junction_page.html Copyright © 2011 Four Peaks Technologies].
33. Linsebigler, A.L., Lu, G.Q. and Yates, J.T., *Photocatalysis on TiO2 surfaces: Principles mechanisms and selected results.* Chemi. Rev., 1995. **95**(3): p. 735-758.
34. Murphy, A., *Band-gap determination from diffuse reflectance measurements of semiconductor films, and application to photoelectrochemical water-splitting.* Solar Energy Materials and Solar Cells, 2007. **91**(14): p. 1326-1337.
35. Fox, A.M.a.D., T.M., *Heterogeneous photocatalysis* Chem. Rev., 1993. **93**(1): p. 341-357.
36. Zhang, J., Zhou, P., Liu, J. and Yu, J., *New understanding of the difference of photocatalytic activity among anatase, rutile and brookite TiO2.* Phys. Chem. Chem. Phys., 2014. **16**(38): p. 20382-6.
37. *Direct and indirect band gap semiconductors*. 2015; http://www.doitpoms.ac.uk/tlplib/semiconductors/direct.php Copyright © 2004-2015 University of Cambridge].
38. Fujishima, A., Zhang, X. and Tryk, D.A., *TiO2 photocatalysis and related surface phenomena.* Surf. Sci. Rep., 2008. **63**(12): p. 515-582.

39. Schneider, J., Matsuoka, M., Takeuchi, M., Zhang, J., Horiuchi, Y., Anpo, M. and Bahnemann, W.D., *Understanding TiO2 photocatalysis: mechanisms and materials.* Chem. Rev., 2014. **114**(19): p. 9919-86.
40. Ochiai, T. and A. Fujishima, *Photoelectrochemical properties of TiO2 photocatalyst and its applications for environmental purification.* J. Photochem. and Photobio. C: Photochem. Rev., 2012. **13**(4): p. 247-262.
41. Peiró, M.A., Colombo, C., Doyle, G., Nelson, J., Mills, A. and Durrant, R.G., *Photochemical reduction of oxygen adsorbed to nanocrystalline TiO2 films: A transient absorption and oxygen scavenging study of pifferent TiO2 preparations.* J. Phys. Chem., 2006. **110**: p. 23255–23263.
42. Tamaki, Y., Furube, A., Murai, M., Hara, K., Katoh, R. and Tachiya, M., *Dynamics of efficient electron–hole separation in TiO2 nanoparticles revealed by femtosecond transient absorption spectroscopy under the weak-excitation condition.* Phys. Chem. Chem. Phys. , 2007. **9**: p. 1453-1460.
43. Yamakata, A., Ishibashi, T. and Onishi, H., *Water-and oxygen-induced decay kinetics of photogenerated electrons in TiO2 and Pt/TiO2: A time-resolved infrared absorption study.* J. Phys. Chem. B 105 (2001) 2001. **105**(30): p. 7258-7262.
44. Yoshihara, T., Katoh, R. , Furube, A., Tamaki, Y., Murai, M., Hara, K., Murata, S., Arakawa, H. and Tachiya, M. , *Identification of reactive species in photoexcited nanocrystalline TiO2 films by wide-wavelength-range (400–2500 nm) transient absorption spectroscopy.* J. Phys. Chem. B, 2004. **108**(12): p. 3817-3823.
45. Colombo, D.P., Jr., and Bowman M.B., *Does interfacial charge transfer compete with charge carrier recombination? A femtosecond diffuse reflectance onvestigation of TiO2 manoparticles.* J. Phys. Chem., 1996. **100**(47): p. 18445–18449.
46. Tamaki, Y., Furube, A. , Murai, M., Hara, K., Katoh, R. and Tachiya, M. , *Direct observation of reactive trapped holes in TiO2 undergoing photocatalytic pxidation of adsorbed Alcohols: Evaluation of the reaction rates and yields.* J. Am. Chem. Soc., 2006. **128**: p. 416-417.
47. Hurum, D.C., Agrios, A.G., Gray, K.A., Rajh, T. and Thurnauer, M.C. , *Explaining the enhanced photocatalytic activity of Degussa P25 mixed-phase TiO2 using EPR.* J. Phys. Chem. B, 2003. **107**: p. 4545-4549.
48. Micic, O., Zhang, Y., Cromack, K.R., Trifunac, A. and Thurnauer, M. , *Photoinduced hole transfer from titanium dioxide to methanol molecules in aqueous solution studied by electron paramagnetic resonance.* J. Phys. Chem. , 1993. **97**: p. 13284-13288.
49. Szczepankiewicz, S.H., Colussi, A.J. and Hoffmann, M.R. , *Infrared spectra of photoinduced species on hydroxylated titania surfaces.* J. Phys. Chem. B, 2000. **104**: p. 9842-9850.
50. Valentin, D.C., Pacchioni, G. and Selloni, A. , *Electronic structure of defect states in hydroxylated and reduced rutile TiO2(110) surfaces.* Phys. Rev. Lett., 2006. **97**: p. 166803-166804.
51. Henderson, A.M., *A surface science perspective on View the MathML source photocatalysis.* Surf. Sci. Rep., 2011. **66**(6-7): p. 185-297.
52. Hoffmann, M.R., Martin, S.T., Choi, W. and Bahnemann, D.W., *Environmental applications of semiconductor photocatalysis.* Chem. Rev. , 1995. **95**(1): p. 69-96.
53. Salvador, P.a.G., C., *The nature of surface states involved in the photo- and electroluminescence spectra of n-titanium dioxide electrodes.* J. Phys. Chem. , 1984. **88**(16): p. 3696-3698.
54. Nakamura, R., Ohashi, N., Imanishi, A., Osawa, T., Matsumoto, Y., Koinuma, H. and Nakato, Y., *Crystal-face dependences of surface band edges and hole reactivity, revealed by preparation of essentially atomically smooth and stable (110) and (100) n-TiO2 (rutile) surfaces.* J. Phys. Chem. B, 2005. **109**: p. 1648-1651.
55. Murakami, Y.M.K., E., Nosaka, A.Y. and Nosaka, Y., *Direct detection of OH radicals diffused to the gas phase from the UV-irradiated photocatalytic TiO2 surfaces by means of*

laser-induced fluorescence spectroscopy. J. Phys. Chem. B, 2006. **110**(34): p. 16808-16811.

56. Zhang, J. and Y. Nosaka, *Mechanism of the OH radical generation in photocatalysis with TiO2 of different crystalline types.* J. Phys. Chem. C., 2014. **118**(20): p. 10824-10832.
57. Draper, R.B.a.F., M.A. , *Titanium dioxide photosensitized reactions studied by diffuse reflectance flash photolysis in aqueous suspensions of TiO2 powder.* Langmuir, 1990. **6**(8): p. 1396-1402.
58. Tachikawa, T., Tojo, S. Fujitsuka, M. and Majima, T., *Photocatalytic one-electron oxidation of biphenyl derivatives strongly coupled with the TiO2 surface.* Langmuir, 2004. **20**(7): p. 2753-2759.
59. Nosaka, Y., Komori, S., Yawata, K., Hirakawa, T. and Nosaka, A.Y., *Photocatalytic ˙OH radical formation in TiO2 aqueous suspension studied by several detection methods.* Phys. Chem. Chem. Phys. , 2003. **5**: p. 4731-4735.
60. Hwang, S.J., Petucci, C. and Raftery, D., *In situ solid-state NMR studies of trichloroethylene photocatalysis: Formation and characterization of surface-bound Intermediates.* J. Am. Chem. Soc., 1998. **120**(18): p. 4388-4397.
61. Nosaka, Y., Daimon, T., Nosaka, A.Y. and Murakami, Y., *Singlet oxygen formation in photocatalytic TiO2 aqueous suspension.* Phys. Chem. Chem. Phys., 2004. **6**: p. 2917-2918.
62. Chen, C.C., Lu, C.S., Chung, Y.C. and Jan, J.L., *UV light induced photodegradation of malachite green on TiO2 nanoparticles.* J. Hazard. Mater., 2007. **141**: p. 520-528.
63. Bhatkhnade, D.S., Kamble, S.P., Sawant, S.B., and Pangarkar, V.G., *Photocatalytic and photochemical degradation of nitrobenzene using artificial ultraviolet light.* Chem. Eng. J., 2004. **102**: p. 283-290.
64. Chong, M.N., Lei, S., Jin, B., Saint, C. and Chow, C.W.K., *Optimizaion of an annular photoreactor process for degradation of Congo red using a newly synthesized titania impregnated kaolinite nano-photocatalyst.* Sep. Purif. Tech., 2009. **67**: p. 355-363.
65. Gaya, U.I. and A.H. Abdullah, *Heterogeneous photocatalytic degradation of organic contaminants over titanium dioxide: a review of fundamentals, progress and problems.* J. Photochm. Photobiol. C: photochem. Rev., 2008. **9**: p. 1-12.
66. Renz, C., *Lichtreaktionen der oxyde des titans, cers und der erdsäuren.* Helv. Chim. Acta., 1921. **4**: p. 961-968.
67. Goodeve, C.F.a.K., J.A., *Photosensitisation by titanium dioxide.* Trans. Faraday Soc., 1938. **34**(1): p. 570-579.
68. Goodeve, C.F.a.K., J.A., *The mechanism of photosensitisation by solids.* Tran. Faraday Soc., 1938. **34**: p. 902-908.
69. Markham, M.C. and K.J. Laidler, *A kinetic study of photo-oxidations on the surface of zinc oxide in aqueous suspensions.* J. Phys. Chem., 1953. **57**: p. 363-369.
70. Stephens, R.E., Ke, B. and Trivich D. , *The efficiencies of some solids as catalysts for the photosynthesis of hydrogen peroxide.* J. Phys. Chem. , 1955. **59**: p. 966-969.
71. Kennedy, R.D., Ritchie, M. and Mackenzie, J. , *The photosorption of oxygen and nitric oxide on titanium dioxide*

. Trans. Faraday Soc., 1958. **54**: p. 130-138.

72. Filimonov, N.V., *Photocatalytic Oxidation of gaseous isopropanol on ZnO and TiO2* Doklady Akademii Nauk SSSR, 1964. **154**: p. 922-925.
73. Kato, S. and F. Mashio, *TiO2 photocatalyzed oxidation of tetraline in liquid phase.* J. Chem. Soc. Japan., Indust. Chem. Sect. , 1964. **67**: p. 1136-1140.
74. McLintock, S.I. and M. Ritchie, *Reactions on titanium dioxide: Photo-adsorption and oxidation of ethylene and propylene.* Trans. Faraday Soc., 1965. **61**: p. 1007-1016.
75. Frank, S.N.a.B., J.A., *Heterogeneous photocatalytic oxidation of cyanide and sulfite in aqueous solutions at semiconductor powders.* J. Phys. Chem., 1977. **81**: p. 1484–1488.

76. Frank, S.N. and A.J. Bard, *Heterogeneous photocatalytic oxidation of cyanide ion in aqueous solution at TiO2 powder.* J. Am. Chem. Soc., 1977. **99**: p. 303-304.
77. Noguchi, T., Fujishima, A., Sawunyama, P. and Hashimoto, K., *Photocatalytic degradation of gaseous formaldehyde using TiO2 film.* Environ. Sci. Tech., 1998. **32**(3831-3833).
78. Obuchi, E., Sakamoto, T., Nakano, K. and Shiraishi, F., *Photocatalytic decomposition of acetaldehyde over TiO2/SiO2 catalyst.* Chem. Eng. Sci., 1999. **54**: p. 1525-1530.
79. Alberici, M.R. and F.W. Jardim, *Photocatalytic destruction of VOCs in the gas-phase using titanium dioxide.* Appl. Catal. B: Environ., 1997. **14**: p. 55-68.
80. Ollis, D.F., Pelizzetti, E. and Serpone, N., , *Photochemical conversion and storage of solar energy.* Environ. Sci. Tech., 1991. **25**.
81. Fei, H., Leng, W., Li, X., Cheng, X., Xu, Y., Zhang, J. and Cao, C., *Photocatalytic oxidation of arsenite over TiO2: Is superoxide the main oxidant in normal air-saturated aqueous solution?* Environ. Sci. Technol., 2011. **45**: p. 4352-4539.
82. Sunada, K., Watanabe, T. and Hashimoto, K, *Studies on photokilling of bacteria on TiO2 thin film.* J. Photochem. Photobio. A: Chem., 2003. **156**: p. 227-233.
83. Sclafani, A. and J.M. Herrmann, *Comparison of the photoelectronic and photocatalytic activities of various anatase and rutile forms of titania in pure liquid organic phases and in aqueous solutions.* J. Phys. Chem., 1996. **100**(32): p. 13655-13661.
84. Yang, D., Liu, H., Zheng, Z., Yuan, Y., Zhao, J., Waclawik, E.R., Ke, X. and H. and Zhu, *An efficient photocatalyst structure: TiO2(B) nanofibers with a shell of anatase nanocrystals.* J. Am. Chem. Soc., 2009. **131**(49): p. 17885-17893.
85. Collins-Martinez, V., A.L. Ortiz, and A.A. Elguezabal, *Influence of the anatase/rutile ratio on the TiO2 photocatalytic activity for the photodegradation of light hydrocarbons.* International Journal of Chemical Reactor Engineering, 2007. **5**.
86. Di Paola, A., Bellardita, M. and Palmisano, L., *Brookite, the least known TiO2 photocatalyst.* Catalysts, 2013. **3**(1): p. 36-73.
87. Srivatsa, K.M.K., Bera, M. and Basu, A., *Pure brookite titania crystals with large surface area deposited by plasma enhanced chemical vapour deposition technique.* Thin Solid Films, 2008. **516**(21): p. 7443-7446.
88. Moellmann, J., Ehrlich, S., Tonner, R. and Grimme, S., *A DFT-D study of structural and energetic properties of TiO2 modifications.* J. Phys.: Condens. Matter., 2012. **24**(42).
89. Ishioka, K. and H. Petek, *Raman generation of coherent phonons of anatase and rutile TiO2 photoexcited at fundamental absorption edges.* Phys. Rev. B

, 2012. **86**.

90. Alberti, A., Bongiorno, C. and Pellegrino, G., *Anatase/rutile nucleation and growth on (0002) and (11-20) oriented ZnO:Al/glass substrates at 150°C.* Thin Solid Films, 2014. **555**: p. 3-8.
91. Hengerer, R., Bolliger, B., Erbudak, M. and Grätzel, M., *Structure and stability of the anatase TiO2 (101) and (001) surfaces.* Surf. Sci., 2000. **460**: p. 162-169.
92. Burnside, D.S., Shklover, V., Barbe, C., Comte, P., Arendse, F., Brooks, K. and Grätzel, M., *Self-organization of TiO2 nanoparticles in thin films.* Chem. Mater., 1998. **10**: p. 2419-2425.
93. Ruzycki, N., Herman, C.S., Boatner, A.L. and Diebold, U., *Scanning tunneling microscopy study of the anatase (100) surface.* Surf. Sci., 2003. **529**: p. L239-L244.
94. Shklover, V., Nazeeruddin, K.M., Zakeeruddin, M.S., Barbe, C., Kay, A., Haibach, T., Steurer, W., Hermann, R., Nissen, U.H and Grätzel, M., *Structure of nanocrystalline TiO2 powders and precursor to their highly efficient photosensitizer.* Chem. Mater. , 1997. **9**(2): p. 430-439.
95. Pan, J., Liu, G., Lu, G.Q. and Cheng, H.M., *On the true photoreactivity order of {001}, {010}, and {101} facets of anatase TiO2 crystals.* Angew. Chem. Int. Ed., 2011. **50**(9): p. 2133-2137.

96. Ramamoorthy, M., Vanderbilt, D. and King-Smith, D.R., *First-principles calculations of the energetics of stoichiometric TiO2 surfaces.* Phys. Rev. B, 1994. **49**.

97. Beltrán, A., Gracia, L. and Andrés, J., *Density functional theory study of the brookite surfaces and phase transitions between natural titania polymorphs.* J. Phys. Chem. B, 2006. **110**: p. 23417-23423.

98. López, R. and R. Gómez, *Band-gap energy estimation from diffuse reflectance measurements on sol–gel and commercial TiO2: A comparative study.* J. Sol-Gel Sci. Tech., 2011. **61**(1): p. 1-7.

99. Valencia, S., Marin, M.J. and G. and Restrepo, *Study of the bandgap of synthesized titanium dioxide nanoparticules using the sol-gel method and a hydrothermal treatment.* Open Mater. Sci. J., 2010. **4**: p. 9-14.

100. Kaur, K. and C.V. Singh, *Amorphous TiO2 as a photocatalyst for hydrogen production: A DFT study of structural and electronic properties.* Energ. Proc., 2012. **29**: p. 291-299.

101. Lee, Y.C., Chang, Y.S., Teoh, L.G., Huang, Y.L. and Shen, Y.C., *The effects of the nanostructure of mesoporous TiO2 on optical band gap energy.* J. Sol-Gel Sci. Tech., 2010. **56**(1): p. 33-38.

102. Tian, G.L., He, H. B. and Shao, J.D., *Effet of microstructure of TiO2 thin films on optical band gap energy.* Chin. Phys. Lett, 2005. **22**(7): p. 1787-1790.

103. Liu, G., Wang, L., Sun, C., Yan, X., Wang, X., Chen, Z., Smith, C.S., Cheng, H.M. and Lu, G.Q., *Band-to-band visible-light photon excitation and photoactivity induced by homogeneous nitrogen doping in layered titanates.* Chem. Mater., 2009. **21**(7): p. 1266-1274.

104. Romero-Gomez, P., Rico, V., Borras, A., Barranco, A. , Espinos, P.J., Cotrino, J. and Gonzalez-Elipe, R.A., *Chemical state of nitrogen and visible surface and schottky barrier driven photoactivities of N-Doped TiO2 thin films.* J. Phys. Chem. C 2009. **113**(30): p. 13341–13351.

105. Wu, Y., Xing, M., Tian, B., Zhang, J. and Chen, F., *Preparation of nitrogen and fluorine co-doped mesoporous TiO2 microsphere and photodegradation of acid orange 7 under visible light.* Chem. Eng. J., 2010. **162**(2): p. 710-717.

106. Maeda, M. and T. Watanabe, *Visible light photocatalysis of nitrogen-doped titanium oxide films prepared by plasma-enhanced chemical vapor deposition.* J. Electrochem. Soc., 2006. **153**(3): p. 186-189.

107. Zhang, L. and J.C. Yu, *A sonochemical approach to hierarchical porous titania spheres with enhanced photocatalytic activity.* Chem. Comm., 2003(16): p. 2078.

108. Alem, A. and H. Sarpoolaky, *The effect of silver doping on photocatalytic properties of titania multilayer membranes.* Solid State Sci., 2010. **12**(8): p. 1469-1472.

109. Liu, R., Wang, P., Wang, X., Yu, H. and Yu, J., *UV- and visible-light photocatalytic activity of simultaneously deposited and doped Ag/Ag(I)-TiO2 photocatalyst.* J. Phys. Chemi. C, 2012. **116**(33): p. 17721-17728.

110. Benotti, M.J., Stanford, B.D., Wert, E.C. and Snyder, S.A., *Evaluation of a photocatalytic reactor membrane pilot system for the removal of pharmaceuticals and endocrine disrupting compounds from water.* Water Res., 2009. **43**(6): p. 1513-1522.

111. Mozia, S., Tomaszewska, M. and Morawski, A.W., *Photocatalytic membrane reactor (PMR) coupling photocatalysis and membrane distillation—Effectiveness of removal of three azo dyes from water.* Cat. Today, 2007. **129**(1-2): p. 3-8.

112. Sobczyński, A., Duczmal, Ł. and Zmudziński, W., *Phenol destruction by photocatalysis on TiO2: an attempt to solve the reaction mechanism.* J. Molec. Cat. A: Chemi., 2004. **213**(2): p. 225-230.

113. Andreozzi, R., Caprio, V., nsola, A. and Marotta, R., *Advanced oxidation processes (AOP) for water purification and recovery.* Cat. Today, 1999. **53**: p. 51-59.

114. Moslehyani, A., Ismail, A. F., Othman, M.H.D. and Matsuura, T., *Hydrocarbon degradation and separation of bilge water via a novel TiO2-HNTs/PVDF-based photocatalytic membrane reactor (PMR).* RSC Adv., 2015. **5**(19): p. 14147-14155.

115. Ayllon, J.A., Figueras, A., Garelik, S., Spirkova, L., Durand, J. and Cot, L., *Preparation of TiO2 powder using titanium tetraisopropoxide decomposition in a plasma enhanced chemical vapor deposition (PECVD) reactor.* J. Mater. Sci. Lett., 1999. **18**: p. 1319-1321.
116. Kment, Š., Gregora, I.. Kmentová, H., Novotná, P., Hubička, Z., Krýsa, J., Sajdl, P., Dejneka, A., Brunclíková, M., Jastrabík, L. and Hrabovský, M., *Raman spectroscopy of dip-coated and spin-coated sol–gel TiO2 thin films on different types of glass substrate.* Journal of Sol-Gel Science and Technology, 2012. **63**(3): p. 294-306.
117. Krýsa, J., Baudys, M., Zlámal, M., Krýsová, H., Morozová, M. and Klusoň, P., *Photocatalytic and photoelectrochemical properties of sol–gel TiO2 films of controlled thickness and porosity.* Cat. Today, 2014. **230**: p. 2-7.
118. Molinari, R., Pirillo, F., Loddo, V. and Palmisano, L., *Heterogeneous photocatalytic degradation of pharmaceuticals in water by using polycrystalline TiO2 and a nanofiltration membrane reactor.* Cat. Today, 2006. **118**(1-2): p. 205-213.
119. Bosc, F., Ayral, A., Albouy, P. A. and Guizard, C., *A simple route for low-temperature synthesis of mesoporous and nanocrystalline anatase thin films.* Chem. Mater., 2003. **15**(12): p. 2463-2468.
120. Ayral, A., Guizard, L. and Cot, L., *Synthesis and application of hybrid organic-inorganic colloidal gels.* J. Mater. Sci. Lett., 1994. **13**: p. 1538-1539.
121. Shon, K.H., Phuntsho, S. and Vigneswaran, S., *Effect of photocatalysis on the membrane hybrid system for wastewater treatment.* Desalination, 2008. **225**(1-3): p. 235-248.
122. Chu, S., Luo, L., Yang, J., Kong, F., Luo, S., Wang, Y. and Zou, Z., *Low-temperature synthesis of mesoporous TiO2 photocatalyst with self-cleaning strategy to remove organic templates.* Appl. Surf. Sci., 2012. **258**(24): p. 9664-9667.
123. Bosc, F., Ayral, A. and Guizard, C., *Mesoporous anatase coatings for coupling membrane separation and photocatalyzed reactions.* J. Membr. Sci., 2005. **265**(1-2): p. 13-19.
124. Bosc, F., Lacroix-Desmazes, P. and Ayral, A., *TiO2 anatase-based membranes with hierarchical porosity and photocatalytic properties.* J. Colloid. Interface. Sci., 2006. **304**(2): p. 545-548.
125. Kim, G.M., Lee, S.M., Michler, G.H., Roggendorf, H., Gosele, U. and Knez, M., *Nanostructured pure anatase titania tubes replicated from electrospun polymer fiber templates by atomic layer deposition.* Chem. Mater., 2008. **20**(9): p. 3085-3091.
126. Leong, S., Razmjou, A., Wang, K., Hapgood, K., Zhang, X. and Wang, H., *TiO2 based photocatalytic membranes: A review.* J. Membr. Sci., 2014. **472**: p. 167-184.
127. Zhang, X., Wang, D.K. and J.C. and Diniz da Costa, *Recent progresses on fabrication of photocatalytic membranes for water treatment.* Cat. Today, 2014. **230**: p. 47-54.
128. Pelaez, M., Nolan, T.N., Pillai, C.S., Seery, K.M., Falaras, P., Kontos, G.A., Dunlop, S.M.P., Hamilton, Jeremy, J.W., Byrne, J. A., O'Shea, K., Entezari, H.M. and Dionysiou, D.D., *A review on the visible light active titanium dioxide photocatalysts for environmental applications.* Appl. Cat. B: Environ., 2012. **125**: p. 331-349.
129. Zhang, X., Zhang, T., Ng, J., and Sun, D.D., *High-performance multifunctional TiO2 nanowire ultrafiltration membrane with a hierarchical layer structure for water treatment.* Adv. Funct. Mater., 2009. **19**: p. 3731–3736.
130. Zhang, X., Du, A.J., Lee, P., Sun, D.D. and Leckie, O.J., *TiO2 nanowire membrane for concurrent filtration and photocatalytic oxidation of humic acid in water.* J. Membr. Sci., 2008. **313**: p. 44-51.
131. Albu, P.S., Ghicov, A., Macak, M.J., Hahn, R. and Schmuki, P., *Self-organized, free-standing TiO2 nanotube membrane for flow-through photocatalytic applications.* Nano Lett. , 2007. **7**: p. 1286–1289.
132. Liao, J., Lin, S., Pan, N., Li, S., Cao, X. and Cao, Y., *Fabrication and photocatalytic properties offree-standingTiO2 nanotube membranes with through-hole morphology.* Mater. Charact., 2012. **66**: p. 24-29.

133. Zhang, X., Du,J.A., Lee, P., Sun, D.D. and Leckie,O.J., *Grafted multifunctional titanium dioxide nanotube membrane: separation and photodegradation of aquatic pollutant.* Appl. Catal. B: Environ., 2008. **84**: p. 262-267.
134. Zhang, X.W., D.K., Lopez, D.R.S and Costa, J.C.D.D, Chem. Eng. J. , 2013.
135. Liu, L., Liu, Z., Bai, H., Sun, D.D., *Concurrent filtration and solar photocatalytic disinfection/degradation using high-performance Ag/TiO2 nanofiber membrane.* Water Res., 2012. **46**: p. 1101-1112.
136. Song, H., Shao, J., He,Y., Liu, B. and Zhong, X., *Natural organic matter removal and flux decline with PEG-TiO2-doped PVDF membranes by integration of ultrafiltration with photocatalysis.* J. Membr. Sci., 2012. **405-406**: p. 48-56.
137. Rahimpour, A., Madaeni, S.S., Taheri, A.H. and Mansourpanah, Y., *Coupling TiO2 nanoparticles with UV irradiation for modification of polyethersulfone ultrafiltration membranes.* J.Membr.Sci.313(2008). 2008. **313**: p. 158-169.
138. Rahimpour, A., Jahanshahi, M., Rajaeian, B. and Rahimnejad, M., *TiO2 entrapped nano-composite PVDF/PES membranes: Preparation, characterization, antifouling and antibacterial properties.* Desalination, 2011. **278**: p. 343-353.
139. Damodar, A.R., You, S.J. and Chou, H.H., *Study the self cleaning, antibacterial and photocatalytic properties of TiO2 entrapped PVDF membranes.* J. Hazard. Mater., 2009. **172**: p. 1321-1328.
140. Mansourpanah, Y., Madaeni, S.S., Rahimpour,A., Farhadian, F. and Taheri, A.H., *Formation of appropriate sites on nanofiltration membrane surface for binding TiO2 photo-catalyst: performance,characterization and fouling-resistant capability.* J. Membr. Sci. , 2009. **330**: p. 297-306.
141. Bredow, T. and K. Jug, *SINDO1study of photocatalytic formation and reactions of OH radicals at anatase particles.* J. Phys. Chem., 1995. **99**: p. 285-291.
142. Kim, S.H., Kwak, S.Y., Sohn,B.H. and Park, T.H., *Design of TiO2 nanoparticle self-assembled aromatic polyamide thin-film-composite (TFC) membrane as an approach to solve biofouling problem.* J. Membr. Sci., 2003. **211**: p. 157-165.
143. Zhang, H., Quan, X., Chen, S. and Zhao, H., *Fabrication and characterization of silica/titania nanotubes composite membrane with photocatalytic capability.* Environ. Sci. Tech., 2006. **40**: p. 6104-6109.
144. Ma, N., Zhang, Y., Quan, X., Fan, X. and Zhao, H., *Performing a microfiltration integrated with photocatalysis using an Ag-TiO2/HAP/Al2O3 composite membrane for water treatment: Evaluating effectiveness for humic acid removal and anti-fouling properties.* Water Res. , 2010. **44**: p. 6104-6114.
145. Ke, X., Ribbens, S., Fan, Y., Liu, H., Cool, P., Yang D. and H. Zhu, H., *Integrating efficient filtration and visible-light photocatalysis by loading Ag-doped zeolite Y particles on filtration membrane of alumina nanofibers.* J. Membr. Sci. , 2011. **375**: p. 69-74.
146. Romanos, E.G., Athanasekou, P.C., Katsaros, K.F., Kanellopoulos, K.N., Diony-siou, D.D., Likodimos, V. and Falaras, P., *Double-side active TiO2-modified nanofiltration membranes in continuous flow photocatalytic reactors for effective water purification.* J. Hazard. Mater. , 2012. **211-212**: p. 304–316.
147. Lin, Y.F., Tung, K.L., Tzeng, Y.S., Chen, J.H. and Chang, K.S., *Rapid atmospheric plasma spray coating preparation and photocatalytic activity of macroporous titania nanocrystalline membranes.* J. Membr. Sci., 2012. **389**: p. 83-90.
148. Rowlette, C.P. and A.C. Wolden, *Pulsed plasma-enhanced chemical vapor deposition of Al2O3–TiO2 nanolaminates.* Thin Solid Films, 2010. **518**(12): p. 3337-3341.
149. Hong, H.J., Sarkar, K.S. and Lee, B.T., *Formationof TiO2 nano fibers on a microchanneled Al2O3–ZrO2/TiO2 porous composite membrane for photocatalytic filtration.* J. Eur. Ceram. Soc. , 2012. **32**: p. 657-663.

150. Frach, P., et al., *Pulse Magnetron Sputtering with high power density – an attempt at a critical evaluation.* IOP Conference Series: Materials Science and Engineering, 2012. **39**: p. 012007.
151. Horáková, M., et al., *Sputter deposition of nanostructured TiO2 thin films.* IEEE Transactions on Plasma Science, 2014. **42**(10): p. 2790-2791.
152. Moser, E.M., Chappuis, S. and Olleros, J., *Production of photocatalytically active titania layers: A comparison of plasma processes and coating properties.* Surf. Coat.Tech., 2013. **227**: p. 2-9.
153. Tavares, C.J., et al., *PVD-Grown photocatalytic TiO2 thin films on PVDF substrates for sensors and actuators applications.* Thin Solid Films, 2008. **517**(3): p. 1161-1166.
154. Zeman, P. and S. Takabayashi, *Nano-scaled photocatalytic TiO2 thin films prepared by magnetron sputtering.* Thin Solid Films, 2003. **433**(1-2): p. 57-62.
155. Horprathum, M., et al., *Fabrication of nanostructure by physical vapor deposition with glancing angle deposition technique and its applications.* 2014: p. 7-11.
156. Heinrichs, J., Jarmar, T., Wiklund, U., and Engqvist, H., *Physical vapour deposition and bioactivity of crystalline titanium dioxide thin films.* Trends Biomater. Artif. Organs, 2008. **22**(2): p. 104-110.
157. Frach, P., et al., *Deposition of photocatalytic TiO2 layers by pulse magnetron sputtering and by plasma-activated evaporation.* Vacuum, 2006. **80**(7): p. 679-683.
158. Alvarez, R., Romero-Gomez, P., Gil-Rostra, J., Cotrino, J., Yubero, F., Gonzalez-Elipe, A.R. and Palmero, A., *Growth of SiO2 and TiO2 thin films deposited by reactive magnetron sputtering and PECVD by the incorporation of non-directional deposition fluxes.* Phys. Stat. Solid (A), 2013. **210**(4): p. 796-801.
159. Bhattacharyya, D., Sahoo, N.K., Thakur, S. AND Das, N.C. , *Spectroscopic ellipsometry of TiO2 layers prepared by ion-assisted electron-beam evaporation.* Thin Solid Films, 2000. **360**: p. 96-102.
160. Giolli, C., et al., *Characterization of TiO2 coatings prepared by a modified electric arc-physical vapour deposition system.* Surface and Coatings Technology, 2007. **202**(1): p. 13-22.
161. Rico, V., Romero, P., Hueso, L.J, Espinós, P.J. and González-Elipe, R.A., *Wetting angles and photocatalytic activities of illuminated TiO2 thin films.* Cat. Today, 2009. **143**(3-4): p. 347-354.
162. Bai, H., Liu, Z. and Sun, D.D., *Hierarchically multifunctional TiO2 nano-thorn membrane for water purification.* Chem. Commun. , 2010. **46**: p. 6542-6544.
163. Cao, X.P., Li, D., Jing, W.H., Xing, W.H. and Fan, Y.Q., *Synthesis of visible-light responsive C, N and Ce co-doped TiO2 mesoporous membranes via weak alkaline sol–gel process.* J. Mater. Chem. , 2012. **22**: p. 15309-15315.
164. Molinari, R., Pirillo, F., Falco, M., Loddo, V. and Palmisano, L., *Photocatalytic degradation of dyes by using a membrane reactor.* Chem. Eng. Proc.: Proc. Intens., 2004. **43**(9): p. 1103-1114.
165. Barni, B., Cavicchioli, A., Riva, E.,Zanoni, L., Bignoli, F., Bellobono, R.I., Gianturco, and D. F., A., Muntau, H., Montanarella, L., Facchetti,S. and Castellano, L., *Laboratory-scale photodegradation of phenol in aqueous solution by photocatalytic membranes immobilizing titanium dioxides.* Chemosphere, 1995. **30**: p. 1847-1860.
166. Rota, F., Cavassi, M., Niego, D., Gorlani, R., Vianelli, L., Tatti, L., Bruzzi, P., Moroni, A., Bellobono, R.I., Bianchi, M. and Muntau, H., *Mathematical modelling of photomineralization of phenols in aqueous solution by photocatalytic membranes immobilizing titanium dioxide.* Chemosphere, 1996. **33**: p. 2159-2173.
167. Barni, B., Cavicchioli, A., Riva, E., Zanoni, L., Bignoli, F., Bellobono, R.I., Gianturco, F., DeGiorgi, A., Muntau, H., Montanarella, L., Facchetti, S. and Castellano, L., *Pilot-plant-scale photodegradation of phenol in aqueous solution by photocatalytic membranes*

immobilizing titanium dioxide(PHOTOPERMs process). Chemosphere, 1995. **30**(1861-1874).

168. Lagrasta, C., Bellobono, R.I. and Bonardi, M., *Photobleaching and photomineralization of azobenzene and substituted azobenzenes in aqueous solution by photocatalytic membranes immobilizing titanium dioxide.* J. Photochem. Photobio. A: Chem., 1997. **11**: p. 201-205.
169. Hu, A., Zhang, X., Oakes, D.K., Peng, P., Zhou, N.Y. and Servos, R.M., *Hydrothermal growth of freestanding TiO2 nanowire membranes for photocatalytic degradation of pharmaceuticals.* J. Hazard. Mater., 2011. **189**: p. 278-285.
170. Alaoui, T.O., Nguyen, T.Q., Mbareck, C. and Rhlalou, T., *Elaboration and study of poly(vinylidene fluoride)-anatase TiO2 composite membranes in photocatalytic degradation of dyes.* Appl. Catal. A: Gen., 2009. **358**: p. 13-20.
171. Morris, E.R., Krikanova, E. and Shadman, F., *Photocatalytic membrane for removal of organic contaminants during ultra-purification of water.* Clean Tech. Environ. Policy, 2004. **9**: p. 96-104.
172. Liu, P., Liu, H., Liu, G., Yao, K. and Lv, W., *Preparationof TiO2 nanotubes coated on polyurethane and sudy of their photocatalytic activity.* Appl. Surf. Sci., 2012: p. 9593-9598.
173. Carlsson, J.O., *Handbook of Deposition Technologies for Films and Coatings*. Vol. "Chemical Vapor Deposition". 1994, Westwood: Noyes Publications.
174. Pierson, O.H., *Handbook of Chemical Vapor Deposition* Second Edition ed. 1999, New York: Noyes Publications.
175. Ahn, K.H., Park, Y. B. and Park, D. W., *Kinetic and mechanistic study on the chemical vapor deposition of titanium dioxide thin films by in situ FT-IR using TTIP.* Surf. Coat. Tech., 2003. **171**(1-3): p. 198-204.
176. Mattox, M.D., *Atomistic film growth and resulting film properties: residual film stress.* Vac. Tech. Coat., 2001.
177. *Plasma Enhanced CVD.* 2015; http://www.hitech-projects.com/dts/docs/pecvd.htm Copyright © 2004 - 2015 Royal Philips Electronics].
178. Maeda, M. and T. Watanabe, *Evaluation of photocatalytic properties of titanium oxide films prepared by plasma-enhanced chemical vapor deposition.* Thin Solid Films, 2005. **489**(1-2): p. 320-324.
179. Wu, C.Y., Hong, S.C., Hwang, F.T., Lai, L. W., Lin, T.W. and Liu, D.S., *Effect of nickel oxide seed layers on annealed-amorphous titanium oxide thin films prepared using plasma-enhanced chemical vapor deposition.* Thin Solid Films, 2011. **520**(1): p. 320-327.
180. Srivatsa, K.M.K., Chhikara, D. and Kumar, M.S., *Synthesis of anatase titania nanostructures at room temperature by PECVD technique.* J. Mater. Sci. Tech., 2011. **27**(8): p. 696-700.
181. Borras, A., Alvarez, R., Sanchez-Valencia, J.R., Ferrer, J. and Gonzalez-Elipe, R.A., *Critical thickness and nanoporosity of TiO2 optical thin films.* Micropor. Mesopor. Mater., 2012. **160**: p. 1-9.
182. Borras, A., Barranco, A. and Gonzalez-Elipe, R.A., *Design and control of porosity in oxide thin films grown by PECVD.* J. Mater. Sci., 2006. **41**(16): p. 5220-5226.
183. Borras, A., Macias-Montero, M., Romero-Gomez, P. and Gonzalez-Elipe, A.R., *Supported plasma-made 1D heterostructures: perspectives and applications.* J. Physics D: Appl. Phys., 2011. **44**(17).
184. Borras, A. and R.A. Gonzalez-Elipe, *Wetting properties of polycrystalline TiO2 surfaces: a scaling approach to the roughness factors.* Langmuir, 2010. **26**(20): p. 15875-15882.
185. Szymanowski, H., Sobczyk, A., Gazicki-Lipman, M., Jakubowski, W. and Klimek, L., *Plasma enhanced CVD deposition of titanium oxide for biomedical applications.* Surf. Coat. Tech., 2005. **200**(1-4): p. 1036-1040.
186. Hodgkinson, J.L.a.S., D.W., *Advances in atmospheric pressure PECVD: The influence of plasma parameters on film morphology.* Surf. Coat. Tech., 2013. **230**: p. 73-76.

187. Battiston, A.G., Gerbasi, R., Gregori, A., Porchia, M., Cattarin, S. and Rizzi, A.G., *PECVD of amorphous TiO2 thin films: effect of growth temperature and plasma gas composition.* Thin Solid Films, 2000. **371**(1-2): p. 126-131.
188. Cho, D.L., Min, H., Kim. J.H., Cha, G.S., Kim, G.S., Kim, B. H. and Ohk, S.H., *Photocatalytic charateristics of TiO2 thin films deposited by PECVD.* J. Ind. Eng. Chem., 2007. **13**(3): p. 434-437.
189. Kim, G.H., Kim, S.D. and Park, S.H., *Plasma enhanced chemical vapor deposition of TiO2 films on silica gel powders at atmospheric pressure in a circulating fluidized bed reactor.* Chem. Eng. Proc.: Proc. Intens., 2009. **48**(6): p. 1135-1139.
190. Kubala, N.G.a.W., C.A., *Self-limiting growth of anatase TiO2: A comparison of two deposition techniques.* Thin Solid Films, 2010. **518**(23): p. 6733-6737.
191. Guillard, C., Debayle, D., Gagnaire, A., Jaffrezic, H. and Herrmann, J.M., *Physical properties and photocatalytic efficiencies of TiO2 films prepared by PECVD and sol–gel methods.* Mater. Res. Bull., 2004. **39**(10): p. 1445-1458.
192. Lee, I.S., Kim, J.W., Youn, C.J., Park, S.K. and Hahn, Y.B., *Preparation and characterization of TiO2 thin films by PECVD on Si substrate.* Korean J. Chem. Eng., 1996. **13**(5): p. 473-477.
193. Sobczyk-Guzenda, A., Pietrzyk, B., Jakubowski, W., Szymanowski, H., Szymański, W., Kowalski, J., Oleśko, K. and Gazicki-Lipman, M., *Mechanical, photocatalytic and microbiological properties of titanium dioxide thin films synthesized with the sol–gel and low temperature plasma deposition techniques.* Mater. Res. Bull., 2013. **48**(10): p. 4022-4031.
194. Rouessac, V., Coustel, R., Bosc, F., Durand, J. and Ayral, A., *Characterisation of mesostructured TiO2 thin layers by ellipsometric porosimetry.* Thin Solid Films, 2006. **495**(1-2): p. 232-236.
195. Tauc, J.a.M., A., *States in the gap.* J. of Non-crystalline Solids, 1972. **8-10**: p. 569-585.
196. Paz, Y.a.H., A., *Photo-oxidatively self-cleaning transparent titanium dioxide films on soda lime glass: The deleterious effect of sodium contamination and its preventio.* J. Mater. Res., 1997. **12**: p. 2759-2766
197. *Phillips product mannual: CLEO fluorescent compact lamp*.
198. Vivien, D., Livage, J. and Mazieres, C., *NATURE OF PRECIPITATED HYDRATED OXIDES OF GROUP-4A METALS .1. THERMAL ANALYSIS AND INFRARED SPECTROSCOPY.* J. Chimie Physique Et De Physico-Chimie Biologique, 1970. **67**(1).
199. Wen, Q., Di, J., Zhao, Y., Wang, Y., Jiang, L. and Yu, Y., *Flexible inorganic nanofibrous membranes with hierarchical porosity for efficient water purification.* Chem. Sci. , 2013. **4**.
200. Daels, N.R., M., Radetic, M. Van Hulle, W.H.S. and De Clerck, K., *Functionalisation of electrospun polymer nanofibre membranes with TiO2 nanoparticles in view of dissolved organic matter photodegradation.* Separ. Purif. Technol. , 2014. **133**.
201. Fischer, K., Grimm, M., Meyers, J., Dietrich, C., Gläser, R. and Schulze, A., *Photoactive microfiltration membranes via directed synthesis of TiO2 nanoparticles on the polymer surface for removal of drugs from water.* J. Membr. Sci. 478, 49 (2015), 2015. **478**.
202. Ammerlaan, A.M.J., R.J. Mc Curdy, J.R. and Hurst, J.S., *International Patent WO 00/75087 A1* 2000.
203. Li, J.H., Yan, B.F., Shao, X.S., Wang, S.S., Tian, H.Y. and Zhang, Q.Q., *Influence of Ag/TiO2 nanoparticle on the surface hydrophilicity and visible-light response activity of polyvinylidene fluoride membrane.* Appl. Surf. Sci., 2015. **324**.
204. Li, J.F., Xu, Z.L., Yang, H., Yu, L.Y. and Liu, M., *Effect of TiO2 nanoparticles on the surface morphology and performance of microporous PES membrane.* Appl. Surf. Sci. , 2009. **255**: p. 4725.
205. Kissinger, G.a.K., W., Phys. Stat. Sol. (A), 1991. **123**.
206. Zhang, X., Wang, D. K., Lopez, D. R. S. and Diniz da Costa, J. C., *Fabrication of nanostructured TiO2 hollow fiber photocatalytic membrane and application for wastewater treatment.* Chem. Eng. J., 2014. **236**: p. 314-322.

207. Bai, H., Liu, L., Liu, Z. and Sun, D. D., *Hierarchical 3D dendritic TiO2 nanospheres building with ultralong 1D nanoribbon/wires for high performance concurrent photocatalytic membrane water purification.* Water Res., 2013. **47**(12): p. 4126-38.
208. Bai, H., Zan, X., Juay, J., and Sun, D. D., *Hierarchical heteroarchitectures functionalized membrane for high efficient water purification.* J. Memb. Sci., 2015. **475**: p. 245-251.
209. Mendret, J., Hatat-Fraile, M., Rivallin, M. and Brosillon, S., *Hydrophilic composite membranes for simultaneous separation and photocatalytic degradation of organic pollutants.* Sep. Purif. Tech., 2013. **111**: p. 9-19.
210. Mendret, J., Hatat-Fraile, M., Rivallin, M. and Brosillon, S., *Influence of solution pH on the performance of photocatalytic membranes during dead-end filtration.* Sep. Purif. Tech., 2013. **118**: p. 406-414.
211. Yang, S., et al., *Polypropylene membrane surface modification by RAFT grafting polymerization and TiO2 photocatalysts immobilization for phenol decomposition in a photocatalytic membrane reactor.* Separation and Purification Technology, 2011. **83**: p. 157-165.

Glossary

E_g: Band gap energy

$E_{CB,min}$: The minimal electronic energy level in conduction band

$E_{VB,max}$: The maximum electronic energy level in valence band

h: Planck constant

v: Velocity of light

c: Frequency of light

λ: Wavelength of light

e^-: Photo-generated electron

h^+: Photo-generated positive hole

F: Driving force

ΔX: Differential potential

δ: Membrane thickness

J: The flux through a membrane

r: Degradation rate

C: Concentration of the solution

t: Irradiation time

k_r: Reaction rate constant

θ_i: Surface coverage

r_{ads}: Adsorption rate

k_{ads}: Adsorption rate constant

r_{des}: Desorption rate

k_{des}: Desorption rate constant

K: Langmuir adsorption constant

k': First-order constant

n_e: Density of electrons in the plasma

n_i: Density of positive ions in the plasma

T_e: Temperature of electrons

T_e: Temperature of positive ions

λ_s: Thickness of sheath layer

F^i： Fluxes of particles in chemical vapor deposition (CVD) process

s_c: The striking coefficient,

k_d: The relative rate constants for neutrals

k_i: The relative rate constants for ion-induced components

N: Density of the atoms in the thin film

σ_f: Thin film stress

t_s: Substrate thickness

t_f: The film thickness

ρ: Radius of curvature

Y_f: Distance from neutral plane to a point in the film

E_s: Substrate Young's modulus

E_f: The film Young's modulus

T_s: Temperature of the substrate in the deposition chamber

$\mathrm{P}_{\mathrm{Ar+TTIP}}$: Partial pressure of argon and precursor in the deposition chamber

P_{O2}: Partial pressure of oxygen and precursor in the deposition chamber

$\mathrm{W}_{\mathrm{real}}$: The real power on upper electrode

W_{f}: Forward power from the generator

W_{r}: Reflected power to the generator

d_{p}: Plasma distance (i.e. the distance between the two electrodes)

T_p: Post-annealing temperature

D: Dimension of TiO_2 nanocrystal

$\Delta 2\theta_{FWHM}$: Full-width at half maximum of XRD peak at 2θ angle

n: Refractive index

k: Optical absorption coefficient

R_{ST}: Photodegrading conversion rate of stearic acid

I_0: Intensity of incident light

ε: Molar extinction coefficient

l: The length of light path

V: Volume of the solution

Δt: Measuring duration

S: Membrane surface area

M_0: The initial amount (mol) of organic solute in feed tank

M_i: The total amount (mol) of organic solute in feed tank at instant time

R_{AO7}: Photodegrading conversion rate of acid orange 7

R_{MB}: Photodegrading conversion rate of methylene blue

δ_{MB}: Destroyed amount (mol) of methylene blue per unit reaction time and per membrane surface area

J_{water}: Pure water flux through membrane

c_i: Concentration of i-component (the organic solute) in solution

τ: Adsorption time or reaction time

V: Volume of solution

V_{MS}: Volume of TiO_2-ceramic composite membrane

δ_M: Thickness of TiO_2 coating layer

δ_S: Thickness of ceramic support

ρ_M: Density of TiO_2 coating layer

ρ_S: Density of ceramic support

ε_M: Porosity in TiO_2 coating layer

ε_S: Porosity in ceramic support

r_{ads}^M: Adsorption rate in TiO_2 coating layer

r_{ads}^S: Adsorption rate in ceramic support

q_i^M: Concentration of adsorbed i-component in photocatalyst TiO_2 layer

q_i^S: Concentration of adsorbed i-component in ceramic support

q_*^M: Concentration of adsorption sites in TiO_2 layer

A_M: Surface area of TiO_2-ceramic composite membrane

D_{Mi}: Diffusion coefficient of organic solute in TiO_2 coating layer

D_{Si}: Diffusion coefficient of organic solute in the ceramic support

x: Axial coordinates along the thickness of membrane

Q_{sat}: Adsorbed amount of organic solute at saturation

k_a or k_{ads}: Adsorption rate constant

k_d or k_{des}: Desorption rate constant

D_S: Diameter of the ceramic support

C_{eq}: Equilibrium concentration of the organic solution

k_a^S: Adsorption rate constant in the ceramic support

k_d^S: Desorption rate constant in the ceramic support

Θ_{eq}: Equilibrium surface coverage

K_{eq}: Equilibrium constant of sorption

Θ_{eq}^S: Equilibrium surface coverage of the ceramic support

K_{eq}^S: Equilibrium constant of sorption of the ceramic support

K_{ads}^M: Equilibrium constant of sorption of TiO_2 layer

Z: Axial coordinate

D_{ax}: Axial dispersion coefficient

D_{Si}: Effective axial dispersion coefficient in ceramic support

D_{Mi}: Effective axial dispersion coefficient in photocatalyst TiO_2 layer

v: Velocity

$\mathcal{V}_{ij}^{b}$: Stoichiometric coefficient in bulk reaction in tube

r_b: Reaction rate of bulk reaction in tube

$\mathcal{V}_{ij}^{s}$: Stoichiometric coefficient in surface reaction in tube

r_s: Reaction rate of surface reaction

$\mathcal{V}_{ij}^{RC}$: Stoichiometric coefficient in retentate compartment

r_j^{RC}: Reaction rate of bulk reaction in retentate compartment

r_t: Radius of tube

L_t: Length of tube

V^{FT}: Volume of solution in feed tank

V^{RC}: Volume of solution in retentate compartment

V^{PT}: Volume of solution in permeate tank

c_i^{FT}: Molar concentration of i-component in feed tank

c_i^{P} or c_i^{PC}: Molar concentration of i-component in permeate solution

c_i^{R} or c_i^{RC}: Molar concentration of i-component in retentate solution

c_i^{M}: Molar concentration of i-component in membrane

$\dot{V}^{F}$: Volumetric flow of feed solution

$\dot{V}^{P}$: Volumetric flow of permeate solution

$\dot{V}^{R}$: Volumetric flow of retentate solution

s_f: Separative factor (s_f = 0 no permeate cycling and s_f = 1 all permeate cycling to feed tank)

π_w: Water permeance through the membrane

p^P: Pressure in permeate compartment

p^R: Pressure in retentate compartment

Δp: Cross-membrane pressure drop

$\overline{V}_M$: Local interstitial fluid velocity in porous space of TiO_2 layer

r_{ads}^M: Rate of adsorption of i-component in photocatalyst TiO_2 layer

r_{dec}^M: Rate of photocatalytic decomposition of i-component in TiO_2 layer

c_h: Concentration of photo-generated holes in photocatalyst TiO_2

k_{dec}: Photocatalysis decomposition constant

Nouvelles membranes photocatalytiques poreuses à base de TiO_2 préparées par dépôt chimique en phase vapeur assisté par plasma (PECVD) pour la dégradation de polluants organiques dans les technologies de traitement d'eau.

Résumé :

Le dépôt chimique en phase vapeur assisté par plasma est appliqué pour préparer des couches minces amorphes de TiO_2 à basse température. Un recuit à 300 °C pendant un temps minimum de 4,5 h permet de former la phase cristalline anatase. Les principales caractéristiques de ces couches minces comme leur structure cristalline, leur microstructure, leur largeur de bande interdite et leur hydrophilie de surface, sont déterminées. Leurs performances fonctionnelles comme photocatalyseurs sont d'abord examinées selon le test breveté par Pilkington, consistant à éliminer sous irradiation UV de l'acide stéarique préalablement adsorbé sur les couches de TiO_2 ici déposées sur des plaquettes de silicium. Des membranes M100 (couche continue de TiO_2) et M800 (couche de TiO_2 couvrant les grains de support) sont préparées sur les couches de surface macroporeuses de supports poreux en alumine, de tailles moyennes de pores respectives, 100 nm et 800 nm. Ces membranes sont testées en condition "statique", avec la diffusion d'un soluté organique dilué dans l'eau. Pour le bleu de méthylène, on montre que la quantité de composé détruit par unité de surface de membrane et par unité de temps est égale à 2×10^{-8} mol m^{-2} s^{-1} pour la membrane M100 et 1×10^{-8} mol m^{-2} s^{-1} pour la membrane M800. Ces membranes sont également testées dans des conditions "dynamiques", à savoir en procédé baromembranaire, avec deux configurations différentes (couche photocatalytique du côté de l'alimentation ou du côté du perméat) et trois composés organiques différents (bleu de méthylène, acide orange 7 et phénol). La modélisation du procédé (adsorption et réaction photocatalytique) est finalement réalisée à partir des données expérimentales disponibles.

Mots clés : Membrane photocatalytique ; PECVD ; photodégradation de composés organiques; Modélisation de procédé.

Novel photocatalytic TiO_2-based porous membranes prepared by plasma-enhanced chemical vapor deposition (PECVD) for organic pollutant degradation in water treatment technology.

Summary:

Plasma-enhanced chemical vapor deposition is applied to prepare amorphous TiO_2 thin films at low temperature. Post-annealing at 300 °C for minimal staying time 4.5 h is required to form crystalline anatase phase. Characteristics of the TiO_2 thin films including crystalline structure, microstructure, band gap and surface hydrophilicity, are determined. Functional performance of these anatase thin films as photocatalysts is first examined with patented Pilkington assessment by removing, under UV irradiation, stearic acid initially adsorbed on TiO_2 layers here deposited on silicon wafers. Membranes M100 (TiO_2 continuous layer) and M800 (TiO_2-skin on support grain) are prepared on the macroporous top layer of porous alumina supports with an average pore size of 100 nm and 800 nm, respectively. These membranes are tested in "static" condition under the effect of diffusion of an organic solute in water. For Methylene Blue it is shown that the quantity of destroyed compound per unit of membrane surface area and per unit of time is equal to 2×10^{-8} mol m^{-2} s^{-1} for M100 and 1×10^{-8} mol m^{-2} s^{-1} for M800. These membranes are also tested in "dynamic" conditions, i.e. pressure-driven membrane processes, with two different configurations (photocatalytic layer on the feed side or on the permeate side) and three different organics (Methylene Blue, Acid Orange 7 and phenol). Process modeling (adsorption and photocatalysis reaction) is finally carried out from the available experimental outputs.

Keywords: Photocatalytic membrane; PECVD; organics photodegradation; process modeling.